UTILIZATION OF SUPERCRITICAL FLUIDS IN THE FISCHER-TROPSCH

SYNTHESIS OVER COBALT-BASED CATALYTIC SYSTEMS

Except where reference is made to the work of others, the work described in this thesis is my own or was done in collaboration with my advisory committee. This dissertation does not include proprietary or classified information.

_____

Nimir O. M. Elbashir

Certificate of Approval:

_____	_____
James A. Guin Professor Chemical Engineering	Christopher B. Roberts, Chair Uthlaut Professor Chemical Engineering
_____	_____
Said S. E. H. Elnashaie Professor Chemical Engineering	Ram B. Gupta Alumni Professor Chemical Engineering
_____	_____
Gerald P. Huffman Professor Chemical and Materials Engineering University of Kentucky	Stephen L. McFarland Dean, Graduate School

UTILIZATION OF SUPERCRITICAL FLUIDS IN THE FISCHER-TROPSCH SYNTHESIS OVER COBALT-BASED CATALYTIC SYSTEMS

Nimir O. M. Elbashir

A Dissertation

Submitted to

the Graduate Faculty of

Auburn University

in Partial Fulfillment of the

Requirements for the

Degree of

Doctor of Philosophy

Auburn, Alabama

December 17, 2004

DISSERTATION ABSTRACT

UTILIZATION OF SUPERCRITICAL FLUIDS IN THE FISCHER-TROPSCH SYNTHESIS OVER COBALT-BASED CATALYTIC SYSTEMS

Nimir O. M. Elbashir

Doctor of Philosophy, December 17, 2004
(M.Eng. (Chemical) Universiti Teknologi Malaysia, 1998)
(B.Sc. (Honors) Chemical Engineering, University of Khartoum, 1994)

Directed by Christopher B. Roberts

Fischer-Tropsch synthesis (FTS) holds great potential for the production of ultra-clean transportation fuels, chemicals, and other hydrocarbon products through the conversion of readily available syngas (CO/H_2) from abundant resources (coal, natural gas, and biomass). Utilization of supercritical phase in FTS as a medium that has superior properties (liquid-like density and heat capacity, and gas-like diffusivity) represents a new challenge to the 80-years old FTS technology. The objective of this research is to establish optimum operating conditions for FTS within the supercritical region that would maximize the production of value added chemicals and middle distillate hydrocarbons (gasoline fuel, jet fuel, and diesel fuel fractions) and at the same time minimize the production of methane and carbon monoxide. Chapters 3-5 of this dissertation are designed to examine the effects of supercritical fluid (SCF) (*n*-pentane or hexane) on FTS

over an alumina supported cobalt catalyst in a fixed-bed-reactor. The influence of reaction conditions (such as temperature (210-260 °C), pressure (20-80 bar), syngas feed ratio (H_2/CO ratio of 0.5-2), contact time and space velocity (50-150 sccm/g_{cat})) on the FTS activity, selectivity, and hydrocarbon product distributions in the supercritical fluids (SCF) media was studied. Our results show that the adjustable thermophysical properties of the SCF significantly impact the FTS reaction performance and in most cases the SCF-FTS operations yield higher activity and better selectivity towards the most desired products compared to conventional gas-phase FTS operations. An excellent opportunity to maximize the production of desired fuel fractions, through a simple tuning process of the reaction environment from liquid-like properties to vapor-like properties, can be achieved in the SCF-FTS conditions as discussed in Chapter 4. An approach to understand the enhanced chain growth probability in SCF-FTS conditions is reported in Chapter 5. This phenomenon was attributed to the enhanced α-olefins incorporation in the chain growth process. Chapter 6 covers a preliminary examination of the kinetics of the FTS reactions under high-pressure high-temperature conditions in both conventional gas-phase FTS and supercritical hexanes FTS (SCH-FTS). Our findings illustrate that the classical surface reaction kinetics model fails to predict the rates in the SCH-FTS. Our findings also show that the cobalt-based catalytic systems show excellent stability in terms of activity and selectivity as well as their structure under the SCF-FTS conditions for relatively long time-on-stream (up to 13 days). The influence of the cobalt-based catalyst characteristics on the FTS performance in both SCH-FTS and conventional gas-phase FTS is addressed in Chapters 7 and 8.

ACKNOWLEDGEMENTS

My sincere appreciation and gratitude goes to Prof. Christopher Roberts, my research advisor. Prof. Roberts' kindness, support, scientific guidance, and friendship that he offers to his research group, colleagues, and everyone around him, including myself, always lead to success.

Prof. Roberts and I are very grateful for the financial support of this research by the Consortium of Fossil Fuel Science (CFFS), and also for Nippon Oil Corporation (Japan). I would like to extend an acknowledgment to my colleague Dr. Xiwen Huang, for his contribution in this research especially in experimental and writing of Chapter 3. I am also grateful to my colleagues from the SCF research group; Christopher Kitchens, Chandler McLeod, Philip Bell, Deborah Borough, Madhu Anand, Daniel Obrzut, and John Abner for their invaluable scientific discussions, technical assistants, and continuous support. My acknowledgments are also extended to Prof. Mohindar Seehra and his research group (Dr. Prasanta Dutta, and Mani Manivannan) at West Virginia University for assisting us in the characterizations of our catalysts and writing the publications included in Chapters 7 & 8.

I am very grateful to my committee members; Prof. Said Elnashaie (and his research group), Prof. James Guin, and Prof. Ram Gupta. My gratitude also extended to Prof. Gerald Huffman (University of Kentucky, and the Director of the Consortium of Fossil Fuel Science) for his kind acceptance to serve as a committee member for this

research. My sincere gratitude also goes to Prof. Mahmoud El-Halwagi (University of Texas A&M and former Professor at Auburn University), and to Prof. Ahmed Abasaeed (King Saud University, and Alumni of Auburn University) for helping me to join the graduate program at Auburn University.

I would also like to acknowledge the continuous support and valuable scientific discussion of my friends and colleagues Mukund Karanjikar, and Fadwa Eljack. I would like to acknowledge the kindness of Sue Ellen Abner the Administration Assistant at the department which eases the life of all graduate students in the department.

Last, but absolutely not least, to my wife Dr. Magda Barkat, my kids (Ryan, Ahmed, and Munira), and to my parents to whom I dedicate this work. Their care and support has paced the road that has led to this stage of my career.

TABLE OF CONTENTS

LIST OF TABLES

LIST OF FIGURES

CHAPTER 1

FISCHER-TROPSCH SYNTHESIS TECHNOLOGY

1.1 Importance of the Fischer-Tropsch Synthesis and Gas-To-Liquid (GTL) Technologies

Extensive research efforts in the past eight decades have focused on the utilization of C_1-chemistry as a future resource for fuels and chemicals. C_1-chemistry refers to the utilization of single carbon-bearing molecules; such as carbon monoxide, syngas (a mixture of CO and hydrogen), carbon dioxide, methane, and methanol for the production of valuable chemicals, petrochemical intermediates, and ultra-clean transportation fuels. C_1-chemistry could also be used to produce high-purity hydrogen or premium chemicals from synthesis gas or from methanol. The main resources of C_1 molecules are natural gas, coal, biomass, and organic wastes. According to the Energy Information Administration (EIA), natural gas is projected to be the fastest-growing component of primary world energy consumption up to 2020, closely followed by coal (see Fig 1.1) (EIA 2001). Because of the abundance of those raw materials in the environment C_1-chemistry has become a major area of research interest for the production of highly pure chemicals and transportation fuels.

One of the best known and most important routes for the conversion of coal, natural gas and biomass to fuels is through their conversion to an intermediate synthesis

gas (or syngas), a mixture of CO and H_2. The utilization of syngas started at the beginning of the 20th century by the production of methane from the hydrogenation of carbon monoxide in 1902. This was followed by the discovery of the Fischer-Tropsch synthesis and its subsequent use to manufacture methanol and higher alcohols (Wender 1996). The use of syngas offers the opportunity to furnish a broad range of environmentally clean fuels, additives and chemicals. A flow chart of the wide spectrum of syngas applications is shown in Figure 1.2 (Stelmachowski and Nowicki 2003).

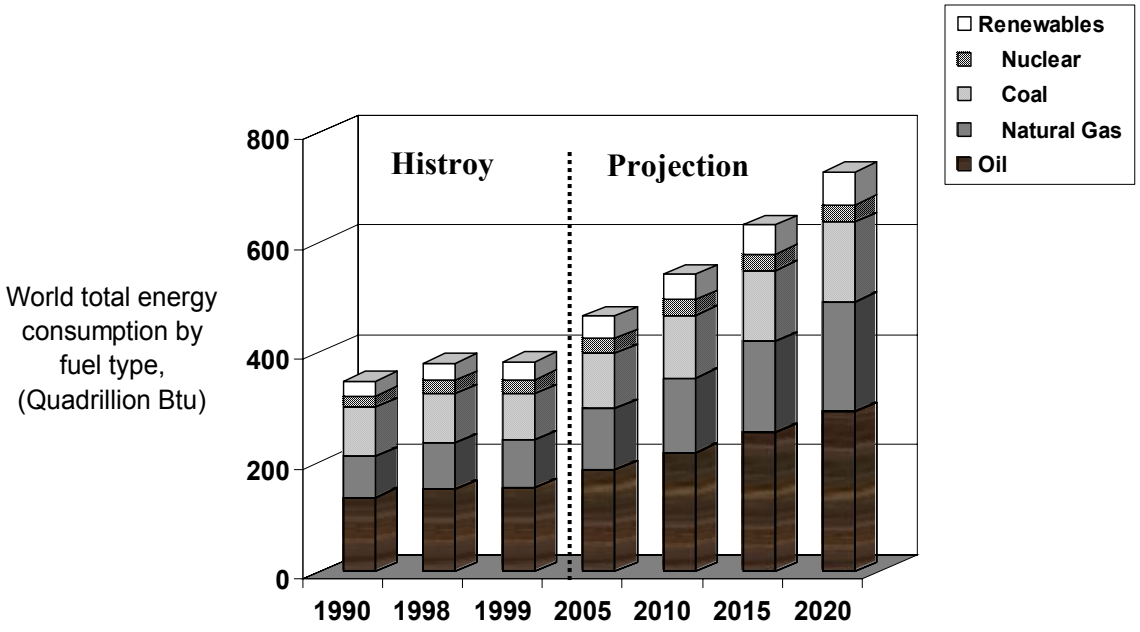

Figure 1.1 The total world energy consumption by fuel type from 1990 projected to 2020 (EIA, International Energy Outlook 2002 Report (EIA 2001)).

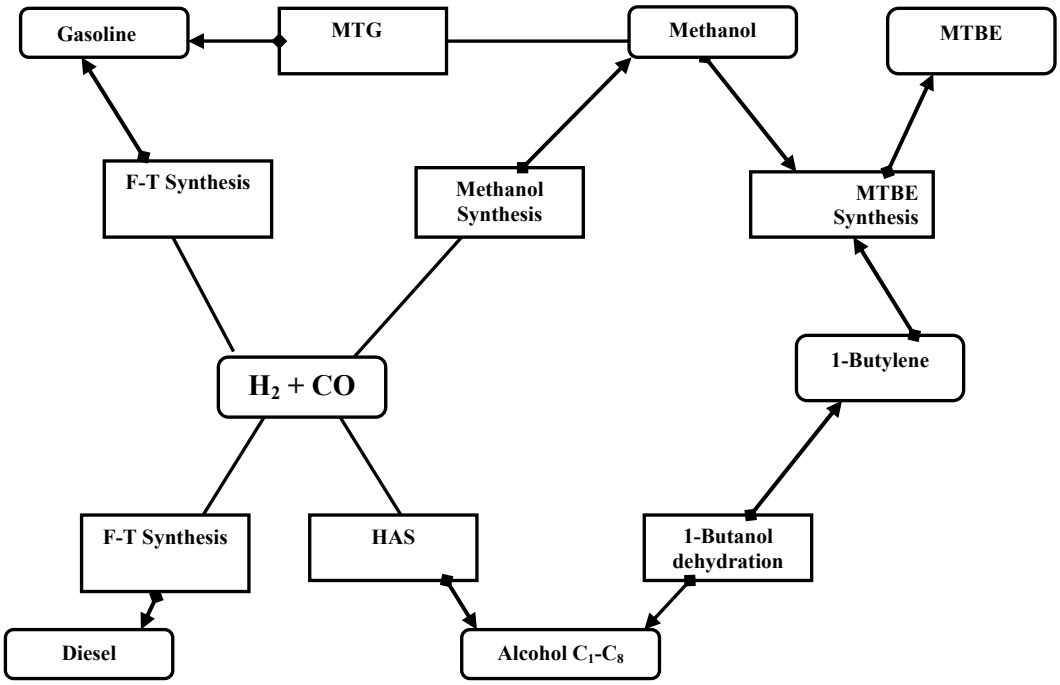

Figure 1.2 Applications of syngas to generate fuels, additives, or intermediate products for further synthesis (Stelmachowski and Nowicki 2003).

Fischer-Tropsch synthesis (FTS) involves the catalytic conversion of syngas (H_2, and CO) to ultra clean transportation fuels (gasoline and diesel fractions), chemical intermediates, oxygenates and heavy wax. In the near future, increasing demand for fuels derived from coal and natural gas is a virtual certainty. The FTS reaction takes place on a catalyst surface of Co, Fe, Ru, Ni, etc. or mixed catalysts. The key challenge in applying the Fischer-Tropsch process to produce transportation fuels is to make the capital production cost economically feasible relative to the comparatively low cost of existing petroleum resources (Roberts and Elbashir 2003).

Utilization of coal and natural gas in syngas production and thus for Gas-To-Liquid applications has recently become a major part of the U.S. Department of Energy

(DOE) "Vision 21" program (Wolfe and Mills 1999). "Vision 21" is an effort to develop the "energy plant of the future," an advanced multi-fuel power concept that would produce electricity, fuels and chemicals, and other marketable products with unprecedented efficiencies and virtually no pollutants. Recently, the U.S. DOE, in a joint program with Syntroleum Corp. and other companies, has started a new ultra clean transportation fuel plant in Tulsa, Oklahoma that uses FTS for the production of approximately 4,000 gallons per day of high-performance, sulfur free, environmentally-friendly transportation fuel from 1 million cubic feet of natural gas (Lopatto and Malcomb 2003). Also, the DOE has concentrated its efforts on a coal program that emphasizes activities through 2010 and is focused almost exclusively on power generation technologies and production of ultra-clean fuels using Fischer-Tropsch technology (Wolfe and Mills 1999). Coal is by far the largest fossil fuel resource in the U.S., with known reserves adequate to meet expected demand without major increases in production costs well beyond the year 2010 (EIA 2001). In contrast, domestic natural gas, its principal fossil fuel competitor for power generation, is a more limited resource and increases in production cost and decreased availability are projected to occur after the year 2000 (Yakobson 2003). For the manufacture of liquid and gaseous fuels, coal is projected to become competitive with other resources (petroleum, oil shale and bitumen) in the 2021–2040 time period (EIA 2001).

1.2 History of the Fischer-Tropsch Technology Invention and Application

The lack of a domestic petroleum supply in Germany at the beginning of the 20th century encouraged the government at that time to devote an amazing amount of

diligence and money towards research on alternative fuel resources. The German researchers mainly focused on the conversion of their abundant coal supplies into synthetic liquid fuels as part of the drive to make their country energy independent (Stranges 2003a). In early1923, Franz Fischer (1877-1947) and Hans Tropsch (1889-1935) at the Kaiser-Wilhelm Institute for Coal Research (KWI) in Mülheim, Ruhr, invented a process for the conversion of syngas, into higher gaseous, liquid, and solid hydrocarbons. This process was carried out in a catalytic reactor under atmospheric pressure in the presence of iron and cobalt catalysts (Fischer and Tropsch 1926c). This invention was soon upgraded to an industrial plant by Ruhrechemie A. G. (Oberhausen, Germany) in 1935. Within a short period of time, eight industrial plants using Fischer-Tropsch technology for fuel production were operating in Germany (Pichler 1952). Meanwhile, many countries in Europe (France, and Great Britain), Asia (Japan), and North America (United States) built their own plants using the technology developed by Fischer and Tropsch. One of the first and largest commercial plants in the United States for the production of liquid fuels from carbon monoxide and hydrogen was designed by Hydrocarbon Research Inc., for Carthage Hydrocol, Inc. and went into operation in 1950, in Brownsville, Texas.

Fischer and Tropsch played a key role in the development of this technology (Fischer and Tropsch 1925a; Fischer and Tropsch 1926c; Fischer and Tropsch 1926a; Fischer and Tropsch 1926b; Fischer and Tropsch 1928; Fischer and Tropsch 1932), however, many scientists contributed to the development of the synthesis of liquid fuels. Friedrich Bergius (1884-1949) in Rheinau-Mannheim began the German drive for energy independence with his invention and early development of high-pressure coal

hydrogenation or liquefaction in the years 1910-25 (Stranges 2003a). A decade after Bergius began his work Fischer and Tropsch invented the second important process for the synthesis of liquid fuel FTS technology.

The Bureau of Mines in the United States established a program to develop a coal-based supply of transportation fuels in 1943. This work involved both direct and indirect processes and was under the direction of H. H. Storch (Davis 2003b). At that time, the United States petroleum production was not significantly hampered by the war effort and the industry expanded to provide about four of the five billion barrels of fuel needed for the Allied effort in Europe (Davis 2002). In 1925, almost 70% of the world's petroleum was produced by the United States, however, during the 1940s there was a serious fear that the United States and the world were running out of petroleum.

Before engaging in the design and operation of the coal liquefaction plants, the Bureau of Mines was involved in reviewing and translating documents retrieved from Germany following World War II, as well as providing experts for several of the teams that surveyed the German plants and interviewed personnel who worked in the plants (Davis 2003b). Bureau workers concluded that by 1944, most of the basic ideas for the design of Fischer-Tropsch reactors had been formulated and tested on at least a pilot-plant scale. Much of the Bureau work concentrated on synthesis with the catalyst in the liquid phase, and most of the emphasis was on the oil recirculation process (Davis 2003b). The catalytic systems tested were primarily cobalt, iron, and nickel in a combination of gas and oil circulation from bottom to top of the reactor to maintain the catalyst in suspension inside the reactor.

Just before World War II, Japan established a scientific agreement with Germany that would allow them to transfer many of the newly invented German technologies (Stranges 2003b). Japan, a country with a huge population faced at that time major challenges in maintaining its supplies of many essential natural resources, including petroleum, coal, and iron ore. To achieve independence in petroleum, the Japanese developed a dual approach: they would acquire natural petroleum sources in Southeast Asia and at the same time establish a synthetic fuel industry for the conversion of coal to oil. Actually, the Japanese had begun research on synthetic fuel in the 1920s, only a few years after other countries like Germany and Britain that also lacked sources of natural petroleum (Stranges 2003b). The Japanese scientists conducted an excellent laboratory scale demonstration of coal hydrogenation and FTS at that time; however, they did not enjoy the same success in large-scale production. This unsuccessful attempt was attributed by many historians to the bypass of intermediate plant levels and their rush to construct large synthetic plants (Stranges 2003b).

Research interest in the Fischer-Tropsch technology in Russia began in about 1920, at the Institute of Organic Chemistry of the USSR Academy of Sciences. Prof. Ya. T. Eidus and later his student and colleague Prof. A. L. Lapidus established a strong scientific school that created most of the Russian published literature in Fischer-Tropsch Technology (Anikeev et al. 2003). The main emphases were on the design of new catalysts for Fischer-Tropsch processes and the modification of existing catalysts based on cobalt, iron, copper, manganese, etc (Eidus and Zelinskii 1942; Eidus 1944). The effect of various promoters on the reaction rate and mechanism were studied. Much

attention was focused on the effect of support, catalyst preparation and regeneration procedures.

Sasol Company, South Africa's largest oil company, has played a major role in recent developments in FTS technologies, especially in the reactor design and new catalytic systems. The worldwide climate in the 1940s and the high consumption levels of crude oil reserves, followed by significant increases in the price of crude oil in the 1950s, led to the construction of Sasol One (the first project and Fischer-Tropsch plant owned by Sasol) (Dry 1996). As the result of sharply rising crude oil prices in the 1970s, Sasol expanded its operations by developing two new plants, Sasol Two and Sasol Three, in 1980 and 1982, respectively. The major technical contribution of Sasol is its scaling-up of Kellogg's pilot plant unit with a capacity of 4–5 bbl/day, to the first two commercial Circulated Fluidized Bed (CFB) units with an approximate capacity of 2200 bbl/day, at Sasolburg, South Africa. Sasol also invented Sasol Advanced Synthol (SAS) technology that uses a less-expensive reactor without the CFB complexity of the reactor–hopper–standpipe system suspended in a complex structure (Duvenhage and Shingles 2002). Time lines showing the development of Sasol's reactors developments are given in Figures 1.3 and 1.4.

One of the reasons for Sasol One's survival was that besides liquid fuel, it also produced high priced Fischer-Tropsch waxes. From 1955 up to 1993, Sasol used only Arge tubular fixed bed reactors (TFBR's) for low temperature FTS (LTFT). In 1993, after a 10-year research program, a slurry phase reactor (2500 bbl per day) for LTFT synthesis was commissioned (Espinoza et al. 1999). The commercialization of the slurry

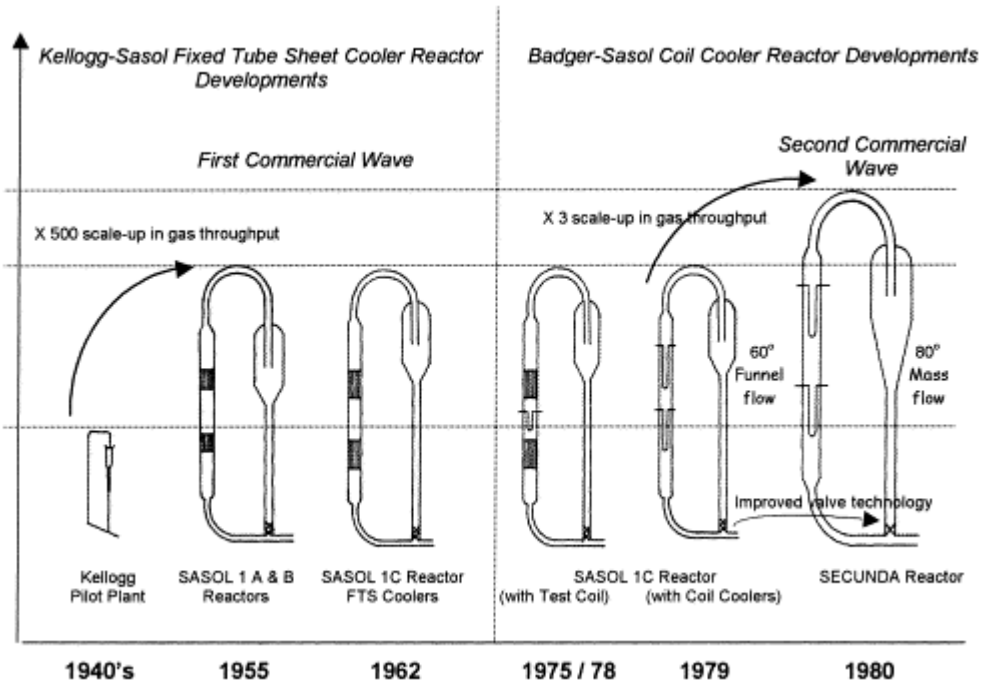

Figure 1.3 Synthol CFB reactor developments. (Duvenhage and Shingles 2002)

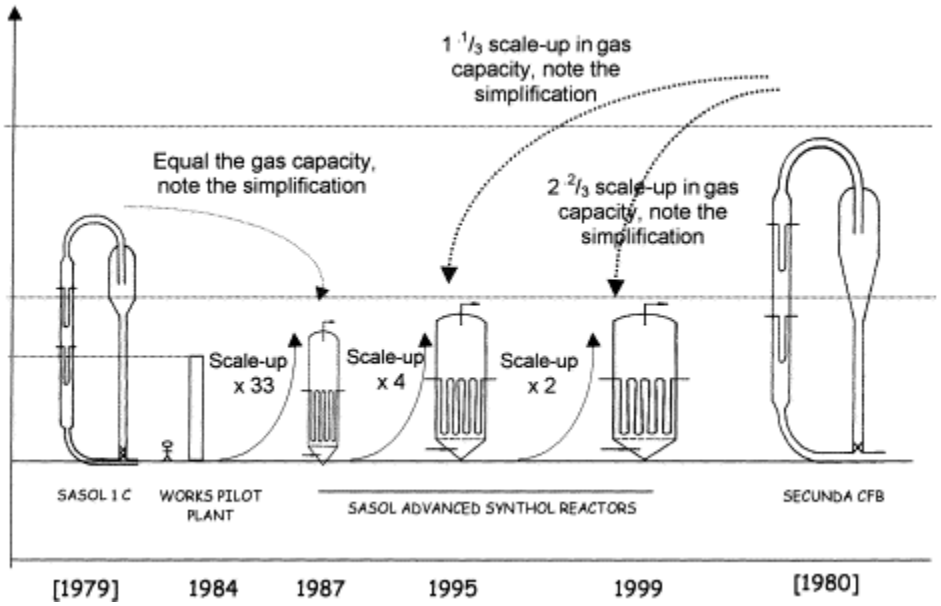

Figure 1.4 Synthol reactor developments: CFB to SAS. (Duvenhage and Shingles 2002)

phase technology for FTS applications was made possible by the development of Sasol's proprietary catalyst/wax separation process. Sasol converts 45 million tons per year of coal into over 150,000bbl/day fuels and chemicals via Fischer-Tropsch technology with annual turnover of about 3 billion U.S. dollars (Hill 1999). More recently, the Mossgas synthetic fuels plant was constructed in Mossel Bay. This plant produces liquid fuels through the synthesis of natural gas and condensates from offshore fields using similar technology. There have been discussions about the possibility of Mossgas becoming a site for petrochemical production. Recently, many countries are becoming involved in developing or using existing Fischer-Tropsch technologies for the production of liquefied fuels from natural gas and coal. In 1985, a synfuel plant based on Mobil's MTG technology came on stream in New Zealand (Dry 1996). In 1993, Shell commissioned a fixed bed (cobalt based catalyst) Fischer-Tropsch operation in Malaysia. QGPC, Phillips, and Sasol are developing a new Gas-To-Liquid (GTL) plant in Qatar, a joint venture with shares of 51%, 15%, and 34%, respectively (Hill 1999). Chevron Nigeria and Sasol are also developing a new plant at Escravos River in Nigeria that expected to be in operation by 2009, with capacity of 30000 bbl/day of diesel and naphtha.

1.3 Fischer Tropsch Catalysts

1.3.1 Cobalt-Based Catalysts

The production of liquid hydrocarbons over cobalt catalysts was first reported in 1913 in a patent granted to BASF; in that patent the conversion of CO and H_2 takes place

at very high pressures (100 atm and more) and relatively high temperatures (>300 °C) (Pichler 1952). The first industrial application of the Fisher-Tropsch technology utilizing catalysts was based on a cobalt catalyst, but it operated under atmospheric or low pressure conditions (Stranges 2003a). Cobalt catalytic systems for FTS then passed through several developments, started from simple moderately-active Kieselguhr-supported cobalt promoted with thorium to sophisticated, high-activity, highly-optimized catalysts supported on alumina, silica, or titania and promoted with noble metals and basic oxides. The design of the Co catalytic systems for FTS was initially done by trial and error, based on reactor experimental investigations. Nowadays, very sophisticated techniques are used to control the distribution of the metal(s) on the support at a nanoscale using state-of-the-art advanced characterization techniques, such as x-ray diffraction (XRD), transmission electron microscopy, electron magnetic resonance (EMR), and so on.

Advances in cobalt catalyst design during the last 90 years have been categorized according to the following historic periods (Bartholomew 2003): (1) discovery (1902-1932), (2) commercial development of cobalt and iron catalysts (1933-1954), (3) the iron age (1950-1985), (4) rediscovery (1973-1990), and (5) GTL and the return to cobalt (1990-present). During the first period, cobalt catalysts were established as the most active and selective for FTS. During the second period, commercial processes based on cobalt catalysts technology was developed in Germany significantly improved their ability to produce gasoline and chemicals from coal. Supported cobalt catalysts are important for the FTS of high molecular weight, paraffinic waxes which can then be

hydrocracked to produce lubricants and diesel fuels. Advances in cobalt catalytic systems are focused on improving the catalyst activity by increasing the number of active Co metal sites that are stable under reaction conditions. Therefore, most of the recent studies have focused on the structural parameters of the catalyst and its influence on the activity and the stability (Craxford 1947; Fan et al. 1992; Iglesia 1997b; Iglesia 1997a; Ernst et al. 1999; Kraum and Baerns 1999). For example, to improve the number of active sites, the Co is most often present as dispersed clusters on a high surface area support such as SiO_2, TiO_2, or Al_2O_3. Cobalt catalysts are known to be sensitive to the reaction conditions, specifically pressure, as the product distribution of hydrocarbons varies with total pressure as seen in Figure 1.5. As shown in the figure the density (g/cm^3) of produced hydrocarbons such as diesel fraction and paraffin components was found to be dependent on the pressure. Figure 1.5 also shows an existence of optimum pressure for those fractions for the low pressure operation (< 20 atm). As shown in the same figure light hydrocarbons and gasoline fractions were likely to decrease as the pressure increases (Pichler 1952). The loading of the metal on the support also influences the overall activity of the catalyst, as seen in Figure 1.6. At low metal loadings and relatively high dispersions, C_{5+} selectivity increases with decreasing dispersion and/or increasing metal loading (due to a decreasing metal-support interaction with decreasing dispersion, resulting in less methane formation and an increasing extent of olefin readsorption (Iglesia 1997b).

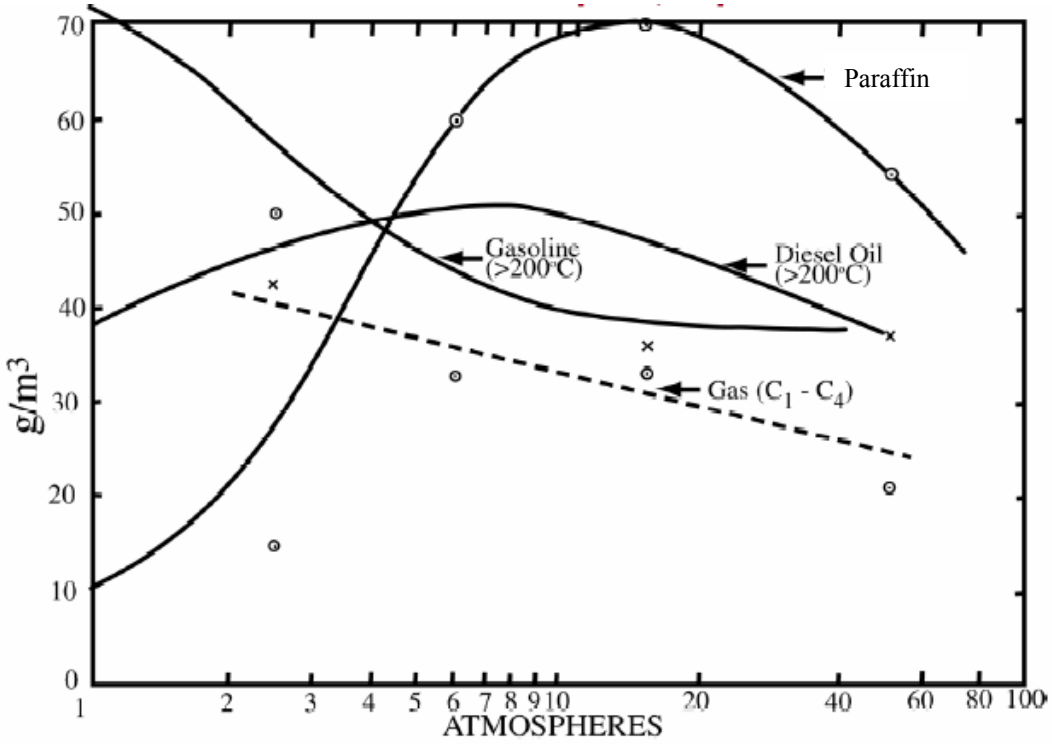

Figure 1.5 Effect of the pressure on the FTS selectivity of cobalt catalyst (Pichler 1952).

In general, cobalt catalysts are found to give the highest yields and have the longest life time, producing mainly linear alkanes (paraffins) (Chaumette et al. 1995). Since cobalt catalysts are not inhibited by the water-gas-shift (WGS), they make possible a high productivity for higher syngas conversion (Van Berge and Everson 1997). This property illustrates the major difference between cobalt catalysts and iron catalysts for FTS reactions, as the latter is known for its high WGS activity. For each hydrocarbon (e.g. CH_2) formed during the synthesis, the cobalt catalyst will produce water while the iron catalyst will produce CO_2. Water vapor has been shown to influence the performance of the cobalt catalysts in a variety of ways. For example, it was observed that water

reversibly enhances the activity of some cobalt catalysts, but not all (Iglesia 1997a; Li et al. 2002a). Other studies also reported an inhibition effect of water vapor on the catalyst's activity (Hilmena et al. 1999).

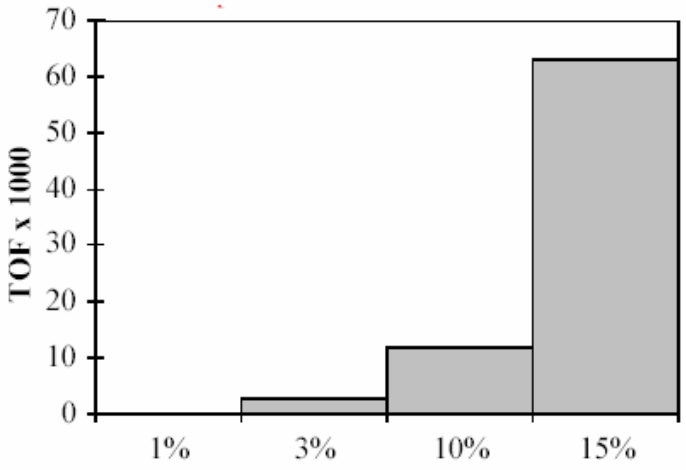

Figure 1.6 Effect of cobalt loading on the turn-over-frequency (Bartholomew and Reuel 1985).

1.3.2 Iron-Based Catalysts

Iron group metals have been used in FTS by converting them to interstitial compounds, carbides, nitrides and borides, and mixed compounds of two or more of the interstitial elements, such as carbonitrides (Anderson 1984). Precipitated and fused iron catalysts are examples of FTS iron catalysts. These catalysts are typically oxides before use and need to be activated by reduction to the zero valent state. The activation procedure generally involves reducing with hydrogen to metallic iron or with carbon

monoxide or syngas to various iron carbides. Phase transition on iron catalysts normally takes place during the FTS reaction, either due to one of the products (such as water) or the operating conditions (namely reaction temperature). Mössbauer spectroscopy has proven to be the ideal way to obtain quantitative analysis of the phases present in Fe catalysts (Anderson 1984; Li et al. 2001).

FTS catalysts based on Fe provide an attractive complement to Co-based catalysts. Fe-based catalysts produced more olefinic compounds and lower propotions of methane and paraffins than Co-based catalysts. They can also work at relatively higher temperatures for a wide range of syngas feed ratios. Co based-catalysts normally work at low temperatures (190 °C- 230 °C) in order to obtain the desired selectivity of C_{+5} hydrocarbons and control the quality of diesel fuels, which may be affected by the high temperature operations (Brady and Pettit 1981). The lower apparent FTS rates on Fe-based catalysts have been linked to the lower dispersion of their active components (Schulz 1999). Therefore, the increase in the surface area and in the density of active sites during synthesis and during the initial stages of use in synthesis gas have been assumed to bring Fe-based catalysts into the range of productivity and reaction conditions typical of Co-based catalysts (Li et al. 2002b). Recent developments in Fe-based catalysts have focused on controlling the dispersion of the metals on the active sites to produce catalysts that are active at low temperatures and with low selectivity towards CO_2. Such active Fe-based catalysts would also allow direct comparisons of FTS turnover rates on Fe and Co catalysts under similar conditions. Such comparisons require reliable measurements of the number of exposed active components in both catalysts (Li et al. 2002b).

1.3.3 Ruthenium-Based Catalysts

Ruthenium based catalysts have been applied to the reduction of carbon monoxide to methane since the mid 1920s giving the best results with the highest selectivity towards value added chemicals and activity in this reaction (Fischer and Tropsch 1925b). During the 1970s, researchers from Gulf Oil discovered that catalysts containing a small amount of Ru (1wt% Ru) give much higher activity than catalyst containing high amounts of Co (20% Co) (Cornils et al. 1994). Ru has been chosen as an ideal catalyst by many workers in FTS, because Ru is neither oxidized nor carburized during synthesis.

Ruthenium catalysts also show high activity in FTS at low reaction temperatures (<150 °C) compared to Fe-based and Co-based systems (Vannice 1976). Even though FTS reactions over Ru-based catalysts normally require high synthesis gas pressures (>100 bar), they produce high molecular weight hydrocarbons via "polymethylene synthesis" (Schulz and Claeys 1999). This offers a good opportunity to understand the mechanism of the reaction and to develop the catalytic performance based on simple chain growth model. One more advantage of the Ru-based catalysts is that water (a by-product of the synthesis) has no influence on their activity since ruthenium is active even if suspended in liquid water and thus has an inbuilt resistance to in situ oxidation (Vannice 1976; Kellner and Bell 1981; Iglesia et al. 1993a). Nevertheless, ruthenium-based catalytic systems are quite expensive and so far they are limited to research purpose (have not been used in industry).

1.4 Fischer-Tropsch Chemistry and Reaction Sequence

In the light of the potential economic importance of Fischer–Tropsch synthesis (FTS), a detailed mechanistic understanding of the process is highly desirable. Such an understanding might enable the industrial applications of the reaction to be made more efficient (Overett et al. 2000). At the present time, there is general agreement that the FTS is a polymerization reaction of surface species that contains one carbon molecule (CH_x). Nevertheless, the mechanism by which this polymerization takes place to yield a variety of products, from olefins, paraffins, oxygenates, and isomers to products such as CO_2, H_2O, and coke (see the reactions in Fig 1.7), is still uncertain. The earliest theories concerning the CO hydrogenation mechanism were proposed by Fischer and Tropsch in early 1926 (Fischer and Tropsch 1926a). They hypothesized that CO reacts with the metal catalyst to form a bulk carbide, which subsequently undergoes hydrogenation to form methylene groups. In the following section we will provide a brief review of some of the reaction pathways and chain growth mechanisms that are widely accepted.

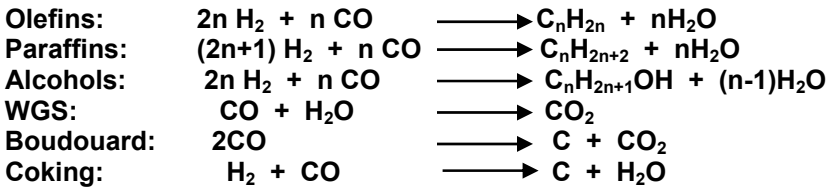

Figure 1.7 Major reactions taking place on the Fe, Co, Ru, or Ni catalyst surface during the Fischer-Tropsch synthesis (WGS is the water-gas-shift reaction).

1.4.1 Mechanism of the Fischer-Tropsch Synthesis Reaction

Carbide Mechanism

Craxford and Rideal (Craxford and Rideal 1939; Craxford 1947) proposed the carbide mechanism for FTS as a modified version of the model suggested by Fischer and Tropsch (Fischer and Tropsch 1926c). The carbide mechanism for the formation of hydrocarbon and oxygenate products includes the formation of the metal carbide, followed by hydrogenation of the metal carbide to produce the various products. It is also suggested that only surface carbides need to be considered and that the methylene groups ($-CH_3-$) formed by hydrogenation of the carbide react to produce adsorbed macro molecules. The formation of low molecular weight olefins and paraffins was assumed to occur via hydrocracking of these macromolecules.

This version of the carbide mechanism was subjected to criticism based on the results of thermodynamic ^{14}C tracer and synthesis studies performed on iron and cobalt catalysts (Kummer and Emmett 1953; Kokes and Emmett 1960). These studies were performed on iron carbide using the reaction of a reduced iron catalyst and radioactively labeled ^{14}CO. The fraction of methane ($^{14}CH_4$) produced when synthesis was affected by unlabeled CO was used as a measure of the direct hydrogenation contributed by the iron carbide to the synthesis. Their results showed that the carbide hydrogenation could be responsible for no more than 8-30% of the methane produced, even at low syngas conversion rates. In addition, the same conclusion applied to the higher carbon number compounds. Allowance was made, however, for the possibility that chemisorbed carbon atoms might still be acting as intermediates (Bell 1981).

Enol Mechanism

Several alternatives were proposed to replace the early carbide theories. Eidus et al. (Eidus et al. 1976) suggested that molecularly adsorbed CO is hydrogenated to form a hydroxycarbene or enol, M=CH(OH) (as seen below), which then undergoes further hydrogenation to produce a methylene group. The growth of hydrocarbon chains was expected to occur by polymerization of these latter species. The formation of enol

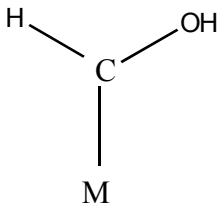

intermediates was also proposed by Storch et al. (Storch et al. 1951), who suggested that chain growth takes place by the condensation of enol groups as illustrated in Scheme 1. The results obtained by Hall, et al. (Hall et al. 1960) for their ^{14}C-tracer studies provided strong support for this mechanism. In their studies, they added ^{14}C -labeled alcohol or alkene at atmospheric pressure, together with synthesis gas and then they determined the distribution of isotopically labeled products.

Insertion Mechanism

The generally accepted insertion mechanism involves the insertion of CO into a metal-methyl group or metal-methylene carbon bond, which is then hydrogenated to produce an alcohol or alkene; the alcohol or alcohol precursors can also be used to eliminate oxygen or produce an alkene product. Hydrogenation and water elimination of the COH_2 surface species are assumed to be the rate controlling step (Wender et al. 1958; Davis 2001). The general feature of this mechanism is that CO chemisorbs and

dissociates to adsorbed C and O, followed by rapid hydrogenation of the adsorbed O to produce water. The hydrogenation of adsorbed C to form CH_2 is much slower than the water formation reaction. The CH_2 species may be considered as precursors to methane, as well as centers for hydrocarbon chain growth. This process is postulated to begin by insertion of a methylene group into the metal- carbon bond of the methyl group. This mechanism may be viewed as a revival of the carbide theory, but with the requirement that carbide formation is limited to the surface or layers near the surface.

Oxygenate Mechanism

The basic idea of the oxygenated mechanisms is that CO_2 plays a key role in chain initiation (Koelbel and Tillmetz 1974; Blyholder et al. 1976), particularly for iron catalyst. The oxygenate mechanism is able to account for the initiation by CO_2 as well as requiring chain propagation to occur only by CO, since it appears unreasonable to expect

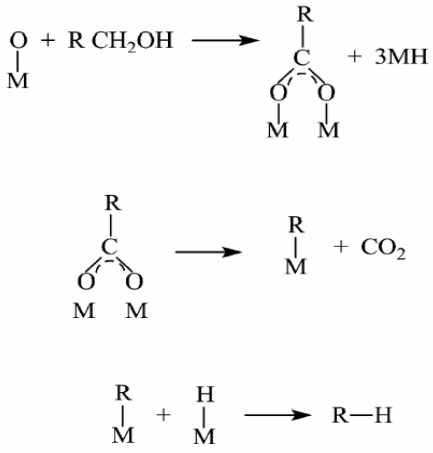

CO_2 to be adsorbed with the structure shown above as suggested by Blyholder et al, 1976 (Davis 2001). The conversion of ^{14}C labeled alcohols is consistent with the above reaction. The reaction allows for the direct formation of CO_2 and an alkene with one less

carbon than added alcohol, and in agreement with the experimental results using ^{14}C labeled alcohols ($CH_3(CH_2)_3{}^{14}CH_2OH$ and $CH_3(CH_2)_3{}^{14}CH_2CH_2OH$)[1]. Kölbel and Tillmetz (Koelbel and Tillmetz 1974), using a pathway similar to the above reaction that would account for the chain initiation, have proposed a similar adsorption model by CO_2. This model suggested that alcohol follows different reaction pathways in the presence and in the absence of syngas. It appears that the oxygen formed by the dissociation of CO is needed to permit the alcohol form CO_2 directly, together with an alkane with one fewer carbon.

1.4.2 Kinetics and Chain Growth Models for Fischer-Tropsch Synthesis

During the past several decades, extensive efforts have been made to understand and model the mechanism by which Group VIII metals catalyze the synthesis of CO and H_2 to form hydrocarbons and oxygenates (Craxford and Rideal 1939; Eidus and Zelinskii 1942; Blyholder et al. 1976; Eidus et al. 1976; Bell 1981; Brady and Pettit 1981; Kellner and Bell 1981; Satterfield and Huff 1982; Dry and Shingles 1983; Sarup and Wojciechowski 1988; Dry 1996; Schulz and Claeys 1999; Zennaro et al. 2000; Davis 2001). The objectives of these studies were to (1) obtain statistically representative kinetic data characterizing Fe, Co, Ru, Ni catalysts and promoted catalysts under commercially representative reaction conditions; (2) report statistical measures of data significant to the FTS reaction; and (3) compare, where possible under a standard set of conditions, the results of their studies with those of previous studies. Ribeiro, et al.(Ribeiro et al. 1997) suggested guidelines for kinetic studies in FTS that include: (1) measuring the rate in the absence of pore diffusion restrictions, film mass transfer

limitations, heat transfer limitations, and deactivation effects; (2) collecting data over a wide range of temperatures and reactant concentrations to facilitate valid comparison with data from other laboratories and to provide meaningful data to determine temperature and concentration dependencies; and (3) reporting rates based on the catalytic surface area.

Most of the kinetic models that are reviewed in the following sections agree on the following features of the FTS reaction: (1) FTS occurs far from the reaction equilibrium, i.e. the reverse reaction in the numerator of the rate equation has no relevance; (2) there is a minimum influence of the water-gas-shift (WGS) reaction (specifically for Ru, and Co catalysts) and consequently, there is no external condition (e.g. reaction equilibrium) that depends on the partial pressures; and (3) the FTS is inhibited by a CO pressure in a particular range, therefore some of the kinetic models include the partial pressure of CO (P_{CO}) in the denominator of the rate equation.

Anderson-Schulz-Flory Product Distribution Model

The FTS products are generally not in thermodynamic equilibrium with respect to either the reactants or the products. As a result, the selectivity data can be very useful in determining the mechanism of the reaction. The initial attempts by Flory (Flory 1936) to understand the synthetic behavior of non homogenous materials of polymerization nature led to the development of the first FTS chain-growth model. The basic structure of that model was later developed in a series of studies (Herrington 1946; Friedel and Anderson 1950; Henrici-Olive and S. 1976) that led to the current, well known Anderson-Shultz-Flory (ASF) product distribution model. According to this model, the polymerization

process in FTS was assumed to be initiated on the surface of the catalyst by a monomer containing one carbon atom, while chain growth takes place by the addition of one monomer at a time. An illustration of this process is seen in Figure 1.8, where N_n is the number of active sites occupied by a chain of length n. As soon as chain growth is terminated, either by addition or subtraction of a hydrogen molecule, the product molecule desorbs from the surface of the catalyst and creates a vacant site for further reaction.

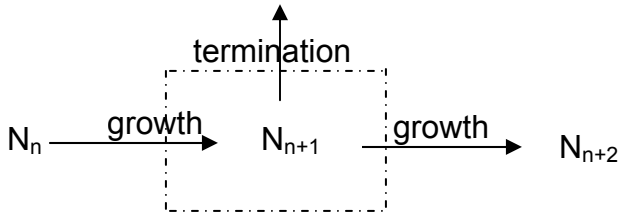

Figure 1.8 Anderson-Schultz-Flory chain growth model of FTS reaction.

The model also assumes that the growth and termination rates are independent of the chain length and are of the same order in the surface concentration of CO and H_2. As a result, the chain growth probability (its α-value) has been defined as follows:

$$\alpha = \frac{N_{n+1}}{N_n} = \frac{R_p}{R_p + R_t} \tag{1.1}$$

where R_p and R_t are the rate of propagation (growth) and rate of termination, respectively. The relation between an active site that is occupied by a chain of length n and a site occupied by a chain of a single carbon molecule can then be extracted from Eqn (1.1) as follows:

$$N_n = \alpha^{n-1} N_1 \tag{1.2}$$

Then, the mole fraction of a chain of length n that occupies the active site, x_n, can be calculated according to Eqn. (1.3), including the substitution of the infinite term:

$$x_n = \frac{N_n}{\sum_{n=1}^{n=\infty} N_n} = \frac{\alpha^{n-1} N_1}{N_1\left[\frac{1}{1-\alpha}\right]} = \alpha^{n-1}(1-\alpha) \tag{1.3}$$

Similarly, the weight fraction of a chain of length n, W_n, can be measured as a function of the chain growth probability, α, as in Eqn. 1.4. The logarithmic relation between W_n and α is seen in Eqn. 1.5:

$$W_n = n\alpha^{n-1}(1-\alpha)^2 \tag{1.4}$$

$$\ln\left(\frac{W_n}{n}\right) = n\ln\alpha + \ln\left(\frac{(1-\alpha)^2}{\alpha}\right) \tag{1.5}$$

According to ASF assumptions, a plot of $\ln(W_n/n)$ vs n (as in Eqn.1.5) should give a straight line for all hydrocarbon products and α can then be determined from the slope of that line. According to the above equations, as α increases more heavy hydrocarbons are produced. The major deficiency in the ASF model is that it is neither a function of the temperature nor of the concentration of reactant molecules. Numerous studies have reported deviations from this standard product distribution yielding, different shapes for the relation between $\ln(W_n/n)$ vs n (Inoue et al. 1987). Many researchers targeted such deviations as a technique to control the product distributions in the FTS reaction and to maximize the production within a specific carbon number range

(e.g. C_5-C_{11} for the gasoline fraction, C_{12}-C_{19} for the diesel fraction, or higher carbons for the heavy wax range).

Many kinetic models have been developed to explain the observed deviations from ASF model. Mass transfer limitations inside the catalyst pores due to the condensation of heavy hydrocarbons have been cited as a reason for the enhanced α-olefin readsorption rate, and thus the increased production of heavy hydrocarbons (Madon et al. 1993). Huff and his coworkers also suggested a model that accounts for two-catalytic sites with two different growth factors (iron promoted catalysts) that yield a positive deviation from ASF (Huff and Satterfield 1984). The pore size effect also known as the molecular sieve effect) (Iglesia et al. 1993b), and the concentration and temperature gradients in fixed bed reactors (Matsumoto and Satterfield 1989) has also been suggested as a reason for non ASF distributions. In a series of publications, Puskas and his coworkers argue that multiplicity in the chain growth probability is the only reason for positive deviations from ASF (Puskas et al. 1993; Hurlbut et al. 1996; Puskas and Hurlbut 2003). Also, experimental artifacts have been blamed for many non-ASF distributions reported in literature (Davis 2003a).

Surface Reaction Model

The surface reaction model is a well known model for FTS originally proposed by Kellner and Bell in the early 1980s (Kellner and Bell 1981), using an alumina-supported Ru catalyst. Rate data for the formation of methane and C_2 through C_{10} olefins and paraffins were fitted by a power law expression. The kinetics observed experimentally can be interpreted in terms of a comprehensive mechanism for CO hydrogenation, in

which CH_x (x=0-3) species play a primary role. This model was later modified by Uner (Uner 1998) to include the water and carbon monoxide formation steps. He also derived the rate of methane and higher hydrocarbon formation in terms of the rate and equilibrium constants of the intermediate steps, as well as the partial pressure of hydrogen and carbon monoxide. The model assumes that the formation of FTS products from CO and H_2 takes place as follows: (i) molecular adsorption of CO with subsequent dissociation, (ii) dissociative adsorption of hydrogen in the surface, (iii) chain initiation, (iv) propagation, and (v) termination. This model agrees in its general features with the insertion mechanism discussed previously. The reaction sequence of the Uner model (Uner 1998) is illustrated in Figure 1.9 below, where (*) represents the active site on the catalyst surface.

(1) $CO + * \rightleftharpoons CO*$

(2) $CO *+ * \rightleftharpoons C*+O*$

(3) $H_2 + 2* \rightleftharpoons 2H*$

(4) $H* +O * \rightleftharpoons OH* + *$

(5) $OH* +H * \longrightarrow H_2O + 2*$

(6) $CO* + O* \longrightarrow CO2 + 2*$

(7) $C* + H* \rightleftharpoons CH* + *$

(8) $CH* + H* \rightleftharpoons CH_2* + *$

(9) $CH_2* + H* \rightleftharpoons CH_3* + *$

(10) $CH_3* + H* \longrightarrow CH_4 + 2*$

(11) $CH_3* + CH_2* \longrightarrow C_2H_5* + *$

(12) $C_2H_5* + * \longrightarrow C_2H_4 + H* + *$

(13) $C_2H_5* + H* \longrightarrow C_2H_6 + 2*$

(14) $C_2H_5* + CH_2* \longrightarrow C_3H_7* + *$

and so forth

Figure 1.9 The modified surface reaction model (Uner 1998).

On the basis of the surface reaction model Kellner and Bell (Kellner and Bell 1981) were able to derive analytical expressions for rates, chain growth probability, and olefin/paraffin ratios by using the following assumptions: (1) the surface of the catalyst was saturated with CO, (2) water is the primary product through which the oxygen is eliminated from the surface, (3) hydrogen addition to surface species is in equilibrium, and (4) the chain growth probability is independent of the chain length which agrees with the standard ASF model. Nevertheless, the final assumption, which is also inherent in the ASF distributions, has been revisited in the light of new experimental evidence (Iglesia et al. 1991; Madon and Iglesia 1993; Madon et al. 1993; Puskas et al. 1993). A detailed discussion of this phenomenon is reported elsewhere (see Chapter 4). However, the surface reaction model has generally been preferred due to the inherent simplicity of incorporating the adsorbate mobilities in terms of the rate parameters (Uner 1998). The derived rate equation of the modified surface reaction model is as follows:

$$(1-\alpha)^{4/3}/\alpha = KP_{H_2}^{1/3}P_{CO}^{-2/3} \tag{1.6}$$

where α is the chain growth probability, and P_{H2} and P_{CO} are the partial pressure of hydrogen and carbon monoxide, respectively. K represents the equilibrium rate constant that is generated from the rate of each step in the reaction, as illustrated above, and its value is represented below:

$$K = \frac{k_{tp}\,K_3^{1/3}}{\left[k_p^2 k_6 K_1^2 K_2 K_7 K_8 K_9^{-1}\right]^{1/3}} \tag{1.7}$$

where $K_i = k_{forward,\ i}/k_{backward,i}$, k_p is the rate of methane production, and k_{tp} is the rate constant of termination steps, with paraffin as the product. The results of this model are consistent with the experimental data (Kellner and Bell 1981; Uner 1998).

Langmuir-Hishelwood-Hougen-Watson Models

Sarup and Wojciechowski (Sarup and Wojciechowski 1988; Sarup and Wojciechowski 1989b; Sarup and Wojciechowski 1989a) developed a series of kinetic models for the FTS reaction over a cobalt catalyst using the Langmuir-Hishelwood-Hougen-Watson method. Their models all follow the same concept of the surface reaction model and include both the dissociation of CO and H_2 and the surface reaction of the adsorbed molecules to form H_2O and oligmer (CH_2) (see Figure 1.10). The latter was assumed to play the key role in chain growth process. The reaction pathway of the synthesis process and the chain growth mechanism is illustrated in Scheme 2. These models' usefulness are that they overcome many of the disadvantages of previous models that were compared to experimental data at high temperature and low-pressure, as the products are mostly gases and therefore easier to handle. The models also account for the formation of methane not only by the hydrogenation of surface carbon, but also by the reaction of hydrogen with molecularly adsorbed carbon monoxide. The reaction sequence follows the same intial steps (1) to (3) as in the surface reaction model, Figure 1.9. However, the termination to water in step (5) is assumed to take place additionally through hydrogen assisted dissociation (the formal radical), as seen below.

(5') $OC.*+H.* \Leftrightarrow HOC.*+*$

(5'') $HOC.*+H.* \Leftrightarrow C.*+H_2O+*$

The rate expression for CO conversion is written on the basis of the assumed rate-controlling step, i.e. the hydrogenation of carbon species, and is expressed as follows;

$$-r_{CO} = \frac{kP_{CO}^{1/2}P_{H_2}^{1/2}}{\left(1+K_1P_{CO}+(K_2+K_3)P_{CO}^{1/2}+K_4P_{H_2}^{1/2}\right)^2} \qquad (1.8)$$

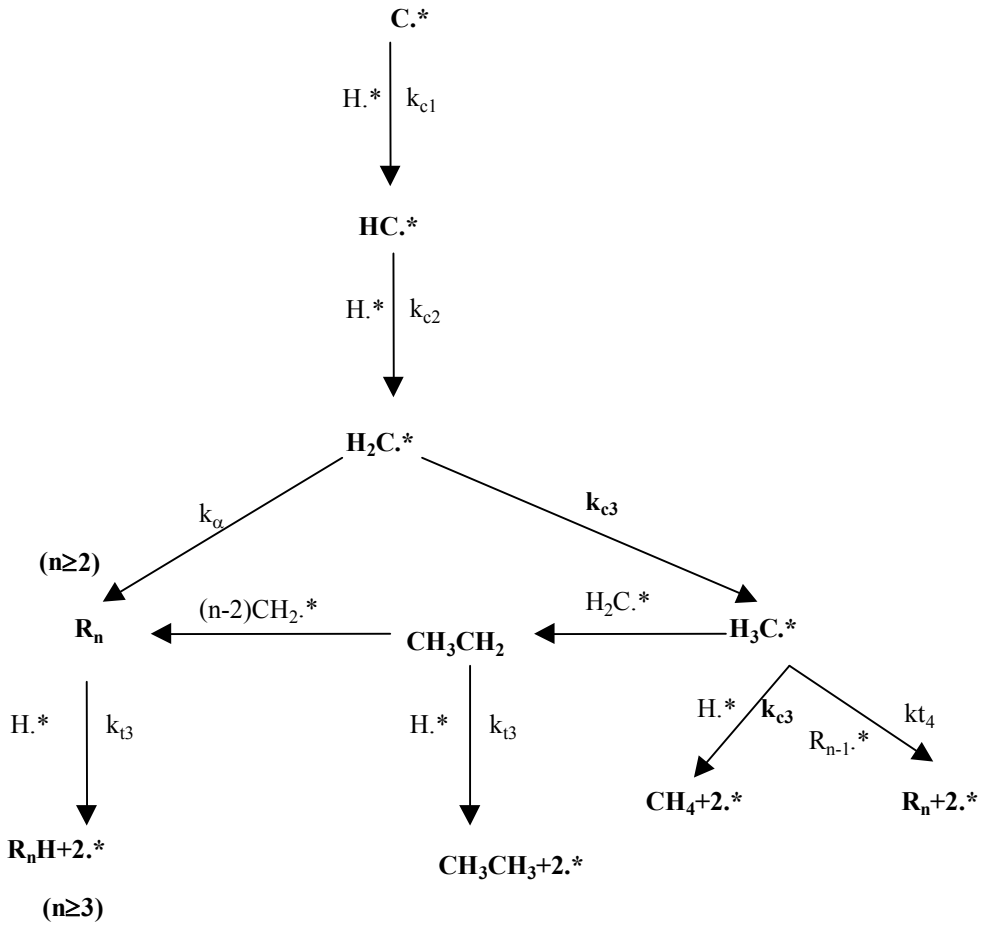

Figure 1.10 Reaction pathway and chain propagation in FTS reaction on an active site(*) (Sarup and Wojciechowski 1988).

Two of the six Langmuir-Hishelwood-Hougen-Watson models proposed by Sarup and Wojciechowski based on different assumptions for the rate controlling step, provide a satisfactory fit for the CO consumption experimental data (Sarup and Wojciechowski 1988).

Diffusion-Enhanced Olefin Readsorption Model

The earliest stage of the readsorption mechanism in FTS reaction was suggested by Herrington (Herrington 1946), who stated that the hydrocarbon chains produced in the catalyst surfaces terminated as paraffins or olefins and were later reabsorbed to initiate new growing chains. Later, Friedel and Anderson (Friedel and Anderson 1950) used thermodynamic arguments to conclude that α-olefin and oxygenates were the major products. Iglesia, Madon, and coworkers (Iglesia et al. 1991; Madon et al. 1991; Iglesia et al. 1993b; Madon and Iglesia 1993; Madon et al. 1993) developed the *Diffusion-Enhanced Olefin Readsorption* model based on the previous findings of Herrington (Herrington 1946). This model is based on extensive experimental investigations of FTS product distribution over Ru and Co catalysts under different reaction conditions. A simple illustration of their reaction network model, describing hydrocarbon chain growth and termination, is seen in Figure 1.11. According to this model, growth occurs by addition of CH_2 surface intermediates to surface alkyl groups; termination occurs by hydrogen elimination or addition reactions involving the alkyl groups giving normal and branched olefins and paraffins. They defined the primary products (reaction 1 of Scheme 3) as those formed by a reaction intermediate on the FTS chain growth site, (*), and the secondary product (reactions 2, and 3 of Figure 1.11) as those produced by the

readsorption of primary products on other active sites, (*` or *``). According to the *Diffusion-Enhanced Olefin Readsorption* model, chain growth cannot take place on the surfaces of *` and *`` .

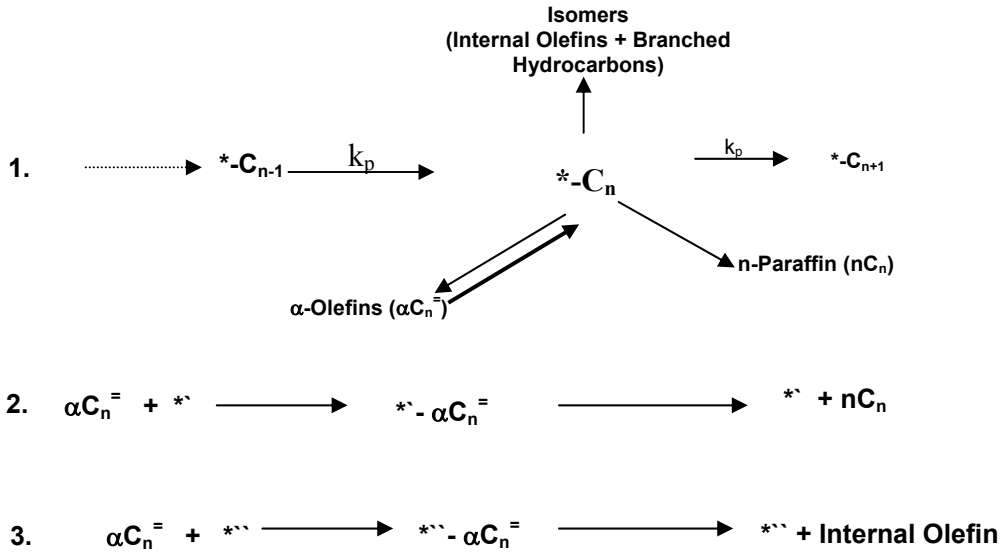

Figure 1.11 FTS reaction network according to the Diffusion Enhanced Olefin Readsorption Model (Madon et al. 1991).

All the products in reaction 1 (Figure 1.11) are defined as the primary products of the synthesis process. The readsorption of α-olefin denoted by a heavy arrow in Figure 1.11, is a secondary reaction. However, once an α-olefin ($C_n^=$) readsorbs onto a site *, it becomes an FTS intermediate. This intermediate is indistinguishable from any other C_n chain growth intermediate, and it can grow and terminate as a longer chain α-olefin, paraffin, or isomer. Note that these latter products, even though they are influenced by secondary readsorption of α-olefin, are still primary products. The hypothesis of the model is as follows: *If a product can be formed by a single sojourn of a reaction*

intermediate on an FTS site, then it is considered as a primary product, regardless of the number of surface sojourns actually required to form it (Madon et al. 1991).

n-Paraffins and isomerized products can be formed by either primary or secondary reaction pathways. This depends on the catalyst used and the reaction conditions (Iglesia et al. 1992). The model has not resolved whether *n*-paraffins are secondary products formed exclusively by hydrogenation of α-olefin or whether they can be formed by direct termination of a surface chain. The *Diffusion-Enhanced Olefin Readsorption* model explains why hydrocarbon selectivities always differ from conventional product distribution (i.e. ASF), which reflects chain propagation and termination rates that are independent of chain size. The total rate termination (R_t) equals the sum of rates for various termination pathways. In general, termination predominantly occurs through hydrogen addition (R_H) and abstraction (R_o) by a similar procedure after isomerization (R_I; double bond and skeleta) of surface cites. The general idea of the model is that it includes a carbon-number-dependent rate ($R_{r,n}$) that equals the rate of α-olefin readsorption and chain initiation. The termination parameter (β_n), or Herrington parameter, is then defined as follows:

$$\beta_n = R_{t_n} / R_p = (R_H + R_o + R_I - R_{r,n}) / R_p \qquad (1.9)$$

where R_p represent the chain growth rate.

This expression clearly shows that α-olefin readsorption and initiation effectively reduce the net chain termination rate since $R_{r,n}$ increases with n which results in a decrease of β_n as seen in Eqn. 1.9. This will occur until all products are readsorbed and reacted ($R_o = R_{r,n}$). Large α-olefins diffuse slowly through the pores of the catalyst, and

thus they have a higher readsorption probability. This condition will vanish when no olefins remain in the gas phase products (i.e. $R_o = R_{r,n}$). At this point, a constant upper limit of α (chain growth) and lower limit of β (chain termination) is obtained, which leads the reaction towards termination of α-olefins by executive hydrogenation. This hypothesis and the chain growth kinetics discussed above are in consistent with the experimental data obtained from Ru-based and Co-based catalysts (Iglesia et al. 1991; Iglesia et al. 1993b; Madon and Iglesia 1993; Madon et al. 1993).

The main conclusion of the *Diffusion-Enhanced Olefin Readsorption* model is that while the standard ASF distribution is still applicable for regular reaction sites, non ASF distribution is highly acceptable as the residence time inside the catalyst pore increases which results in a higher readsorption probability for high molecular weight α-olefins (Madon and Iglesia 1993).

1.5 Summary

Generally, the history of the Fischer–Tropsch process has been influenced by the political and economic fortunes of nations, as up till now it has only been economically feasible for countries with abundant coal reserves and limited access to oil. The current focus of this technology is derived from environmental concerns (e.g. the need for ultra clean fuels with the least emissions), and the recent developments in GTL processes. The price of petroleum oils and the doubtful political stabilities of countries with the greatest crude oils resources signal the increased importance of GTL technologies and a renewed interest in the Fischer-Tropsch synthesis.

CHAPTER 2

UTILIZATIONS OF SUPERCRITICAL FLUIDS IN HETEROGENEOUS REACTIONS

2.1 Supercritical Fluid Properties and Applications

A supercritical fluid (SCF) refers to a substance that is heated beyond its critical temperature and compressed beyond its critical pressure. At the critical point, the properties of the liquid and gas phases become identical (Figure 2.1). Increases in pressure of a substance maintained beyond the critical temperature will not result in liquefaction. SCFs have unique characteristics intermediate between those of gases and liquids; the density is sufficient to afford substantial dissolution power and solvating properties close to those of liquids, but this is combined with a diffusivity and viscosity comparable to that of a gas (Figure 2.2). As is also shown in Figure 2.2, the viscosities of SCFs are much lower than those of liquids, while diffusivities are usually an order of magnitude larger than those found in the liquid phase. Diffusivity increases as the temperature of the fluid rises, while the viscosity and density both decrease. The solvent properties of these materials can in fact be controlled very precisely by small manipulations in the pressure (and therefore density) at which the SCF is used. An example of pressure tunability and its dramatic influence on the physical properties of SCFs is seen in Figure 2.3 for the case of supercritical CO_2 (later referred to as $ScCO_2$). It

is clear from Figure 2.3 that the physical and transport properties of the fluid can be altered drastically, from gas-like to liquid-like behavior, simply by isothermally varying the pressure around P_c, the critical pressure (Subramaniam 2001).

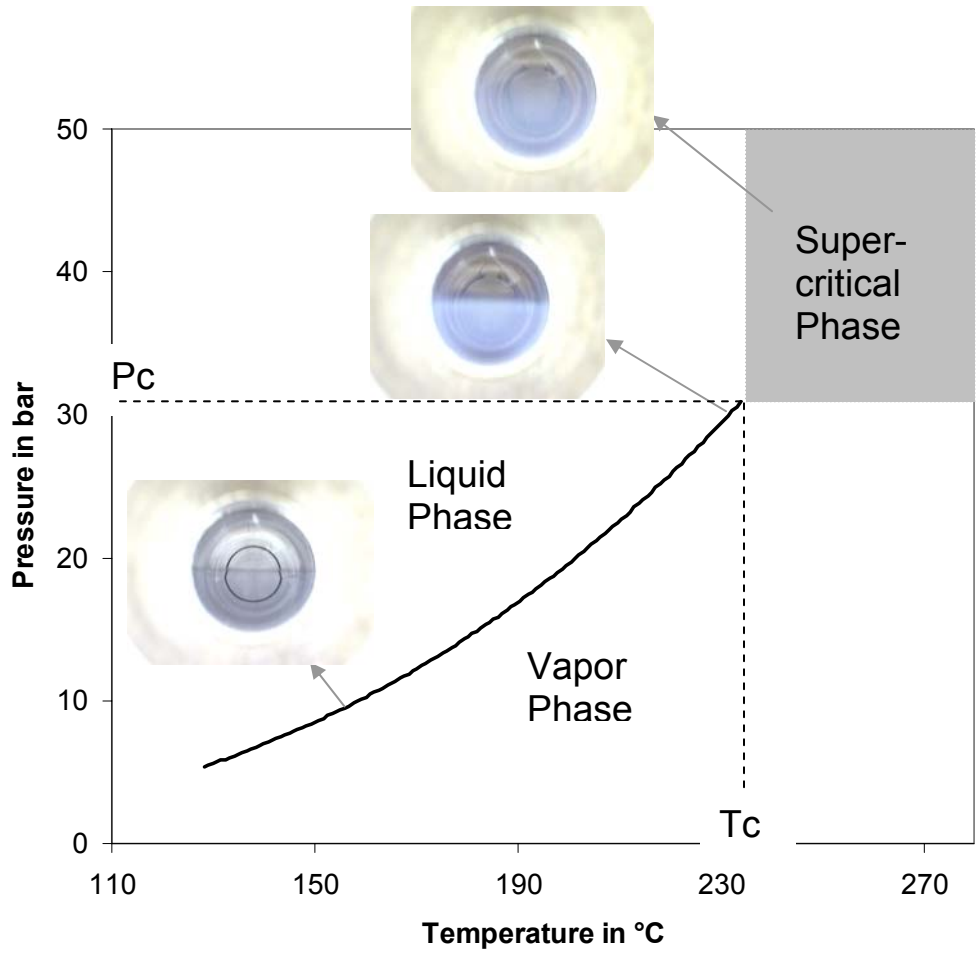

Figure 2.1 Phase behavior (P-T) diagram of pure hexane, measured in a variable volume view cell (VVVC), shows the existence of three phases (vapor phase, liquid phase, and supercritical phase). The solid line represents the vapor-liquid-equilibrium (VLE). The bottom image shows the existence of two phases (vapor and liquid); the meniscus between the two phases is in the center of the VVVC. Closer to critical point, the image shows the appearance of supercritical opalescence, and at the critical point the meniscus disappears and a single phase (supercritical phase) is shown (Elbashir and Roberts 2004a).

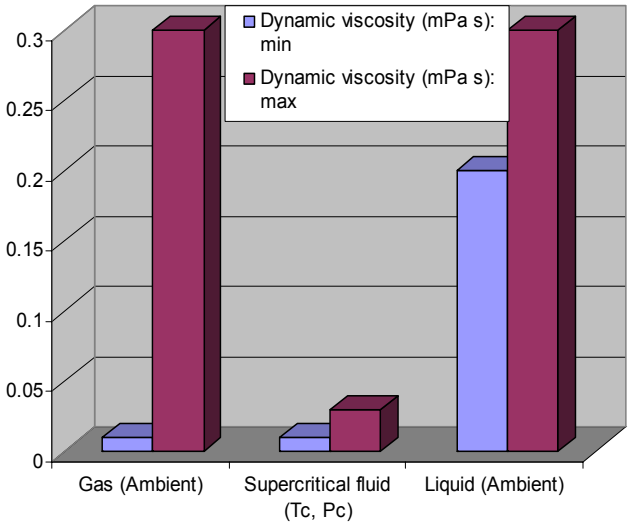

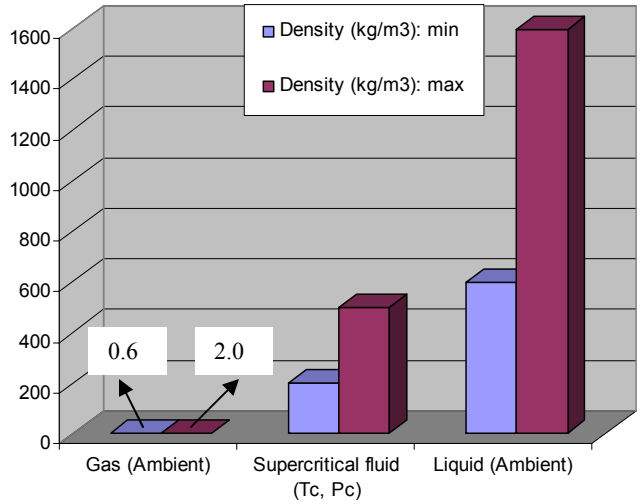

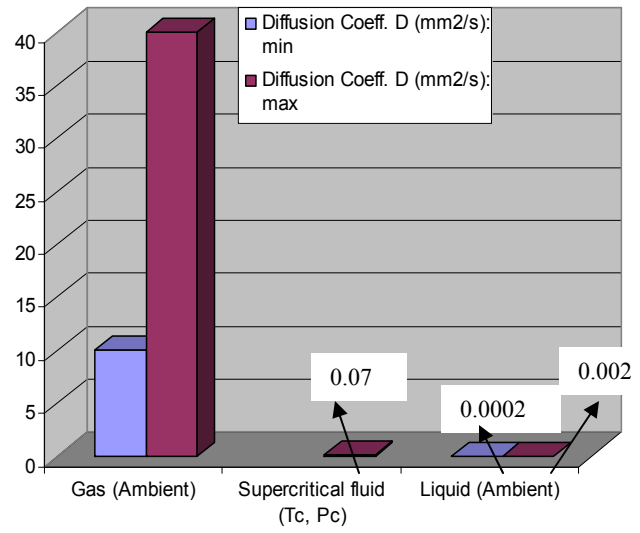

Figure 2.2 Physical properties (maximum and minimum) of SCFs at the critical temperature (Tc) and critical pressure (Pc) compared with physical properties of gas and liquid at ambient conditions. Data taken from (Taylor 1996).

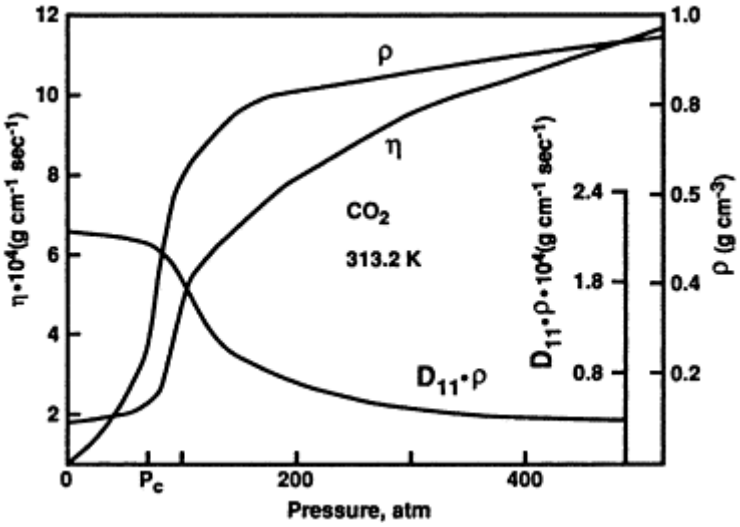

Figure 2.3 Pressure tunability of the density (ρ), viscosity (η) and $D_{11}\rho$ for CO_2 in the vicinity of the critical point (Subramaniam 2001).

In addition, supercritical fluids have unique properties in the sense that compounds which are insoluble in a fluid at ambient conditions can become soluble in the fluid at supercritical conditions (McHugh and Paulaitis 1980), or conversely, compounds which are soluble at ambient conditions can become less soluble at supercritical conditions (Tester et al. 1993a; Tester et al. 1993b). In near-critical conditions of pure fluids, transport coefficients experience dramatic changes in behavior. The heat conduction coefficient tends to infinity, the heat capacity at constant pressure tends to infinity, and the heat diffusivity is vanishingly small, while the isothermal compressibility diverges. Near critical fluids have been extensively studied as non-moving objects by physicists (Stanley 1971; Zappoli 2003). Also, one of the physical advantages of SCFs that largely benefit catalytic reactions suffering from mass transfer limitations is that the surface tension is low, enabling easy penetration into the catalyst pores (solid matrix) and thus facilitating extraction of non-volatile materials. However, little still is known, compared to incompressible and normal compressible fluids, about

the hydrodynamic behavior of these fluids since it falls between incompressible fluid mechanics and gas dynamics.

The recent heightened awareness of environmental impacts associated with many established chemical processes that produce waste chemicals as byproducts has led to considerable pressure on the chemical industry. Legislators in many countries around the globe, as a result of increased consumer awareness of global warming and other environmental issues, are forcing the chemical industry to adopt environmentally safe processes. The need for cleaner and more benign chemical technologies has led to the development of a new concept in chemistry and chemical engineering that is known as the *Green Chemistry* or *Green Process Engineering*. SCFs are an environmentally benign alternative to conventional industrial solvents and in their utilization in industry they are considered *Green Solvents*.

Since the early 1980s, utilization of supercritical fluids (SCF) in industry has received considerable attention. The first generation of SCF technology was used to extract commodity chemicals and synthetic fuels. By the mid 1980s, research on new applications of SCF shifted towards more complex and valuable substances that undergo a much broader range of physical and chemical transformations. A great deal of innovation took place in studies of reactions, separations, and materials processing of polymers, foods, surfactants, pharmaceuticals, and hazardous wastes (Johnson and Penninger 1989). The field dealt primarily with extraction of relatively simple molecules that dissolve in fluids such as carbon dioxide. Since then, the attention has shifted to

significantly more complex molecules, such as polymers, biomolecules, or growing crystals, which often contain high value substances.

2.2 Supercritical Fluids in Heterogeneous Reactions

The idea of using supercritical fluids as reaction solvents has been around since the discovery of a `peculiar state of matter' early in the nineteenth century by Baron Charles Cagniard de LaTour, a French experimental physicist (Cagniard de LaTour 1822). SCFs have become a unique medium for chemical reactions because they offer single phase operation, with a density that is sufficient to afford substantial dissolution power and diffusivity higher than that in liquids, accompanied by lower viscosity than liquids. These properties result in significant enhancement of mass transfer and/or heat transfer. Conducting chemical reactions at supercritical conditions affords greater opportunities to tune the reaction environment (solvent properties), to eliminate transport limitations on reaction rates, and to integrate reaction and product separation (Baiker 1999). This greatly enhances the extraction of low volatile products (e.g. heavy hydrocarbons) from porous catalysts in situ (Subramaniam 2001).

Conducting heterogeneous reaction in SCF media would result in significant changes in the physical and chemical sequence of catalytic reactions. These changes may result in enhancement in the reaction performance by increasing the rates, as well as the selectivity. An excellent demonstration of the influence of the SCF operation on the physical and chemical steps of solid-catalyzed gas/liquid reactions, such as the hydrogenation of a liquid substrate over a porous catalyst, was illustrated by Baiker

(Baiker 1999), as shown in Figure 2.4. In fact, catalyst activity in these reactions will only be effective if the reactants (hydrogen, substrate) reach both the external and internal surfaces of the catalyst. The physical and chemicals steps shown in Figure 2.5 include: (1) transfer of gaseous reactant from the bulk gas phase to the gas/liquid interface (diffusion), (2) progressing from there to the bulk liquid phase (absorption and diffusion); (3) transfer of both reactants (gas and liquid) from the bulk liquid to the external surface of the catalyst particle (i.e. diffusion through the stagnant external film surrounding the catalyst particle); (4) transfer of reactants into the porous catalyst (internal diffusion); (5) adsorption of reactants following either step 3 or 4; (6) surface reaction; and finally (7) desorption and transfer of product(s) by (8) internal or (9) external diffusion to the bulk liquid or gas phase. Figure 2.5*c* depicts the mass transfer resistances for the same reaction under supercritical conditions and shows that the gas/liquid resistance is eliminated under supercritical conditions. In principle, all the above steps can be affected either directly or indirectly by pressure, particularly when the reaction medium is changed from near-critical to supercritical conditions. Therefore, this provides an interesting opportunity for controlling both the rate and selectivity of heterogeneous catalytic reactions. Figure 2.5*c* also includes a representative section of the reactor content, mass-transfer resistances, and a corresponding reactant concentraion profile for the same reaction under supercritical conditions. Note that under supercritical conditions, the gas/liquid transfer resistance is eliminated (steps 1 and 2) and the external fluid film diffusion resistance (step 3) is lowered due to the lower viscosity of SCF.

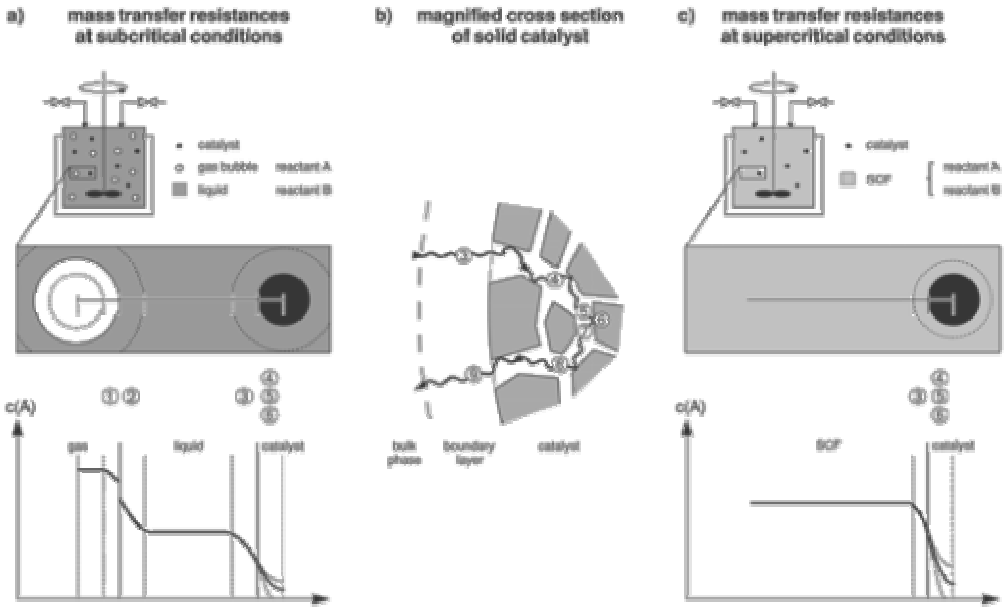

Figure 2.4 Sequence of physical and chemical steps occurring in a heterogeneous catalytic gas/liquid reaction (e.g., hydrogenation of a liquid compound). Part a shows a representative section of the reactor content, consisting of a gas bubble, a solid catalyst particle and the corresponding mass-transfer boundary layers (resistances) under near-critical conditions. Part b provides a magnified cross section of the catalyst particle. A representative concentration profile of reactant A is depicted below part c (Baiker 1999).

The main areas of heterogeneously catalyzed hydrogenation research were classified by (Hyde et al. 2001) according to the following categories: (1) the hydrogenation of food compounds such as fatty acids or oils to produce higher value derivatives; (2) the formation of precursor building blocks for pharmaceuticals and fine chemicals, and (3) asymmetric hydrogenation. In their book, McHugh and Krukonis (McHugh and Krukonis 1994), addressed the uniqueness of applying a supercritical medium to many of the above classes of heterogeneous reaction, as well as to homogenous reactions such as selective oxidations, hydrogenations, hydroformylations, alkylations, and polymerizations. Another review article (Subramaniam 2001) addressed many of the advantages of using SCF as a reaction medium in heterogeneous catalysis compared to other conventional media (gas-phase and liquid-phase reactions). His emphasis on the ability of the SCF medium to extract low volatile hydrocarbons from porous catalysts in situ, which normally results in increased pore accessibilities, enhanced catalyst stability to coking, and increased primary product selectivity. Coke formation inside catalyst pores normally results in a drop in activity and eventually leads to complete deactivation of the catalyst. Coke formation inside the catalyst pores is controlled by many factors, including reaction temperature, reaction pressure, acidity, and catalyst structure (Guisnet and Magnoux 1997). In order to stabilize the catalyst activity, the rate of coke formation should be balanced by the rate at which coke precursor is removed before further accumulation can take place inside the catalyst pores. Demonstration of effective in situ removal of the coke precursors by a near-critical reaction medium is shown in Figure 2.5. The liquid-like density and gas-like transport

properties offer a superior medium to mitigate coke buildup and, therefore, alleviate pore diffusion limitations. This results in a flatter foulant accumulation profile in the catalyst (Subramaniam 2001).

SCF also offers a unique medium for continuous heterogeneous reactor systems. Continuous reactors for SCFs have the advantage over batch reactors that they do not require depressurization to feed in the reactants or to recover the products (Hyde et al. 2001). Separation of catalyst and product in a supercritical flow reactor may also be simpler than in batch or semi-batch processes because the catalyst is fixed within the reactor. On an industrial scale, it may also be possible to isolate individual catalyst chambers for refilling while avoiding total shutdown and depressurization of the reactor. An excellent example of a continuous SCF reactor was designed by Thomas Swan Co. Ltd, and an illustration is shown in Figure 2.6. Their design is highly flexible and can be used for up to 1000 tons per annum for fine chemical synthesis in an $ScCO_2$ based process (Freemantle 1997).

2.3 Applications of Supercritical Fluids in the Fischer-Tropsch Synthesis

2.3.1 Background

Conducting FTS under supercritical fluid (SCF) solvent conditions (later referred to as SCF-FTS) affords unique opportunities to manipulate the FTS reaction environment, and to enhance production of liquid fuels and value-added chemicals (such

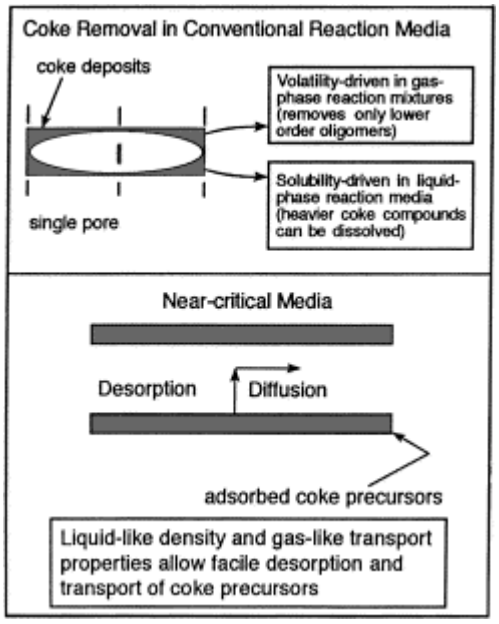

Figure 2.5 In situ mitigation of coke buildup in near-critical and supercritical reaction media (Subramaniam 2001).

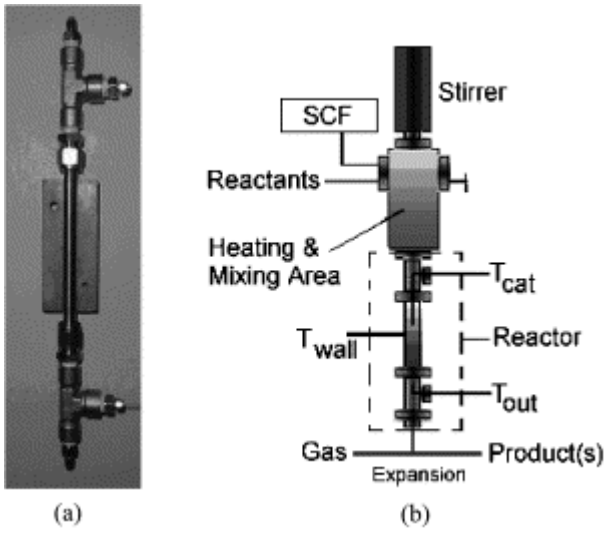

Figure 2.6 Illustration of the typical layout of a continuous flow supercritical reactor. The close-up photograph of the actual reactor (a) represents the area within the dotted box in (b). The actual reactor is 25 cm in length (Hyde et al. 2001).

as α-olefins) from the synthesis gas, or syngas (a mixture of H_2 and CO). Industrial gas-phase FTS is inevitably accompanied by local overheating of the catalyst surface and high degrees of methane selectivity, thereby decreasing the yield of desired products (Kolbel and Ralek 1980). Furthermore, slurry phase Fischer-Tropsch reaction processes suffer from slow diffusion of syngas into catalyst pores, resulting in lower rates of reaction (Lang et al. 1995). These considerations have directed research efforts on FTS towards the application of supercritical fluid solvents in order to improve product control in the liquid fuels range. Supercritical fluid solvents combine the desirable properties of gas-like diffusion with liquid-like heat transfer and solubility, thus overcoming several of the current industrial limitations (Baiker 1999). Fine adjustments in operating conditions near the critical point can result in superior control of the FTS process, including tunable product distributions.

Previous studies of SCF-FTS attributed the enhancement in the reaction performance compared to conventional gas-phase FTS and liquid-phase FTS to the followings: (1) in situ extraction of heavy hydrocarbons from the catalyst resulting due to high solubility in the supercritical phase (Yokota et al. 1990; Bochniak and Subramaniam 1998; Jacobs et al. 2003); (2) elimination of interphase transport limitations, thus promoting reaction pathways toward the desired products (Bochniak and Subramaniam 1998); (3) enhanced desorption of α-olefins that promotes the chain growth process prior to secondary reactions (Bukur et al. 1997), and (4) superior heat transfer compared to gas-phase reaction, resulting in more long chain products (Yokota et al. 1990; Huang and Roberts 2003).

The pioneer study on the application of SCF's in FTS reactions was conducted by Fujimoto's research group at the University of Tokyo, Japan (Yokota et al. 1990). Their study demonstrated that conducting FTS reactions using SCF media offers unique characteristics, such as high diffusivity of reactant gases, effective removal of reaction heat and in situ extraction of high molecular weight hydrocarbons (wax). However, their findings also show that the rate of reaction in an SCF medium and the diffusion of reactant gases are lower than those in conventional gas-phase FTS. Nevertheless, they showed that conducting FTS reactions in SCF media enhance the removal rate of waxy products from inside catalyst pores much more effectively than the removal rates in the gas-phase. They also found that olefin (primary product) contents in SCF-FTS are much higher than in either gas-phase FTS or liquid-phase FTS. Bukur's research group at Texas A&M supported Fujimoto's findings of the enhancement in α-olefin selectivity when conducting FTS reactions under SCF media (Lang et al. 1995; Bukur et al. 1997). Their findings show that the total olefin and 2-olefin selectivities were essentially independent of reaction temperature but changed significantly when conditions were changed from conventional gas-phase and near-critical operations to supercritical operation. Subramaniam's research group at the University of Kansas then developed an on-line GC method for analysis of C_1-C_{30} products from FTS reactions conducted in a supercritical hexane medium over an iron catalyst in a continuous fixed-bed reactor (Snavely and Subramaniam 1997). In another study, Subramanian's group also addressed the influence of pressure on the SCF-FTS operation, particularly its effect on the catalyst effectiveness factor and pore diffusivity (Bochniak and Subramaniam 1998). Other contributions in the SCF-FTS field have come from Davis' research group at the University of Kentucky

(Jacobs et al. 2002; Jacobs et al. 2003). In these studies Jacobs et al. addressed the issue of catalyst stability in SCF-FTS reaction over 25% Co/Al_2O_3 by using a mixed supercritical solvent composed of 45 volume% pentane and 55 volume% hexane. Their findings show that operating FTS reactions under SCF, the condensation of high molecular weight hydrocarbons that leads to catalyst activations can be avoided (Zhang et al. 2003). Roberts' research group at Auburn University has continued these efforts in exploring the advantages of operating FTS reaction under supercritical hexane and supercritical pentane medium over alumina supported cobalt catalysts (15%Co-Pt/Al_2O_3 and 15% Co/Al_2O_3) (Huang et al. 2002a; Huang and Roberts 2003). They reported that syngas conversion, α-olefin selectivity, and heavy hydrocarbon productions can be enhanced in SCF-FTS compared to gas-phase FTS. While examining the temperature profile inside the catalyst reactor, they also observed that the temperature distribution is significantly flatter in the supercritical phase compared to gas-phase FTS, suggesting that the SCF medium does a much better job in distributing the generated heat. As a result, methane selectivity is significantly suppressed under SCF-FTS (Huang and Roberts 2003).

In the following subsections, we will briefly review the work that has been done on the utilization of the supercritical fluids in the FTS reaction for published or in press literature from 1990 up to 2004. More comprehensive reviews for the application of supercritical fluids in homogeneous and heterogeneous chemical reactions can be found in Savage et al. (Savage et al. 1995), while heterogeneous reactions were addressed by

Baiker (Baiker 1999), Hyde et al. (Hyde et al. 2001) and Subramanian (Subramaniam 2001).

2.3.2 Selection of supercritical solvents for the FTS reaction

Only hydrocarbons (e.g. propane, pentane, and hexane) have so far been used as supercritical solvents for FTS reactions (Yokota et al. 1990; Fan et al. 1992; Bukur et al. 1997; Fan and Fujimoto 1999; Zhang et al. 2000; Huang et al. 2002a; Tsubaki et al. 2002; Huang and Roberts 2003; Jacobs et al. 2003; Elbashir and Roberts 2004b). Hydrocarbon solvents are preferred for FTS conditions because their critical properties (specifically temperature) are within the activity range of the Co, Fe and Ru catalysts used in the FTS reaction. Table 2.1 shows a summary of the critical properties of light hydrocarbons (C_2-C_8) compared to the well known green solvents $ScCO_2$ and supercritical water. The criteria for selecting appropriate solvents for SCF-FTS were previously addressed by Fan and Fujimoto (Fan and Fujimoto 1999) as follows:

1. The critical temperature and pressure should be slightly lower than the typical reaction temperature and pressure. In this case, selecting CO_2 as the SCF is not appropriate since its critical temperature (30.9 °C) is much lower than that needed for the FTS reaction (approximately >180 °C for Co and Ru based-catalysts and >200 °C for Fe based-catalysts), while its critical pressure (73.8 bar) was considerably higher than that used for either a gas phase or a liquid phase FTS reactor (approximately 20 bar).
2. The solvent should not poison the catalyst and should be stable under the reaction conditions. The low molecular weight paraffins chosen for SCF-FTS studies are

Table 2.1 Critical properties of hydrocarbon solvents compared to those of CO_2 and water. Solvents highlighted are commonly used in SCF-FTS. Data obtained from *NIST Scientific and Database* website http://webbook.nist.gov/chemistry/name-ser.html.

Solvent	Critical Temperature Tc, °C	Critical Pressure Pc, bar
Green solvents		
Carbon dioxide (CO_2)	30.9	73.75
Water (H_2O)	373.9	220.6
Hydrocarbons		
Ethane (C_2H_6)	32.2	48.84
Ethene (C_2H_4)	9.1	50.41
Propane (C_3H_8)	96.6	42.5
Propene (C_3H_6)	91.6	46.01
Butane (C_4H_{10})	151.85	38.0
Isobutene (i.C_4H_8)	144.75	40.0
Isobutane (i.C_4H_{10})	134.5	36.5
Pentane (C_5H_{12})	196.65	33.6
Hexane (C_6H_{14})	233.3	29.7
Heptane (C_7H_{16})	266.85	27.84

both unreactive and stable. Also, the paraffins (i.e. SCF solvents) are not coke precursors, even under the mild temperatures of FTS (Jacobs et al. 2003).

3. The solvent should have a high affinity for aliphatic hydrocarbons in order to extract the wax from the catalyst surface and reactor. As shown in Table 2.1, most of the solvents that are used in SCF-FTS operations (those highlighted) have this ability.

In earlier study, Jacobs, at al.(Jacobs et al. 2003) suggested that using solvent mixture composed of 55 volume% hexane/45 volume% pentane should give favorable liquid-like densities, while still maintaining gas-like transport properties at a pressure of approximately 82.4 bar. They used a Hysys 2.1 process simulator for the determination of the critical properties of this solvent mixture and the effect of pressure on its density, as shown in Figures 2.7 & 2.8, respectively. However, to maintain a constant space velocity inside the reactor they used argon as a balancing gas. The presence of Argon in the solvent mixture may have significantly altered the phase-behavior of the solvent mixture shown in Figures 2.7 & and 2.8, and thus produced an environment closer to compressed gas than the supercritical phase. Fan and Fujimoto.(Fan and Fujimoto 1999) reported SCF-FTS performance in both hexane environment and pentane environment. They concluded that operating an FTS reaction in a supercritical pentane (Tc = 196.7 °C, and Pc=33.6 bar) environment is preferred for wax synthesis experiments where the reaction temperature is low, while for the production of light hydrocarbons and middle distillates that require a high

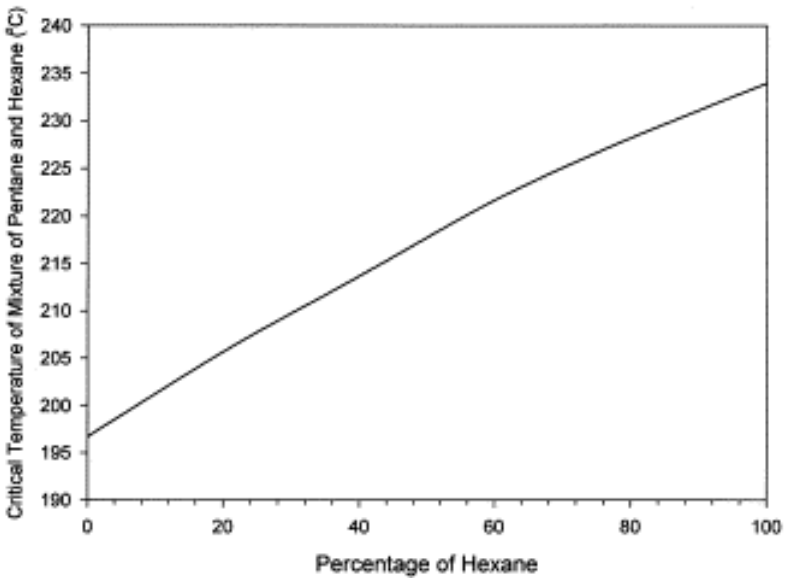

Figure 2.7 Critical temperature of pentane and hexane mixture with increasing hexane percentage (Jacobs et al. 2003).

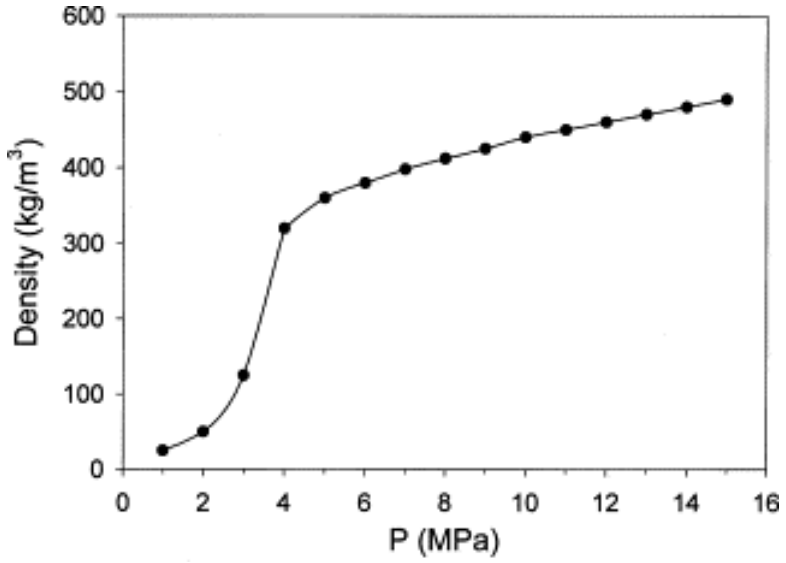

Figure 2.8 Density versus pressure for a mixture of 55% hexane and 45% pentane at 220 °C (Jacobs et al. 2003).

reaction temperature hexane can be chosen as supercritical solvent (Tc = 233.3 °C, and Pc=29.7 bar).

Huang, et al.(Huang et al. 2004) reported a comparison between the performances of Sc-pentane-FTS and Sc-hexane-FTS over an alumina supported catalyst and under similar reaction temperatures and densities. In order to achieve the same density condition ($\rho \approx 0.3$ g/cm^3), higher pressures are required in pentane (45 bar in hexane vs 65 bar in pentane at 240 °C). The results presented in Figure 2.9*a* demonstrate that there is not much difference in the hydrocarbon distributions for carbon numbers less than C_{20} in either supercritical pentane FTS or supercritical hexane FTS reactions at constant density. Similarly, α-olefin selectivity shows no significant difference under constant density operation in Sc-pentane and Sc-hexane (see Figure 2.9*b*). Nevertheless, a higher CO conversion of 92% was observed in Sc-pentane-FTS as opposed to 61% in Sc-hexane-FTS, which was attributed to the influence of pressure on the reaction kinetics.

2.3.3 Catalyst activity and stability during supercritical FTS operation

Deactivation of a catalyst during conventional FTS reaction results in a drop in syngas conversion and hydrogenation activity and has been attributed to many reasons; the poisoning or blocking of catalytic active sites by products or carbonaceous species (Anderson et al. 1949; Madon and Iglesia 1994), or the partial reoxidation of the catalyst (especially cobalt-based catalysts) at the surface by water or the oxygen produced by CO

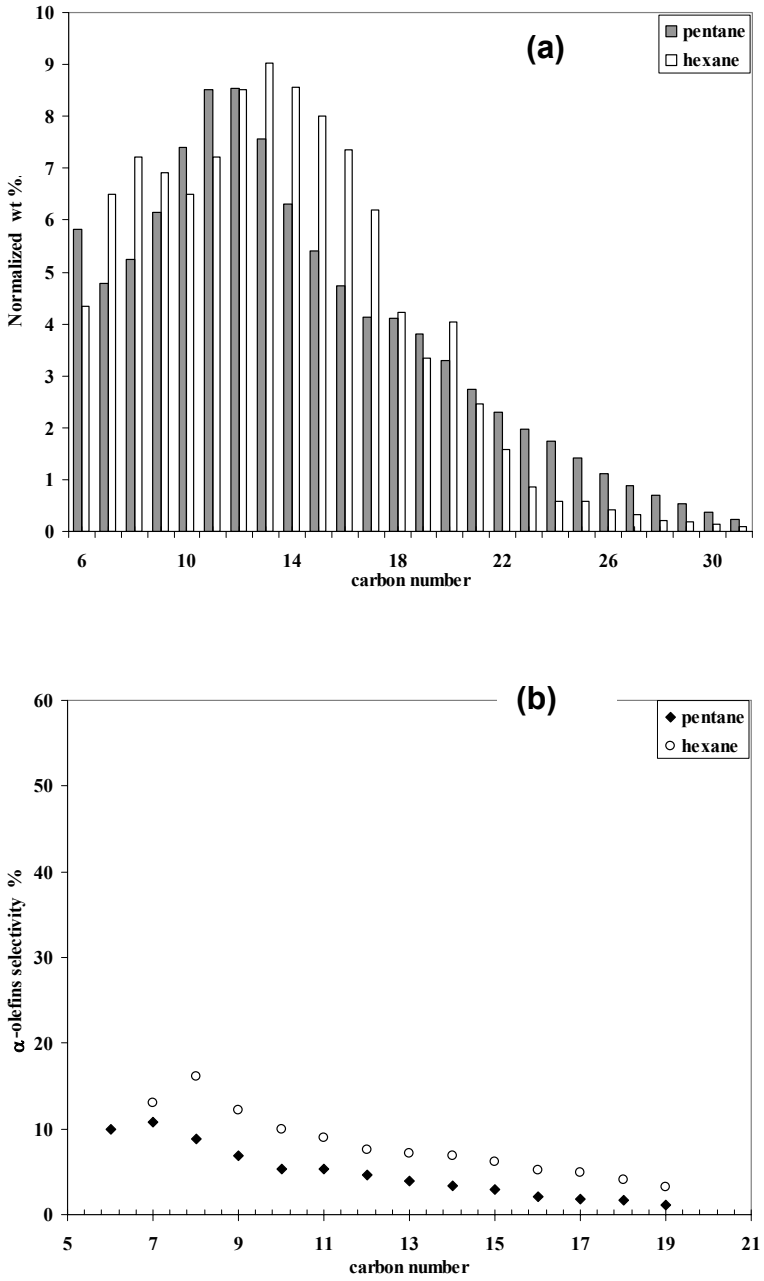

Figure 2.9 Hydrocarbon selectivity (a) Normalized weight percentage vs carbon number, and (b) α-olefin selectivity at constant medium solvent density ($\rho_{solvent}$ = 0.335 g/cm^3) in supercritical pentane and hexane phase FTS. Pentane: 240 °C, 65 bar, flowrate of 1 ml/min, and CO conversion of 92%. Hexane: 240 °C, 38 bar, flowrate of 1 ml/min, and CO conversion: 61%. For both cases, a syngas flowrate of 50 sccm/g_{cat}; and H_2/CO ratio of 2.0 were used (Huang et al. 2004).

dissociation (Lahtinen et al. 1994; Jager and Espinoza 1995). Effective in situ extraction of heavy hydrocarbon products from the catalyst pores was assumed to decrease significantly due to the deactivation of FTS catalysts (Jacobs et al. 2003). However, stability in catalyst activity was observed even over a long time-on-stream (TOS) FTS operation when conducting the reaction in supercritical fluid medium. This was early explained by the model proposed by Yokota et al. (Yokota et al. 1990), shown in Figure 2.10.The model shows that the desorption and diffusion of FTS products are well-balanced in the supercritical phase. Therefore, the overall mass transfer of the products is most effective, which inhibits secondary reactions during the chain propagation. Lang, et al. (Lang et al. 1995) demonstrated that operating FTS under supercritical propane (the results of which are shown in Figure 2.11) over a precipitated iron catalyst stabilize the catalyst activity for a relatively long period of time (120 hr) with higher CO conversion and H_2/CO usage ratio than for the conventional gas phase reaction (included as a base-line condition in Figure 2.11 for comparison). They also showed that returning to the gas-phase reaction after operating in SCF sustains the catalyst activity for more than 250 hr in total.

Huang and Roberts (Huang and Roberts 2003) have also shown that activity in SCF-FTS is higher than in gas-phase FTS despite the fact that mass transport and product bulk diffusion rates are higher in the gas phase than in the supercritical phase. Their steady state data (20 h for SCF and 30 h for gas -phase), presented in Figure 2.12, show that operating FTS in Sc-hexane yields higher CO conversions (ca. 70%) relative to the gas-phase FTS (ca. 50%). In addition, their findings show that steady-state operation was

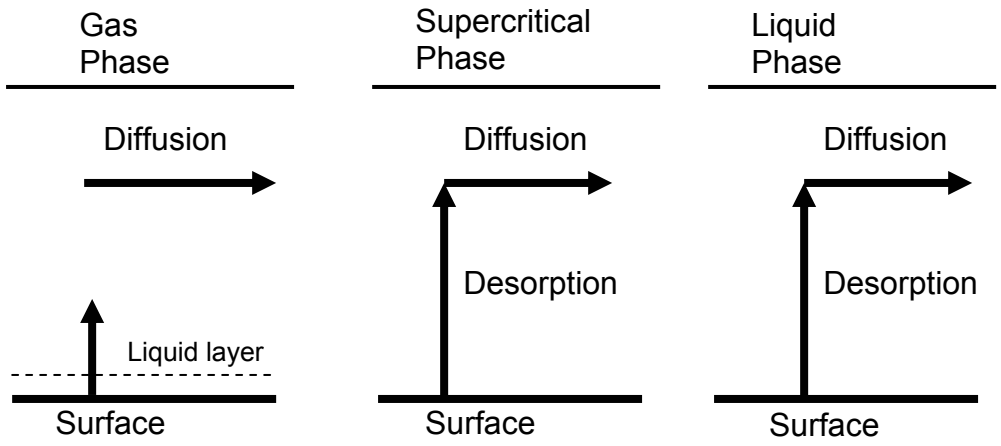

Figure 2.10 Model of overall diffusion of the products in three reaction phases (Yokota et al. 1990).

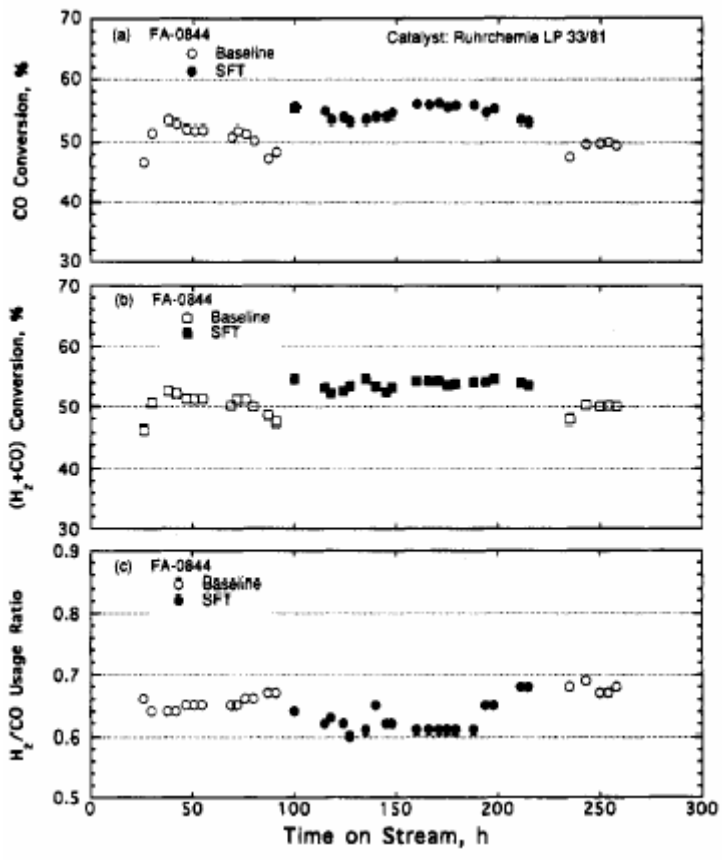

Figure 2.11 Variations in (a) CO conversion, (b) (H_2 + CO) conversion, and (c) H_2/CO usage ratio with time on stream in run **FA-0844.** Baseline process conditions: P_{H2+CO} = 1.48 MPa, 250 °C, L(NTP)/(h.g_{cat}), H_2/CO = 0.67**;** SFT = supercritical Fischer- Tropsch synthesis *(P_{H2+co}* = 1.48 MPa, P_{C3H8} = 5.52 MPa; P_{tot} =**7** MPa) (Lang et al. 1995).

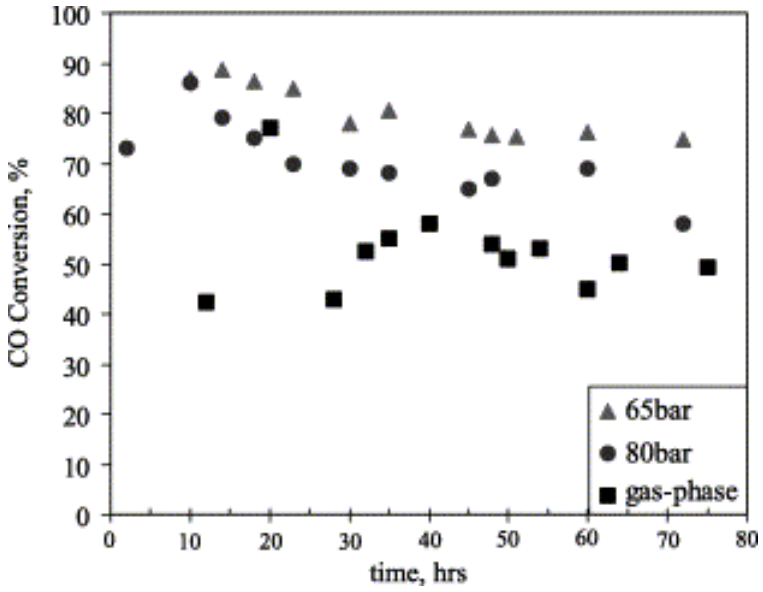

Figure 2.12 CO conversion in gas-phase and supercritical-phase FTS (temperature: 250 °C; pressure (SCF phase): 65, 80 bar; syngas partial pressure (gas phase and SCF phase): 20 bar; hexane flow rate: 1 ml/min; syngas flow rate: 50 sccm/$g_{catalyst}$; syngas ratio (H_2/CO): 2:1) (Huang and Roberts 2003).

achieved more rapidly under SCF-FTS than in gas-phase FTS. They attributed these results to the higher solubility and in situ extractability of the SCF, resulting in suppressed coke formation inside the catalyst pores. Moreover, the liquid-like gas membrane resistance that occurs on the catalyst surface in gas-phase FTS could be reduced under supercritical-phase operation by the solubility-driven removal of heavy hydrocarbons (Huang and Roberts 2003). By using a tailor-made wax, Jacobs et al. (Jacobs et al. 2003) were able to simulate the extraction process of heavy wax from inside the catalyst pores for the three phases, as shown in Figure 2.13. Their findings show that wax can easily and quickly be extracted from the catalyst pores in both the supercritical phase and liquid-phase (up to 80% extraction within 1 hr), while little was extracted during gas-phase operation.

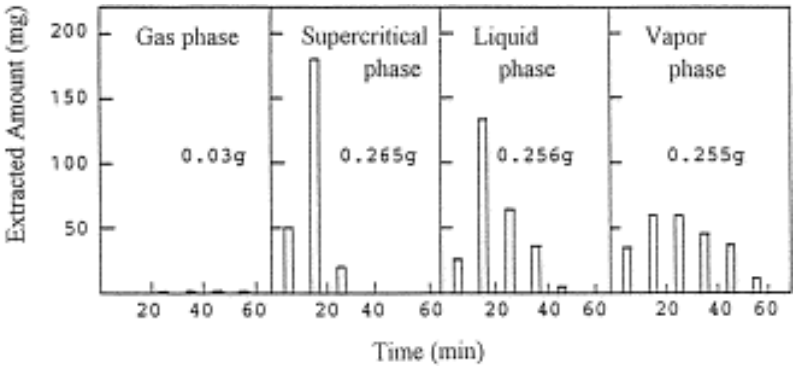

Figure 2.13 Model in situ extraction experiment 17 wt.% paraffin wax on silica support, standard reaction conditions. The weights in the figures are the total weights of the extracted hydrocarbons (Jacobs et al. 2003)

2.3.4 Hydrocarbon product distribution and control of selectivity in SCF-FTS

Deviations from the ASF product distribution model (discussed in detail in section 1.4.2) were targeted by many studies as a means of controlling the hydrocarbon distribution in FTS in order to maximize the production of hydrocarbons within specific carbon number ranges (e.g. C_5-C_{11} for the gasoline fraction, C_{12}-C_{19} for the diesel fraction, or higher carbons for the heavy wax range). Success in deviating the product distribution from the standard ASF model represents a breakthrough in FTS technology, allowing high selectivity towards desired products such as desired transportation fuels (e.g. diesel fuels) (Dry 2001). As we mentioned earlier, enhancement in chain growth probability and increase of selectivity towards high value added chemicals (e.g. α-olefins) were observed in SCF-FTS (Yokota et al. 1990; Bukur et al. 1997). Higher productivity of α-olefins, the primary product in the FTS chain growth process, indicates suppression of secondary reactions such as hydrogenation to paraffins, isomerization and oxygenations. An example of the enhanced productivity of α-olefins in supercritical phase FTS compared to the conventional FTS processes is illustrated in Figure 2.14 (Yokota et al. 1990; Bukur et al. 1997), which shows in that α-olefins are always higher in the supercritical phase, with a peak shoulder within the middle distillate products (C_7-C_{14}). α-olefins are also known to incorporate in the chain-growth process and behave similarly to the FTS building blocks by either initiating a new chain or becoming a part of a growing one.

Deviations from the standard ASF distributions were observed when conducting FTS reactions in supercritical phase solvents. Tsubaki, et al. (Tsubaki et al. 2002)

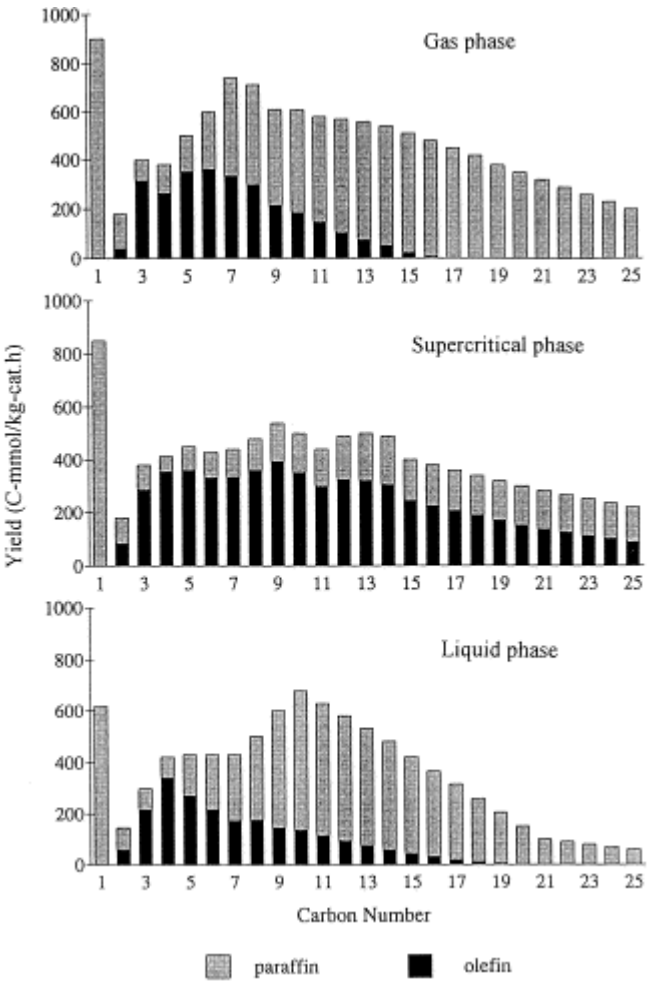

Figure 2.14 Olefin distribution in hydrocarbon products of FTS reactions in various phases over Ru/Al_2O_3 catalyst (Yokota et al. 1990).

reported a surprising non-ASF product distribution in the supercritical pentane phase at a reaction temperature of 200 °C over a silica supported cobalt catalyst. The authors reported a hydrocarbon product distribution that showed that the formation rate of hydrocarbons from C_7-C_{28} was totally independent of the carbon number, with an α-value higher than 0.96 (see Figure 2.15). They suggested that the high ability of the olefins (C_nH_{2n}) formed to readsorb in the supercritical phase and initiate new chain-growth processes acts to increase the formation rate of heavy hydrocarbons. However, the authors have not explained the mechanism by which C_8 and C_{26} behave equally in initiating new chains, promoting heavier hydrocarbon production with a similar rate of formation.

However, another study (Jacobs et al. 2003) that employed mixed supercritical solvents (55% hexane-45% pentane) with an alumina supported cobalt catalyst at 220 °C and over a wide range of pressures (from 23 bar to 54.5 bar) showed that hydrocarbon distributions beyond C_{10} followed closely the ASF distributions model (see Figure 2.16). No information about the light hydrocarbon (C_1-C_9) distribution was presented in this communication. Bochniak and Subramaniam (Bochniak and Subramaniam 1998) reported non-ASF distributions in SCH-FTS on Ruhrchemie iron catalyst at a temperature of 240 °C by varying the pressure from 35 bar (gas-like density) to 70 bar (liquid-like density). Their product distributions, shown in Figure 2.17, illustrate the existence of a shoulder in the carbon fractions from C_5-C_{10} that decreased with increasing pressure; however there were no significant changes in the light product distribution (C_1-C_4) with pressure. This phenomenon was reported to disappear after 80 hr time-on-stream

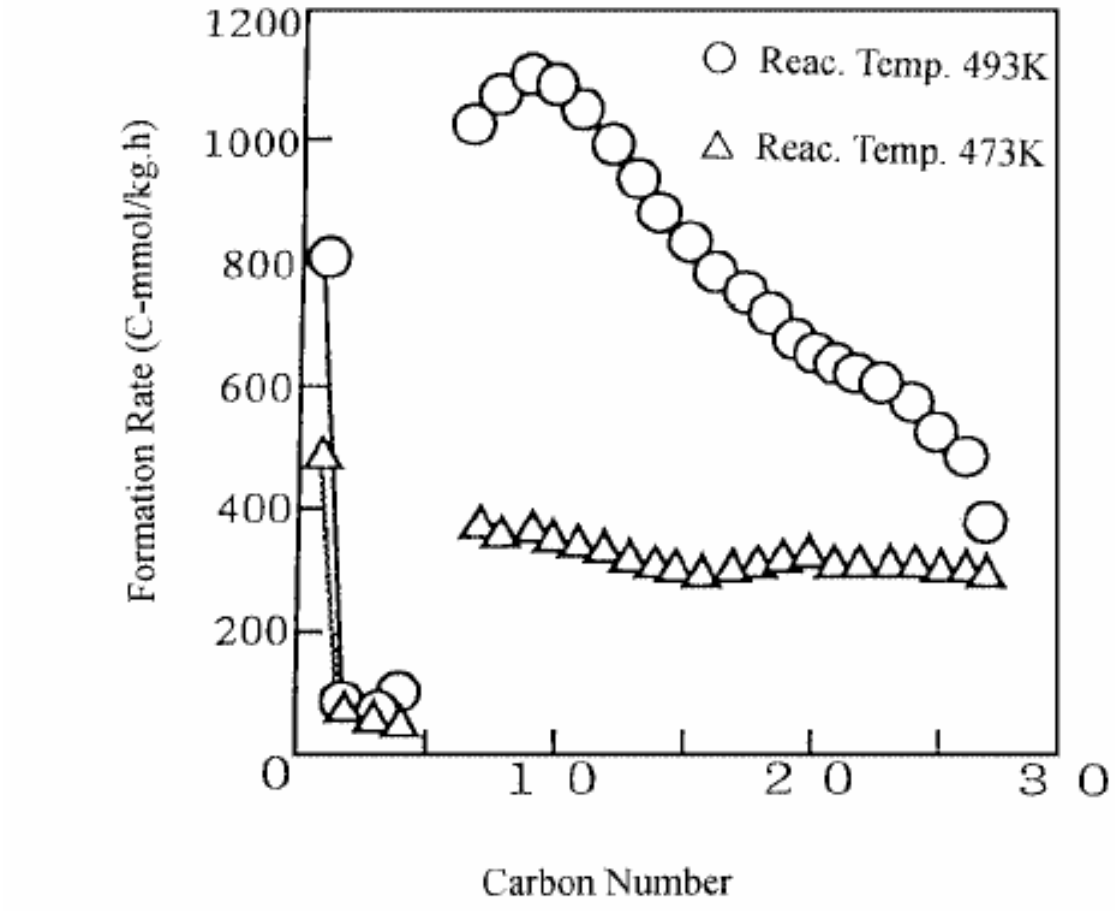

Figure 2.15 Anti-ASF hydrocarbon distribution in FTS reactions with supercritical-phase *n*-pentane. Co/SiO_2 =40/100 (wt); *P* (total)=45 bar; *P* ($CO+H_2$)=10 bar; *P* (*n*-pentane)=35 bar; CO/H_2 =1/2; W/F (CO+H2)=9 g/mol h^{-1} (Tsubaki et al. 2002).

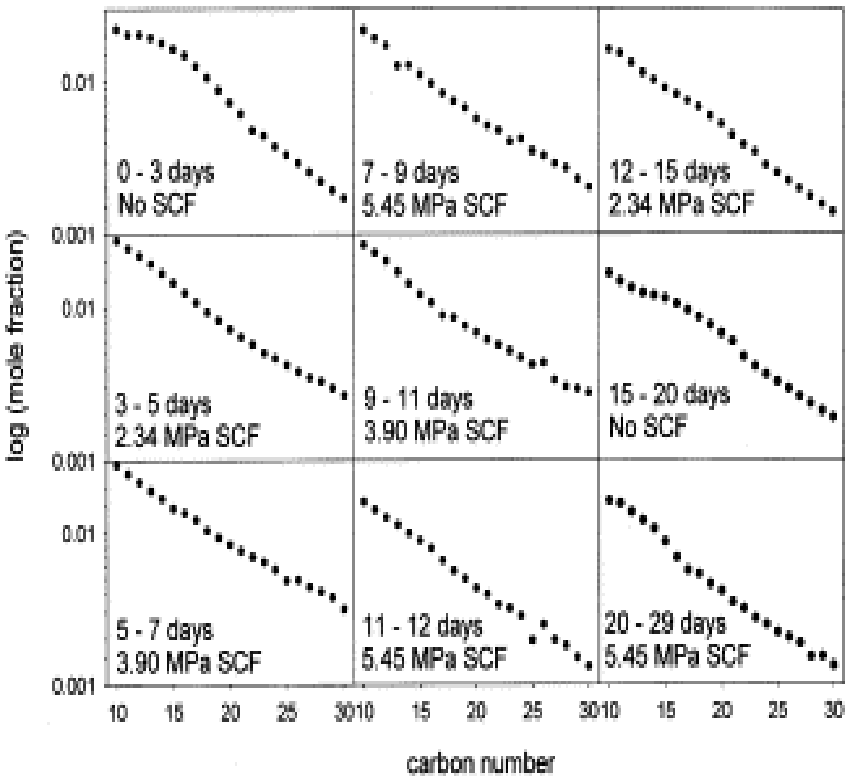

Figure 2.16 Product distribution for C_{10}-C_{30} Carbon number products during various operating periods (Jacobs et al. 2003).

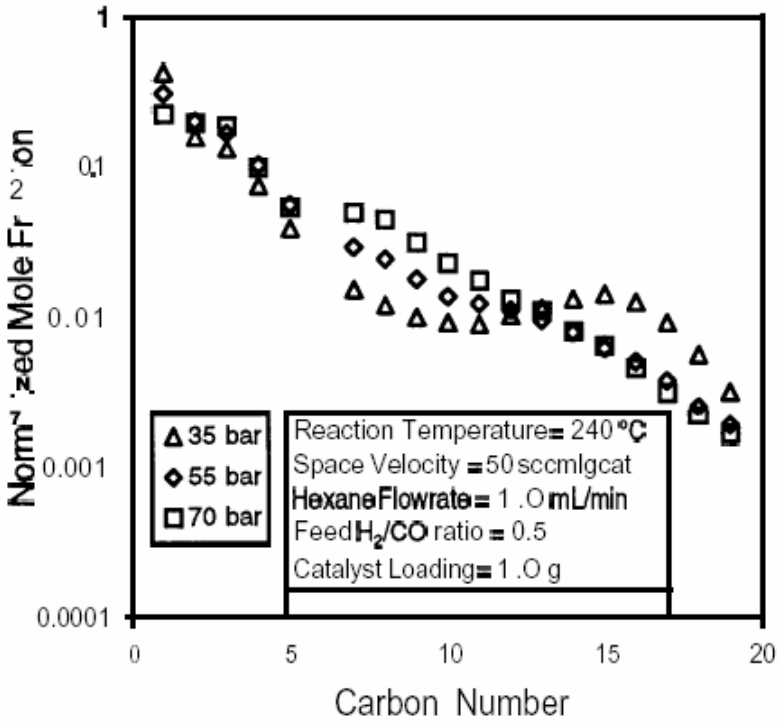

Figure 2.17 Pressure tuning effects on steady-state ASF product distribution (α) (Bochniak and Subramaniam 1998).

Furthermore, they (Bochniak and Subramaniam 1998) attributed the enhanced chain growth probability in SCH medium to the enhanced extraction of heavier olefins in the liquid-like medium prior to any secondary reactions. Meanwhile, at high pressure (70 bar) they suggested that the diffusion rate of α-olefins decreased significantly, and results in regular ASF distributions (Bochniak and Subramaniam 1998).

Elbashir and Roberts (2004a) reported significant deviation from the standard ASF model within Sc-hexane-FTS in near-critical and supercritical conditions (controlled by tuning the reaction temperature and/or pressure) over an alumina supported cobalt catalyst. The degree of deviation from the ASF model was found to vary from near-critical to supercritical and from liquid-like density to gas-like density. They suggested that the hydrocarbon product distribution in Sc-hexane FTS should be represented by more than one chain growth probability for the different ranges of hydrocarbons, as shown in Figure 2.18. Very high chain growth probability (α-value ≈ 0.95) was observed within the middle hydrocarbon distillates (i.e. C_5-C_{15}) as shown in Figure 2.18. This phenomenon was attributed to the enhanced α-olefin incorporation in the chain growth process and a model for the reaction network and chain growth pathway was proposed accordingly (Elbashir and Roberts 2004a).

2.3.5 Phase behavior of SCF-FTS reaction mixture

Few studies have dealt with the phase behavior of the reaction mixture within supercritical phase FTS (Joyce et al. 1999; Gao et al. 2001; Polishuk et al. 2004). Joyce and his coworkers (Joyce et al. 1999) studied the vapor-liquid composition for a mixture of hexane (supercritical solvent) + C_{16} (FTS wax) at three different temperatures (199,

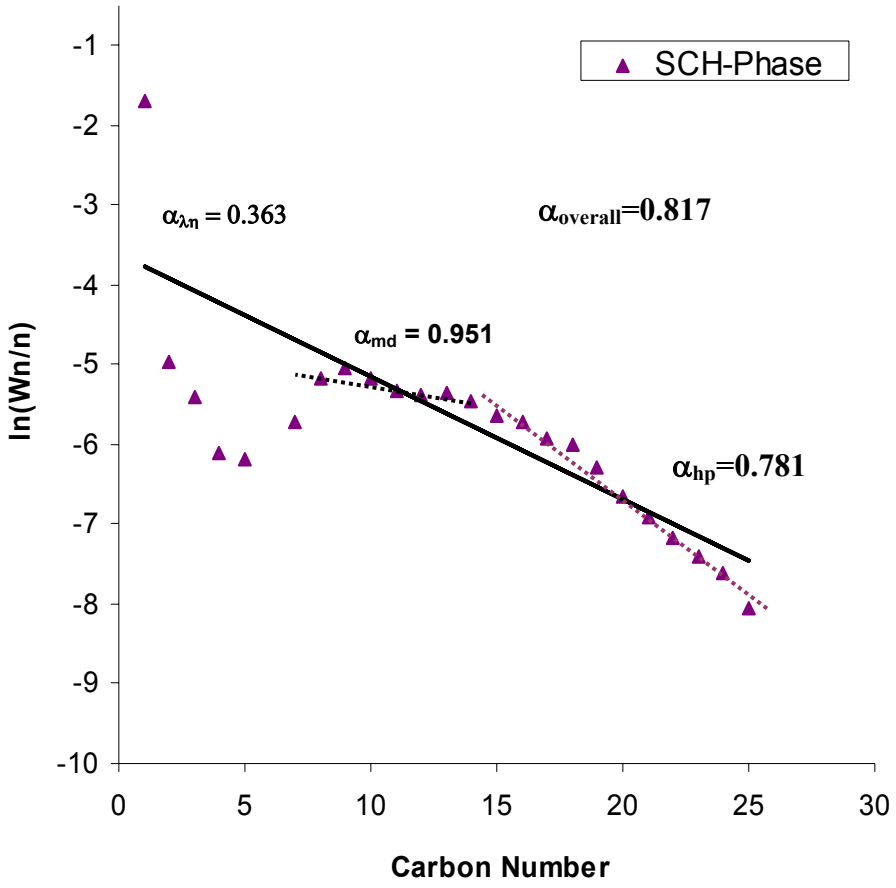

Figure 2.18 A typical hydrocarbon product distribution in Sc-hexane-FTS. $\alpha_{overall}$ represents the slope of the solid line and was calculated from the standard ASF model; α_{lp}, α_{md}, α_{hp} represent the chain growth probability of the light hydrocarbons, middle distillates, and heavy hydrocarbons, respectively (Elbashir and Roberts 2004a).

252, and 300 °C). Hexadecane and hexadecene (C_{16} hydrocarbons) was used to simulate the changes in the phase behavior of hexane as the percentage of heavy hydrocarbons in the product stream increased. Their findings showed that for a 0.0326 mole fraction of C_{16} in the hexane+hexadecane mixture, the critical pressure and temperature of the mixture were 33.76 bar and 252 °C, respectively. These results can be considered as a significant change in the critical properties of the dominant hexane medium, since the critical pressure and temperature of pure hexane are 32.4 bar and 234.5 °C, respectively. In another study, Gao et al. (Gao et al. 2001) reported the phase behavior of the hexane (above 94% by mole) + reactant (CO, and H_2) mixture at different moles ratios. They reported that the critical temperature and critical density of the solvent-reactant mixture decreased as the concentration of CO and H_2 increased, hence the critical pressure increases with CO+ H_2 concentration. More recently, Polishuk et al. (Polishuk et al. 2004) used thermodynamic modeling to predict the critical and the near-critical data for very asymmetric systems that represent the FTS product spectrum, such as propane-*n*-hexatetracontane. They used the global phase diagram approach (GPDA) and the predictive Soave–Redlich–Kwong model (PSRK), to describe the experimental data in the binary homologous series of *n*-alkanes. Their results showed that the reliability of GPDA in comparison with PSRK becomes evident when predicting the data of asymmetric systems.

In another study, (Elbashir and Roberts 2004a) reported the influence of temperature and pressure on the location of the critical point and the boundary for a single phase SCH-FTS operation. In addition to the solvent (hexane), the mixture in this study referred to the reactants (CO, and H_2) and products (hydrocarbons, CO_2, and H_2O)

collected from the outlet of the reactor under a typical supercritical hexane FTS conditions. The reaction mixture is composed of 75 mole% hexane, 5 mole% syngas, and 20 mole% hydrocarbons (C_1-C_{30}) and water. The measured critical pressure of the FTS sample mixture was found to be 37.2 bar (7 bar higher than that of pure hexane), however, the critical temperature (238.2 °C) of the mixture was found to be slightly higher than that of pure hexane (234.5 °C). However, it should be noted that while this measured critical point represents the bulk reaction mixture, it does not necessarily represent that of the reaction mixture within the catalyst pores (Elbashir and Roberts 2004a).

2.3.6 Kinetics and modeling of reaction pathways in supercritical FTS

Few studies reported mechanism and kinetics modeling of SCF-FTS (Fan et al. 1992; Bochniak and Subramaniam 1998; Elbashir and Roberts 2004b). Fan et al. (Fan et al. 1992) suggested the following empirical power rate law for Sc-hexane-FTS over Ru catalysts of different pore diameter and pore size:

$$r = k P_{H_2}^{x} P_{CO}^{y}$$

where k is the rate constant and x and y are the exponential constants. They referred to previous FTS kinetic models (Karn et al. 1965; Vannice 1976) that suggested that the rate of an FTS reaction on ruthenium catalysts is first order in H_2. As a result, they were been able to calculate the apparent rate constant for each catalyst (of different pore diameter and size) and defined the catalyst effectiveness factor as the ratio between the rate of reaction in supercritical fluid to that in gas phase reaction.

Bochniak and Subramaniam (Bochniak and Subramaniam 1998) used the diffusion-enhanced readsorption model (Madon et al. 1991) to explain the deviation of product distribution in supercritical hexane from the standard ASF model. In order for them to explain the increase in syngas conversion with reactor pressure in a supercritical fluid medium, they correlated the effectiveness factor (ηks) with the pressure. The effectiveness factor was derived by assuming a plug-flow reactor and that the syngas conversion is pseudo first order reaction in H_2 (they referred to Anderson's (Anderson 1984) model for syngas conversions below 60%). The general stoichiometric equation (below) was used to derive the effectiveness factor

$$H_2 + 2CO \rightarrow \frac{1}{n}(CH_2) + CO_2$$

The derived effectiveness factor was then found to be;

$$\eta k = \left(\frac{F_{S0}}{F_T F_{S0} W} \right) \left(- F_0 \ln(1 - x_A) + 2F_{A0} \{ \ln(1 - x_A) + x_A \} \right)$$

The calculated effectiveness factor (ηk) was found to increase with pressure in the system, which they attributed to the alleviation of pore diffusion limitations (viz., maintenance of wider pore channels) as a result of enhanced extraction of heavier hydrocarbons from the catalyst pores by the liquid-like densities, yet significantly better-than-liquid diffusivities, of *n*-hexane (Bochniak and Subramaniam 1998).

Both of the suggested rate equations for the SCF-FTS (Fan et al. 1992; Bochniak and Subramaniam 1998) rely on gas-phase and liquid-phase kinetic models, which result in very simplified rate equation formulas. Recently, Elbashir and Roberts (2004b) suggested a reaction network for SCF-FTS that takes into account the role of enhanced α-olefin

incorporation in the chain growth process under SCF operation. The model assumes that operating FTS in SCF medium promotes the in situ extraction of heavy products from the catalyst pores and as a result accessibility to active sites increases. Those vacant sites (due to the enhanced extraction) were assumed to promote both adsorption of CO and H_2 and incorporation of α-olefins in the chain growth process. The kinetics model and the reaction pathway were derived from the surface reaction kinetic model (see Section 1-3.1) (Bell 1981; Kellner and Bell 1981; Uner 1998). The proposed reaction pathway shown in Figure 2.19 assumes that the characteristics of Co catalyst site very much control the initial stages of the synthesis (stages 1-3), implying the supercritical solvent has the least influence at these stages. The reaction rate equations were then derived by using the simplified assumptions of Sarup and Wojcichowski (Sarup and Wojciechowski 1988) to yield the following rate expression for CO consumption:

$$-r_{CO} = \frac{kP_{CO}^{1/2}P_{H_2}^{1/2}}{[1 + K_1P_{H_2}^{1/2} + (K_2 + K_3)P_{CO}^{1/2} + K_4P_{CO}]^2}$$

This model was found to be in a good agreement with the experimental results obtained from the gas-phase FTS, though, it poorly predicted the behavior under Sc-hexane-FTS. The authors (Elbashir and Roberts 2004b) suggested improving the kinetic model to predict SCH-FTS behavior by including thermodynamic nonidealities into the rate expression, and quantifying the influence of modified active site (evacuated ones, *S**).

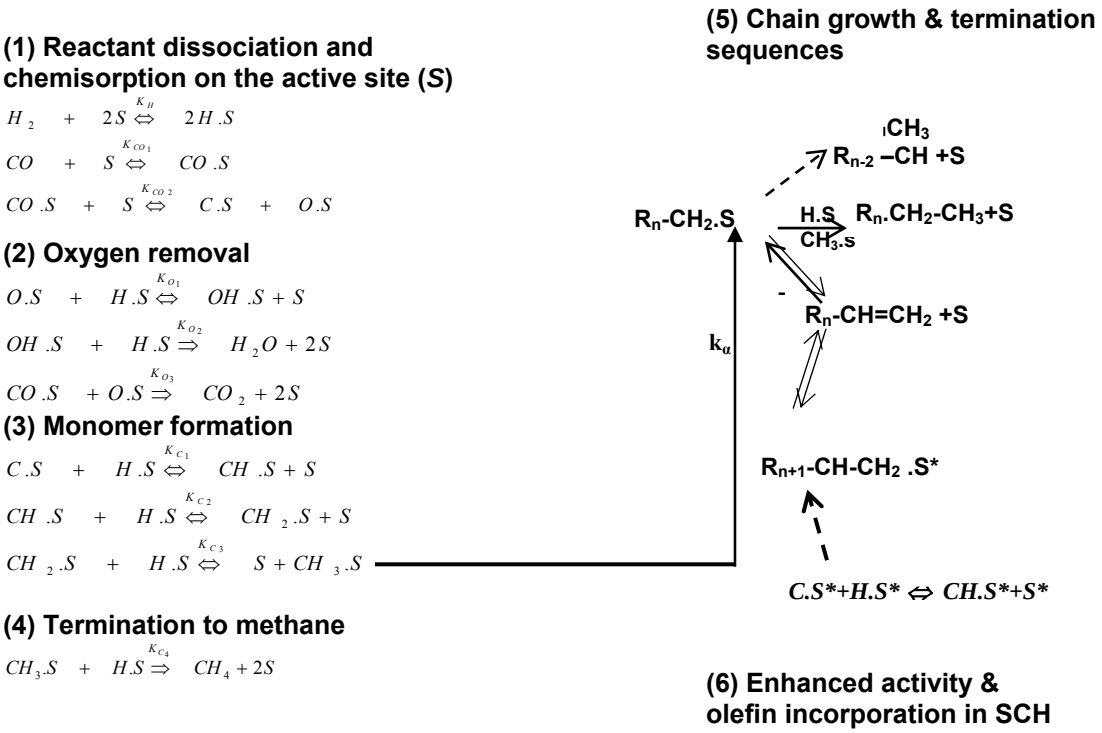

Fig 2.19 FTS reaction network including the enhanced activity and olefin incorporation sites (Elbashir and Roberts 2004b).

2.4 Conclusions

In general, SCF technology is still expensive compared to conventional processes; however, it presents a variety of specialized opportunities to produce new and improved products. Many industrial applications find this an obstacle, as well as the fact that high-pressure equipment can be quite costly. Despite these difficulties, the attraction of combining natural catalysts with natural solvents has provided the driving force behind a growing body of literature concerning the development of new economically feasible SCF processes (Prajapati and Gohain 2004). A better understanding of the phenomena associated with operating under near-critical and supercritical conditions, combined with the optimum utilization of those properties in improving the process performance, is the major challenge for future researchers in this field.

The major role of SCFs in the FTS reactions arises from their ability to desorb heavy hydrocarbons (that typically have low volatilities in low density gas-phase FTS) and transporting them out of the catalyst's pores, creating more vacant sites for the synthesis process. The operating conditions in SCF-FTS that provide the optimum fluid properties for maximizing a given performance criterion (catalyst activity, catalyst stability and effectiveness, control of selectivity, etc.) are not only governed by the critical properties of the fluid (solvent), but are rather governed by the properties of the FTS mixture obtained after establishing steady-state conditions. The physical properties of that mixture can be tuned from a liquid-like density to a gas-like density by simply changing the reaction pressure and/or reaction temperature. However, such changes also influence the kinetics and the rates of the different reactions taking place on the catalyst

surface, as well as the chain growth mechanism. This requires a quantitative knowledge of the influence of reaction parameters, not only on the phase behavior of the FTS mixture but also on the reaction kinetics. Therefore, more studies in SCF-FTS are needed to explore the unique characteristics of the operation and to enhance the advantages of the technique over the conventional process before the process become economically attractive.

CHAPTER 3

SUPERCRITICAL SOLVENT EFFECTS ON HYDROCARBON PRODUCT DISTRIBUTIONS FROM FISCHER-TROPSCH SYNTHESIS OVER AN ALUMINA-SUPPORTED COBALT CATALYST

3.1 Introduction

Fischer-Tropsch synthesis (FTS) continues to receive attention as an alternative for the production of ultraclean transportation fuels, chemicals, and other hydrocarbon products through the heterogeneous catalytic conversion of readily available syngas (CO/H_2) resources. Diesel fractions from FTS have unique characteristics that include very low sulfur and aromatic content, high cetane index, and exceptional clean burning in compression-ignition engines (Dry 2001). Compared to crude-oil-derived diesel, FTS diesel fuel has been shown to reduce the emissions of CO, nitrogen oxides, hydrocarbons, and other particulates. More importantly for the FTS process, it can take full use of rich sources of natural gas and coal as a supplement to decreasing oil resources.

The FTS reaction is a surface-catalyzed polymerization process, whereby adsorbed CO and H_2 molecules react on the surface of a catalyst with adsorbed hydrogen to form monomers (e.g., CH_x) that further react to give a wide spectrum of carbon products (C_1-C_{60}). The products include hydrocarbons (olefins, paraffins, isomers) and oxygenates, in addition to CO_2 and water. The primary products of the polymerization

reactions on either cobalt-, iron-, or ruthenium-based catalysts are α-olefins and straight paraffins (Kellner and Bell 1981; Gaube et al. 1982; Madon et al. 1991; Hanoglu et al. 1995; Patzlaff et al. 2002) α-olefins can be utilized in the petrochemical industry as intermediates for many industrial products (e.g. in the polymer industry, as raw materials for plasticizers, as household detergents, and as sanitizers) (Lappin et al. 1996). In addition to α-olefins, transportation fuel fractions of FTS (e.g., middle distillate hydrocarbons C_5-C_{11} gasoline fractions, and C_{12}-C_{19} diesel fractions) are also of significant importance to the economic value of the process.

The major challenge in FTS technology involves control of the product distribution within a specific carbon number range or hydrocarbon type (i.e. olefins, paraffins, isomers, etc.). This is due to the fact that controlling the in situ polymerization reactions involved in the FT process is very difficult. A chain growth intermediate on the catalyst surface can undergo either propagation, to form another intermediate of higher carbon number, or termination, to produce hydrocarbons (paraffins, olefins) and oxygenates with the same carbon number. If the hydrocarbon chain is formed stepwise by the insertion or addition of one monomer at a time with constant growth probability, then the chain length distribution is described by the Anderson-Schulz-Flory (ASF) distribution model (Friedel and Anderson 1950; Henrici-Olive and S. 1976). The basic assumption of the ASF model is that neither propagation reactions nor termination reactions are dependent on the carbon number. Therefore, there is a linear relationship between the logarithm of the weight of hydrocarbons at a specific carbon number divided by that carbon number (W_n/n) versus the carbon number (n) as described in Eqn. 3.1.

$$\ln\left(\frac{W_n}{n}\right) = n\ln\alpha + \ln\left(\frac{(1-\alpha)^2}{\alpha}\right) \tag{3.1}$$

Numerous studies have reported deviations from this model and show the existence of two (or more) chain growth probabilities (the α-value as given Eqn. 3.1) in the product distribution profile, instead of a single α-value, as suggested by the standard ASF distribution model (Huff and Satterfield 1984; Stenger et al. 1984; Snel and Espinoza 1987; Snel and Espinoza 1989; Madon et al. 1993; Puskas et al. 1993; Kuipers et al. 1995; Sun et al. 2002).

A variety of models have been proposed to explain non-ASF product distribution behavior. Satterfield and Huff (Satterfield and Huff 1982) and Stenger and co-workers (Stenger et al. 1984) suggested the existence of two different reactive sites that yield different chain growth probabilities. Iglesia, Madon and co-workers developed the enhanced α-olefins readsorption model; this model takes into account readsorption of α-olefins on the catalyst and their incorporation into the chain growth process, thus providing explanation for the non-ASF product distributions observed with ruthenium and cobalt catalysts (Iglesia et al. 1991; Madon et al. 1991; Madon and Iglesia 1993; Madon et al. 1993). They indicate that diffusion limitations inside the catalyst pores and longer bed residence times of α-olefins can increase the probabilities of readsorption of α-olefins and, hence, chain growth. They also showed that readsorption probability increases with molecular size as the rate of olefins removal decreases, because of intraparticle diffusion limitations. The following conclusion has been drawn: in the absence of mass transfer limitations inside the catalyst pore, an ideal ASF distribution characterized by a constant growth probability should be expected. Kuipers et al (Kuipers

et al. 1995; Kuipers et al. 1996) gave a different explanation for enhanced α-olefin readsorption, indicating that the probability of readsorption is dependent on three factors: the heat of physisorption of the olefins, their heat of dissolution inside the catalyst pore, and the olefin diffusivity through the formed wax. They suggest that the probability of readsorption can be increased for the larger olefins, because of their higher solubility or higher tendency towards physisorption (Kuipers et al. 1996). Patzlaf, et al. (Patzlaff et al. 1999b; Patzlaff et al. 2002) reached a conclusion that the deviation from the ideal ASF product distribution is not only attributed to the readsorption mechanism, but is also a consequence of two different chain mechanisms that cause a superposition of two ASF product distributions.

Conducting FTS reactions in supercritical fluid (SCF) media has been demonstrated to have certain advantages over the traditional routes(Yokota et al. 1990; Lang et al. 1995; Fan et al. 1997; Bochniak and Subramaniam 1998; Yan et al. 1998; Fan and Fujimoto 1999; Jacobs et al. 2003). The advantages can be attributed to SCF solvents offering high diffusivities (relative to a liquid) and high solubilities and improved heat transfer (relative to a gas). The characteristics of increased solubility and in situ extraction of heavy compounds during the supercritical phase reaction provides a novel route to the production of larger compounds compared to the conventional FTS process. Tsuaki, and Fujimoto (Tsubaki and Fujimoto 2000) showed that waxy hydrocarbon formation increased significantly while light hydrocarbon formation rates were suppressed effectively within the supercritical pentane environment. Bochniak and Subramaniam (Bochniak and Subramaniam 1998) showed that the catalyst effectiveness factor and pore accessibility each increased with pressure, because the extraction of

heavy hydrocarbons was enhanced by the supercritical hexane liquidlike density. In our previous study (Huang and Roberts 2003) in supercritical hexane, we also found an enhancement of product molecular weight with an increase in the reaction pressure, which demonstrates the existence of an optimum pressure within the supercritical phase, whereby the effect of pressure on bulk diffusion and pore diffusivity was well-balanced. Deviations from standard ASF distributions and the existence of two α-values was observed in many SCF-FTS studies (Bochniak and Subramaniam 1998; Tsubaki et al. 2002; Huang and Roberts 2003). Generally, the yield of heavy products ($>C_{10}$) in the SCF medium was found to be higher than that in the gas phase medium. This has been attributed to the increased solubility of hydrocarbons in the SCF medium and enhanced extraction of heavy compounds from the catalysts pores (Jacobs et al. 2003). As a result, more vacant reactive sites can be made available, thus strengthening the driving force for olefin readsorption and incorporation in the FTS chain growth process.

Proper selection of reaction conditions (such as temperature, pressure) certainly plays a pivotal role in producing desired compounds with high α-value at reasonable reactant conversion. As a matter of fact, varying either the temperature or the pressure of the reaction environment will significantly affect the thermophysical characteristics of the supercritical phase (density, diffusivity, thermal conductivity, solubility, etc.) while also affecting the kinetics. A more fundamental understanding of the effect of these process conditions is necessary to quantify the influence of the SCF environment on FTS and, specifically, the chain growth probability. In this paper, we examine various solvent effects on supercritical FTS under different reaction conditions and compare these studies to conventional gas-phase FTS reactions. This study is designed to explore the

relationship between the process conditions and the product distributions and the chain growth probabilities. The influence of tuning temperature and pressure (i.e., density) on the overall product distribution is reported. Given the dramatic influence of the density-dependent properties on FTS, one particular set of experiments was designed to directly compare hexane and pentane solvent effects at constant density and temperature (significantly higher pressures were required in pentane to achieve the same solvent density).

3.2 Experimental Section

3.2.1 Reaction System

The high pressure FTS reaction system (as shown in Figure 3.1) includes three sections: a syngas and solvent delivery section, a reaction section and a product analysis section. Detailed information about this unit is given elsewhere (Huang et al. 2002a; Huang and Roberts 2003). The catalyst used in this study is an alumina-supported cobalt catalyst (15% Co/Al_2O_3), which was purchased from United Catalyst. Table 3.1 presents Brunauer-Emmit-Teller (BET) surface areas and pore volumes of the fresh catalyst and the used catalysts from both gas-phase and supercritical-hexane-phase experiments. The supercritical solvents used in this study are *n*-pentane (99.9% purity) (purchased from Fisher; HPLC grade H399-4) and hexanes (99.9% purity) (purchased from Fisher; HPLC grade H302-4 composed of 86.10% *n*-hexane, 9.7% methylcyclopentane, and 4.2% methylpentane). These solvents were used as received. Three standard gas cylinders (Air Products Company) containing certified mixtures composed of CO, N_2 and H_2

(31.1% H_2, 2.08% N_2, and balance CO; 31.07% CO, 2.04% N_2, and balance H_2; and 48.06% H_2, 4.07% N_2, and balance CO) were used in this study.

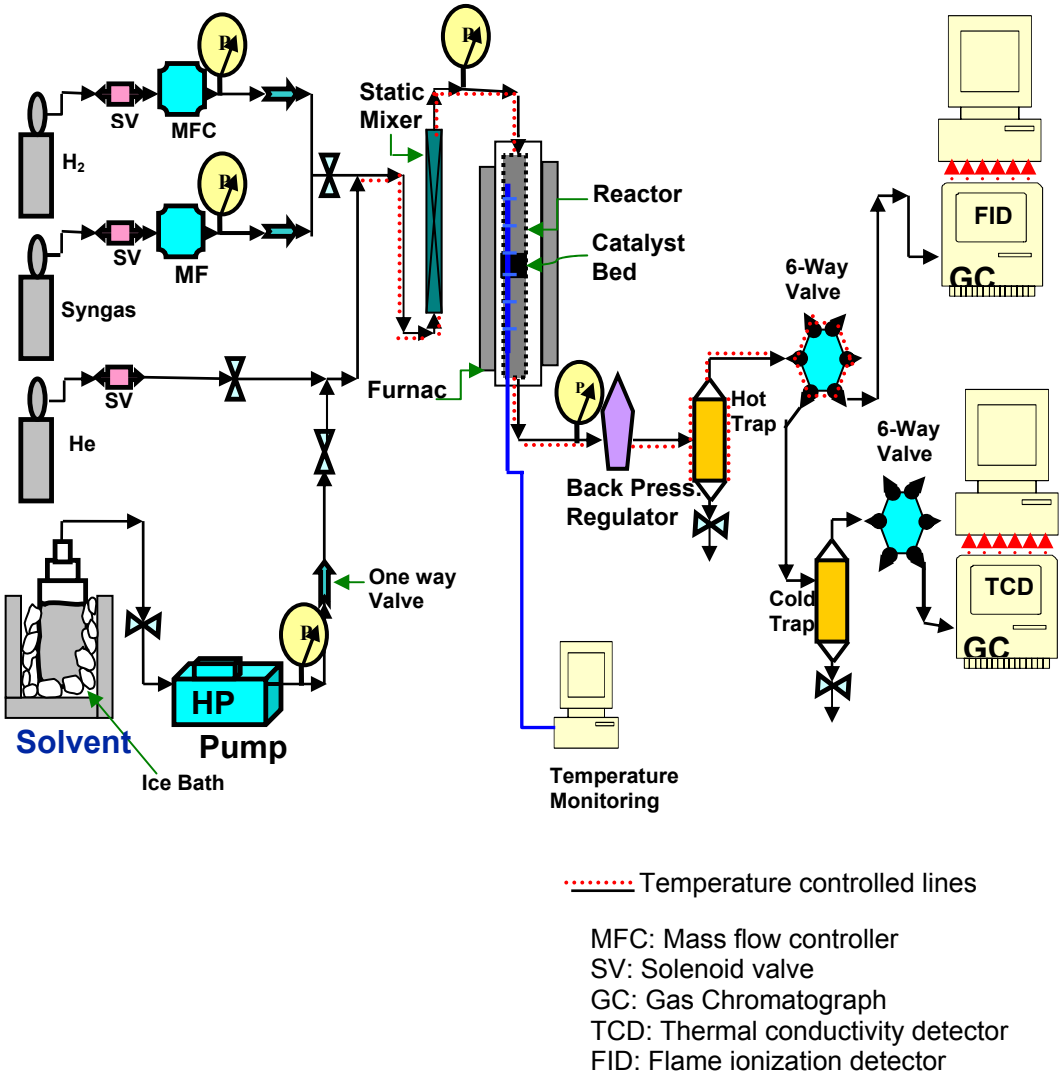

Figure 3.1 Schematic diagram of the high- pressure SCF-FTS reactor and analysis system.

Table 3.1 BET surface area and pore volume of the alumina supported cobalt (15%) catalyst before and after use in gas-phase FTS and SCF-FTS.

	Pore volume (cc/g)	Surface area, m^2/g
Fresh catalyst	0.317	144
Used catalyst (gas phase FTS)	0.285	129
Used catalyst (SCF hexane phase FTS)	0.302	138

Reaction Temperature: 250 ^oC; Reaction Pressure in SCF-FTS: 80bar; Time on stream: > 80 hours.

The catalyst (15% Co/ Al_2O_3) was located in the middle of the reactor and placed between two adjacent thermocouples of a profile thermocouple probe (Omega) that was inserted along the radial axis of the reactor. The profile thermocouple contains 8 thermocouple junctions, evenly spaced 1.4 in. apart from each other along the length of the reactor (see Figure 3.2). One gram of the catalyst (screened to 100-150 μm) was loaded into the reactor, such that the top of the catalyst bed was located below one thermocouple junction and the bottom of the catalyst bed was located above the successive thermocouple junction as shown in Figure 3.2. The reactor (with a cross-sectional area of 1.27 cm×25.4 cm and an effective volume of 32 cm^3; High-Pressure Equipment Company) used in this study is a conventional downflow fixed-bed reactor. A fused quartz disc (Quartz Plus, Inc.) with a diameter of 15 mm, a thickness 2~3 mm, and porosity 4~15 μm was fixed in the middle of the reactor to support the cobalt catalyst. To position the disc in the middle of the reactor, the inner diameter of the reactor above the disc was machined to match the disc diameter exactly. A hole 1/8 in. (0.32 cm) in diameter was machined in the center of the quartz disc, to allow insertion of the profile thermocouple. This profile thermocouple allows axial tracking of the temperature distribution along the length of the reactor. Glass wool was added at the top and bottom, to prevent any catalyst particles from entering the transfer lines.

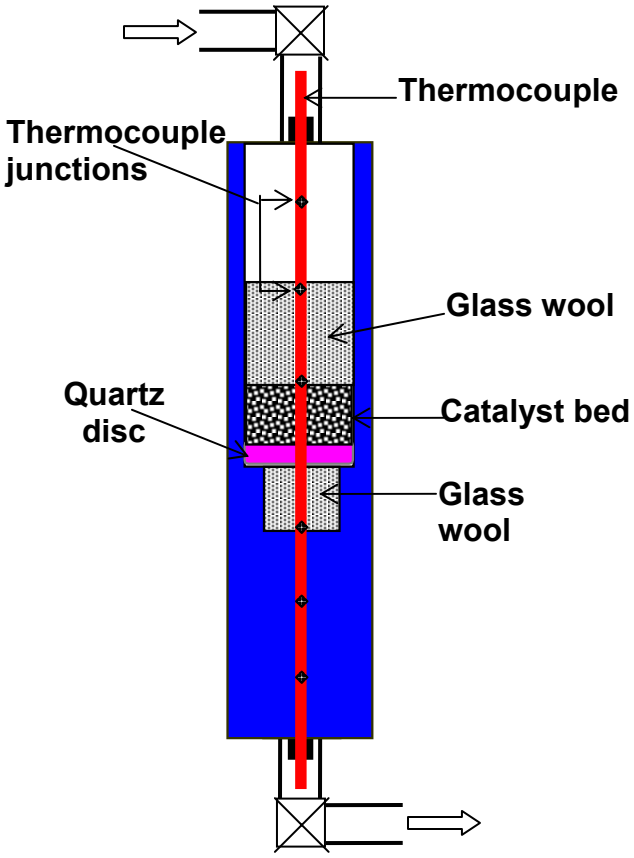

Figure 3.2 Catalyst bed and temperature readings diagram.

3.2.2 Product Analysis

Two gas chromatographs (GCs) were used for the product analysis, including a Varian model 3300 with a capillary column (DB-5) and flame ionization detection (FID) for the analysis of C_1-C_{40} hydrocarbons and oxygenates, and a Varian model CP-3800 with a packed column and a thermal conductivity detector (TCD) for the analysis of permanent gases (CO, CO_2, H_2) and C_1-C_3 hydrocarbons. The C_5 (in the case of pentane) and C_6 (in the case of hexane) products could not be accurately determined in the FID analysis, because they are masked by the high concentration of the supercritical solvent

(pentane or hexane) in the product stream. In a few of the pentane experiments, the C_2-C_4 products could not be determined, because of a technical problem with the FID detector. As such, the C_{5+} products are presented in all experiments, to provide direct comparisons of the hydrocarbon distributions in both pentane and hexane solvent media. In addition, methane selectivity was determined using the TCD analysis.

Online sampling into the two GCs was periodically carried from the hot and the cold traps using two Valco six-port-valves, as indicated in Figure 3.1, one of which was located inside a heated box with temperature control for the introduction of the product sample into the GC with FID. The effluent stream from the hot trap contains up to C_{40} hydrocarbons, as confirmed by the capillary column on-line GC. To keep the on-line sample above its dew point, the transfer line that connects the hot trap to the GC is heated and set to 200 °C. The transfer line is thermostated and wrapped with fiberglass insulation tape up to the GC. In addition, liquid samples from the effluent of the cold trap were manually injected onto the GC with FID and used to confirm the hydrocarbon product distributions.

3.2.3 Chromatograph analysis of reactants and products

The response factor of N_2 (assumed as unity) and the quantitative results of the TCD GC were used to calculate CO, H_2, and syngas ($CO+H_2$) conversions, in addition to CO_2, CH_4, C_2 (ethane and ethylene) selectivities. The response factor of a specific gas is a result of multiplying the mole ratio of that gas to that of N_2 by the area ratio of N_2 to that of the gas (as detected by the TCD). Syngas conversion ($CO+H_2$ conversion) was defined

as the molar ratio of the hydrogen and carbon monoxide consumed to those fed to the reactor; whereas, selectivities of CH_4 and C_2 are defined as moles of the gases produced per moles of CO and hydrogen consumed. Detailed information about these calculations is given in Appendix A.

The quantitative analysis of the FID chromatogram was used to determine the weight percentage of hydrocarbons (C_2 to C_{30}) in the product stream. Due to the high concentration of the supercritical solvent in the product stream, C_5 products in case of pentane and C_6 products in case of hexane, were masked and unable to be determined. The FID response factors for hydrocarbons are known to be nearly identical for the individual species (Dietz 1967). Thus, no correction was applied for the differences in individual responses, and the area percentages of the hydrocarbon species were used to represent their weight percentage. The selectivity of methane (S_{CH4}) from the TCD analysis was calculated according to equation 3.2 below.

$$S_{CH_4} = \frac{n_{1CH_4} \times N_{CH_4}}{n_{0CO} - n_{1CO}} \times 100\% \tag{3.2}$$

The moles of methane in the outlet stream are denoted by n_{1CH4}, N_{CH4} is carbon number of methane, n_{0CO} and n_{1CO} is the initial moles (before reaction) and final moles (in the reactor effluent) of CO, respectively. The calculations of the number of moles are mainly dependent on the response factor of methane compared to that of N_2, which is assumed to be unity. A similar procedure was followed for the CO_2, ethane and ethylene selectivity calculations. On the other hand, hydrocarbon product distributions (i.e. selectivity data) were calculated from the FID analysis. The weight of hydrocarbons (α-olefins, *cis*, *trans*-

olefins, paraffins, and oxygenates) of a specific carbon number (from C_2 to C_{40}) was calculated from the response factors of the measured peaks area. The response factors of all hydrocarbon species from the FID peaks are known to be nearly identical (Dietz 1967), therefore no correction factor was considered to convert peak areas to weight percentage. The selectivity (S_n) of specific species was calculated from both TCD and FID analysis using equation 3.3 below.

$$F_i = \frac{n_i \times A_{N_2} \times F_{N_2}}{n_{N_2} \times A_i} \tag{3.3}$$

The area of the species peak as obtained from the FID analysis is denoted by $A_{n,\,FID}$, $A_{C2H4,\,FID}$ is the area of the ethylene peak as obtained from FID results, while $S_{C2H4,\,TCD}$ is the calculated selectivity of ethylene from the TCD data using the same method stated in equation 3.2.

The weight of hydrocarbons at a carbon number of n (w_n) was calculated as the sum of the weight of olefins, paraffins, and oxygenates of that carbon number. The normalized weight percentage (W_n) of a specific carbon number was then calculated from the ratio of w_n to the total weight of hydrocarbon detected by the FID.

3.2.4 Experimental procedures

Before initiating the reaction, the catalyst was pretreated in a flow of CO (50 sccm (standard cubic centimeter per min)) at 280 °C (temperature ramp of 1 °C/min) and 7 bar for 24 h. The catalyst was then cooled in a helium blanket to 150 °C. The flow of solvent was then initiated at a rate of 1.0 mL/min, using a high-performance liquid

chromatograph (HPLC) pump to control the flow rate; meanwhile, the temperature and pressure were increased to the desired reaction conditions. After the temperature and pressure were stabilized, a predetermined syngas flow rate was initiated and controlled by a Brooks mass flow controller. The reactions were allowed to run continuously run until a steady state was achieved, with respect to conversion and selectivity, as determined by product analysis from the GC data. Achieving steady state operation, as indicated by a constant CO conversion and a constant product distribution profile, required ~24 h (time-on-stream) in the supercritical hexane and pentane environment, whereas >48 h were required in the gas-phase environment. Reaction temperatures and pressures ranged from 240 ^{o}C to 260 °C and 35 bar to 80 bar in hexane, and from 210 °C to 250 °C and 45 bar to 65 bar in pentane. Studies in hexane, pentane, and gas-phase FTS were performed with identical loadings of the catalyst. The aforementioned conditions correspond to a reduced temperature range of 1.01 to 1.05 for hexane and a reduced temperature range of 1.02 to 1.11 for pentane. Within this region, the density of the solvent, as well as the density-dependent thermophysical properties, are strong functions of both temperature and pressure, as shown in Figure 3.3, which shows a plot of ρ (in units of g/cm^3) versus pressure (given in bar).

3.3 Results and Discussion

3.3.1 Product Distributions in Supercritical-Phase and Gas-Phase FTS

Figure 3.4a and b presents a comparison of the product distributions (ASF and normalized weight percentage versus carbon number) obtained from gas-phase, supercritical-hexane-phase and supercritical-pentane-phase FTS at 250 °C.

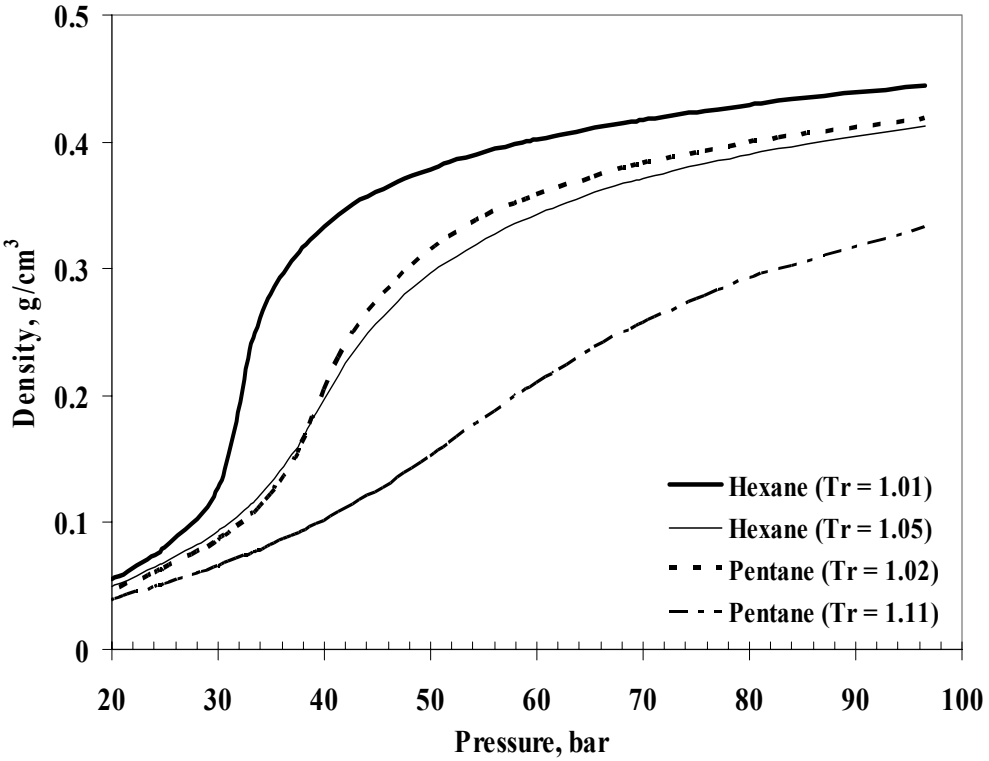

Figure 3.3 Plot of solvent density as function of pressure at different temperatures (240 ^{o}C and 260 ^{o}C in hexane and 210 ^{o}C and 250 ^{o}C in pentane). Densities were estimated using the Peng-Robinson equation of state.

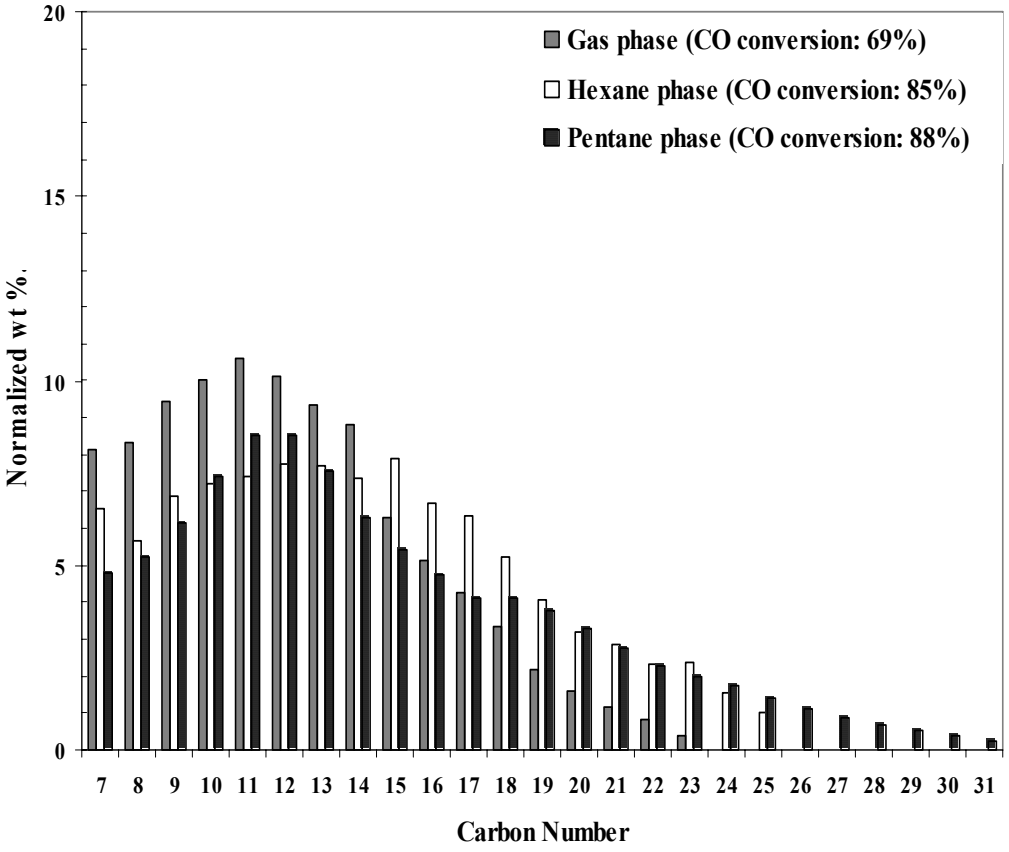

Figure 3.4a Normalized weight percentage versus carbon number in gas phase, supercritical hexane phase and supercritical pentane phase FTS (temperature: 250 °C; pressure: 80 bar (SCF hexane phase); 65bar (SCF pentane phase); syngas partial pressure: 20 bar (gas phase and SCF hexane phase), 15 bar (SCF pentane phase); flow rate of hexane and pentane: 1.0 mL/min; syngas flow rate: 50sccm/g_{cat}; and $H_2/CO = 2.0$).

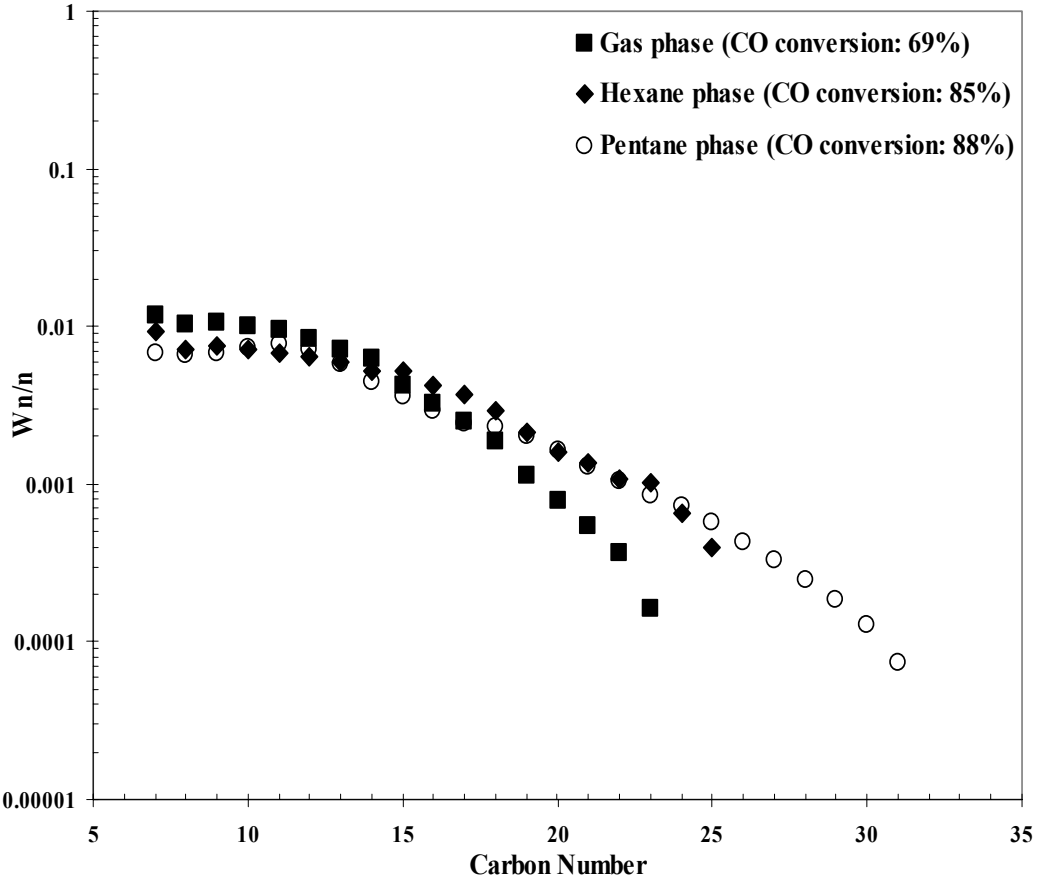

Figure 3.4b ASF plot in gas phase, supercritical hexane phase and supercritical pentane phase FTS (temperature: 250 °C; pressure: 80 bar (SCF hexane phase); 65bar (SCF pentane phase); syngas partial pressure: 20 bar (gas phase and SCF hexane phase), 15 bar (SCF pentane phase); flow rate of hexane and pentane: 1.0 mL/min; syngas flow rate: 50sccm/g_{cat}; and $H_2/CO = 2.0$).

The number, plotted versus the carbon number. The syngas partial pressure in the supercritical pentane media is c.a. 15 bar (total pressure is 65 bar), whereas it is 20 bar in the supercritical hexane reaction (total pressure is 65 bar) and 20 bar in the gas-phase reaction (total pressure is 20 bar). Although the addition of the SCF solvent dilutes the mole fraction of the syngas in the reaction mixture, the production of heavy compounds (up to C_{30}) can still be obtained, relative to that in the gas phase, even at the lower syngas partial pressure in the supercritical pentane experiment. The data in Figure 3.4a, and b demonstrate that the product distribution shifts to higher carbon number in both supercritical-hexane and supercritical-pentane FTS environments, compared to the gas phase. Figure 3.4b indicates the presence of at least two different chain growth probabilities in the ASF distributions under both gas-phase and SCF-FTS. The chain growth probability (α-value) for light hydrocarbons between C_7 and C_{10} ($7<n<10$) in both supercritical-hexane and the gas phase is almost identical (c.a. α =0.71). However, for the heavy products ($n>10$), the slope of the curve corresponding to the gas phase FTS reaction is steeper than that in the supercritical phase FTS. As a result, the overall α-value (for all hydrocarbon products shown in Figure 3.4b) is higher in the SCF-FTS compared to gas-phase FTS (α =0.87 in hexane phase; α =0.85 in pentane phase; α=0.75 in gas-phase). The high α-value in the SCF-FTS is accompanied by higher CO conversion in the supercritical phase (CO conversion of 88% for pentane-phase and hexane phase and CO conversion of 85% for hexane-phase), compared to the gas phase (CO conversion of 69%), under the above reaction conditions.

The higher solubility of heavy hydrocarbons in the supercritical phase medium, compared to the gas-phase medium, may have an important role in the enhancement of

the chain growth probability in FTS. The enhanced solubility of products in the supercritical phase results in the in situ extraction of heavy compounds (Subramaniam 2001) that otherwise condense in the catalyst pores and occupy reactive sites. As such, more free active sites would be available for the chain growth process to occur via the polymerization of reactant molecules (chemisorbed H_2 and CO) and also through the readsorbed α-olefins. Because of the elevated density under the supercritical phase conditions, the residence time of the products (including α-olefins) increases with pressure. This also promotes readsorption of those molecules and, thus, further incorporation in the chain growth process. In gas-phase FTS, the existence of an adsorption layer barrier from condensed heavy product inside the catalyst pores can inhibit reactive site accessibility. The enhanced olefin readsorption model (Iglesia et al. 1991) assumes that such mass transfer limitations (because of the existence of multiple phases such as condensed liquid and vapor phases) would facilitate the readsorption of olefins. However, this condensation of heavy compounds inside the catalyst pores limits the diffusivity of reactant molecules to the active site. The enhanced solubilities and in situ extraction in the SCF media can result in elimination of this mass transfer barrier, while also providing enhanced reactive site accessibility (Huang and Roberts 2003). Indeed, we have observed higher conversions in SCF-FTS, accompanied by higher chain growth probabilities, compared to gas-phase FTS (see Figure 3.4b). The decreased pore diffusivity in the gas-phase process (which is due to condensed heavy products during reaction) would also result in a longer residence time of products (including α-olefins) inside the catalyst pores. Longer residence times facilitate the enhancement of hydrogenation and isomerization of α-olefins to form normal paraffins and branched

products (Yokota et al. 1990; Fan et al. 1997), thus terminating their participation in the chain growth process. Table 3.1 presents the pore volumes and surface areas of the used catalysts from the gas-phase and SCF-FTS, compared to those of the unused catalyst. The pore volume and surface area of the SCF-FTS catalysts are indeed more similar to those of the unused catalyst than the catalyst recovered from the gas phase reaction.

At a reaction temperature of 240 °C, the methane selectivity in supercritical pentane was observed to be 6.6%, whereas that in supercritical hexane was determined to be 8.7%. The selectivity toward methane in both of these solvents is much lower than the methane selectivity of 27.2% obtained in the gas-phase reaction at the same temperature and syngas space velocity.

3.3.2 Effect of Temperature

The kinetics of FTS (the rates of the various reactions that occur on the catalyst surface) are strongly influenced by the reaction temperature. The reaction temperature also affects the phase behavior of the reaction media, as well as the thermophysical properties of the mixture (reactants, solvent, and products). Here, we focus on the influence of the reaction temperature on the product distribution obtained from FTS in supercritical pentane. The product distributions from supercritical pentane FTS at four different temperatures are shown in Figure 3.5a and b. At the lowest reaction temperature of 210 °C (slightly above the critical point of pure pentane of 197 ^{o}C), more-long chain products are produced (up to C_{32}). Interestingly, there are no significant changes in the normalized weight percentage for hydrocarbon products in the range of C_{10}-C_{21} under

these conditions (210 °C), indicating a very high α-value within the middle distillate products at this temperature. For instance, the normalized weight percentage for C_{10} is 5.95% and C_{21} is 3.57%, which is only a 2.4% difference in the overall weight percentage (see Figure 3.5a). At the highest temperature, the normalized weight percentage of C_6 at 250 °C is 17%, whereas that of C_{20} is only 3% (Figure 3.5a). This constitutes a significant decrease in the heavy-products formation, indicating that high reaction temperatures favor the formation of light hydrocarbons. At high-temperature operation (250 °C), the formation of heavy hydrocarbons during the chain growth process is limited to carbon numbers below C_{25}, with a sharp decline in the slope in Figure 3.5b. An interesting trend in the ASF distribution was observed at low temperatures (210 °C and 220 °C), where the curves in the middle distillate range (C_{15}-C_{20}) show an almost horizontal trend with very high α-values within this carbon number range. Similar trends were also observed in supercritical hexane FTS.

The reaction temperature showed a similar influence on α-olefin selectivity (number of moles of α-olefin produced per total number of moles of olefins and paraffins at a specific carbon number) to that on the chain growth probability. As shown in Figure 3.6, the selectivity of α-olefin decreases as the temperature increases, especially for the middle distillate hydrocarbons. At high reaction temperatures of 240 °C and 250 °C the selectivity of α-olefins reaches its lowest values (20%) for light hydrocarbons products and almost disappears for heavier products (C_{11+}). At low reaction temperatures (210°C and 220 °C) the selectivity of α-olefins is above 50% for light hydrocarbons and above 20% for middle distillates (up to C_{18}). Bukur and co-workers (Bukur et al. 1997) have

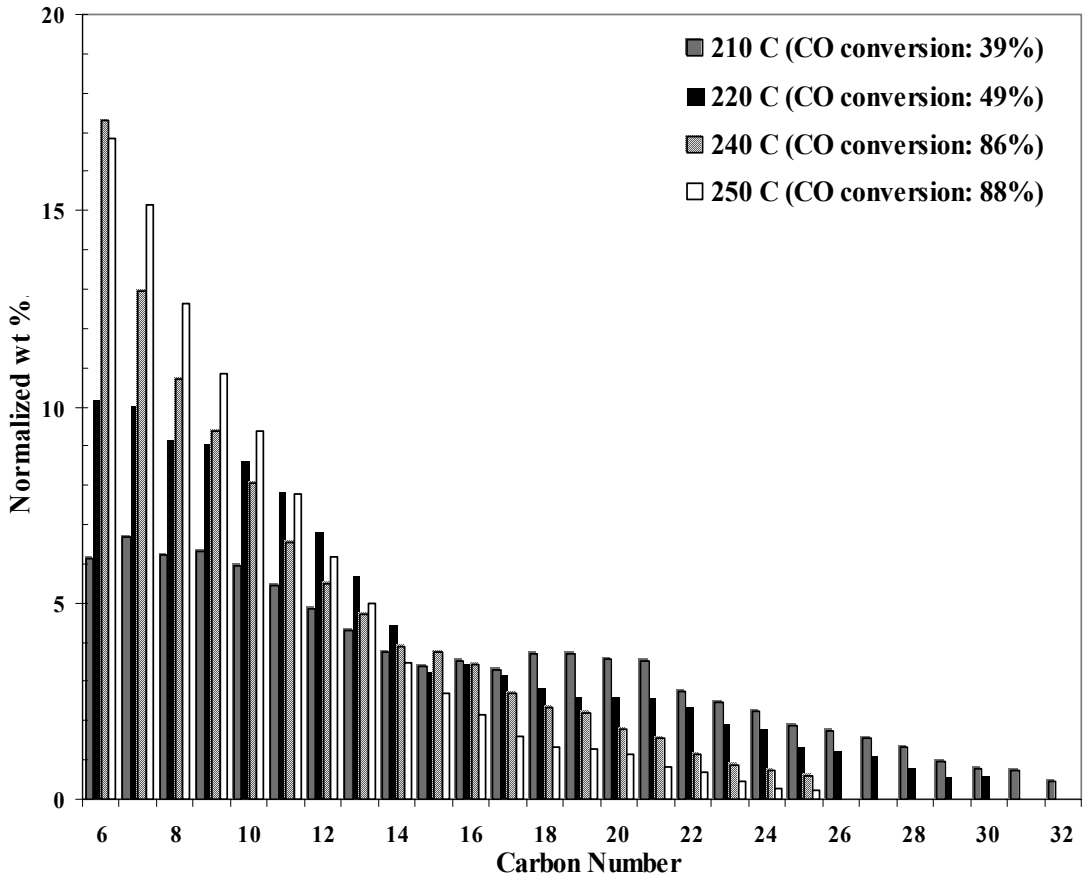

Figure 3.5a Effect of temperature on the normalized weight percentage versus carbon number in supercritical pentane phase FTS. Conditions were as follows: temperature of 210 °C, 220 °C, 240 °C, 250 °C; pressure, 45 bar; pentane flow rate: 1.0 mL/min; syngas flow rate: 50 sccm/g_{cat}; and $H_2/CO = 2.0$).

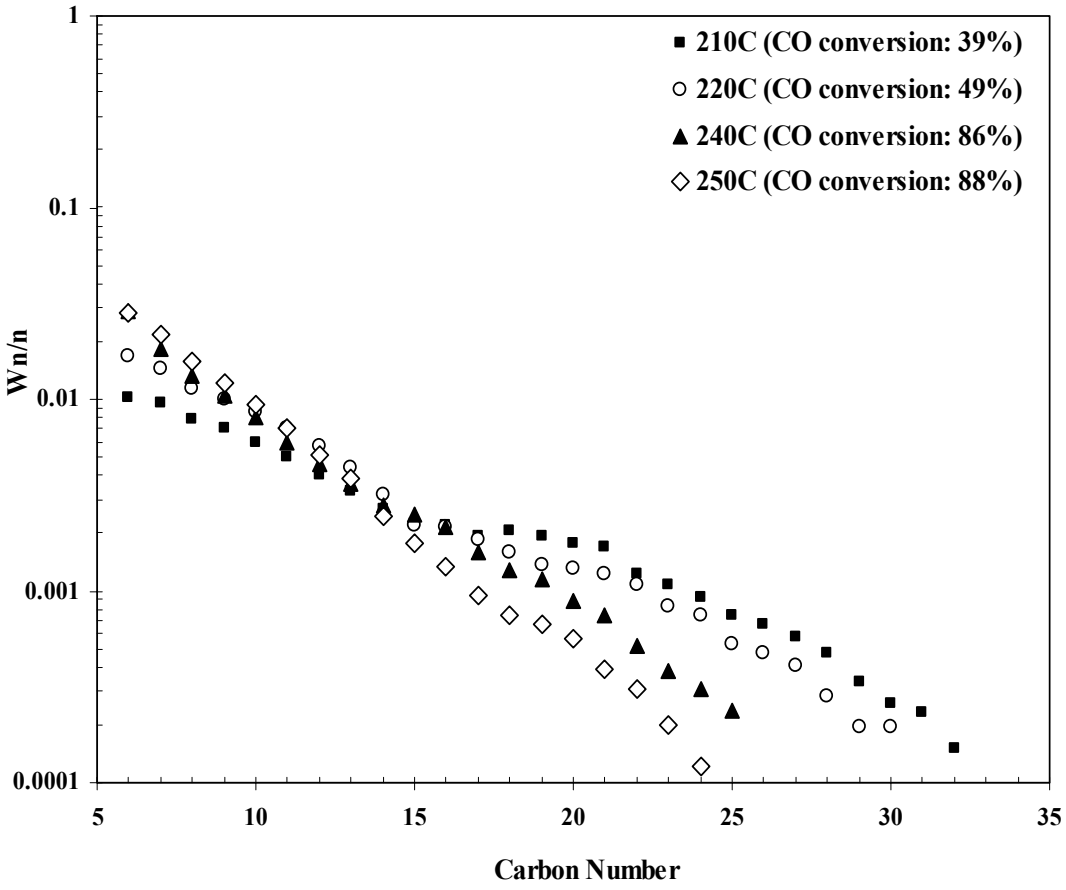

Figure 3.5b Effect of temperature on the ASF plot in supercritical pentane phase FTS. Conditions were as follows: temperature of 210 °C, 220 °C, 240 °C, 250 °C; pressure, 45 bar; pentane flow rate: 1.0 mL/min; syngas flow rate: 50 sccm/g_{cat}; and $H_2/CO = 2.0$).

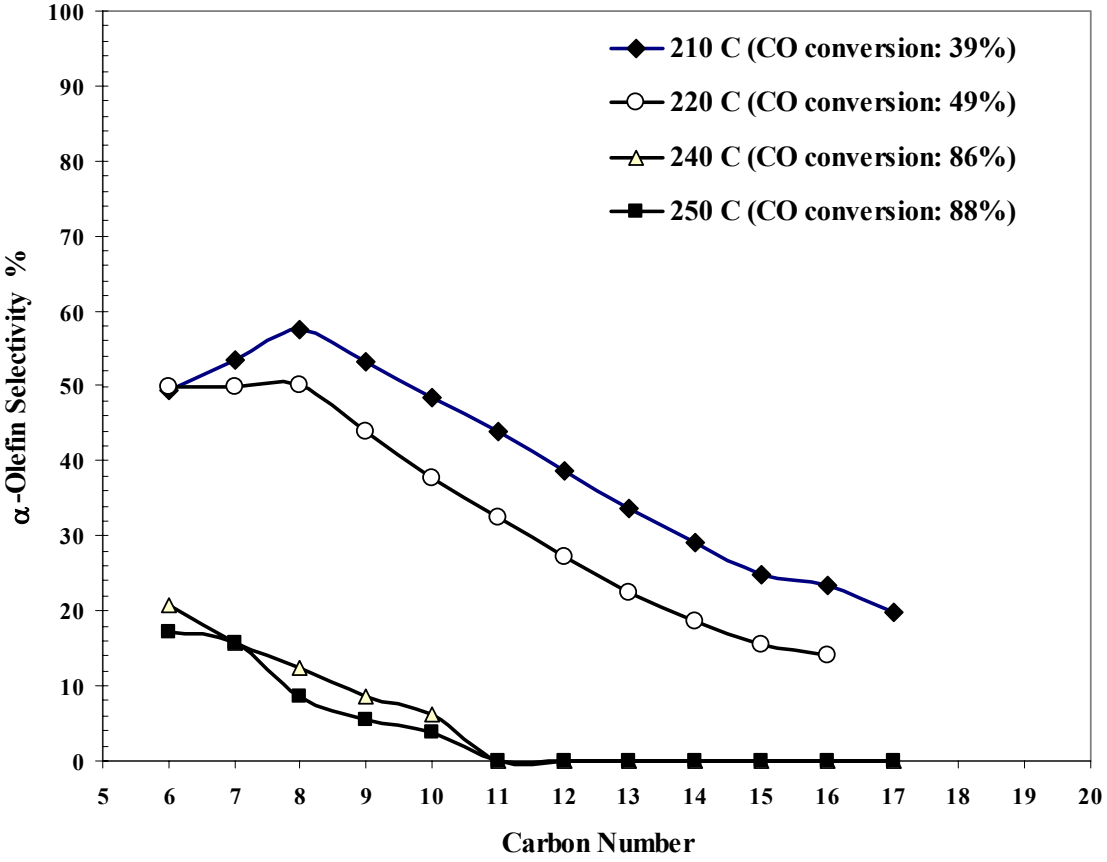

Figure 3.6 Effect of temperature on the α-olefin selectivity in supercritical pentane phase FTS (temperature: 210 °C, 220 °C, 240 °C, 250 °C; pressure: 45 bar; pentane flow rate: 1.0 mL/min; syngas flow rate: 50 sccm/g_{cat}; and $H_2/CO = 2.0$).

demonstrated no significant effects of reaction temperature on the olefins selectivity with an iron catalyst in supercritical propane FTS. Our experimental results demonstrate significant dependence of α-olefins selectivity on the reaction temperature when the reaction is conducted over a cobalt catalyst. This significant effect has not only been observed in supercritical pentane FTS (see Figure 3.6), but also in the case of supercritical hexane FTS (Huang and Roberts 2003). This dissimilarity may be attributed to the utilization of different catalysts in the two studies or because of different reaction conditions (including the solvent).

Table 3.2 shows α-values and CO conversions at the four different temperatures studied in the pentane medium. The α–value at 210 °C is 0.86, whereas, at 250 °C, it decreases to 0.71. From the GC analysis of the permanent gases, the methane production (data not shown), along with CO conversion (see Table 3.2), is significantly higher at 250 ^{o}C than at the low-temperature operation. As such, this indicates that much of the CO converts to CH_4 and other undesirable light hydrocarbons, instead of heavy hydrocarbons, especially those in the diesel distillates and wax ranges. Therefore, there exists an optimal reaction temperature for supercritical phase FTS operation that, on one hand, promotes the production middle distillates and, on the other hand, maintains reasonable conversion levels of the reactants. Simply pursuing the highest CO conversion at the price of sacrificed heavy products production is not the optimal strategy.

3.3.3 Effect of Pressure

Figures 3.7 and 3.9 present an investigation of the effects of pressure on the product distribution at 240 ^{o}C and 220 ^{o}C in supercritical pentane FTS. The general

Table 3.2 Effect of temperature on the chain growth probability (α-value) and CO conversion for the following reaction conditions; pressure: 45 bar; pentane flowrate: 1mL/min, syngas flowrate: 50 sccm/g_{cat}, H_2/CO= 2.0.

Temperature (°C)	α−value	CO conversion%
210	0.86	39
220	0.85	49
240	0.77	86
250	0.71	88

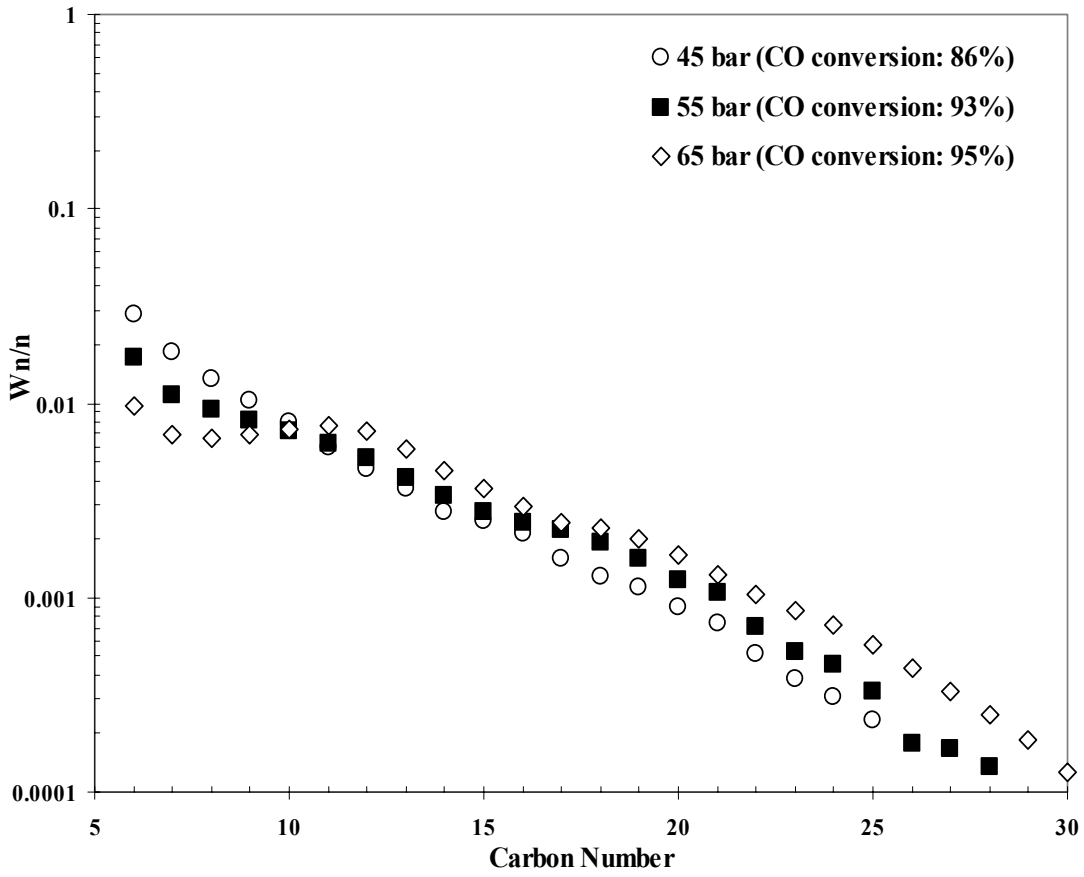

Figure 3.7 Effect of pressure on the ASF plot in supercritical pentane phase FTS (temperature: 240 °C; pressure: 45 bar, 55 bar, 65 bar; pentane flow rate: 1mL/min; syngas flow rate: 50 sccm/g_{cat}; and $H_2/CO = 2.0$).

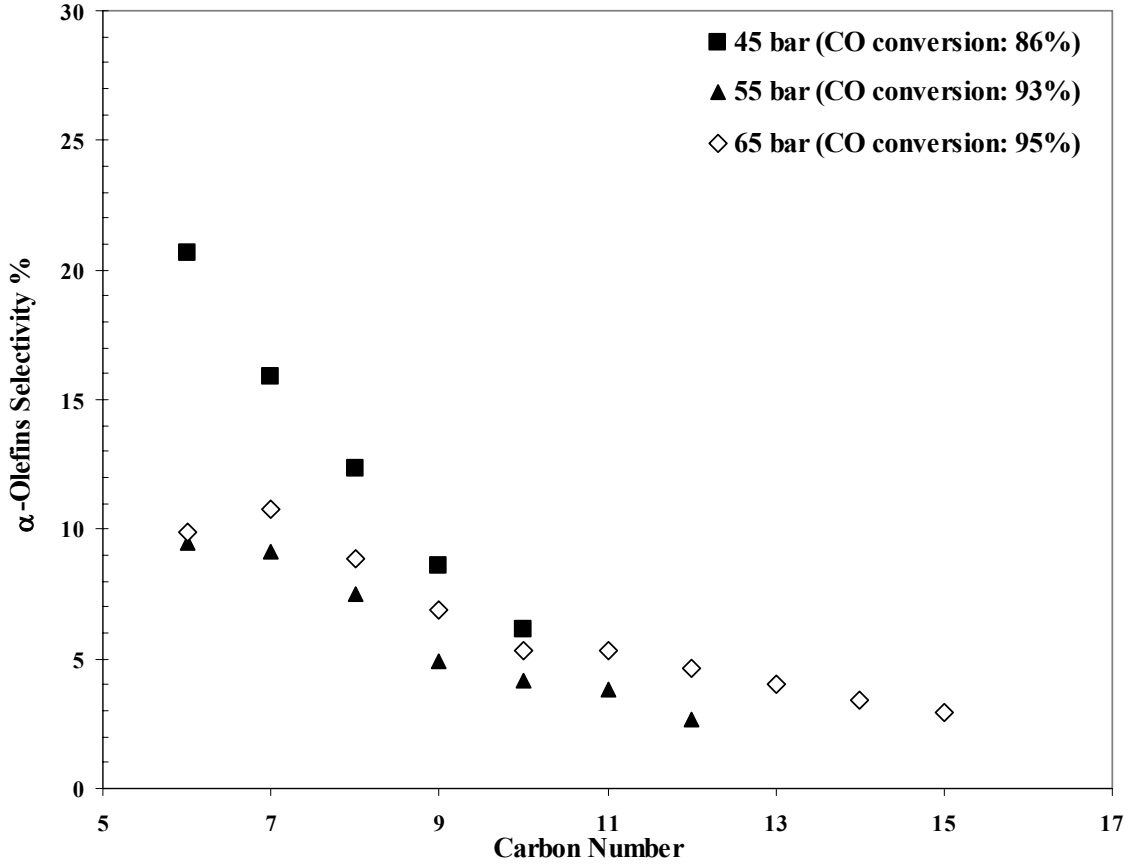

Figure 3.8 Effect of pressure on the α-olefin selectivity in supercritical pentane phase FTS (temperature: 240 °C; pressure: 45 bar, 55 bar, 65 bar; pentane flow rate: 1mL/min; syngas flow rate: 50 sccm/g_{cat}; and $H_2/CO = 2.0$).

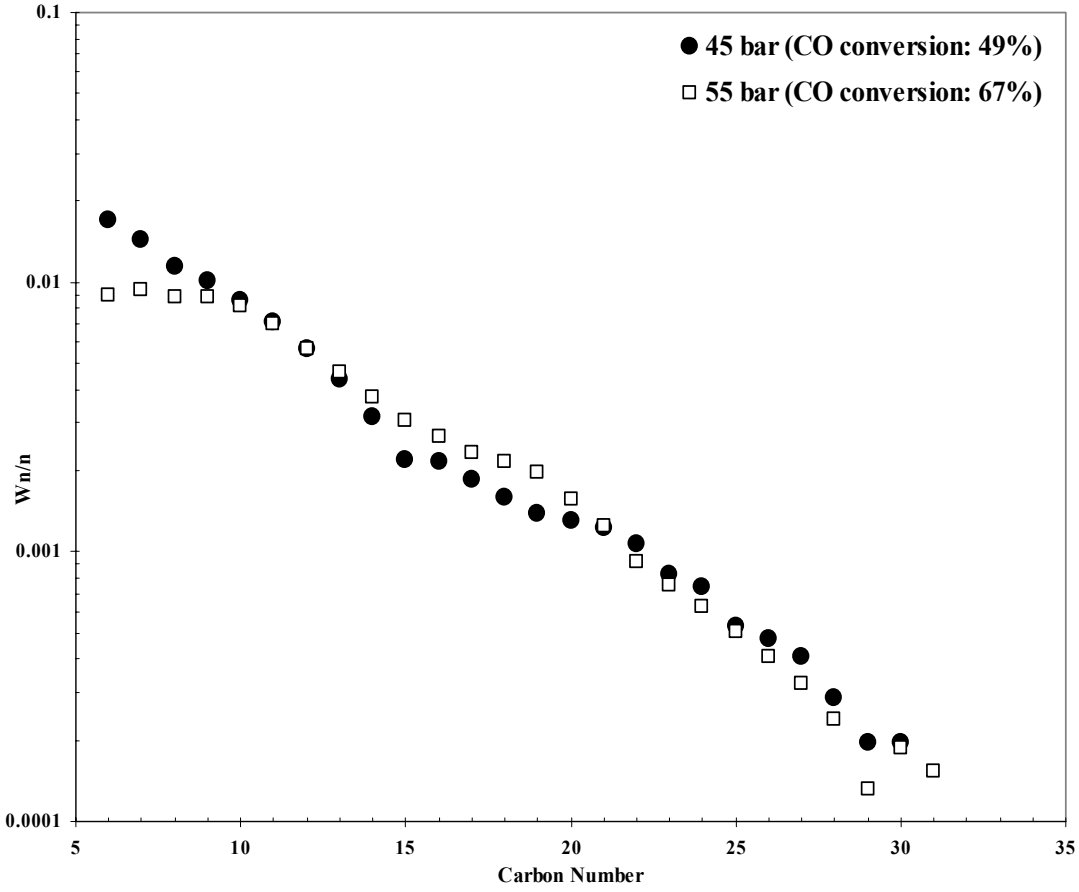

Figure 3.9 Effect of pressure on the carbon number distributions in supercritical pentane phase FTS (temperature: 220 °C; pressure: 45 bar, 55 bar; pentane flow rate: 1.0 mL/min; syngas flow rate: 50 sccm/g_{cat}; and $H_2/CO = 2.0$).

observation from the figures is that the effect of pressure on the product distribution is more pronounced at high reaction temperature (240 °C) than at low reaction temperature (220 °C). At 240 °C, the observed α-value of heavy hydrocarbons (above C_{10}) is 0.77 at 45 bar, which is significantly lower than the α-values at 55 bar ($\alpha = 0.82$) and 65 bar ($\alpha = 0.85$) (see Figure 3.7 and Table 3.3). Similarly, α-olefin selectivity (especially of middle distillates, C_{11+}) increases with pressure at 240 °C (Figure 3.9). For light hydrocarbons ($<C_{10}$), the selectivity of α-olefins reaches its highest values at the lowest pressure (45 bar), whereas an opposite trend is observed for the middle distillates, C_{11+}) which show the highest selectivity at the highest pressure of 65 bar. At the high temperature of 240 °C, an increase in pressure favors the production of heavier hydrocarbons with higher overall chain growth probability.

However, under low reaction temperature operation (220 ^{o}C), a different behavior was observed, as shown in Figure 3.9 and Table 3.3. The α-value at low pressure (45 bar) is 0.85, whereas that at high pressure (55 bar) is essentially unchanged at 0.86. The α-olefin selectivity at 220 °C also demonstrates no significant change as the pressure increases from 45 bar to 55 bar, as shown in Figure 3.10. The constant chain growth probability, despite the significant increase of pressure at 220 °C, indicates that the influence of pressure on the chain growth probability is more significant at high temperatures than at low temperatures. Note that the influence of temperature or pressure on the reaction behavior should not only be taken into consideration independently but also through their impact on the phase behavior of the reaction medium.

Table 3.3 Effect of pressure on the chain growth probability (α-value) for supercritical pentane FTS at the following conditions; pentane flowrate: 1mL/min, syngas flowrate: 50 sccm/g_{cat}, H_2/CO= 2.0.

	α-value		
T (^{o}C)	P = 45 bar	P = 55 bar	P = 65 bar
220	0.85	0.86	_
240	0.77	0.82	0.85

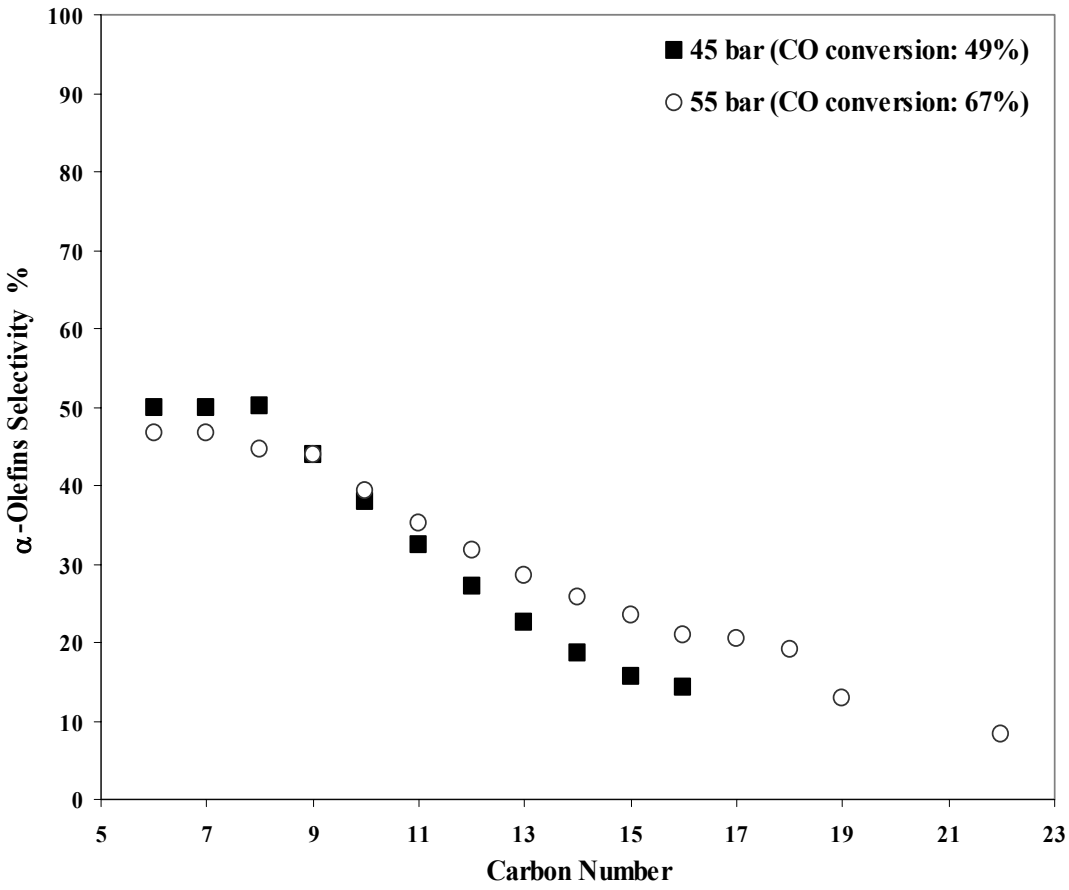

Figure 3.10 Effect of pressure on the α-olefin selectivity in supercritical pentane phase FTS (temperature: 220 °C; pressure: 45 bar, 55 bar; pentane flow rate: 1.0 mL/min; syngas flow rate: 50 sccm/g_{cat}; and $H_2/CO = 2.0$).

Generally, increases in pressure under our prescribed conditions would lead to an increase in the solvent density at a given temperature and thus result in the dissolution of heavy compounds from the catalyst surface. This would provide better accessibility to the active sites of the catalyst and, at the same time, enhance the in situ extraction of heavy compounds from the pores due to the high solubility in the liquid-like density media. As a result, this would create more opportunity for α-olefins readsorption and their further incorporation in the chain growth process.

3.3.4 Comparison of Supercritical Hexane and Pentane FTS at Constant Temperature and Density

The density of the SCF medium is a fundamental factor that affects the internal diffusion rate of the catalyst pore and the readsorption of α-olefins. By adjusting the medium density, both bulk diffusion and internal diffusivity can be changed significantly. Increasing the medium density through isothermal pressure increases can, on one hand, enhance the internal diffusivity, by strengthening the in situ extraction and removal of heavy compounds from the catalyst pores. On the other hand, this high medium density also results in lower bulk diffusion rates. An ideal balance between the positive enhancement in pore diffusivity and the decrease in bulk diffusion rate with enhanced medium density should be achievable. Given the dramatic influence of the density-dependent properties on FTS performance, we designed a set of experiments to directly compare hexane and pentane solvent effects at constant density and temperature. To have the same density ($\rho \approx 0.33$ g/cm^3) at constant temperature, higher pressures are required in pentane (65 bar in pentane versus 38 bar in hexane at 240 °C). Under such conditions, if

density and transport properties were the dominant factors that control the reaction behavior (especially chain growth), then the same medium density in two different solvents (e.g., hexane versus pentane) should lead to similar behavior. The results presented in Figure 3.11 illustrates that there is not much difference in the hydrocarbon distributions for carbon numbers less than C_{20} in either supercritical pentane FTS or supercritical hexane FTS reaction at constant density. However, for carbon numbers beyond C_{20+}, more wax products can be obtained in supercritical pentane than in hexane. Figure 3.12 demonstrates a small effect of the solvent on the α-olefin selectivity at constant density. Interestingly, a much higher CO conversion of 92% was observed in pentane, as opposed to 61% in hexane, suggesting a possible pressure effect on the reaction kinetics.

3.3.5 Effect of the Syngas Feed Ratio (Composition of Reactants)

The effect of the feed composition (H_2/CO ratio) on the activity and selectivity of FTS over the 15% Co/Al_2O_3 catalyst was studied in supercritical pentane. It is well-known that the syngas feed composition (H_2/CO ratio) can impose significant influence on the activity and selectivity of the FTS process. Based on economic considerations, it would be preferred to use a lean syngas (H_2/CO ratio of <2), because less-than-stoichiometric ratios are often obtained from reformed methane. To verify the influence of the syngas composition on supercritical pentane FTS, three H_2/CO ratios were investigated and the product distributions were obtained at 220 °C and 45 bar with a syngas flow rate of 100 sccm per gram of the catalyst. Figure 3.13 shows that the lower H_2/CO ratio in the feed leads to higher chain growth probability. The α-values decrease

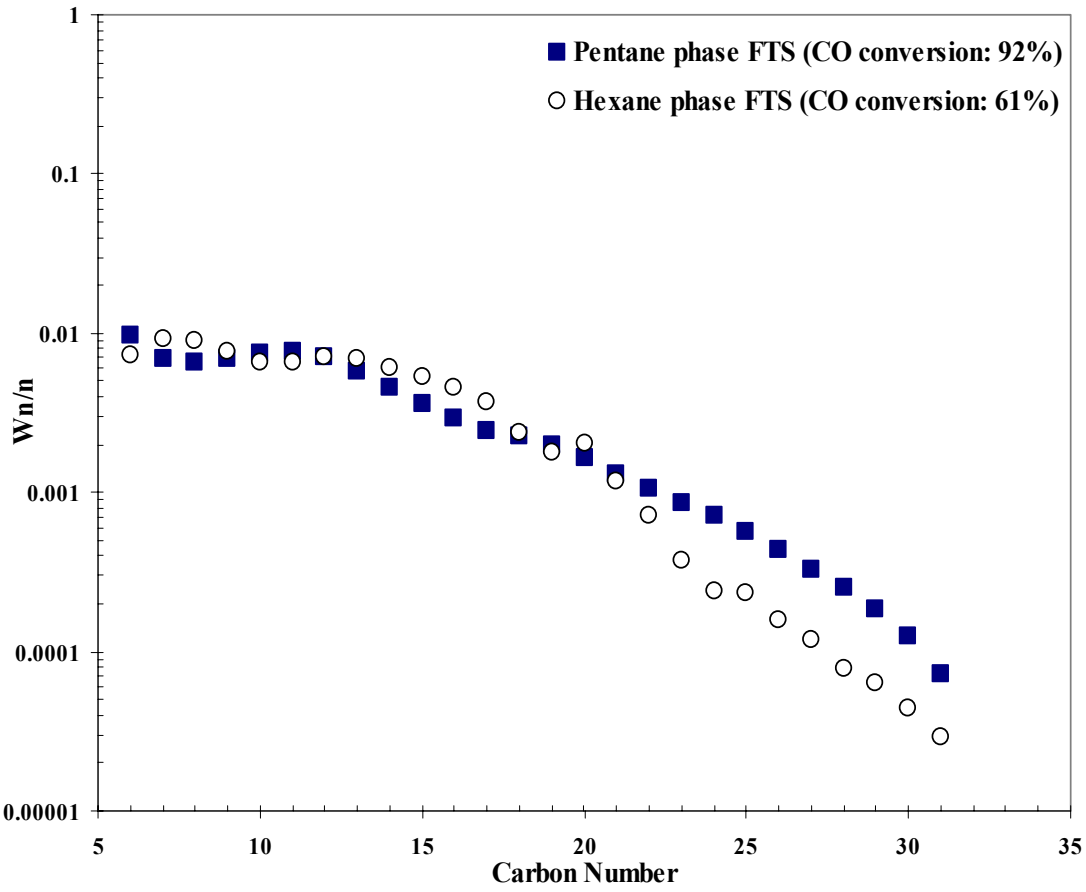

Figure 3.11 ASF plots at constant solvent density ($\rho_{solvent} \approx 0.33$ g/cm^3) in supercritical pentane and hexane phase FTS. Pentane: 240 °C, 65 bar, flowrate of 1 mL/min. Hexane: 240 °C, 38 bar, flowrate of 1.0 mL/min. For both cases, a syngas flowrate of 50 sccm/g_{cat}; and a H_2/CO ratio of 2.0 were used.

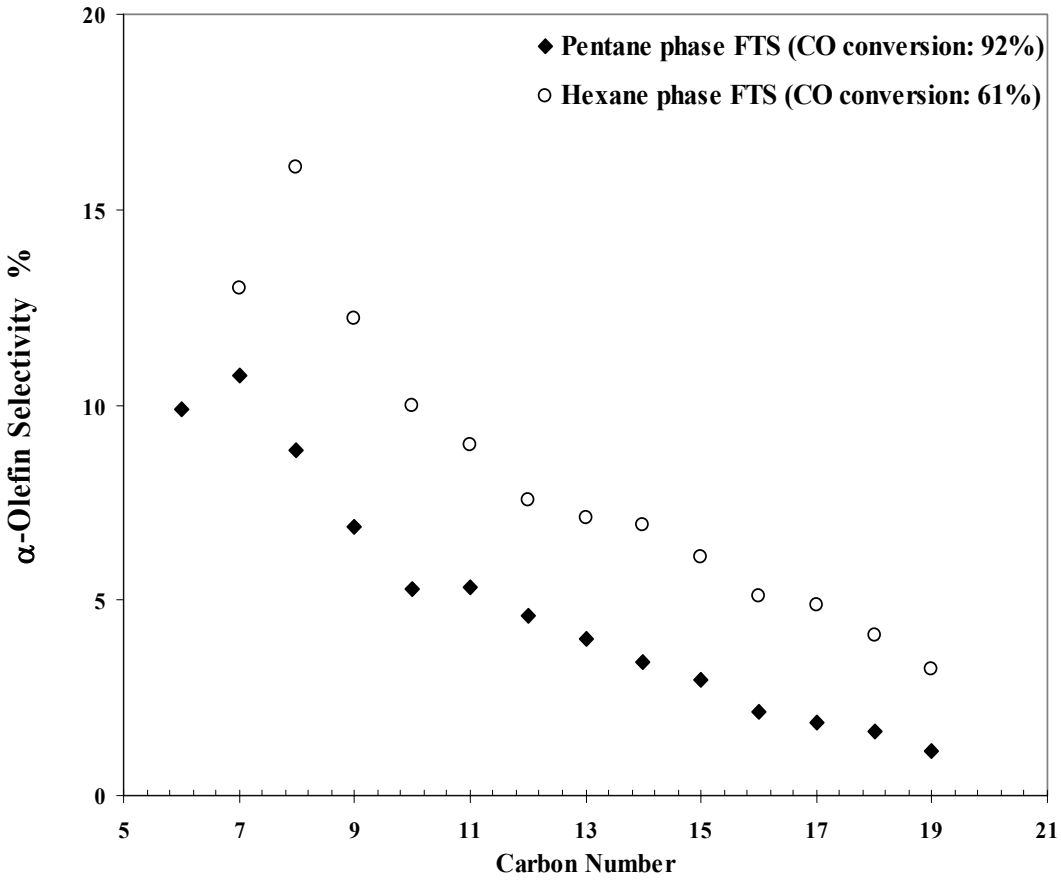

Figure 3.12 α-olefin selectivity at constant solvent density ($\rho_{solvent} \approx$ 0.33 g/cm^3) in supercritical pentane and hexane phase FTS. Pentane: 240 °C, 65 bar, flowrate of 1 mL/min. Hexane: 240 °C, 38 bar, flowrate of 1.0 mL/min. For both cases, a syngas flowrate of 50 sccm/g_{cat}; and a H_2/CO ratio of 2.0 were used.

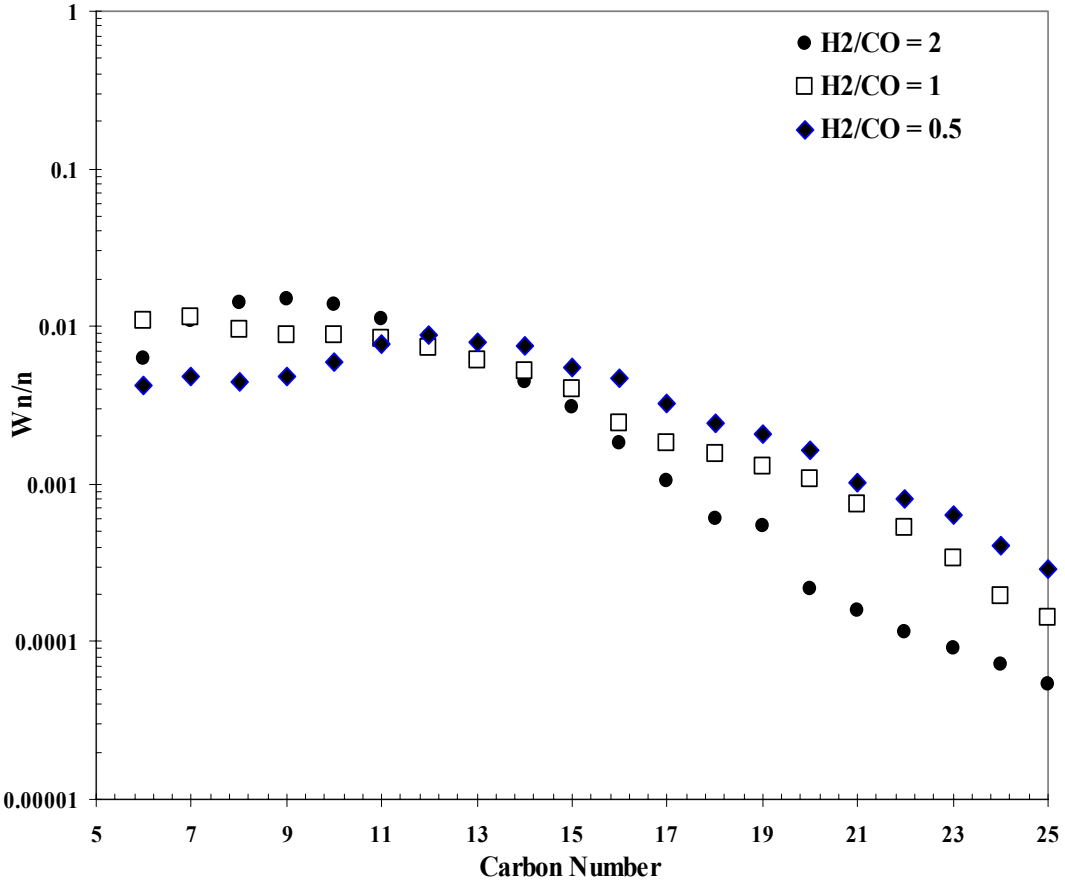

Figure 3.13 Effect of syngas feed ratio on ASF plots in supercritical pentane FTS (temperature: 220 °C; pressure: 45 bar; pentane flowrate: 1.0 mL/min; and syngas flowrate: 100 sccm/g_{cat}).

as the feed ratio is increased. Another observation is that heavy products (>C_{20}) almost disappear at a H_2/CO ratio of 2/1. An interesting phenomenon is observed in the case of a H_2/CO feed ratio of 0.5: an almost-horizontal line can be observed in Figure 3.13 for the middle distillate hydrocarbons (C_{10}-C_{16}).

These results agree well with the general concept that high hydrogen concentrations increase termination probability by hydrogen addition (to give paraffins) in the FTS reaction. Termination to methane and paraffins is irreversible and negatively impacts the chain growth process.

3.3.6 Effect of Syngas Flow Rate

Three different syngas flow rates (50, 75, and 100 sccm) were examined in supercritical pentane FTS at 220 °C and 45 bar (Figure 3.14). This set of experiments was designed to provide a preliminary investigation on the influence of gas hourly space velocity (GHSV) and contact time on the chain growth process, although the range of flow rates studied is not wide, because of the mechanical limitations of our apparatus. As seen in Figure 3.14, no significant effect of syngas flow rate on the hydrocarbon chain growth is observed for hydrocarbon production below C_{20}; however, there is a significant influence in the heavy hydrocarbon range (hydrocarbons above C_{20}). The C_{25+} products are diminished significantly at the highest flow rate (100 sccm/g_{cat}), whereas heavy hydrocarbons up to C_{35} were produced at lowest flowrate (50 sccm/g_{cat}). Interestingly, in the conventional gas-phase reaction, a decrease in GHSV is known to result in increased chain growth probability for middle distillate hydrocarbons (Madon and Iglesia 1993).

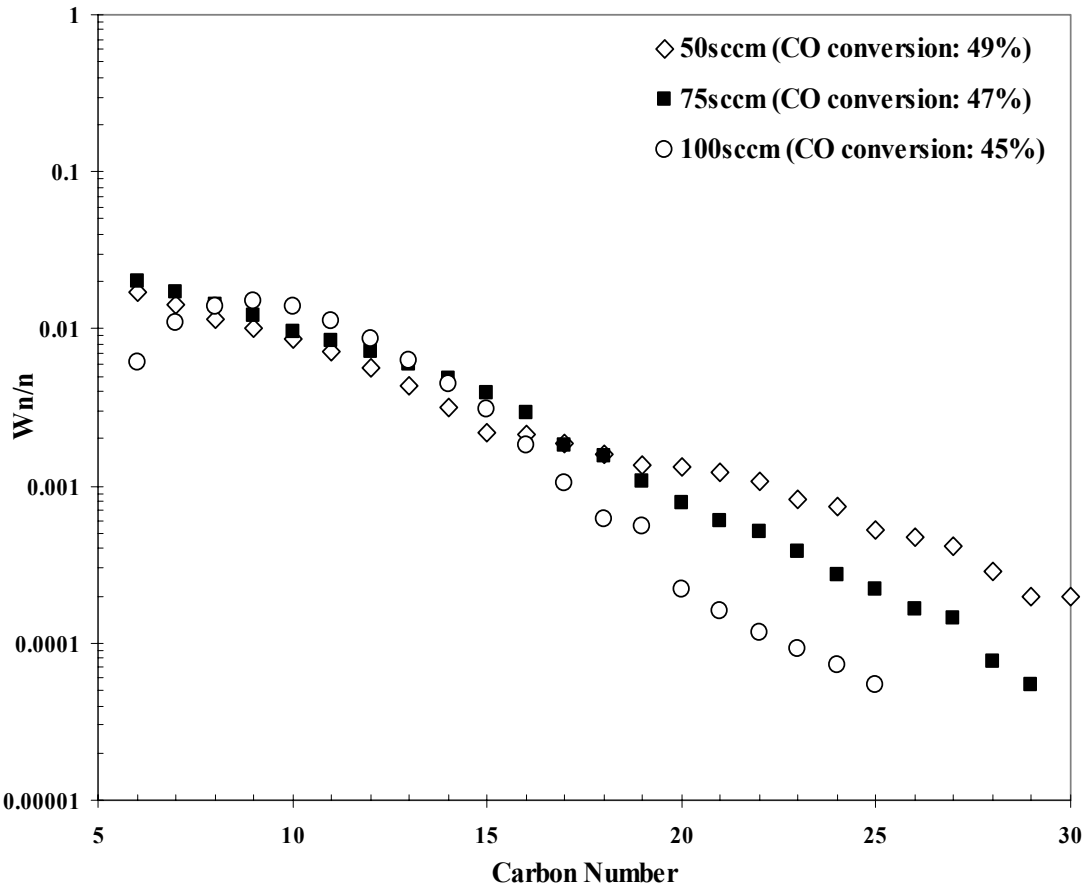

Figure 3.14 Effect of syngas flow rate on ASF plots in supercritical pentane FTS (temperature: 220 °C; pressure: 45 bar; pentane flowrate: 1.0 mL/min; and $H_2/CO = 2.0$).

3.3.7 An Approach to Understand the Enhanced Chain-Growth Mechanism in Supercritical-Phase FTS

Deviations from the standard ASF distributions have been attributed by many authors to the readsorption and incorporation of α-olefins in the chain growth process (Iglesia et al. 1988; Madon et al. 1991; Madon and Iglesia 1993; Kuipers et al. 1995; Kuipers et al. 1996; Bianchi and Ragaini 1997). Diffusion limitations inside the catalyst pores have often been assumed to be the main cause for the enhanced α-olefin readsorption (Madon and Iglesia 1993). However, a recent assessment of the importance of the diffusion limitations in FTS mechanism shows that the impact of internal diffusion limitations on the enhanced α–olefin readsorption may become significant *only* when there is internal diffusion limitation of the reactants (CO, and H_2) (Zhan and Davis 2002). They also indicated that a longer residence time of an α-olefin does not necessarily account for the increased probability of its readsorption, unless there is an existence of an internal diffusion restriction on the reactant gases.

Our investigations of the alumina-supported cobalt catalyst in supercritical-phase FTS over a wide range of conditions showed pronounced deviations from the standard ASF product distribution. The introduction of supercritical fluid as a reaction medium can result in a significant alleviation of the internal diffusion restrictions within catalyst pores (those pores are often liquid-filled in the conventional FTS operation). Therefore, attributing the enhanced readsorption of α-olefins to internal diffusion limitations may not be appropriate in the case of SCF-FTS operation.

The introduction of a SCF solvent that has similar characteristics to those of the products improves the solubility of those products in the medium significantly. As such,

one possibility that may explain the enhanced chain growth in SCF-FTS involves alleviation of mass transfer limitations, because of this enhanced solubility of products. This may promote desorption of primary products and thus provide more free active sites for growth to occur. The assumption here is that the introduction of the SCF medium will improve solubility and, thus, the removal of those heavy hydrocarbons from the catalyst pores. Nevertheless, this postulation can be challenged by the fact that, under such conditions, standard ASF distributions should more likely be expected than non-ASF behavior because of the elimination of mass transfer resistances. However, this argument in favor of more standard ASF distribution does not take into account opportunities for primary products, mainly a-olefins, to readsorb on the evacuated active sites in the SCF medium.

3.4 Conclusions

Our study has focused on the effects of reaction temperature, pressure, solvent type, reactant feed composition, and the space velocity on Fischer-Tropsch synthesis (FTS) reaction over a 15% Co/ Al_2O_3 catalyst. Our investigations mainly focused on how the density of the supercritical phase (tuned by either changing temperature or pressure) can influence the chain growth probability and the distributions of the hydrocarbon products. Our results show that lower reaction temperatures promote chain growth and, therefore, favor the production of middle distillate hydrocarbons and wax components. Temperatures well above the critical temperature of the solvent were observed to have a significant negative effect on the α-olefin selectivity in both pentane and hexane SCF (Huang and Roberts 2003). The density of the solvent under supercritical FTS operation

had a pronounced effect on both the chain growth probability and the α-olefin selectivity, yielding enhanced chain growth at high densities. Readsorption of α-olefins, followed by subsequent incorporation in the chain growth process, are suggested to be the main reason behind the enhancement of chain growth probability under supercritical phase operation. However, this phenomenon cannot be attributed to internal diffusion limitation effects, as has been done in conventional gas-phase FTS. Instead, this work indicates that factors such as increased solubility in the SCF medium, increased accessibility of vacant adsorption sites, and the elimination of the adsorption layer barrier, have a key role in enhancing the chain growth process in supercritical-phase FTS.

CHAPTER 4

SELECTIVE CONTROL OF HYDROCARBON PRODUCT DISTRIBUTION IN SUPERCRITICAL PHASE FISCHER-TROPSCH SYNTHESIS TOWARDS DESIRED FUEL FRACTIONS

4.1 Introduction

There is significant interest in developing new technologies to improve the classical C1 chemistry routes for fuel and petrochemical production (Roberts and Elbashir 2003). In particular, the ability to better control the production of gasoline, jet fuel, and diesel fractions from Fischer-Tropsch synthesis (FTS) is needed. Our efforts in this study are directed at utilizing the unique solvent characteristics of supercritical media in enhancing the production of middle distillate fuel products from syngas, such as, gasoline, jet fuels, and diesel fractions. Supercritical fluids offer several advantages for these catalytic reactions including the ability to manipulate the reaction environment through simple changes in temperature and pressure to enhance solubility of reactants and products, to eliminate interphase transport limitations, and to improve heat transfer in these exothermic reactions. Industry has begun to focus on this SCF-FTS technology. Recently, Shell (SMDS scheme) revealed it's FTS technology in its new plant, in Bintulu,

Malaysia, which employs C_5 or C_6 hydrocarbon injection for cooling, thus improving productivity by reducing heat transfer limitations (Editor 2003).

In the previous chapter, we have demonstrated that conducting FTS under SCF conditions (using pentane or hexane as a solvent) afford unique opportunities to manipulate the reaction environment and to enhance the production of liquid fuels and value-added chemicals (such as α-olefins) from synthesis gas. Our results showed that varying the reaction parameters (such as pressure and temperature) have significant effect on FTS reaction performance. Generally, as the pressure is increased, the product's molecular weight significantly increases as does the catalyst activity. Nevertheless we have noticed an existence of an optimum pressure, whereby the effect of pressure on bulk diffusion and pore diffusivity is well balanced (see Chapter 5). We also reported that the product distribution in supercritical phase FTS exhibited at least two α-values (non-ASF distribution). Comparing SCF- FTS to gas phase FTS we found that the yield of heavy products ($>C_{10}$) in the SCF medium is higher than that in gas phase medium. This phenomenon has been attributed to the increased solubility of hydrocarbons in the SCF medium coupled with the enhanced extraction of heavy compounds from the catalysts pores (see Chapter 6).

Proper selection of reaction conditions (such as temperature, pressure) certainly plays a vital role in producing desirable compounds with high α-value at reasonable reactant conversion. As a matter of fact, varying either the temperature or the pressure of the reaction environment will significantly affect the thermo-physical characteristics of the supercritical phase (density-dependent properties) as discussed previously in Chapter 3. More fundamental understanding of the process conditions is necessary to quantify the

influence of the SCF environment on FTS. In this chapter, we examine various solvent effects on supercritical FTS under different density conditions and compare these studies to the conventional gas-phase reaction. The influence of tuning temperature and pressure (i.e. density) on the selectivity of light hydrocarbons (C_1-C_4), gasoline fuel fractions (C_5-C_{10}), jet fuel and diesel fractions (C_{11}-C_{19}), and heavy hydrocarbons (wax) (C_{20+}) is reported. The activity of the catalyst was measured by CO conversion, H_2 conversion, and syngas ($CO+H_2$) conversion and is reported as a function of the operating conditions. The effect of the SCF reaction media environment on CO conversion, methane selectivity, product distributions and α-value was examined by adjusting the SCF reaction densities from gas-like to liquid-like through variations in temperature and pressure.

.

4.2 Experimental

The high pressure FTS unit that used to measure the reaction performance of two cobalt-based catalysts (of 15% Co/Al_2O_3 catalyst purchased from United Catalysts Company, and a 15% Co/SiO_2 catalyst prepared in our laboratory (see Chapter 7)) was illustrated in Figure 3.1. Detailed information about the unit and the high pressure reactor setup was also given in Chapter 3 (Section 3.2). In a typical experiment, the flow of *n*-pentane or hexanes flow at a rate of 1.0 mL/min. After the temperature and pressure stabilized, syngas gas-hourly-space-velocity (GHSV) of 187.5 hr^{-1} is initiated. The reactions experiments were continued until steady state was reached in terms of both catalyst activity (CO and syngas conversion) and product distribution. The reported results in this study represent samples that were collected after at least 50 hr of time-on-

stream for both gas-phase and SCF-FTS experiments. The analysis of reactants and products were conducted by two online gas chromatographs as shown in Figure 3.1. The finger prints of the peaks were used for the selectivity and conversion calculations as discussed in detail in Section 3.2.3.

4.3 Results and Discussion

4.3.1 Supercritical Phase FTS versus Gas Phase FTS

The overall product distributions of hydrocarbons from gas phase FTS and supercritical phase (hexanes (SCH) or *n*-pentane (SCP)) FTS were measured at 240 °C and partial pressure of syngas ($CO+H_2$) ca. 20 bar. The supercritical solvent partial pressure was kept constant at 45 bar in all cases. Figure 4.1, presents the light hydrocarbon fraction, gasoline fuel fraction, jet fuel and diesel fuel fraction, and wax fraction for the product distributions from the FTS studies under the conditions stated above. As seen in Figure 4.1, the overall product distribution shifts towards heavier products in both SCH and SCP FTS conditions compared to gas phase FTS. Light hydrocarbons have not been reported for SCP due to technical difficulties in analyzing the light fractions from the FID-GC in that set of experiments. Previously (Chapter 3: Figures 3.3a-c), we have shown that that the chain-growth probability (α-value) for heavier hydrocarbons (C_{10+}) in supercritical pentane and hexane is close to 0.85 while in the gas phase it is about 0.75.

Considering the gas-phase reaction as the base line case, Figure 4.1 shows that there is a significant improvement (134%) in the gasoline fraction in SCH-FTS compared to the gas phase-FTS. In SCP-FTS slight improvement was obtained in the gasoline fraction

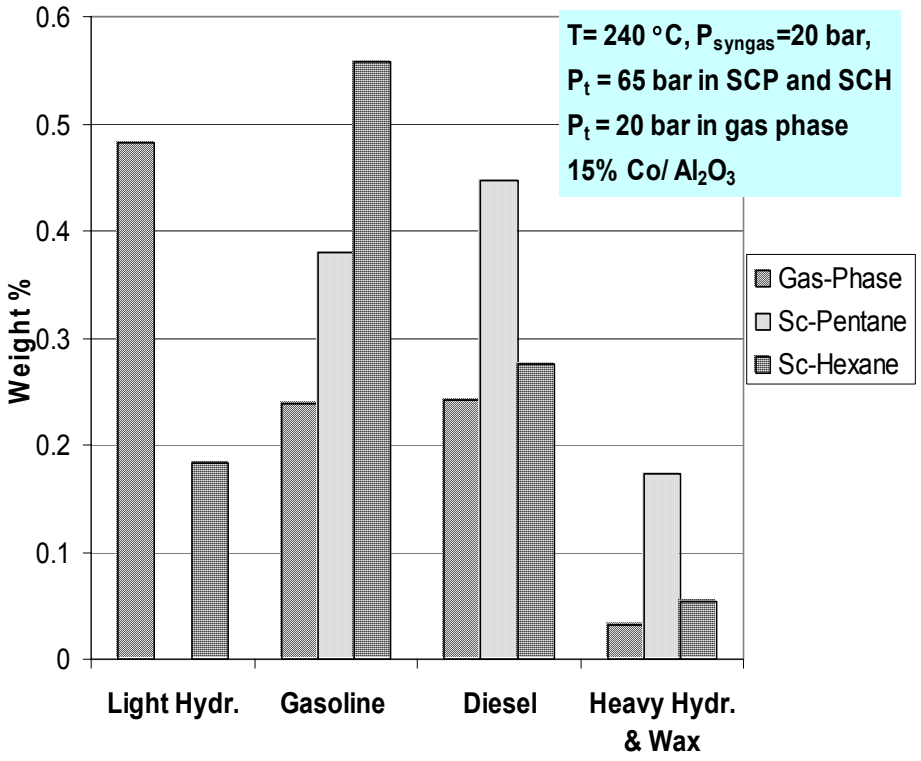

Figure 4.1 Hydrocarbons and fuel fractions distributions in gas phase, SCH, and SCP environment at 240 °C. H_2/CO feed ratio is 2/1.

compared to gas phase-FTS with even more significant improvements in the diesel and wax fractions. In the SCF phase reaction media, the solubility of heavy compounds is increased and as a result in situ extraction of heavy compounds that occupy active sites on the catalyst surface increases, thereby freeing up more active sites for readsorption and enhanced chain growth. Another reason for this enhanced production of heavy components is that the enhanced solubility in SCH and SCP results in an increase in the concentration of α-olefins at the catalyst surface that promotes readsorption and further incorporation in the chain-growth process. Detailed description of the enhanced olefin incorporation mechanism has been given in Chapter 5. The formation of two phases inside the catalyst pores in gas phase FTS (as result of condensation of heavy hydrocarbons) results in longer residence times of α-olefins inside the catalyst pores. The increase in residence time of α-olefins inside the catalyst pores can lead to secondary reaction such as hydrogenation and isomerization to form normal paraffins and branched products (Yokota et al. 1990; Fan et al. 1992). This production of paraffins and isomers terminates the chain-growth process (Iglesia et al. 1991) resulting in lower chain growth probability. SCF-FTS operation, on the other hand, results in elimination of multiple phases as well as improved extraction and removal of α-olefins from the catalyst pores thereby decreasing secondary reactions and promoting chain growth.

Due to the liquid-like heat capacity and thermal conductivity in SCH and SCP, the production of undesired products such as methane and carbon dioxide was significantly suppressed compared to gas phase FTS as shown in Table 4.1. In the gas phase reaction, local heat generation (inside the catalyst pores) during the reaction can result in temperatures that are significantly higher than the bulk temperatures measured along the

Table 4.1 Activity and selectivity of 15% Co/ Al_2O_3 at 240 °C in gas-phase, SCH, and SCP reaction environment. H_2/CO feed ratio is 2/1 and the GHSV of syngas is 187.5 h^{-1} for 1 gram of catalyst while the flow rate of supercritical solvent is 1.0 mL/min.

	Gas Phase	**SC-Hexane**	**SC-Pentane**
CO conversion %	67.6	78.4	85.6
CO consumption rate (μmol CO reacted.g_{cat}^{-1}.sec^{-1})	7.6	7.95	12.7
H_2+CO conversion %	60.6	61.5	91.3
CH_4 Selectivity %	27.2	8.7	6.6
CO_2 Selectivity %	2.9	0.09	0.16

length of the reactor. Evidence of much better temperature control and improved heat distribution in SCH phase-FTS compared to gas phase-FTS has been previousely described (Huang et al. 2002b; Huang and Roberts 2003). The large amounts of heat generated in the FTS reaction can result in the cracking of long chain hydrocarbons into smaller ones if this heat is not efficiently removed from the catalyst pores (Chaumette et al. 1995). In the supercritical phase, the heat transfer rate can be improved due to the higher heat capacity and thermal conductivity.

The conversion and consumption rates of CO, as shown in Table 4.1, are higher in SCH and SCP than in gas phase-FTS. While it might be anticipated that conversions would be higher in gas phase FTS due to the higher diffusivities in the gas phase compared to the SCF medium (Yokota et al. 1990), we find that other density dependent factors have an important impact on the conversion in the SCF medium (see Figure 3.3). The liquid-like density of the SCF medium results in high solubilities of the reactants and efficient extraction of products from the catalyst pores (Bochniak and Subramaniam 1998), thereby freeing up more active sites for enhanced conversion. Under supercritical-phase FTS conditions, the formation rate of heavy products and coke precursors is balanced by their removal rate as a result of the liquid-like solubility and in situ extraction within the supercritical medium. The rapid desorption of the extracted and dissolved heavy hydrocarbons effectively create more vacant reactive sites available to the reactants. It is also important to mention that at 240 °C and 65 bar the density of pentane is lower (closer to gas-like) than that of hexane and thus facilitates better activity than SCH medium.

4.3.2 Effect of temperature on selectivity towards fuels fractions.

The distribution of light hydrocarbon, gasoline fraction, diesel fraction, and wax as function of reaction temperature for both SCP and SCH was studied at constant pressure (45 bar for SCP, and 65 bar for SCH), as shown in Figure 4.2*a* and 4.2*b*, respectively. In the case of SCP (Figure 4.2*a*), the highest reaction temperature (240 °C) favors light hydrocarbons and gasoline with less wax and heavy hydrocarbon production. At the lower temperature (210 °C) maximum yields of the diesel fraction and wax were obtained. Surprisingly, the trend in SCH medium showed an optimum temperature for each hydrocarbon fractions (see Figure 4.2*b*).

For production of the gasoline fraction, 240 °C is the optimum temperature with selectivity close to 50% compared to the other fractions. At 250 °C the product shifted to the diesel fraction with selectivity close to 46%, while the wax and heavy hydrocarbons selectivity is similar for 230 °C and 250 °C. At the high temperature of 260 °C, the maximum peak of the product distribution is totally shifted towards light hydrocarbons (C_1-C_5) with selectivity close to 60%, however it showed a similar selectivity towards gasoline fractions as that at 250 °C.

Figure 4.3 shows the profile of CO conversion and chain-growth probability in SCP-FTS at different temperatures. As the temperature is increased from 210 °C to 240 °C, CO conversion significantly increased, while the α-value slightly decreased with the temperature. This trend is in good agreement with the temperature effects illustrated in Figure 4.2a. On the other hand, the effect of reaction temperature on activity and

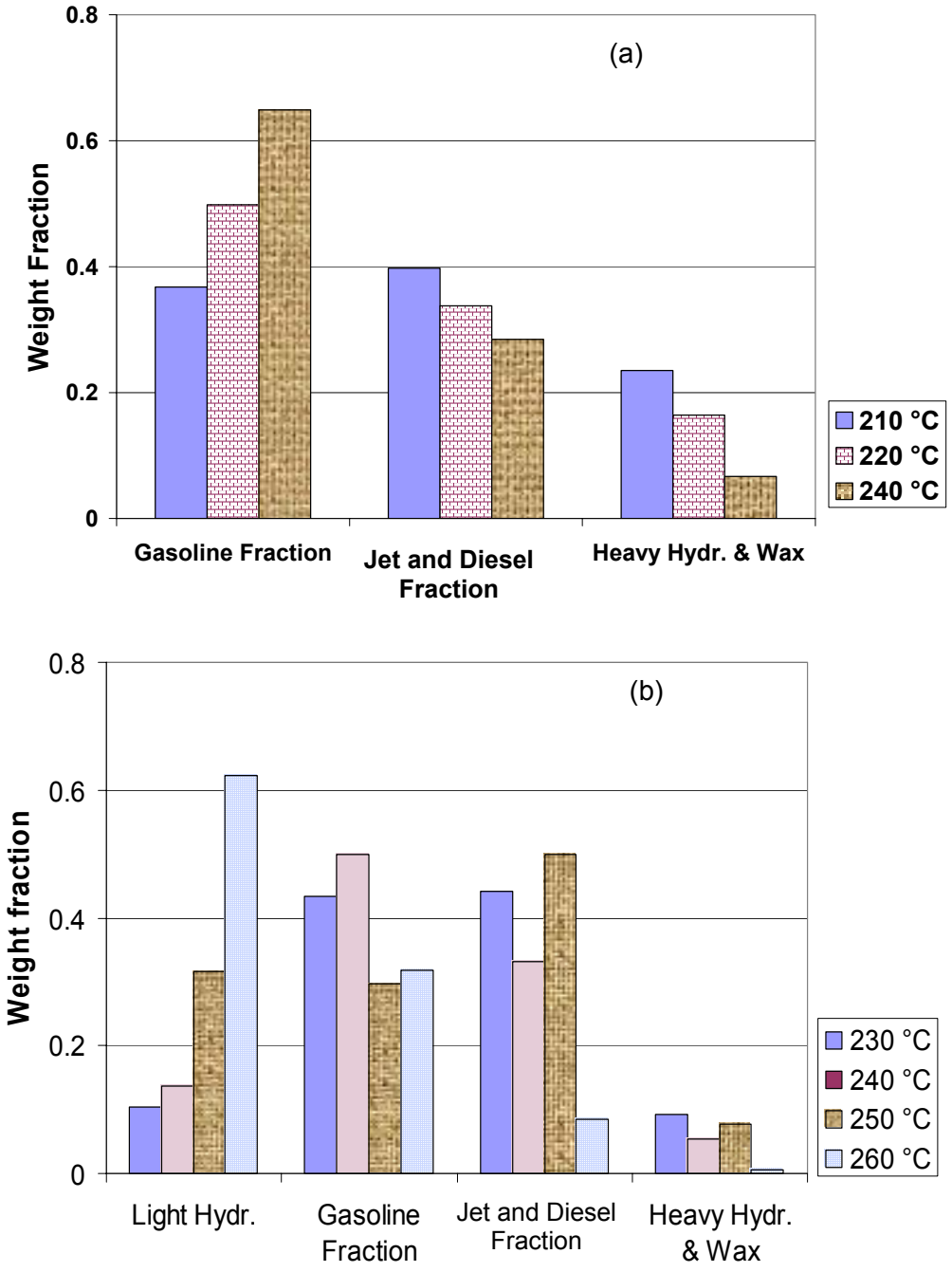

Figure 4.2 Distributions of fuel fractions and heavy hydrocarbons (a) SCP-FTS environment at constant pressure of 45 bar and three different temperatures, and (b) SCH-FTS environment at constant pressure of 65 bar and four different temperatures.

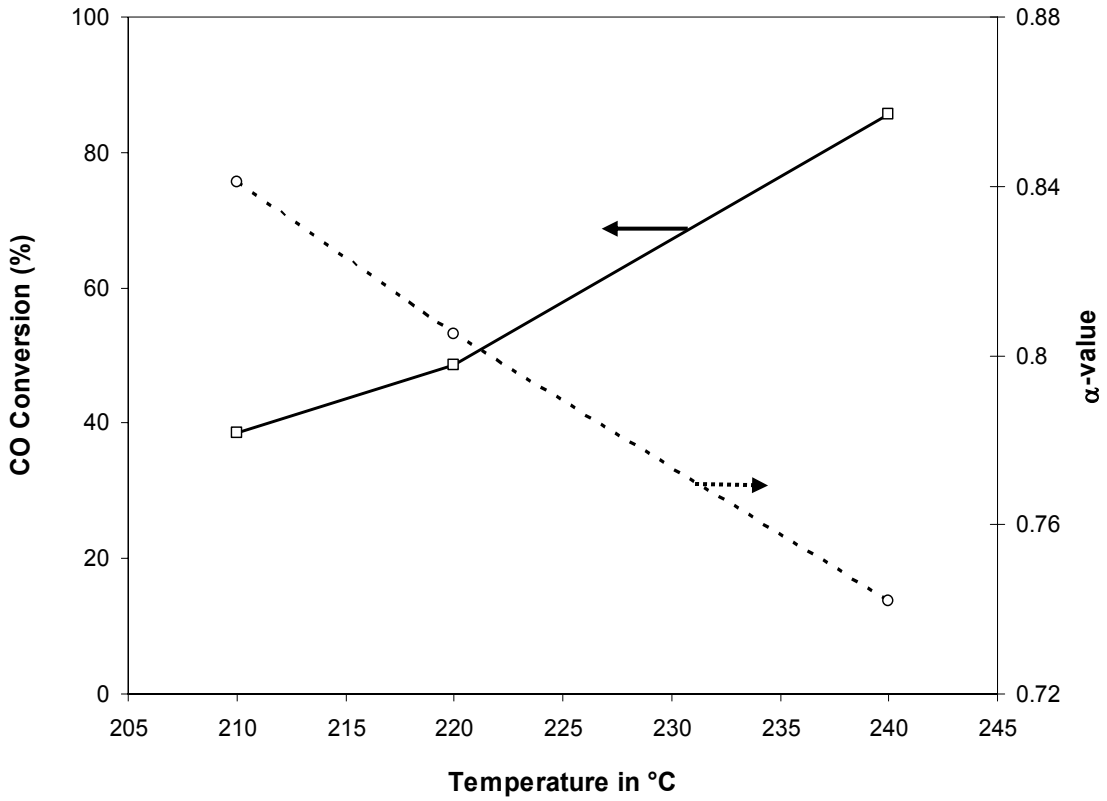

Figure 4.3 Effect of reaction temperatures on carbon monoxide conversion, and chain growth probability in SCP environment at constant pressure of 45 bar.

selectivity in SCH-FTS follows a different trend. The general trend reported in Figure 5.6shows that there is an existence of optimum temperature (250 °C) for both chain growth probability and CO conversions (this phenomenon is discussed in details in Chapter 5). The measured CO_2 selectivity was found to be less than 1% over the range of temperature studied in SCH environment.

In absence of pore diffusion limitations, the diffusion rate of CO and H_2 to the active sites is very temperature sensitive in the SCF phase due to the reliance of the density dependent properties on temperature in the near critical region. At low temperature, α-olefins readsorption dominates the competitive adsorption process

facilitating the longer carbon chain propagation. High coverage of α-olefins on the catalyst surface is an obstacle to the adsorption of CO, which can result in a lower CO conversion (Huang and Roberts 2003). The results in SCH suggests that there is a very fine balance between liquid-like density needed to extract heavy hydrocarbons and wax from inside catalyst pores and gas-like diffusivity required for the reactant and olefins to reach the active sites and incorporate in the chain growth and synthesis process. A previous study has shown that there is an existence of a reversible relationship between the coverage of α-olefins on the surface and the CO conversion by adding certain α -olefins to the reaction process (Hindermann et al. 1993). More details on the effect of temperature on chain growth probability and the phase behavior of the reaction mixture and its influence on improving diesel fractions at the optimum reaction temperature (250 °C) is discussed in details in Chapter 5.

4.3.3 Effect of pressure on selectivity in toward fuel fractions

As will be discussed in Chapter 5, there is a very slight change in the chain growth probability of higher hydrocarbons (C_{10+}) as the pressure increases from 35 (gas-like density) up to 80 bar (liquid-like density) at the constant temperature of 250 °C (see Chapter 5, and Figure 5.7). Changes of the density of the reaction media, as a result of tuning the pressure, would of course change the residence time of the reactant molecules inside the catalyst bed. The variation in residence time with adjustments to density and pressure was estimated using the Peng-Robinson equation of state (PR-EOS) and Soave-Redlich-Kwong equation of state (SRK-EOS) setting the values of kij's of all

components (reactants and solvent) equal to zero. Figure 4.4a and Figure 4.4b shows the effect of residence time on the hydrocarbon product distribution and fuel fraction in SCH media at temperature of 250 °C and SCP media at temperature of 240 °C, respectively. Increase of the residence time results in higher selectivity towards diesel and wax fractions in the case of SCH-FTS (see Figure 4.4a). However, no significant changes were observed in the light hydrocarbon and gasoline fractions as a result of changing the total pressure. On the other hand, in SCP the effect of residence time is more pronounced as shown in Figure 4.4b. At lower residence time (6 s), more than 65 % of the products are in the gasoline fraction, whereby at the highest residence time (10s) more than 60% of the products are in the diesel and heavy wax fractions. According to the basic model of the chain-growth mechanism and the polymerization nature of the FTS reaction, increasing the residence time of the reactant molecules would result in an increased probability of chain growth, therefore, the weight percentage of the heavier hydrocarbon would increase (Flory 1936). The rate of secondary reactions of α-olefins (especially readsorption, and incorporation in chain growth) is also affected by the residence time; the more rapid the removal of α-olefins from the catalyst bed (lower residence time) the lower the possibility for readsorption (Madon and Iglesia 1993). However, this is not always the case since longer residence time and readsorption of α-olefins may also result in hydrogenation to paraffins, and isomerization to *cis* and *trans*-olefins, thus terminating the chain growth.

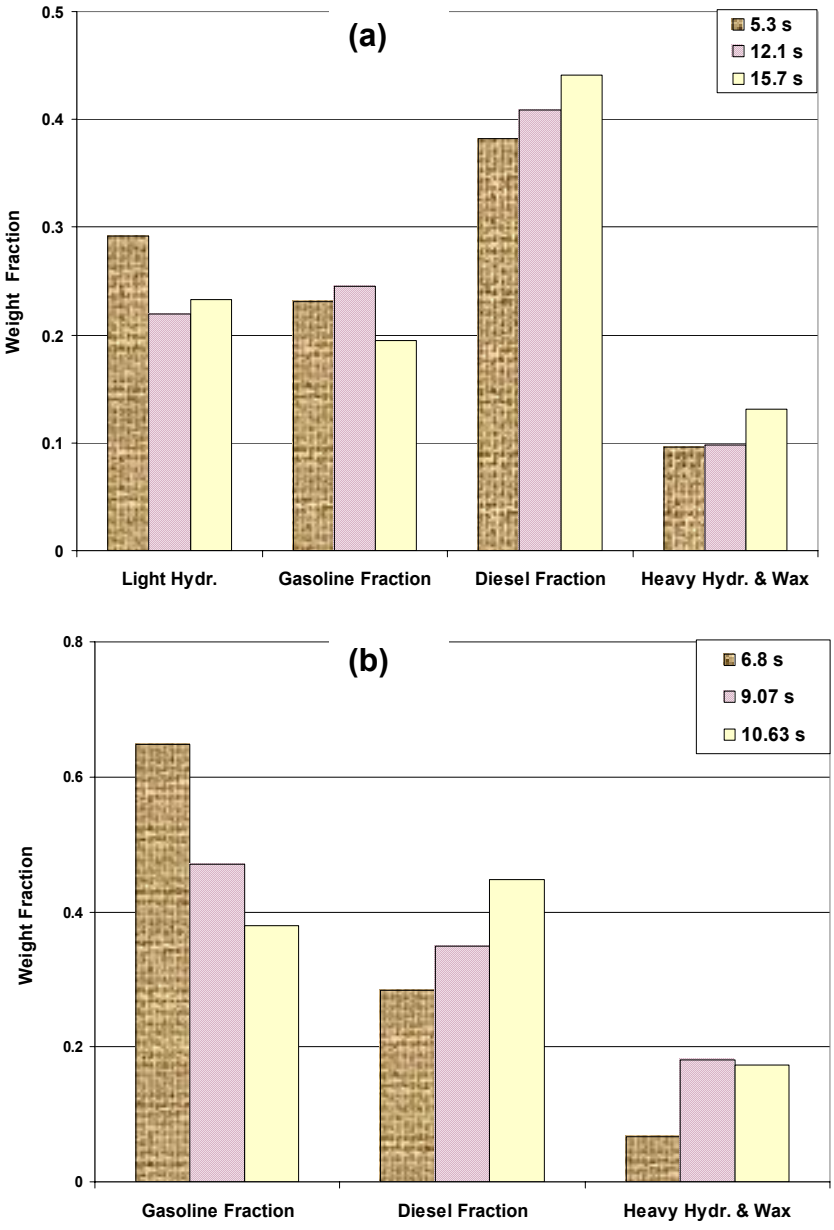

Figure 4.4 Effect of the residence time on the hydrocarbon distributions in (a) SCH media at constant temperature of 250 °C, and (b) SCP media at constant temperature of 240 °C.

Besides the bed residence time and the pressure, other factors such as heat of adsorption of the light olefins, the solvent medium properties and phase behavior, and solvent-reactant feed ratio play a role in determining the degree of the incorporation of the α-olefins in the chain-growth mechanism (Elbashir and Roberts 2004a).

4.3.4 An opportunity to selectively maximize isomerization synthesis for jet fuels

Aviation turbine fuel (jet fuel) is a mixture of many different hydrocarbons in the range of C_9-C_{16} (boiling range 190-230 °C). The range of hydrocarbon sizes (molecular weights or carbon numbers) in jet fuels is restricted by the distillation, freezing point, and sometimes naphthalenes and smoke point requirements for the product. Hydrocarbons in jet fuels are mainly iso-paraffins and isomers as well as kerosene. Recent interest in jet fuels from FTS is mainly due to their negligible sulfur content and clean-burning process. Recently, a product produced by the FTS process was approved in DEF STAN 91-91 as a jet fuel component after a thorough review process (Bacha et al. 2000). Since the major hydrocarbon products from the FTS reaction are mainly α-olefins and *n*-paraffins, isomerization reactions are usually required for FTS wax (Zhou et al. 2003).

We observe an interesting phenomenon in our studies of a silica-supported cobalt catalyst (15% Co/SiO_2-HSA; preparation method of this catalyst and its characterizations is shown in Chapter 7). Figure 4.5 shows the weight percentage of *n*-paraffins and isomers as obtained at three different hexane/syngas molar ratios (3/1, 6/1, and 9/1) at 240 °C and pressure of 57 bar over the 15% Co/SiO_2-HSA. As illustrated in the figure, at 3/1 molar ratio the hydrocarbon products are mainly n-paraffins with a clear shoulder in

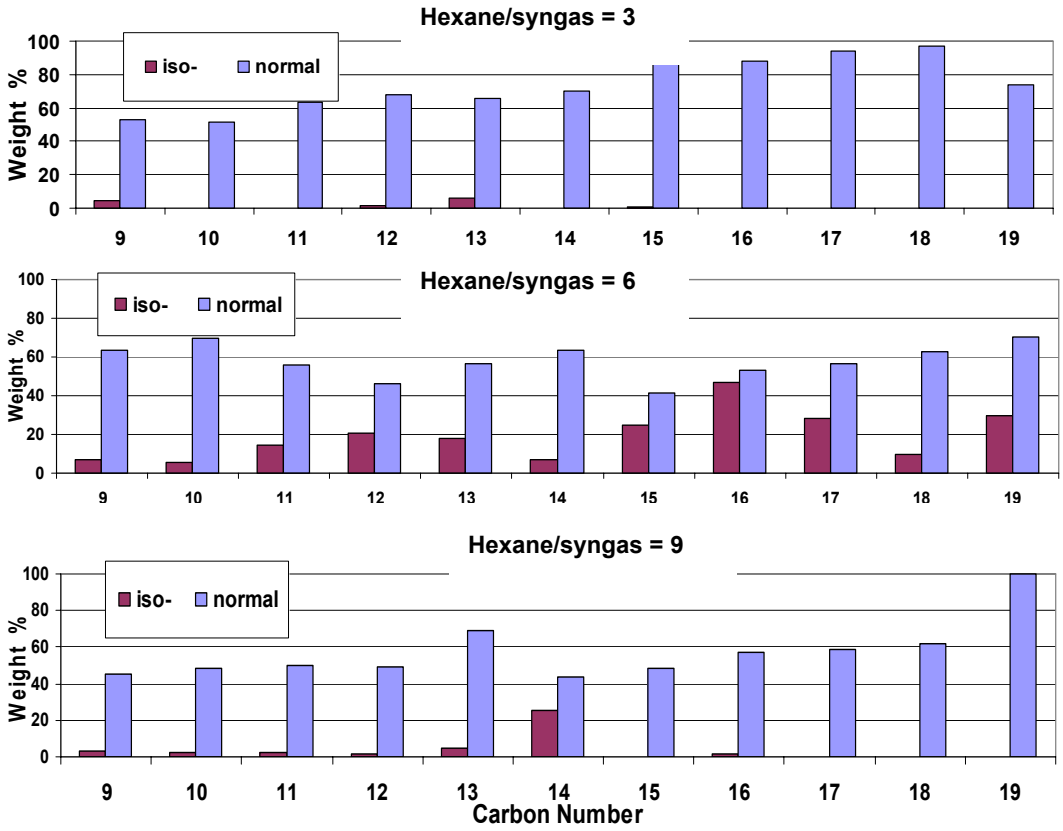

Figure 4.5 Effects of hexane/syngas molar ratio on the *n*-paraffin and isomers productivity in SCH-FTS at 240 °C, H_2/CO ratio 2/1 and total pressure of 65 bar over a 15% Co/SiO_2 catalyst.

the products in the range of C_{15}-C_{18}. However, as the ratio of hexane/syngas increases to 6/1, isomers concentration in the products significantly increases specifically within the jet-fuel range (C_{10}-C_{17}). In addition, the distribution of hydrocarbons is almost similar in the overall range of the reported products. However, upon increasing the ratio to 9/1 negligible isomers were produced at C_9-C_{14} with maximum concentration of products obtained at heavy products (i.e. C_{18} and C_{19}). These results demonstrate that the ratio of solvent/syngas can participate in the synthesis processes, specifically in the secondary reactions such as isomerization.

4.4 Conclusions

Significant improvement in the product distribution towards heavier hydrocarbons (high α-value) has been obtained in SCF-FTS compared to that of the gas-phase FTS media. This influence has been attributed to the effect of temperature and pressures on both thermo-physical properties of the reaction mixture (namely density and density dependent properties) and the reaction kinetics. Quantitative analysis of these effects is required for better control of the overall reaction performance. Our results have shown that tuning the reaction environment from liquid-like properties to vapor-like properties and vice-versa significantly influenced the FTS hydrocarbon product distribution. This study illustrates the opportunity to control the reaction selectivity towards the most desired product from the synthesis (i.e. the ultra-clean fuels). The SCF media also offers another opportunity to selectively control isomerization ratios of paraffinic and olefinic hydrocarbons. This would allow optimizing the selectivity of other valuable fuels fractions such as jet fuels.

CHAPTER 5
ENHANCED INCORPORATION OF α-OLEFINS IN THE FISCHER-TROPSCH SYNTHESIS CHAIN-GROWTH PROCESS OVER AN ALUMINA SUPPORTED COBALT CATALYST IN NEAR-CRITICAL AND SUPERCRITICAL HEXANE MEDIA

5.1 Introduction

5.1.1 Utilization of supercritical phase media in Fischer-Tropsch synthesis.

From the time of the discovery of the Fischer-Tropsch synthesis (FTS) in the mid 1920s by Franz Fischer and Hans Tropsch (Fischer and Tropsch 1926c), FTS has become an object of great interest to scientists and engineers engaged in catalysis and reaction engineering, as well as, those concerned with the utilization of coal and natural gas as sources of liquid transportation fuels and petrochemicals. FTS performance in industrial fixed-bed-reactors (gas-phase) suffers from local overheating of the catalyst surface and high degrees of methane selectivity, thereby decreasing yield of desired products (Kolbel and Ralek 1980; Lang et al. 1995). SASOL subsequently developed slurry bubble reactors (liquid-phase) to overcome the limitations of fixed-bed-reactor FTS (Geertesma 1990). Such operation provides an excellent temperature distribution for this highly exothermic reaction since the paraffinic solvent (e.g. octacosane C_{28} hydrocarbon) used as a reaction medium has a thermal mass over 500 times greater than that of the gas-phase operation in a fixed-bed-reactor. However, this process is limited by lower reaction

rates due to slower diffusion of syngas into the catalyst pores through the heavy hydrocarbon solvent. Catalyst attrition and separation of products and catalysts from the heavy liquid medium are other obstacles to the industrial slurry reactor. This chapter presents the investigation of FTS under supercritical fluid (SCF) solvent conditions in order to address some of these issues. The main objective behind conducting FTS in supercritical or near-critical fluid (SCF-FTS) solvent involves employing their unique pressure/temperature tunable fluid properties to overcome certain limitations in the conventional FTS processes. SCFs possess gas-like transport properties (diffusivities), and liquid-like solubilities and heat capacities each of which benefit FTS performance (Subramaniam 2001). The first study that suggested utilization of SCF as a medium for FTS reaction was conducted by Fujimoto and his coworkers (Yokota et al. 1990) wherein they found that SCF medium transported and extracted heavy products more efficiently than gas medium during FTS reaction. This successful attempt was followed by other studies focused on improving the SCF-FTS performance (e.g. catalyst activity and stability, selectivity, and product distribution). The influence of the pressure-tunable density of the supercritical solvent on the catalyst activity, and product distribution was demonstrated by (Bochniak and Subramaniam 1998). Lang and coworkers (Lang et al. 1995) reported significant improvement of α-olefin selectivity in the supercritical phase compared to the conventional gas-phase FTS. Recently, (Jacobs et al. 2003) showed that heavy hydrocarbon (i.e. wax) content in the supercritical phase is always higher than in gas phase FTS. This performance was attributed to the enhanced extraction of heavy hydrocarbon and wax from the catalyst pores in the supercritical phase as result of high solubility of those components in the supercritical solvent. Recent studies (Huang and

Roberts 2003; Huang et al. 2004) also reported significant improvements in heat transfer within the reactor when the reaction was conducted in supercritical hexane (SCH) compared to conventional gas-phase FTS. This improvement in the temperature distribution inside the catalyst bed combined with relatively high solubility of products in SCH facilitate considerable enhancement in α-olefins selectivity and chain growth probability compared to conventional gas-phase FTS.

The introduction of the supercritical solvent as a new parameter to influence FTS performance shifts the problem from a classical catalytic reaction-engineering process to one combined with a thermo-physical puzzle. The phase behavior of the reaction mixture in the near-critical and SCF reigons is strongly influenced by the pressure and temperature of the reaction system (Subramaniam 2001). This offers a unique opportunity to control the FTS reaction medium and tune it from a gas-like environment to liquid-like environment by simply changing either reaction temperature or the pressure. In Chapter 3 and 4, we demonstrated that changing either pressure or temperature has a dramatic effect on selectivity and conversion of the FTS reaction conducted under supercritical solvent (*n*-pentane and hexane) conditions. As a matter of fact, this tuning process will not only affect the bulk physical properties of the reaction mixture (e.g. density, diffusivity, thermal conductivity, viscosity, etc.) but also the rates at which different reactions take place on the catalyst surface. As a result, optimization and control of the performance of supercritical phase FTS requires a quantitative evaluation of the influence of tuning parameters (i.e. temperature and pressure) not only on the phase behavior of the reaction mixture, but also on the rates of the different reactions taking place on the catalyst surface, including the chain growth mechanism.

5.1.2 Deviations from standard ASF product distributions in supercritical phase FTS

The Anderson-Schultz-Flory (ASF) model is a common model used to describe the chain growth mechanism in FTS and is developed based on Flory's (Flory 1936) pioneering studies on the fundamental nature of polymerization. The basic structure of the ASF model was developed through a series of extensive studies (Herington 1946; Friedel and Anderson 1950; Henrici-Olive and S. 1976) that led to the current, well known ASF product distribution model (descriped in details in Section 1.4.2). The mathematical form of the ASF model is shown in Eqns. 4.1 and 4.2. W_n represents the weight percentage of all hydrocarbon products with carbon number n, and α is chain-growth probability which is the rate of growth per the sum of growth and termination rates.

$$W_n = n\alpha^{n-1}(1-\alpha)^2 \tag{4.1}$$

$$\ln\left(\frac{W_n}{n}\right) = n\ln\alpha + \ln\left(\frac{(1-\alpha)^2}{\alpha}\right) \tag{4.2}$$

According to the ASF model, a plot of $\ln(W_n/n)$ vs n (as in Eqn.4.2) should yield a straight line for all hydrocarbon products whereby the α-value can be determined from the slope of that line. From the structure of Eqn. 4.2, a higher α-value indicates that a heavier hydrocarbon weight percentage should be expected. It is noteworthy to mention here that the ASF model is neither a function of the temperature nor the concentration of the reactant molecules.

Numerous studies have reported deviations from this standard linear product distribution in FTS yielding different curvatures for the relation between $ln(W_n/n)$ vs n (Inoue et al. 1987). These deviations from the standard ASF model provide one of the means to control the hydrocarbon distributions and selectivity towards the most desired products such as FTS desired transportation fuels (e.g. diesel fuels) (see Chapter 4).

Many kinetic and reaction route models have been developed to explain the observed deviations from the standard ASF model. Mass transfer limitations inside the catalyst pores due to the condensation of heavy hydrocarbons was one of the reasons suggested for enhanced α-olefin (primary products) readsorption thereby increasing the production of heavy hydrocarbons (Madon et al. 1993). Huff and Satterfield also suggested a model that accounts for two-catalytic sites with two different growth factors (iron promoted catalysts) that yield a positive deviation from the standard ASF model (Huff and Satterfield 1984). Pore size effects (molecular sieve effects) (Iglesia et al. 1993b) and concentration gradients as well as temperature gradients in fixed bed reactors (Matsumoto and Satterfield 1989) were also suggested as causes for non ASF distributions. In a series of studies, Puskas and his coworkers argue that multiplicity in the chain growth probability is the reason for positive deviations from the ASF model (Puskas et al. 1993; Hurlbut et al. 1996; Puskas and Hurlbut 2003). In addition, deviations from the ASF model have also been attributed to experimental artifacts, non steady state operation (Davis 2003a) as well as to transient holdup of higher molecular weight products in the oil phase surrounding the catalyst (Dictor and Bell 1983).

Several studies reported deviations from ASF distributions when the reaction is conducted in supercritical phase solvent. Tsubaki, et al. (Tsubaki et al. 2002) reported a

surprising non-ASF product distribution in supercritical pentane phase at a reaction temperature of 200 °C over a silica supported cobalt catalyst. The authors reported a hydrocarbon product distribution that showed that the formation rate of hydrocarbons from C_7-C_{28} was totally independent of the carbon number with an α-value higher than 0.96. They suggested that the high ability of formed olefins (C_nH_{2n}) to readsorb in the supercritical phase and initiate new chain-growth processes results in an increased formation rate of heavy hydrocarbons. However, the authors have not explained the mechanism by which C_8 and C_{26} behave equally in initiating new chains that promote heavier hydrocarbon production with similar rate of formation. On the contrary, another study (Jacobs et al. 2003) employing mixed supercritical solvents (55% hexane-45% pentane) with an alumina supported cobalt catalyst at 220 °C and over wide range of pressures (total pressures upto 80 bar) showed that hydrocarbon distributions beyond C_{10} followed closely the ASF distributions model. No information about light hydrocarbons (C_1-C_9) distribution was presented in that communication. Another difference between the study of Jacobs et al (Jacobs et al. 2003) and the current study is that they used argon (inert gas) to elevate the pressure of the reaction system which can alter the phase behavior and solvent properties of the reaction mixture. Bochniak and Subramaniam (1998) have reported non-ASF distributions in SCH-FTS on Ruhrchemie iron catalyst at temperature 240 °C by varying the pressure from 35 bar (gas-like density) to 70 bar (liquid-like density). The product distributions they reported showed an existence of shoulder in carbon fractions from C_5-C_{10} that decreases with increasing pressure; however there are no significant changes in light products distributions (C_1-C_4) with the pressure. This phenomenon was reported to disappear after 80 hr time-on-stream.

Furthermore, they (Bochniak and Subramaniam 1998) attributed the enhanced chain growth probability in SCH medium to the enhanced extraction of heavier olefins in the liquid-like medium prior to any secondary reactions. Meanwhile, at high pressure (70 bar), they suggested that the diffusion rate of α-olefins decreased significantly and results in regular ASF distributions (Bochniak and Subramaniam 1998).

Due to the complexity of the supercritical-phase FTS operation, understanding the reaction kinetics and proposing chain growth pathways requires the following; (1) understanding of the phase behavior of the solvent/reactant and the solvent/reactant/product mixture, (2) detailed product distributions from C_1 up to heavier hydrocarbon products under the specified reaction conditions, and (3) an understanding of the interrelation of the phase behavior of the reaction mixture and the FTS performance (e.g. product distributions and consumption rates of the reactants).

The importance of the last point above arises from the fact that the phase behavior of a reaction mixture is different from that of a pure solvent. The SCF-FTS mixture is composed of a solvent (e.g. hexane), and reactant gases (CO, H_2) as well as light (C_1-C_6) and heavy hydrocarbons (C_{7+}). As a result, near-critical and supercritical-phase FTS operations are not governed only by the properties of the supercritical fluid solvent, but are governed rather by the properties of the FTS mixture obtained after establishing steady-state conditions.

5.1.3 Phase behavior of supercritical-phase FTS.

Very few studies have dealt with the phase behavior of the reaction mixture within supercritical phase FTS (Joyce et al. 1999; Joyce et al. 2000; Gao et al. 2001;

Polishuk et al. 2004). Joyce and coworkers (Joyce et al. 1999) have studied the vapor-liquid composition for a mixture of hexane (supercritical solvent) + C_{16} (FTS wax) at three different temperatures (199, 252, and 300 °C). Hexadecane and hexadecene (C_{16} hydrocarbons) have been used to simulate the changes in the phase behavior of hexane as the percentage of heavy hydrocarbons in the product stream increases. Their findings showed that for 0.0326 mole fraction of C_{16} in a hexane+hexadecane mixture the critical pressure and temperature of the mixture are 33.76 bar and 252 °C, respectively. These results can be considered a significant change in the critical properties of the medium since the critical pressure and temperature of pure hexane is 32.4 bar, and 234.5 °C, respectively. In another study Gao et al. (Gao et al. 2001) reported critical points for hexane (> 94 mole %) + reactants (CO and H_2) mixtures at different moles ratios. They observed that the critical temperature and critical density of the solvent-reactant mixture decreases as the concentration of CO and H_2 increases, whereby the critical pressure increases with CO and H_2 concentration. More recently, Polishuk et al. (Polishuk et al. 2004) compared the ability of two semi-predictive thermodynamic models, namely the global phase diagram approach (GPDA) and the predictive Soave–Redlich–Kwong (PSRK), in describing the experimental phase behavior of binary homologous series of n-alkanes that represent the FTS product spectrum. For a symmetric system of n-hexane-n-tetracosane (similar to a solvent-product mixture of the current study) they found that the GPDA predicts very accurately the experimentally measured values of (Joyce et al. 2000) over a wide range of temperature, while PSRK significantly overestimates the bubble-point data.

In this chapter the hydrocarbon product distributions of SCH-FTS over an alumina supported cobalt catalyst is studied over a wide range of operating conditions within the near-critical and supercritical hexane regime. Conditions for single phase FTS operation (near-critical and supercritical hexane conditions) are determined based on measurement of critical properties of the FTS reaction mixture (hexane-syngas-products) collected from the effluent of a high-pressure fixed-bed-reactor. The critical properties of this mixture were measured in a high pressure variable volume view cell apparatus. Deviations in hydrocarbon product distributions from the standard ASF model are observed in most cases with high chain growth probability within the middle distillate hydrocarbon region. The degree of deviation from the ASF model is found to be related to the operating conditions within the near-critical and supercritical single phase media.

5.2 Experimental Section

5.2.1 Phase behavior studies of FTS reaction mixture.

A variable volume view cell (VVVC) unit (Figure 5.1) was used to measure the critical properties of hexane and SCH-FTS mixture. The VVVC unit consists of high-pressure variable volume view cell, manual pressure generator, temperature controller, heating tape, pressure gauge, syringe pump, stirring bar, and stirring plate. The volume of the cell can be adjusted by displacement of an internal movable piston controlled by a manual pressure generator (High Pressure Equipment Model 87-6-5) filled with isopropanol and used to manipulate the pressure in the view cell. The dynamic seal between the piston and the walls of the vessel is achieved by using four Viton O-rings. The Viton O-rings do not swell appreciably in the presence of a solvent such as hexane and it can hold up to pressure of 85 bar at 260 °C. In order to insure no

1	Variable volume cell	6	Injection port	PG	Pressure generator
2	Movable piston	TC	Temperature controller	SP	Syringe pump
3	Viton O-Rings	P	Pressure indicator	MS	Magnetic stirrer
4	Stir bar	PC	Computer	FRL	Fluorescent ring light
5	Quartz window	VC	Video camera		

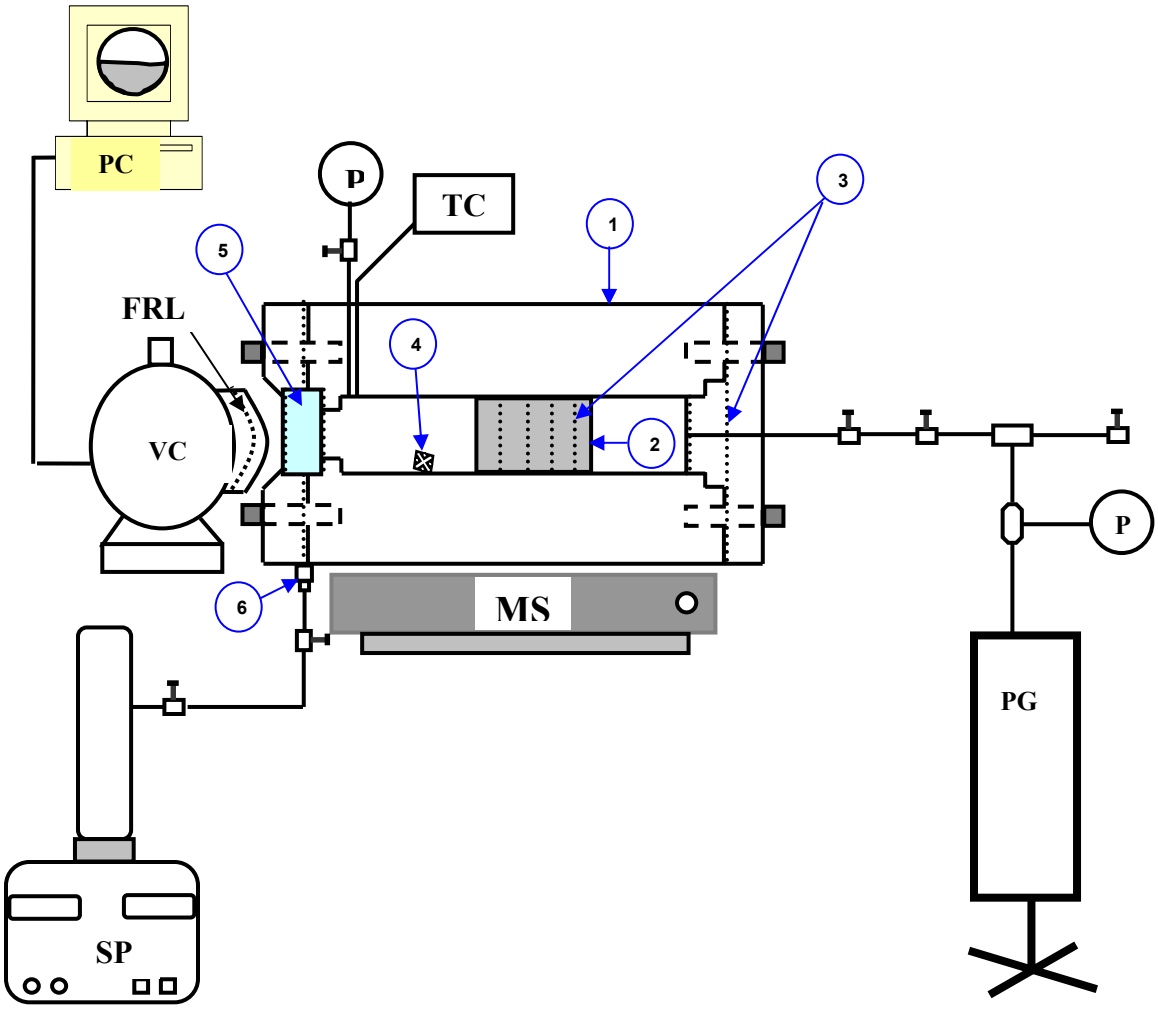

Figure 5.1 Variable volume view cell (VVVC) apparatus for phase behavior and critical property measurements.

leakage of the isopropanol from the back side of the piston, a sample of hexane was injected into a gas chromatograph (GC-3300 with FID detector) before and after measurement of the critical properties. No isopropanol peak was detected which indicates that the Viton O- rings provide the required seal under the pressure and temperature conditions studied. A video camera (QuickCam Pro 4000) system with a fluorescent ring light was mounted close to the ½ inch thick quartz window on the front of the cell. Images of the phase transition from vapor-liquid equilibrium (VLE) to the supercritical phase and vice versa were digitally recorded on a PC. This allows for accurate determination of the critical points of both pure solvent (hexane) and SCH-FTS reactant/product mixtures.

The temperature in the cell was measured and controlled with a type PR-11 1/16" RTD (Omega Engineering) and a self tuning PID controller (Omega CN76030) wired to a magnetic contactor (Omega MC-2-2-40-120), respectively. The cell was heated by using a heavy insulated tape 1/2"×2' (Omega; FGH051) and the accuracy of the measured temperatures was ±0.2 °C. The pressure was measured with a Dynisco flush mount transducer (model TPT-432A) with an accuracy of ±0.5 bar.

In a typical experiment the apparatus was washed thoroughly using toluene and ethanol before drying it in an oven for 4-5 hrs. It was then evacuated using a vacuum pump prior to injection of an appropriate amount of our sample. The cell was then heated slowly to a prescribed temperature and allowed to equilibrate prior to recording the temperature and pressure at equilibrium. In order to accurately locate the critical point of the mixture, the meniscus between the liquid-phase and the vapor-phase was kept in the center of the vessel such that when the critical point is reached the volume of the two phases were equal. The

location of the critical point was determined by observation of the disappearance of the meniscus and the coalescence of the two phases into a single phase.

5.2.2 Activity, selectivity, and poduct distribution measurements of the SCF-FTS 15% Co/ Al_2O_3 catalyst.

Figure 3.1 shows our high pressure FTS unit whereby detailed information about the unit and the high pressure reactor setup is given in Chapter 3. The unit includes a mass flow controller (Brooks 5850E, and Omega FMA-7106E) to deliver syngas, while the volumetric flow rate of our solvent (hexane) was controlled by an HPLC pump (Acuflow Series III, Fisher). Hexanes solvent was purchased from Fisher Co. of purity above 99%, and syngas (31.2% CO, 2.08% N_2 and balance H_2) was purchased and certified by Air Products Company. Hexanes and syngas were combined in a static mixer (OMEGA) before entering the reactor and heated to the desired reaction temperature. The pressure in the reactor was controlled by a back pressure regulator (Tescom Inc.) located between the reactor and the hot condensation trap. One gram (screened to 100 - 150 μm) of the catalyst (15% Co/Al_2O_3 purchased from the United Catalysts Co.) was loaded into our high pressure reactor. Loading method and temperature monitoring inside the reactor was explained in details in Section 3.2.1. The FTS results reported in this chapter represent samples that were collected after at least 100 hrs of time-on-stream (TOS) for both gas-phase and SCH-FTS.

The analysis of reactants and products by two online gas chromatographs was used for the selectivity and conversion calculations as described previously in Section 3.2.2.

Figure 5.2a shows that miniscule amounts of oxygenates and isomers were detected by FID analysis in supercritical hexane FTS, whereby significant amounts of these components

were observed in the gas phase FTS experiments as shown in Figure 5.2b. GC-MS analysis (using HP5890 Series II with 0.25um column) was also conducted on different liquid samples collected after gas-phase FTS and SCH-FTS to quantitatively measure isomers and straight hydrocarbons ratio, and oxygenates content for specific hydrocarbons. Figure 5.2c shows an example of the GC-MS fragments spectra of products from a gas phase reaction. The analysis detected hydrocarbons within the mass range from 30 up to 1000. To ensure accurate detection of all hydrocarbons in the carbon range from C_5 up to C_{40} the temperature of GC-MS during analysis was ramped from 33 °C to 280 °C at a rate of 8 °C/min then fixed at 280 °C for 10 min. The GC-MS results were used to confirm the findings of the FID analysis.

5.3 Results and Discussion

5.3.1 Phase behavior of SCH-FTS reaction mixture.

The phase behavior (vapor-liquid equilibrium (VLE) and critical properties) of pure hexane was measured in our VVVC at the conditions specified earlier. Figure 5.3 shows the P-T diagram of pure hexane that includes the VLE coexistence line and location of the supercritical phase region as defined by the location of measured critical temperature and pressure. The experimentally measured VLE was found to be in a very good agreement with the calculated P-T behavior from both the Peng-Robinson equation of state (Peng and Robinson 1976) and the Antoine equation (Ohe 1976). Similarly, the measured critical temperature (233.2 °C) and critical pressure (30.03 bar) are within the range of reported critical properties of pure hexane (Kreglewski and Kay 1969). Figure 5.3 also shows images of the phase transition taken within our VVVC apparatus from the VLE to the near-critical and supercritical phase regions. The bottom image shown in

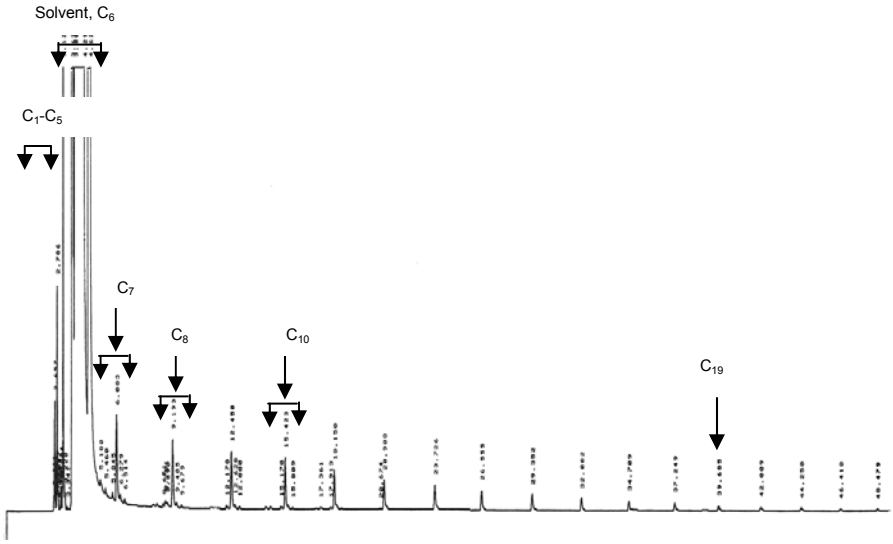

Figure 5.2a FID fingerprints for hydrocarbon compounds from SCH-FTS operation at the following reaction conditions; T= 240 °C, P_{total} = 65 bar, syngas and hexane flowrates of 50 sccm/g_{cat} and 1.0 mL/min, respectively, and H_2/CO feed ratio of 2.

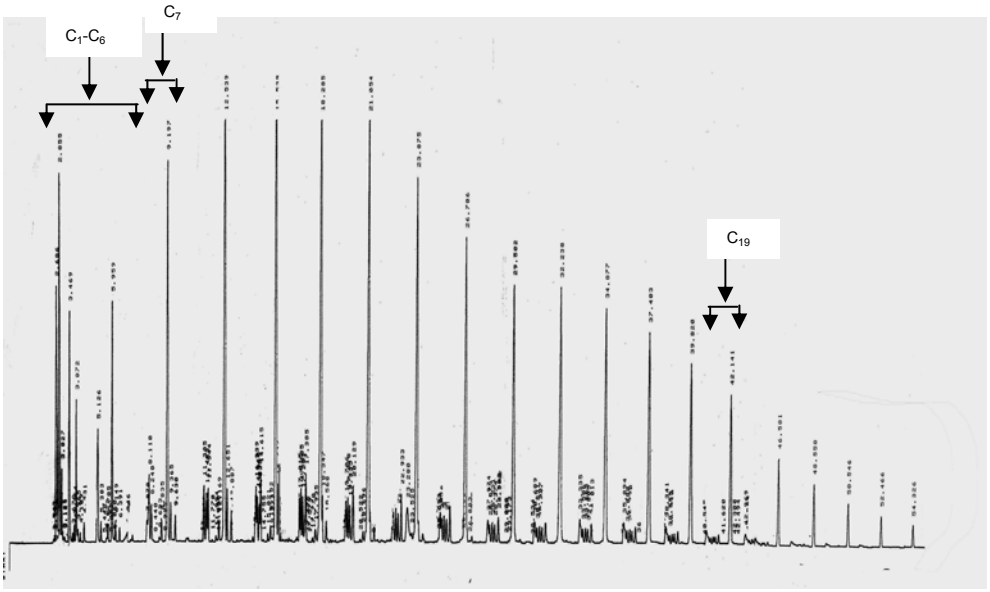

Figure 5.2b FID fingerprints for hydrocarbon compounds from gas-phase FTS operation at the following reaction conditions; T= 240 °C, P_{total} = 20 bar, syngas flowrate of 50 sccm/g_{cat}, and H_2/CO feed ratio of 2.

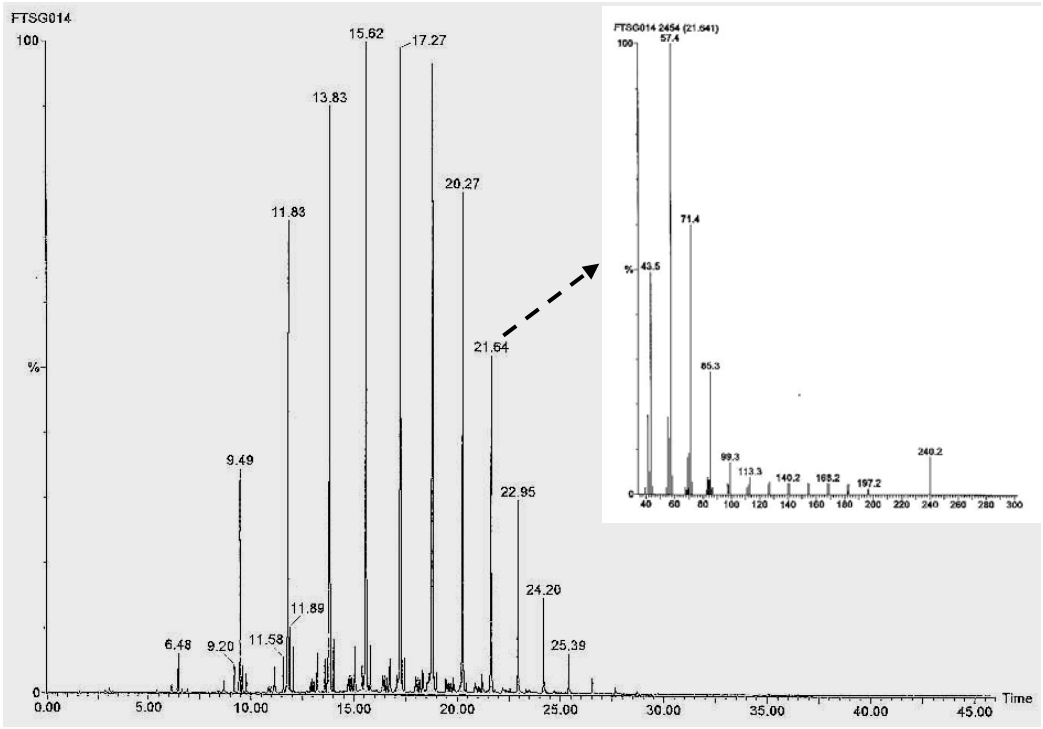

Figure 5.2c GC-MS response chromatograph of FTS hydrocarbon distribution. The upper figure shows the exact mass distribution (up to molecular weight of 280) for a variety of possible ions and isotopes detected at retention time of 21.64 min from the figure below. The injected sample represents a typical product from the reactor outlet for gas-phase FTS at T= 230 °C, P_{total} = 20 bar, syngas flowrate of 50 sccm/ g_{cat} and H_2/CO feed ratio of 2.

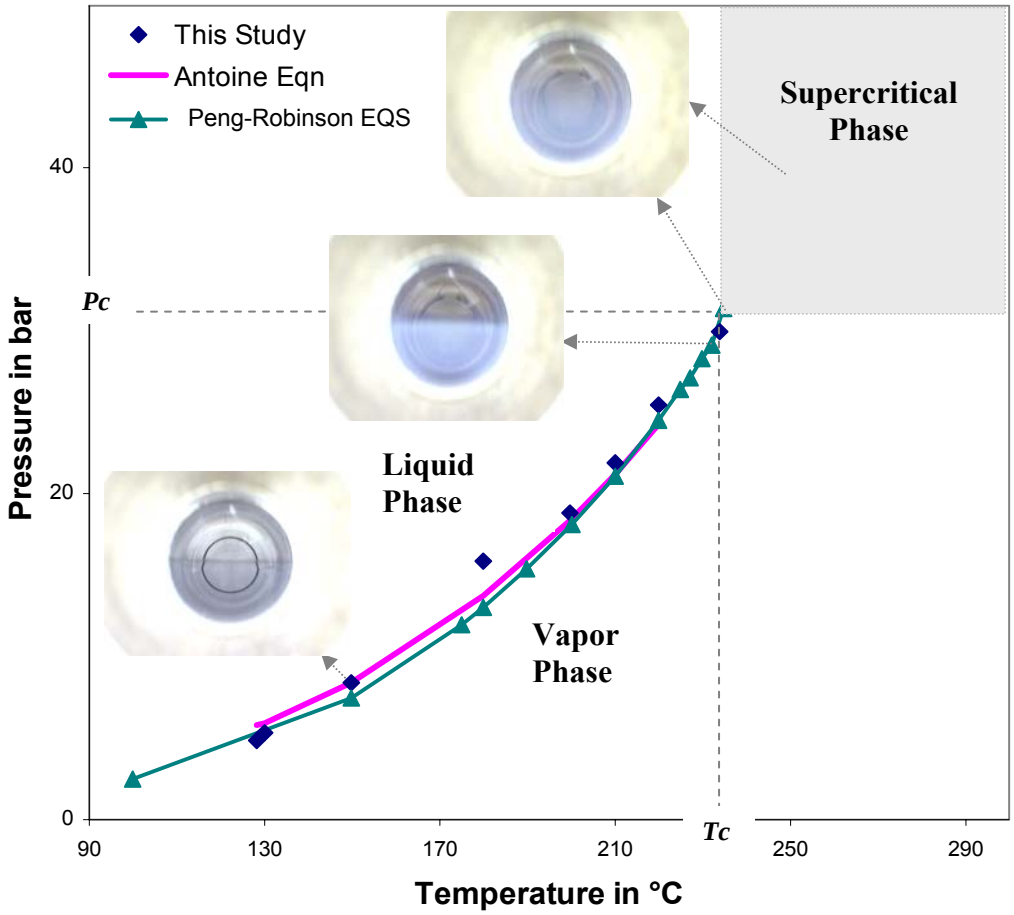

Figure 5.3 Vapor-liquid coexistence curve and critical point loci of the pure solvent hexane as measured using the VVVC (symbols) compared to phase behavior estimated from Peng-Robinson EQS, and Antoine equation (lines). Images show the phase transition from vapor-liquid-equilibrium to the supercritical phase.

Figure 5.3 depicts a typical VLE of pure hexane, whereby the meniscus is positioned at the center of the VVVC. The middle image shows VLE at conditions closer to the critical point (subcritical), whereby the liquid phase looks less dense and the vapor-liquid interface become less distinct. Exactly at the critical point the meniscus (located in the center of the VVVC) disappears indicating the formation of single supercritical phase as shown in the top image. Further increase of the pressure (up to 60 bar) beyond the critical point would result in no change in the single phase (supercritical) as shown in the top image.

The focus of this study involves the phase behavior and critical point location of the FTS reaction mixture represented by the solvent, reactant gases (CO, H_2), and products. The location of the critical point (temperature and pressure) of the FTS mixture was measured by collecting a sample from the reactor effluent. The sample from the reactor effluent (collected from the line between the exit of the hot trap and the entrance to the cold trap) was trapped into a collection container and then transfered into the evacuated VVVC through the high pressure valve shown in Figure 5.1. Prior to phase-behavior analysis, the sample was characterized for composition using gas chromatographs (FID and TCD) and the methods described earlier. An example of the characterization of a typical product stream (at 75% syngas conversion) obtained under SCH operation (c.a. 109 hrs time-on-stream) at 240 °C, and 65 bar is shown in Table 5.1. The sample was allowed to condense inside the VVVC and form two phases (liquid and vapor) prior to the determination of the critical temperature and pressure. The measured critical pressure of the FTS sample mixture, as shown in Figure 5.4, was found to be 37.2 bar (7 bar higher than that of pure hexane), however, the critical temperature (238.2 °C)

Table 5.1 The product distributions of SCH-FTS reaction mixture at 240 °C and 65 bar. Syngas (H_2/CO) feed ratio is 2:1, the volumetric space velocity is 93.75 hr^{-1} and the hexanes to syngas molar ratio is 3 to 1.

	Hydrocarbon Wt%			
	α-olefin	Paraffins	Isomers & Oxygenates	W_n
C1		7.22		0.072
C3	1.298	0.39	0.01	0.017
C4	0.83	0.21	0.11	0.011
C5	0.92	0.28	0.18	0.0137
C6*	NA	NA	NA	NA
C7	1.57	0.644	0.023	0.022
C8	2.96	1.39	0.02	0.044
C9	4.481	1.697	0.091	0.063
C10	4.256	1.603	0.125	0.060
C11	4.095	1.752	0.113	0.059
C12	4.186	1.724	0.083	0.060
C13	3.790	2.42	0.053	0.062
C14	2.66	2.64	0.028	0.053
C15	2.801	2.654	0	0.054
C16	2.926	2.933	0	0.058
C17	2.787	2.96	0	0.057
C18	2.285	3.02	0	0.053
C19	1.86	2.57	0	0.044
C20+	5.765	9.74	0	0.122

* C_6 composition has not been reported because the solvent (hexane) peak in the FID, and GC-MS analysis is dominant over the other products such as olefins, oxygenates and isomers with weight percentage above 80%.

of the mixture was found to be slightly higher than that of pure hexane. However, it should be noted that while this measured critical point represents the bulk reaction mixture, it does not necessarily represent that of the reaction mixture within the catalyst pores.

5.3.2 Fischer-Tropsch synthesis over the alumina-supported cobalt catalyst.

The 15% Co/ Al_2O_3 catalyst performance in the FTS reaction was measured under gas-phase operation (in the absence of the solvent), and under near-critical and supercritical hexane conditions. The scenario of the tuning process of temperature and pressure in the near-critical and supercritical regime is shown in Figure 5.4. Pressure was varied from 35 bar (gas-like density) to 80 bar (liquid-like density), while temperature was varied from 230 °C to 260 °C. A temperature of 260 °C can be considered as an extremely high operating condition for the cobalt catalytic system since they are known to be active much lower temperatures (e.g. 170 °C) (Zennaro et al. 2000). High temperatures in cobalt catalytic systems are known to favor the production of light hydrocarbons and methane. It is noteworthy to mention here that for the operation to be considered under supercritical hexane medium, it should be operated beyond the critical temperature and pressure of the solvent which are T > 230 °C and P > 30 bar. 250 °C and 65 bar were selected at the base conditions as shown in Figure 5.4. This selection is based on our investigation of the catalyst activity and selectivity at near-critical and supercritical hexane conditions at constant H_2/CO ratio of 2 and hexane/syngas molar ratio of 3 (Figure 5.5 and 5.6) where these conditions illustrates optimal performance as discussed below.

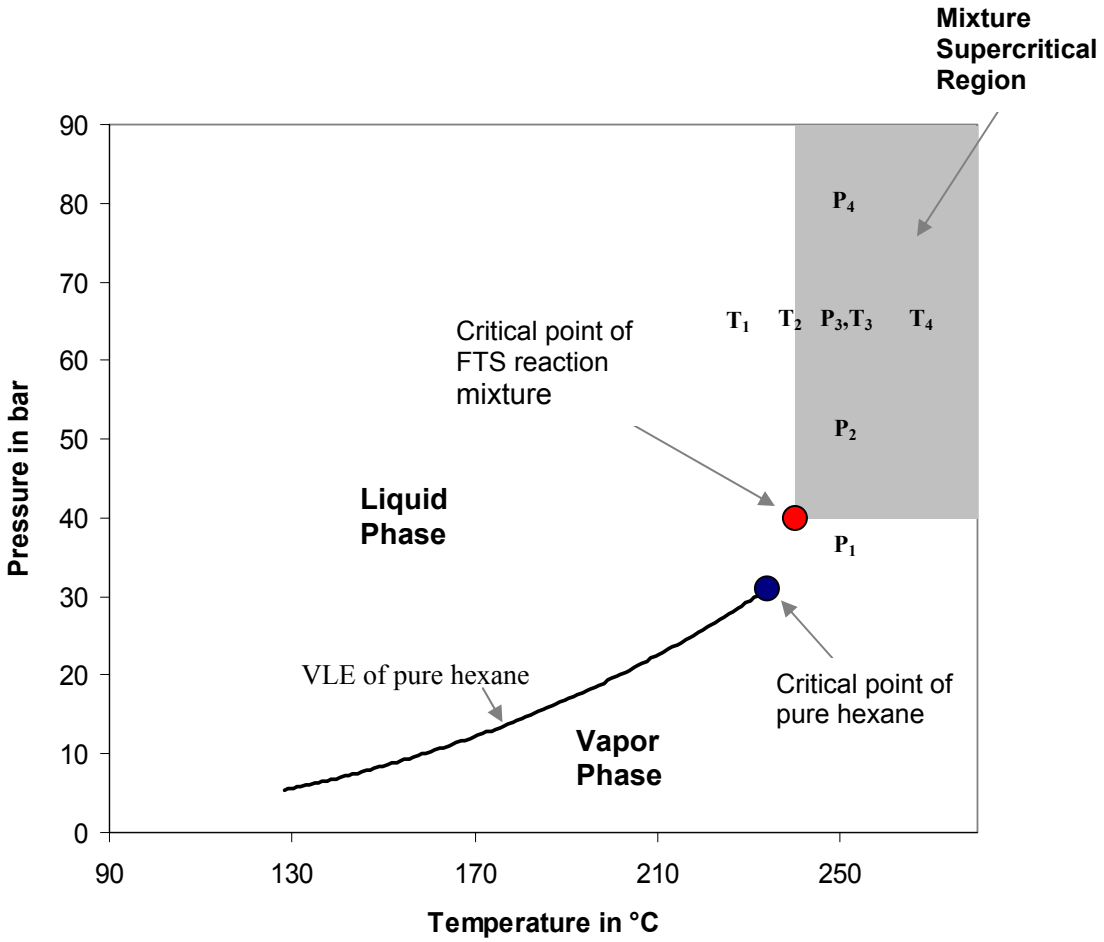

Figure 5.4 Critical point loci of a FTS reaction mixture composed of hexane 75 mole%, syngas (CO and H_2) 5 mole%, hydrocarbons and water (20%) as measured using the VVVC. The hydrocarbon products distribution is shown in Table 1. The FTS performance of the 15% Co/Al_2O_3 was measured at each of the operating points shown in the figure ranging from near-critical to the supercritical conditions. The combination of the operating temperature and pressure include (P_1+T_3, P_2+T_3, P_3+T_3, P_4+T_3, P_3+T_1, P_3+T_2, P_3+T_3, P_3+T_4).

Figure 5.5 shows the influence of reaction temperature on CO conversions and the chain growth probability ($\alpha_{overall}$) in SCH-FTS. The overall chain growth probability ($\alpha_{overall}$) is calculated from the slope of the best fit straight line of $\ln(W_n/n)$ vs n, whereas n initiates with C_1 (methane) and ends with the heaviest hydrocarbon product detected by our GC analysis system. As shown in Figure 5.5, CO conversion increases significantly with temperature up to 250 °C and then no significant change in conversion is shown from 250 °C to 260 °C. The $\alpha_{overall}$ decreases slightly from 230 °C to 240 °C, and then increases to reach its maximum value of 0.85 at 250 °C. A drastic drop in the chain-growth probability then occurs when the temperature is increased to 260 °C ($\alpha_{overall}$ of 0.663). The effect of pressure on both CO conversion and α-value are shown in Figure 5.6. The influence of pressure within the studied range (35 bar to 80 bar) on CO conversion is significant, with a maximum CO conversion of 85% obtained at 65 bar. However, no significant effect of pressure on α-value is observed within the studied pressure range with only a slight decrease at 80 bar. This slight decrease in α-value may be attributed to the significant increase in residence time at this elevated pressure. The rate of secondary reactions of α-olefins (namely readsorption and incorporation in chain growth) would be affected by the residence time such that rapid removal of α-olefins from the catalyst bed (lower residence time) would suppress the probability of readsorption (Madon and Iglesia 1993).

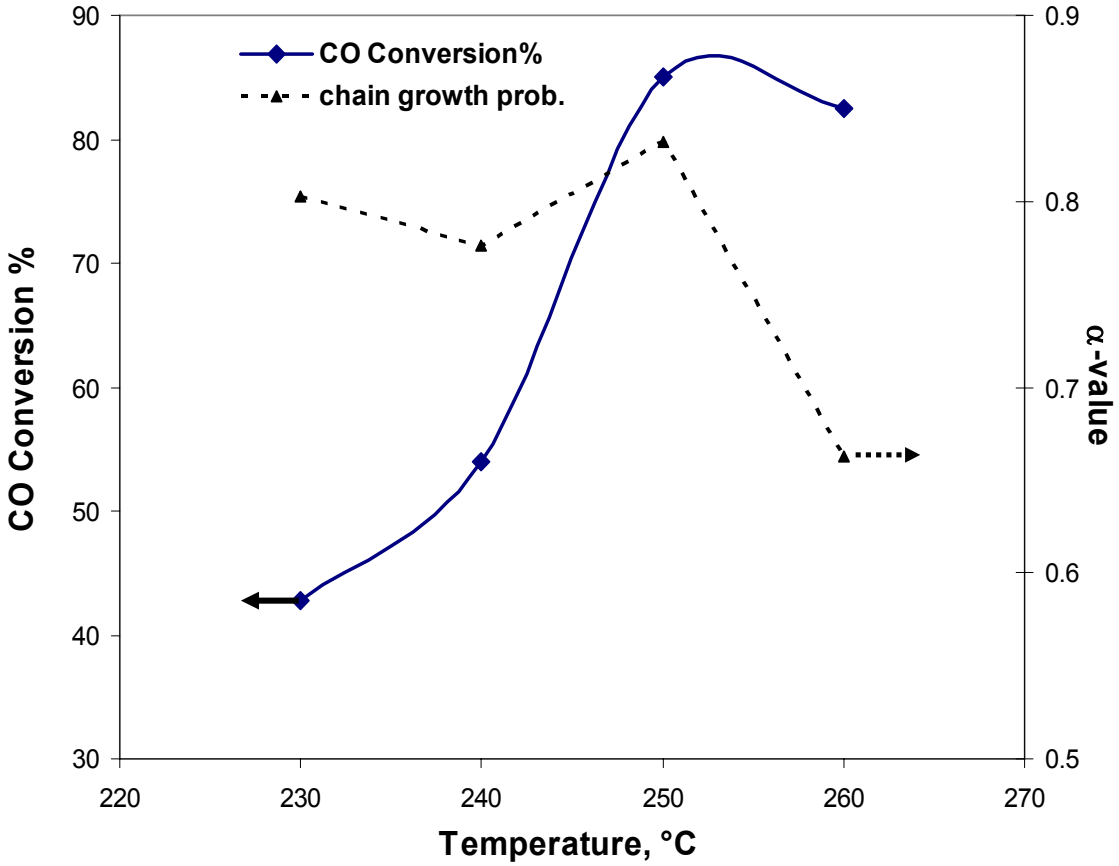

Figure 5.5 Effect of reaction temperature on CO conversion and chain-growth probability (α-value) at a total pressure of 65 bar and syngas/hexane molar ratio of 1/3.

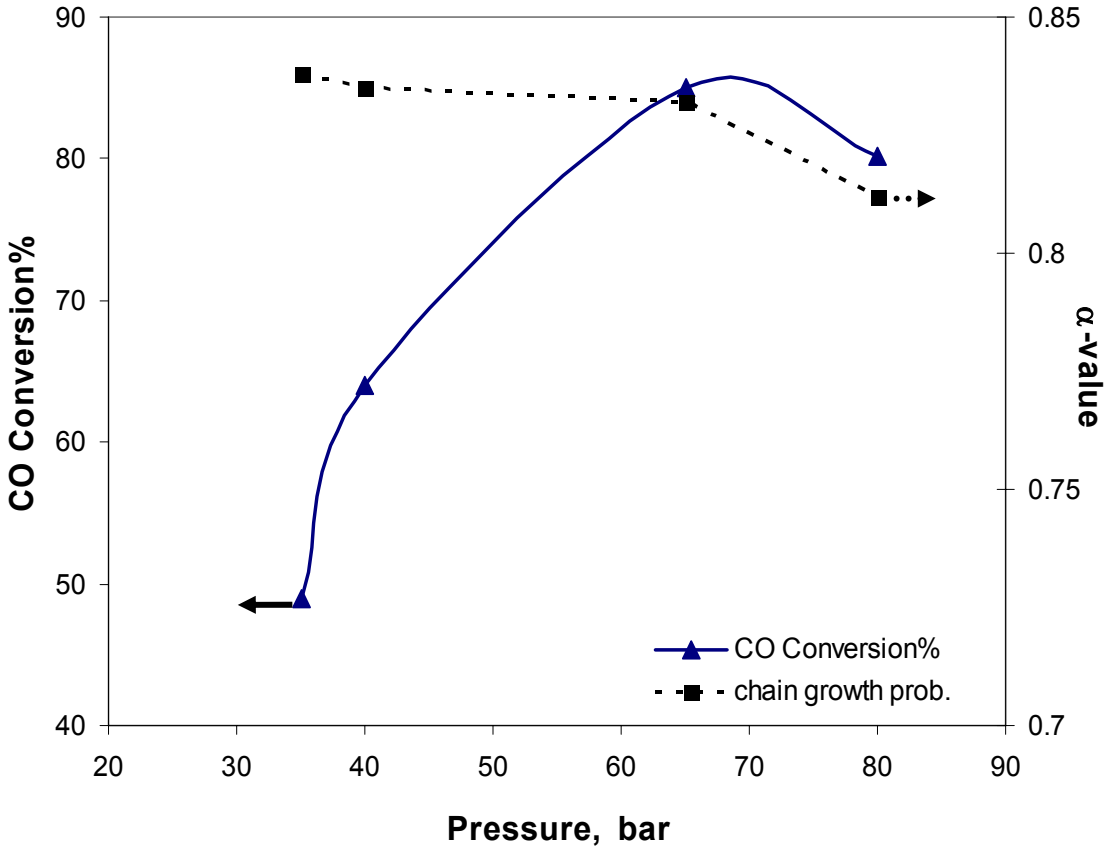

Figure 5.6 Effect of reaction pressure on CO conversion and chain-growth probability (α-value) at 250 °C and syngas/hexane molar ratio of 1/3.

However, this is not always the case since longer residence time and readsorption of α-olefins may also result in hydrogenation to paraffins, isomerization to *cis* and *trans*-olefins, or oxygenation to alcohols, thus terminating the chain growth process. Nevertheless, the existence of an optimum pressure in SCH-FTS is a result of a fine balance between pressure effects on bulk diffusivity, as well as, on pore diffusivity; at very high pressure (80 bar) the significant increase in bulk diffusivity overcomes the enhancement in pore diffusivity through pressure increases (Huang et al. 2002a).

5.3.3 Deviations from the standard ASF distribution in gas-phase FTS and supercritical hexane FTS.

Non ASF distributions, represented by nonlinear plots of the logarithm of the normalized weight percentage versus carbon number, were observed in both conventional gas-phase FTS (Figure 5.7) and SCH-FTS (Figure 5.8) experiments. As mentioned previously, the samples analyzed in determining the product distributions in either gas-phase FTS or SCF-FTS were collected after more than eighty hours TOS, after which both the activity and the selectivity of the cobalt catalyst showed steady performance with time. The deviation from the ASF standard distribution and the overall α-value are significantly different in the two cases. The results illustrated in Figures 5.7 and 5.8 are for a reaction temperature of 250 °C, syngas (H_2/CO ratio of 2/1) of volumetric flow rate of 50 sccm/min and syngas partial pressure of 20 bar.

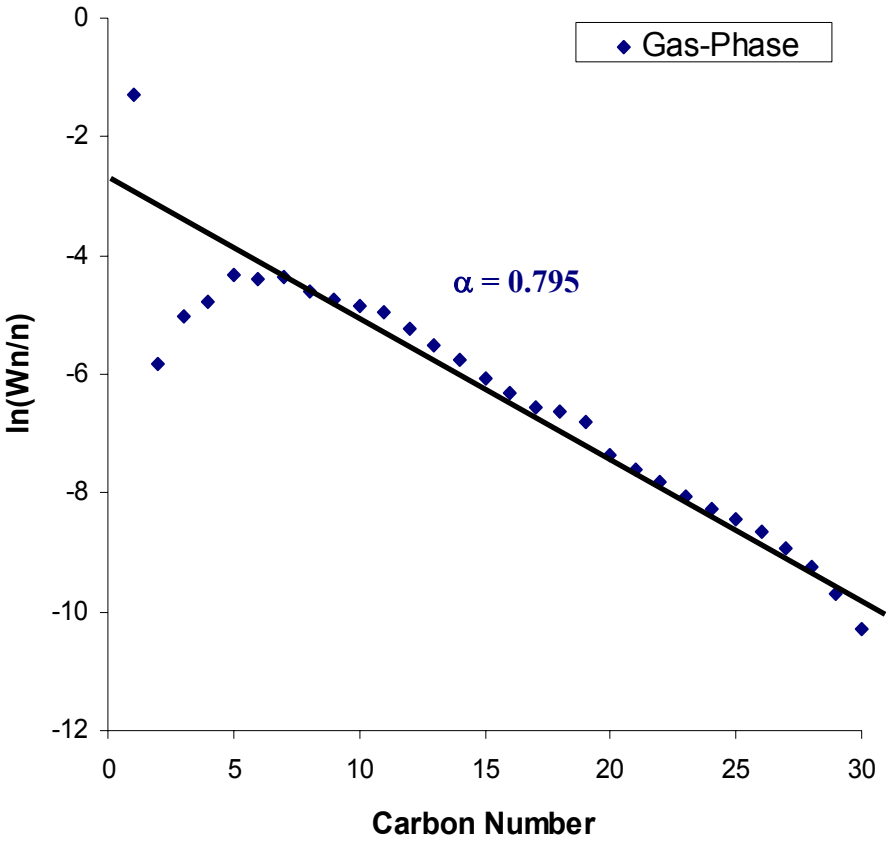

Figure 5.7 Hydrocarbon product distribution from gas-phase FTS at 50sccm/g_{cat} syngas flowrate, T= 250 °C , P_{total} = 20 bar, and H_2/CO feed ratio = 2.

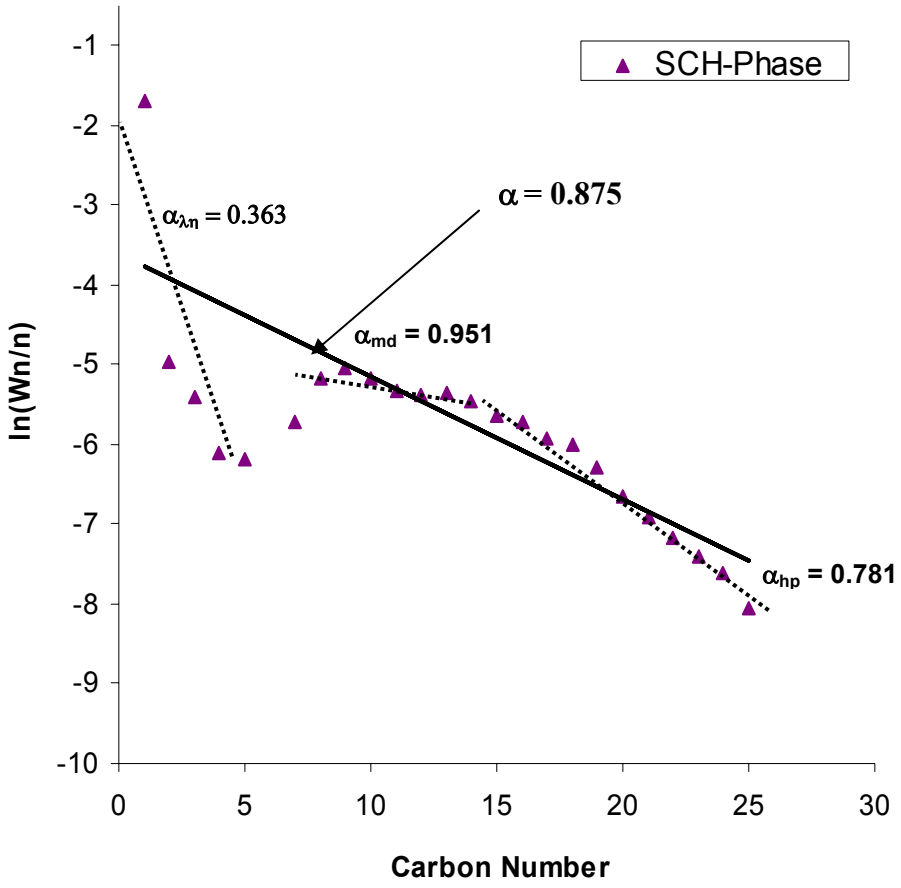

Figure 5.8 Hydrocarbon product distribution from SCH-FTS at 65 bar T= 250 °C, syngas flowrate = 50 sccm/ g_{cat}, hexane flowrate =1.0 mL/min, and H_2/CO feed ratio = 2.

The range of deviation from the standard ASF distributions (linear behavior) in the gas-phase FTS reaction (in absence of hexane) is limited to the light hydrocarbons (belowC_5) product region (see Figure 5.7). As is typical, the methane selectivity is underestimated by the ASF model (Puskas et al. 1993), coupled with a slight dip below the standard distribution in the range C_2-C_3 hydrocarbons. However, the distribution for hydrocarbons above C_5 follows well the standard ASF distribution with a $\alpha_{overall}^{gas\ phase}$ of 0.795. Similar deviations from ASF in gas-phase FTS were also observed at lower temperatures of 230 °C and 240 °C under the same reaction conditions (results not shown), although higher $\alpha_{overall}^{gas\ phase}$ were obtained; 0.811 and 0.805 respectively. Such deviations from the standard ASF model over cobalt-based catalysts in gas-phase reaction is common and have been observed in many studies (Smith et al. 1930; Puskas et al. 1993) as will be discussed below.

Under similar conditions with a hexane partial pressure of 45 bar, the product distributions in SCH-FTS also deviate from the standard ASF model with different trends and magnitudes from that obtained from gas-phase FTS. As shown in Figure 5.8, the $\alpha_{overall}$ of 0.875 is higher than that from the gas-phase FTS; however, the data is poorly fit by single straight line (solid line) and significant deviations from the ASF model are shown in the overall hydrocarbon product distributions. The product distributions in the case of SCH-FTS (65 bar and 250 °C) can be better divided into three stages (dotted lines). The first stage involves the light hydrocarbons product distributions that show steep declines with carbon number up to C_3 to yield a very low chain growth probability of α_{lh} = 0.363. It is noteworthy to mention here that α_{lh} has no significance and it only

represents the slope of the line connecting the experimentally measured W_n of light hydrocarbons. The second stage involves the middle-distillate growth probability indicating very high chain growth probability of $\alpha_{md} = 0.951$ with the least dependence of chain growth on carbon number in this region. The last stage involves the heavy hydrocarbons distributions that showed a decline in chain growth with the carbon number to give $\alpha_{hp} = 0.781$, which is slightly lower than the overall chain growth in the gas phase reaction ($\alpha_{overall}^{gas\ phase}$ of 0.795) shown in Figure 5.7. Another interesting observation is that the dip in the chain growth probability in the light hydrocarbon range is extended to the C_2-C_7 range rather than C_2-C_3 for gas-phase operation.

Numerous studies have investigated the participation of lower alkenes (α-olefins) in the chain growth process and its implication in non-ASF distributions observed in conventional gas-phase and liquid-phase FTS studies. Using elegant experimental methods with the limited analytical techniques available at the time, Smith and his coworkers reported that in the presence of CO and H_2, ethylene reacts on a Co catalyst surface forming large quantities of hydrocarbons and oxygen containing compounds (Smith et al. 1930). Such findings raise questions about the participation of primary products (α-olefins) in the chain growth mechanism. The participation of α-olefins was assumed to take place by either initiating new chains that are indistinguishable from those synthesized from adsorbed CO molecules, or through propagation to form its own chain growth sequence. Snel and his coworkers reported in a series of papers their findings on the participation of ethene, propene, and butene in the chain growth mechanism over an iron catalyst (Snel and Espinoza 1987; Snel 1989b; Snel and Espinoza 1989). The co-feeding of those olefins with syngas in the reaction mixture resulted in enhanced chain

growth which suggested that those olefins participate in the chain growth process by simultaneous bond fissions and formations; however, they are unlikely to propagate hydrocarbon synthesis alone (Snel 1989b). In agreement with the previous findings, (Patzlaff et al. 1999a) affirmed that ethylene can start chain growth and can also be inserted into growing chains, while 1-hexene initiates chain growing but with a lower probability than that of the chains directly formed by synthesis. Olefins up to C_{13} were found to incorporate in the chain growth process, however they were more likely to undergo hydrogenation to paraffins than to initiate a new chain (Puskas et al. 1993). The deviation of the product distributions in gas-phase FTS within the region of light hydrocarbons C_2-C_5 (Figure 5.7) can be attributed to the high readsorption ability of those lower alkenes and their incorporation in the chain growth process. The dip of the product distribution below the linear ASF behavior at C_2 can be attributed to the very rapid conversion of adsorbed C_2 molecules to active species. The extremely active C_2 molecule is believed to strongly compete with the adsorbed-H_2 molecules for available species which both can react. Also because of its lower heat of adsorption, ethene can desorb and adsorb more frequently than the other light α-olefins which make it the most mobile of the primary products (Snel 1989a). Generally, the ability of α-olefins to incorporate in the chain growth process in conventional FTS process decreases with carbon number (i.e. C_2>C_3>C_4 etc.).

5.3.4 Hydrocarbon distribution under near-critical and supercritical hexane FTS

The unusual trend of the product distributions (Figure 5.8) in supercritical hexane phase FTS was followed over a broad range of reaction conditions. By tuning either the

reaction temperature or pressure (as shown in Figure 5.4) we were able to shift the process from near-critical conditions to supercritical conditions and from gas-like density to liquid-like density.

Effect of temperature on hydrocarbon distribution. Figure 5.9a shows the product distributions at reaction temperature T_1 (230 °C). Under such conditions, the reaction mixture is more likely a compressed liquid phase according to the measured critical properties illustrated in Figure 5.4. The overall hydrocarbon distribution followed closely the ASF model with $\alpha_{overall}$ of 0.809 where slight deviations are observed in the light hydrocarbons (C_2-C_4) range. Increasing the temperature to T_2 (240 °C), whereby the reaction mixture is maintained near the critical point, the overall chain growth probability dropped to 0.776 as shown in Figure 5.9*b*. The product distributions in Figure 5.9b follow closely the ASF model in middle distillate and heavy hydrocarbons range whereas marked deviations are observed in the light hydrocarbon range. As shown in Figure 5.9b the deviations extend to C_8 (i.e. deviations are in the range of C_2-C_8). Surprisingly, upon increasing the temperature to T_3 (250 °C) (well within the supercritical region) no drop in the chain growth probability of heavy hydrocarbons (α_{hp} = 0.781) was observed despite the increase in the reaction temperature. In addition, the region of deviation from the ASF model extended up to C_{14} (i.e. deviation range from C_2-C_{14}) as shown in Figure 5.9c. The distribution in both the light hydrocarbons (excluding C_1) and middle distillates range yield very high α-values. A further increase in temperature resulting in a gas-like density (T_4 of 260 °C) resulted in a drastic drop in the chain growth probability ($\alpha_{overall}$ = 0.663) as shown in Figure 5.9*d*. The overall product distribution of hydrocarbons up to C_{20}

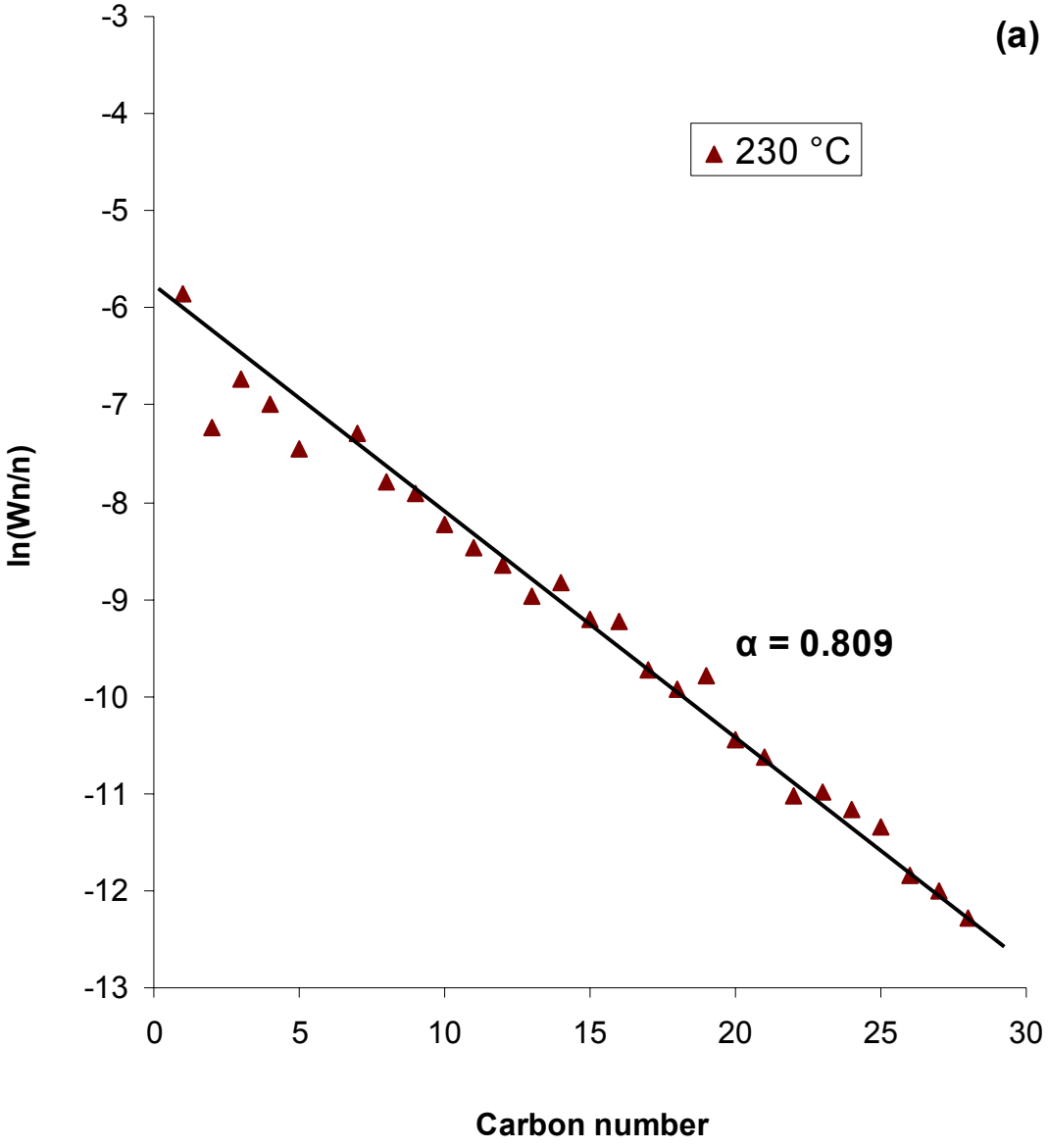

Figure 5.9a Hydrocarbon product distribution from SCH-FTS at 65 bar and T_1= 230 °C. Reaction conditions; 50 sccm/ g_{cat} syngas flowrate, 1.0 mL/min hexane flow rate, and H_2/CO feed ratio = 2.

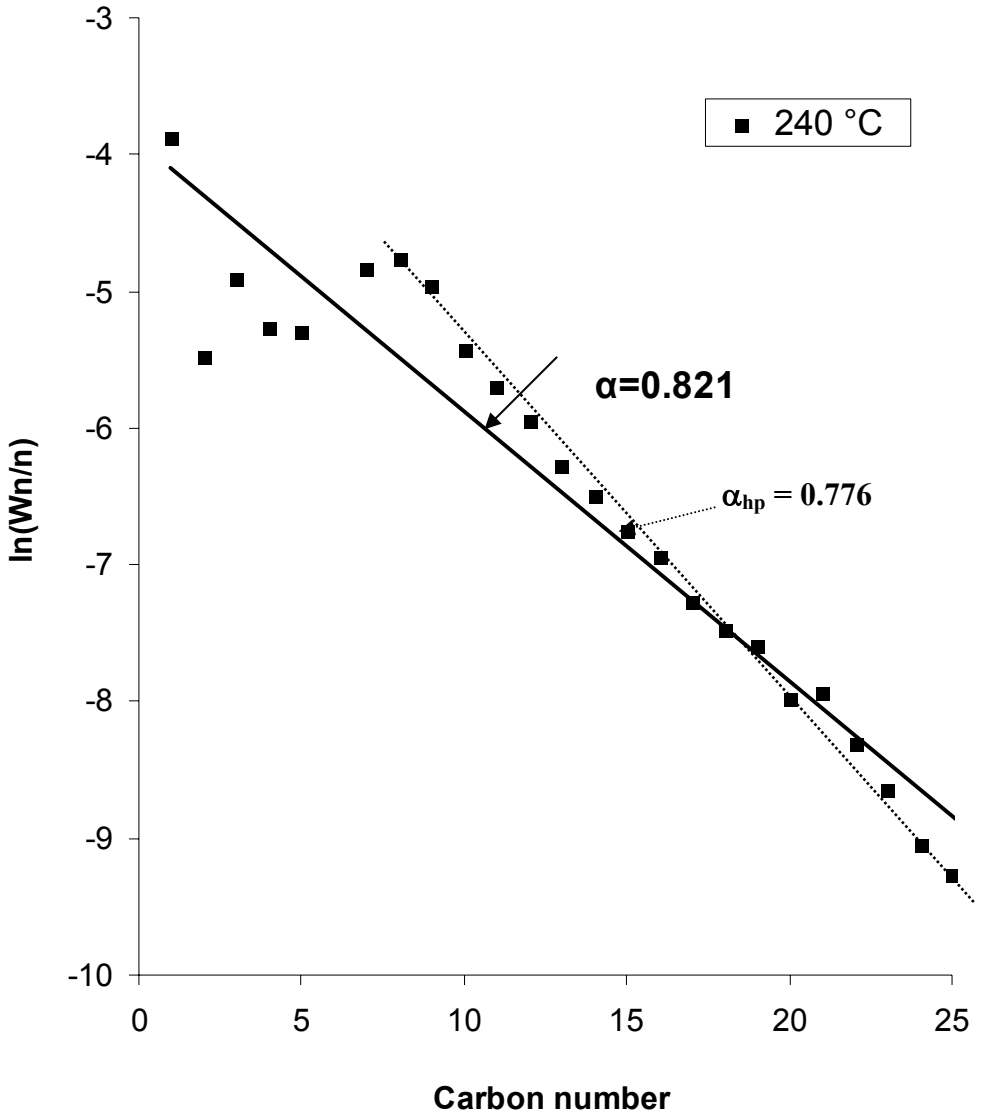

Figure 5.9b Hydrocarbon product distribution from SCH-FTS at 65 bar and T_2= 240 °C. Reaction conditions; 50 sccm/ g_{cat} syngas flowrate, 1.0 mL/min hexane flow rate, and H_2/CO feed ratio = 2.

followed closely the ASF model, while only very slight deviation in C_2 selectivity is shown in the product distribution at this elevated temperature.

The influence of temperature on the performance of FTS reaction is extremely complex. It has a direct influence on both the kinetics (including all reaction rates) and the chain growth mechanism. Primary reactions, secondary reactions (hydrogenations and isomerizations), and chain termination rates are strongly influenced by the reaction temperature. Furthermore, physical properties that control the rate of reaction, such as diffusion, are dependent on the temperature (Hurlbut et al. 1996). The effect of increasing the reaction temperature on FTS operation involves the enhancement of the reactant consumption rates and primary reactions that result in higher activity and better selectivity towards certain products (light hydrocarbons and gasoline fractions). On the other hand, high temperature operation can enhance secondary reaction rates and other side reactions (methanation and CO_2 formation), which negatively affect the overall performance of the FTS process. The major challenge in designing an operation scheme is to finely balance those influences. In this study, the influence of the reaction temperature on the chain-growth mechanism of SCH-FTS (Figure 5.9a-d) was evaluated at constant pressure, space velocity, and gas feed composition (H_2/CO ratio of 2/1). The dramatic changes in hydrocarbon product distributions with variations in temperature can be largely attributed to the impact of density-dependent properties of the solvent rather than to the direct influence of temperature on kinetics and reaction rates (Huang et al. 2004). Our findings show that lower reaction temperatures favor the production of heavy hydrocarbons with linear dependence of the hydrocarbon selectivities on carbon number. Despite the fact that increasing the temperature results in higher termination rates and

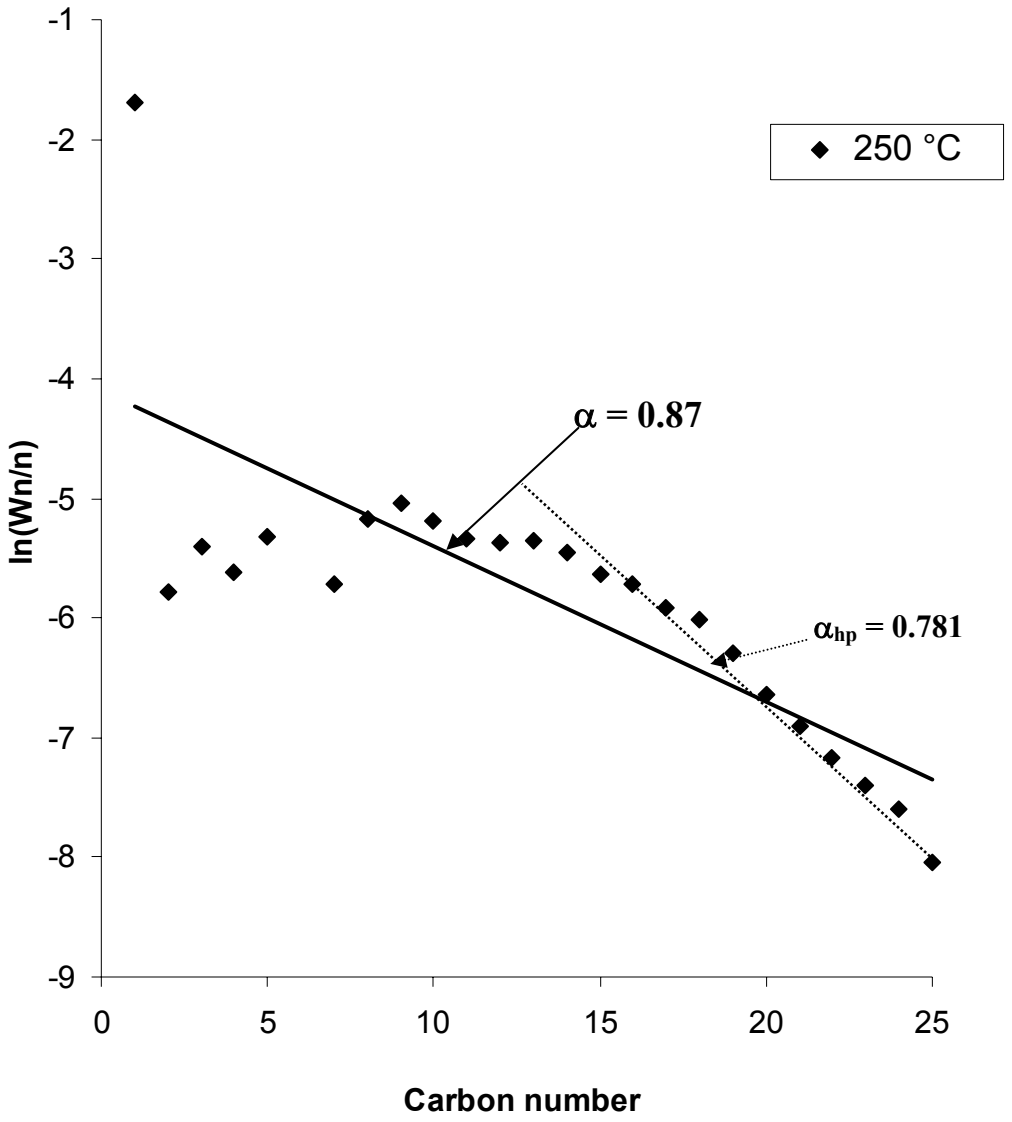

Figure 5.9c Hydrocarbon product distribution from SCH-FTS at 65 bar and T_3= 250 °C. Reaction conditions; 50 sccm/ g_{cat} syngas flowrate, 1.0 mL/min hexane flow rate, and H_2/CO feed ratio = 2.

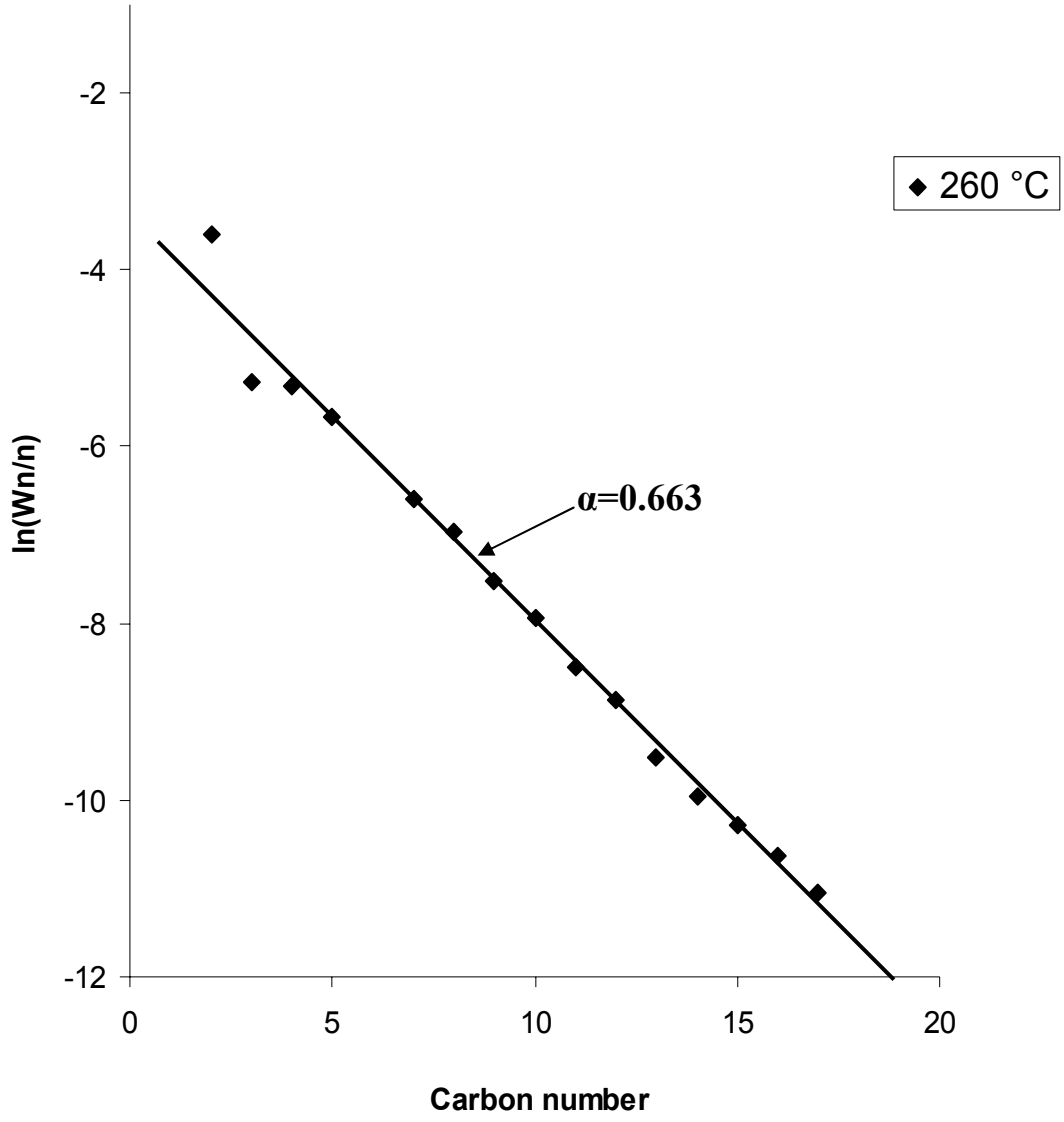

Figure 5.9d Hydrocarbon product distribution from SCH-FTS at 65 bar and T_4= 260 °C. Reaction conditions; 50 sccm/ g_{cat} syngas flowrate, 1.0 mL/min hexane flow rate, and H_2/CO feed ratio = 2.

secondary reaction rates (Kellner and Bell 1981), our findings show that in SCH-FTS the overall chain growth probability ($\alpha_{overall}$) shows an optimum value at 250 °C (see Figure 5.5). Nevertheless, the heavy products chain growth probability (α_{hp}) agrees well with the Kellener and Bell hypothesis (Kellner and Bell 1981) since it is found to decrease as the temperature increases. This in harmony with the findings of Pelsuo, et al for cobalt catalytic systems which showed that the increase in temperature leads to an increase in selectivity for methane, C_2–C_4 and C_5– C_9 while the C_{10}–C_{20}, and C_{21}^+ fractions were reduced (Peluso et al. 2001). Furthermore, deviations from the ASF model in the light hydrocarbon and middle distillate hydrocarbon ranges are found to be affected by changes in the reaction medium (solvent medium) environment ranging from compressed liquid to near-critical to supercritical conditions. Nevertheless, at the highest temperature of 260 °C, where the density is closest to gas-like medium, the influence of density-dependent properties are likely outweighed by the impact of temperature on the kinetics of undesired reaction rates (methanation, hydrogenation, and water gas shift reactions). This yields a low chain growth probability at 260 °C and a hydrocarbon product distribution that follows the standard ASF model very well.

The use of reaction temperature as a tool to selectively control FTS hydrocarbon distribution in fixed bed reactors (gas-phase) and slurry reactors (liquid-phase) has been accounted for by many studies (Sasol's low-temperature-Fischer-Tropsch (LTFT), and high-temperature Fischer-Tropsch (HTFT)) (Jager and Espinoza 1995; Espinoza et al. 1999; Steynberg et al. 1999). However, the observed deviations in hydrocarbon distribution (particularly middle distillates) as a result of changes in temperatures in the

near-critical and supercritical regions require further investigations on the kinetics and the chain growth mechanism under SCF solvent conditions.

Effect of pressure on hydrocarbon distribution. The influence of reaction pressure on the hydrocarbon distribution was also studied according to the scenario illustrated in Figure 5.4. At a pressure lower than the critical pressure of the reaction mixture (P_1 =35 bar), and in the region of gas-like density, the overall distribution favors the productions of heavy hydrocarbons with high chain growth probability (α_{hp} = 0.85) as illustrated in Figure 5.10a. Significant deviations from the ASF model are observed in the middle hydrocarbons range (C_2-C_8). Increasing the pressure to P_2 (50 bar), within the supercritical phase region, resulted in a significant drop in heavy hydrocarbon production (α_{hp} = 0.78), with deviations from the standard ASF model also extending to C_{10} as shown in Figure 5.10b. In the same figure, we can also see that there is a high chain growth probability in both the light and middle distillate hydrocarbon range. As discussed earlier (Figure 5.9c), under the baseline conditions of 65 and 250 °C the deviations from ASF extended to C_{14}, while the heavy hydrocarbons chain growth probability slightly decreases to 0.78. Upon increasing the pressure to 80 bar (liquid-like density), no significant change in heavy hydrocarbons chain growth probability was observed (α_{hp} = 0.80), however the deviations from ASF in the product distributions are extended to C_{16} as shown in Figure 5.10*c*. This illustrates extremely high chain growth probability in the C_5-C_{16} range at this high density.

At constant temperature (250 °C), and syngas (H_2/CO) feed ratio of 2/1 flowing at 50 sccm/g_{cat}, we have studied the product distribution in SCH-FTS over broad range of

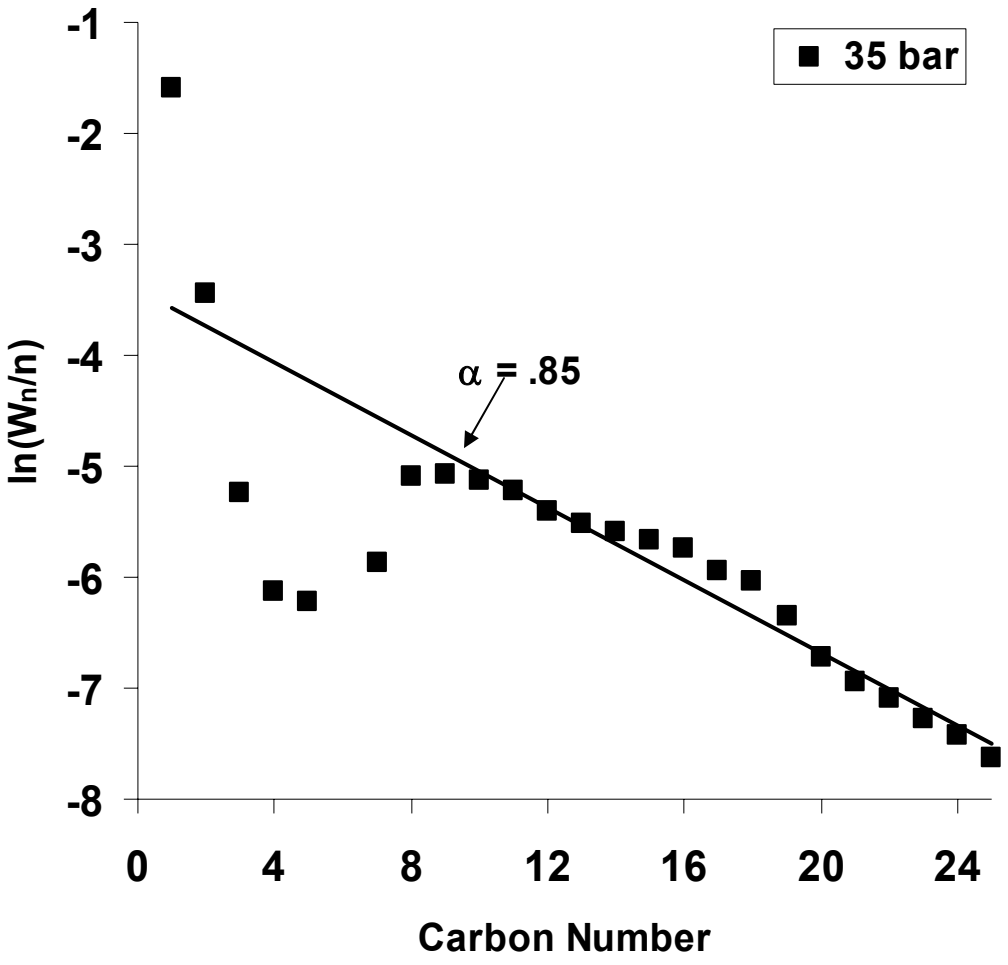

Figure 5.10a Hydrocarbon product distributions in SCH-FTS reaction at 250 °C and P_1= 35 bar. Reaction conditions; 50 sccm/g_{cat} syngas flowrate, 1.0 mL/min hexane flow rate, and H_2/CO feed ratio = 2.

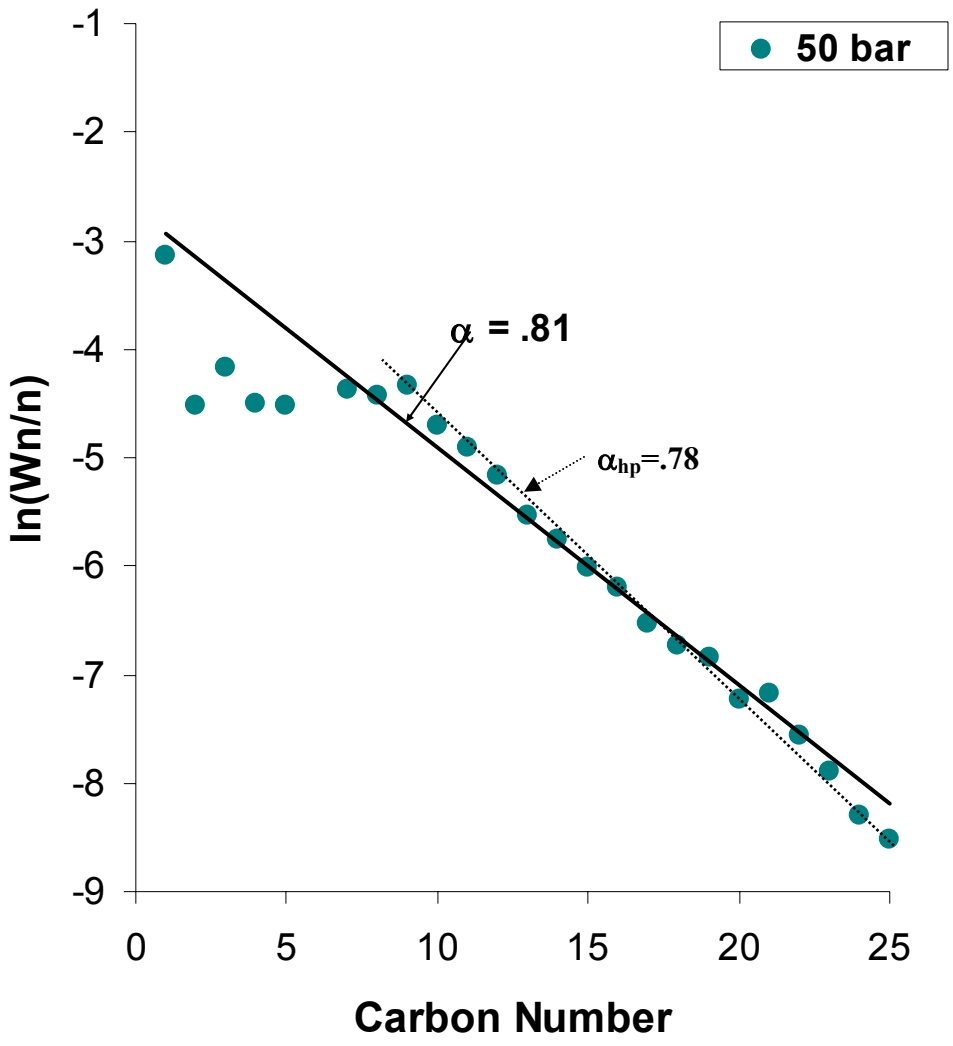

Figure 5.10b Hydrocarbon product distributions in SCH-FTS reaction at 250 °C and P_2=50 bar. Reaction conditions; 50 sccm/g_{cat} syngas flowrate, 1.0 mL/min hexane flow rate, and H_2/CO feed ratio = 2.

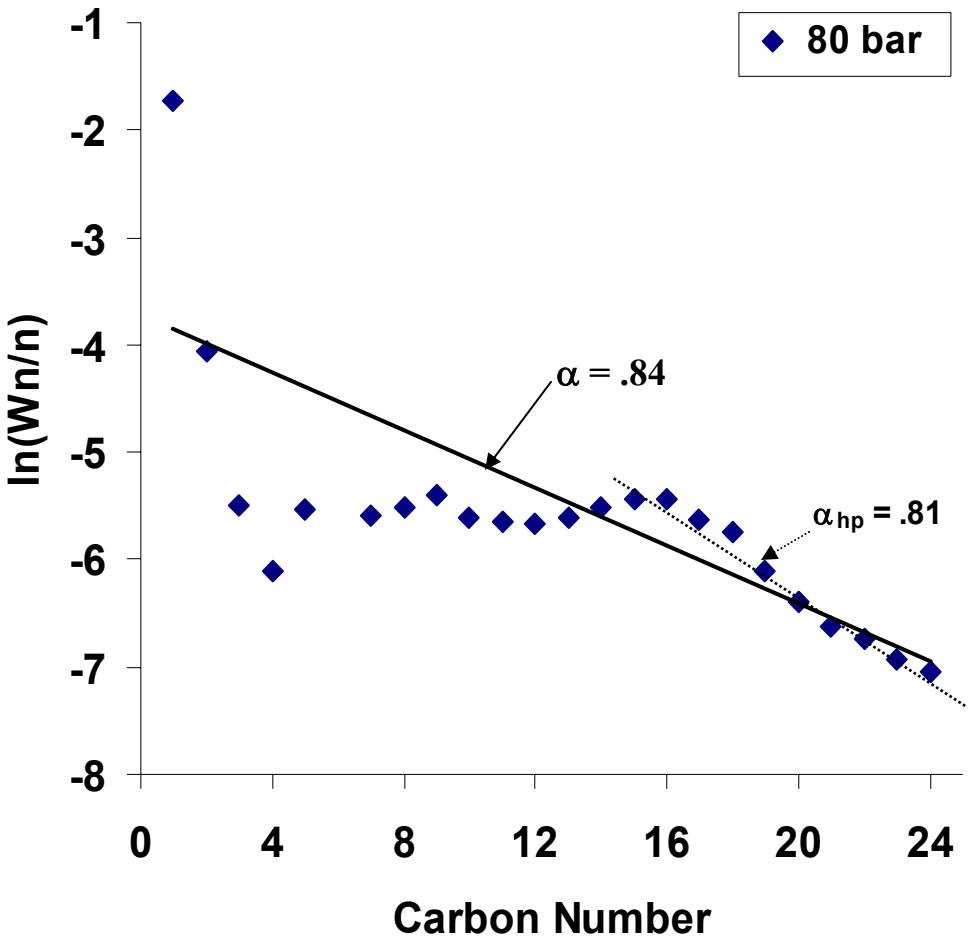

Figure 10c Hydrocarbon product distributions in SCH-FTS reaction at 250 °C and P_3=80 bar. Reaction conditions; 50 sccm/g_{cat} syngas flowrate, 1.0 mL/min hexane flow rate, and H_2/CO feed ratio = 2.

pressures (35-80 bar). It is important to mention here that the partial pressure of syngas was kept constant at 20 bar, while the hexane partial pressure was varied to achieve the desired total pressure. The bed residence time (defined as the volume of feed at the applied pressure passing through the volume of the catalyst bed per second) was changed as a result of varying the total pressure. Predictions of the bed residence times at the conditions studied were performed based on density calculations at the specified temperature and pressure for a mixture composed of 75 mol% hexane, 16.7 mol% H_2, and 8.3 mol% CO. The density of this mixture was determined using the Peng-Robinson equation of state (with $k_{ij} = 0$) in a flash calculation in ICAS Version V software. The volumetric flow rate of the mixture was then obtained from the multiplication of the density with the total molar flowrate (hexane and syngas). Finally, the contact time was estimated by dividing the volume of the catalyst bed by the volumetric flowrate. The contact times were found to vary from 5.3s at 35 bar, 12.1s at 65, to 15.7s at 80 bar. The overall product distribution ($\alpha_{overall}$) and heavy product distribution (α_{hp}) was found to be less affected by the total pressure in the range of 50 bar to 80 bar. However significant changes with regards to the deviation from the ASF model within the middle distillate hydrocarbons are observed as the pressure increases from the gas-like density range (35 bar) to the liquid-like density range (80 bar). It is well known that space velocity has no significant affect on the chain growth probability (Snel 1989a). However, the bed residence time was found to have a pronounced impact on α-value and the non-ASF distribution by enhancing α-olefins readsorption and thus their incorporation in the chain growth process (Iglesia 1997a). The bed-residence time (affected by the total pressure) is believed to influence the dynamic adsorption/desorption equilibrium of the FTS primary

products (mainly α-olefins) allowing higher probability towards the readsorption process. Besides the bed residence time, catalyst type, reactant feed ratio, and properties of the FTS reaction medium would also affect the dynamic adsorption/desorption process. Our suggestion is that the later factor plays the major role when the FTS reaction is conducted in the supercritical-phase. The supercritical solvent phase offers two advantages for FTS over the conventional media; single phase operation, as well as, high solubility of the heavy hydrocarbon products in the solvent resulting in enhanced in situ extraction (Subramaniam 2001; Jacobs et al. 2003).

Unfortunately, most of the well developed models and experimental evaluations of product distributions, selectivity and activity of cobalt catalytic systems in FTS reaction have not covered such high pressure operation in the presence of a solvent (Sarup and Wojciechowski 1988; Iglesia et al. 1992; Van Berge and Everson 1997). Under such high pressure operation, classical chain-growth models can not satisfactorily predict the product distribution in FTS reactions and explain deviations from the ASF model, since even the activation and deactivations of FTS catalytic systems are significantly different from that under conventional operation (Davis 2003c).

5.3.5 Enhanced α-Olefin Incorporation Model

Reaction Network

Figure 5.11 shows our proposed reaction pathway for the FTS reaction in supercritical phase. In the first stage, adsorption and disassociation of CO and H_2 take place on a cobalt catalyst active site. The removal of surface oxygen steps represented by the formation of water and CO_2 is shown in the second stage. The postulation of oxygen

removal was based on the modified (Kellner and Bell 1981) surface reaction model(Uner 1998). The hydrogenation of adsorbed carbon and the formation of oligmers are included in the third stage. The rate of alkyl (CH_3.S) formation and termination to methane by hydrogenation of the monomers are included in the fourth and fifth stages. The corresponding rates for each of the reactions illustrated in Figure 5.11 are beyond the scope of the current study and are covered in a separate chapter (Chapter 6 and (Elbashir and Roberts 2004b)). The scheme of this reaction network is illustrated by stage six and seven as shown in Figure 5.11. The classical route of a alkyl group (R_n) propagation over an active site *S* consists of the primary reaction to produce olefins that can then readsorb to the same active site or another vacant S^*, that has the same characteristics of *S*. Termination takes place whenever secondary reactions are favored yielding paraffins or isomers. The increased availability of S^* is attributed to operation under near-critical and supercritical conditions that facilitates the incorporation of desorbed olefins into the chain growth process (Elbashir and Roberts 2004b).

Model features and assumptions

A typical product distribution for SCH-FTS over the alumina supported cobalt catalyst was used as representation for the enhanced olefin incorporation model (Figure 5.12a and 5.12b). The model assumes that from the primary products only olefins have the capability of readsorbing and incorporating in the chain growth process. Paraffins are primary products of the synthesis and it can also be a product of olefins hydrogenation. We also neglected hydrogenolysis, isomerization, and oxygenation routes. Even though, such an assumption represents simplification to the complex routes of the FTS network, it

(1) Reactant dissociation and chemisorption on the active site (*S*)

$$H_2 + 2S \overset{K_H}{\Leftrightarrow} 2H.S$$

$$CO + S \overset{K_{CO1}}{\Leftrightarrow} CO.S$$

$$CO.S + S \overset{K_{CO2}}{\Leftrightarrow} C.S + O.S$$

(2) Oxygen removal

$$O.S + H.S \overset{K_{O1}}{\Leftrightarrow} OH.S + S$$

$$OH.S + H.S \overset{K_{O2}}{\Rightarrow} H_2O + 2S$$

$$CO.S + O.S \overset{K_{O3}}{\Rightarrow} CO_2 + 2S$$

(3) Monomer formation

$$C.S + H.S \overset{K_{C1}}{\Leftrightarrow} CH.S + S$$

$$CH.S + H.S \overset{K_{C2}}{\Leftrightarrow} CH_2.S + S$$

$$CH_2.S + H.S \overset{K_{C3}}{\Leftrightarrow} S + CH_3.S$$

(4) Termination to methane

$$CH_3.S + H.S \overset{K_{C4}}{\Rightarrow} CH_4 + 2S$$

(5) Chain growth & termination sequences

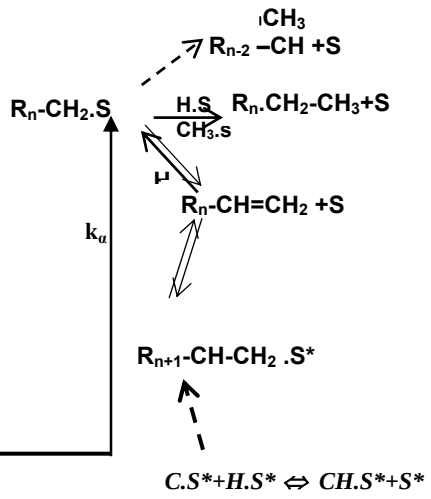

(6) Enhanced activity & olefin incorporation in SCH

Figure 5.11 FTS reaction network including the enhanced activity and olefin incorporation sites.

agrees with our experimental observation for SCH-FTS that shown in Figure 5.2a. As shown in Figure 5.12b, the first point in the curve represents the methane selectivity (which we referred to as *methanation*). The light hydrocarbons (C_2-C_5) selectivity region is defined as the *regular olefin incorporation* range. Those hydrocarbons can participate in the propagation thereby decreasing their concentrations in the synthesis. Such a route will be particularly favored under high pressure operations (Snel 1989a).

Before proceeding in explaining the mechanism described in stages six and seven, we will discuss the role of adsorption/desorption equilibrium in FTS reactions. Figure 5.13 illustrates a general sequence chain growth simulated by a chain consists of three carbon molecules on the surface cobalt catalyst. The primary product butene (C_4H_8) that is attached to the active site could either be readsorbed to the same active site or to another active site which is evacuated due to the enhanced solubility in supercritical hexane solvent. The readsorbed molecule would participate in the chain growth process by initiating a new chain, or propagating as a part of a growing chain. As shown in Figure 5.13 it could either desorbed as an olefin product or go through secondary reaction such as hydrogenation to paraffin (butane C_4H_{10}) or isomerization to give C_4 isomers. As a result, the dynamic adsorption/desorption equilibrium (between steps **A** and **B**) controls the incorporation of C_4H_8 molecule in the chain growth process specifically when such balance tends toward the desorption route. Secondary products (e.g. paraffins and isomers) terminate the propagation process and desorb to the bulk fluid as products. It is important to mention that the secondary reactions but not the primary reactions are influenced by changes in the space velocity and residence time (Madon et al. 1991) caused by varying the pressure of the SCH-FTS operation. Therefore, we believe that the

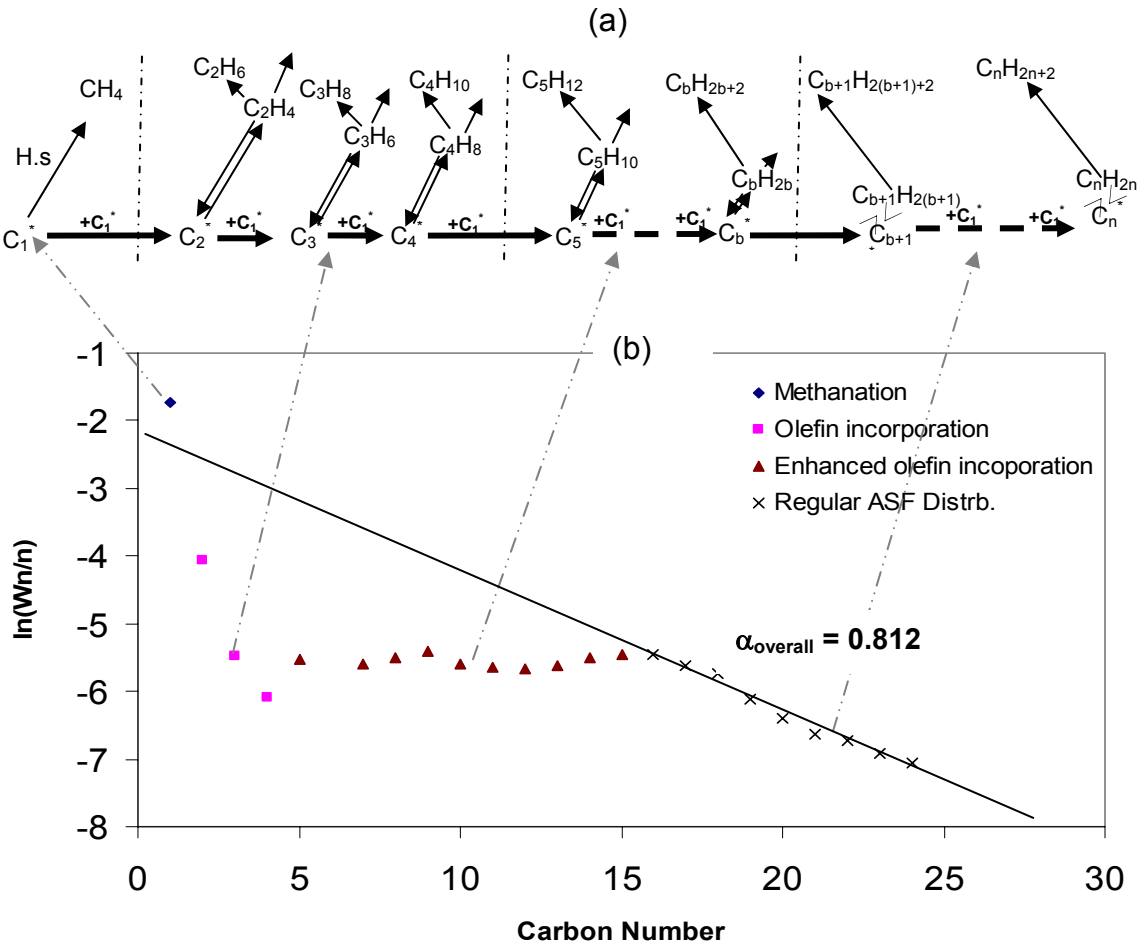

Figure 5.12 (a) Description of the chain growth process in the enhanced-olefin-incorporation model in SCH-FTS starting with methanation and ending with the heaviest hydrocarbon detected under the specific reaction conditions. (b) Typical product distribution curve in SCH-FTS including all regions defined in the chain growth process above.

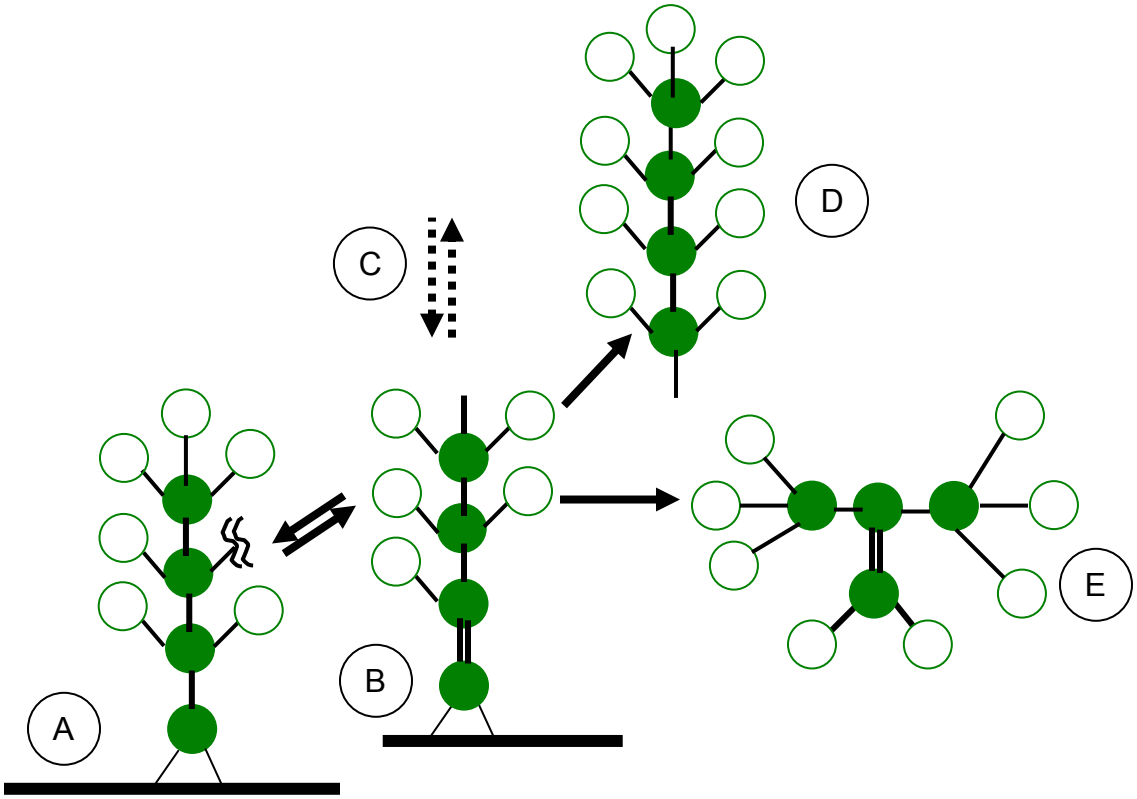

Figure 5.13 Simulated in situ chain-growth pathway for a primary product α-olefin (C_4H_8) inside a cobalt catalyst pore. Closed circles represent carbon atoms and open circles represent hydrogen atoms.

enhanced solubility of the hydrocarbon products in the solvent combined with single phase operation impacts the enhanced chain growth observed in SCH-FTS. Such an environment would suppress secondary reactions routes by enhancing readsorption of those olefins on either the same active site or on another site evacuated due to the enhanced solubility the hydrocarbon products in SCH. The scheme of this reaction network is illustrated by stage six and seven as shown in Figure 5.11. The classical route of a alkyl group (R_n) propagation over an active site *S* consists of the primary reaction to produce olefins that can then readsorb to the same active site or another vacant S^*, that has the same characteristics of *S*. Termination takes place whenever secondary reactions are favored yielding paraffins or isomers. The increased availability of S^* is attributed to operation under near-critical and supercritical conditions that facilitates the incorporation of desorbed olefins into the chain growth process (Elbashir and Roberts 2004b).

Our proposal introduces the *enhanced olefin incorporation* range as a unique contribution of the influence of the near-critical and supercritical solvent (hexane) on the FTS chain growth process (see Figure 5.12a and b). The incorporation of olefins from C_7-C_b (where b represents the carbon number where deviation from linear ASF model no longer exists and the product distributions beyond that carbon number follows the ASF model; see Figure 5.12b) is attributed to the enhanced solubility of primary products in the single phase near-critical and supercritical which affects the adsorption/desorption equilibrium of those species. C_6 hydrocarbons have not been included in the above range due to inability to accurately measure the amounts of C_6 hydrocarbons produced from that of the hexane solvent. As such, the overall chain growth probability ($\alpha_{overall}$) under SCH-FTS is higher than that under gas-phase operation. The chain-growth probability within

this region is very high (α_{md}>0.95). The last region in Figure 5.12b is the regular ASF distribution in the heavy hydrocarbon range. The rate of incorporation of those hydrocarbons in the chain growth process is much lower than the synthesis rate. The overall chain growth probability can be determined more accurately from the slope of the curve at the heavy hydrocarbons distributions since it fits very well with the regular ASF distribution.

The overall scheme of the chain growth network mechanism in SCH-FTS is described in Figure 5.12*a*. This sequence can either take place on the active site *S* or on the evacuated active site S^* on the cobalt catalyst surface. The methanation reaction or the hydrogenation of the monomer (building block, C_1^*) represents the first product in the chain growth sequence. Methane is the only saturated product and it's not a part of the general sequence of FTS chain growth process. Methane selectivity is neither predictable by the ASF model (Puskas et al. 1993) nor the enhanced-olefin incorporation model over the cobalt catalyst. In the olefin incorporation range, readsorbed ethene is then rapidly converted to C_2^* that has similar characteristics of the building block C_1^* produced from the initial hydrogenation of adsorbed carbon molecules. As the C_2^* molecule competes strongly with H_2 for the catalyst active site, the readsorption sequence is more favored than the termination of the chain to ethane. This ability of lower alkenes (C_2-C_5) to readsorb and incorporate is mainly influenced by the characteristics of cobalt catalyst and less affected by the reaction medium (Smith et al. 1930). The incorporation capability decreases with increasing carbon number while hydrogenation increases. In the enhanced olefin incorporation region, the incorporation mobility of the middle distillate olefins is enhanced in SCH-FTS. The tendency towards incorporation in the chain growth process

by inserting into a growing chain of the middle distillate hydrocarbons decreases with carbon number. This trend suggests that either the termination rate to olefinic compounds or the readsorption rate to the active site must be higher than the termination rates to paraffin compounds in both the regular incorporation and enhanced incorporation ranges. This hypothesis is strongly supported by experimental findings of olefin/paraffin ratios and olefin selectivity in the supercritical phase compared to the conventional FTS operations (Fan et al. 1992; Bukur et al. 1997; Fan and Fujimoto 1999; Huang and Roberts 2003; Jacobs et al. 2003). However, in the heavy hydrocarbon range where the distribution follows the regular ASF mode, the hydrogenation rates to paraffinic compounds are much higher than termination rates to olefins or incorporation rates. As an example, only paraffinic compounds are measured in our products beyond C_{18}. These results are in a good agreement with previous experimental findings where even at high carbon number olefins can incorporate into the chain growth however they are more likely to hydrogenate than either initiate a new or insert in a growing chain (Puskas et al. 1993).

Figure 5.14 illustrates that the deviations from the ASF model were shown in both the distributions of olefinic and paraffinic compounds, especially in the middle distillate product range (enhanced olefin incorporation range). This is a surprising phenomenon since it is well known that while olefinic compound distributions deviate from the ASF model due to their incorporation into the chain growth process, paraffin compound distributions typically follow ASF model distribution (Snel 1989a). We attributed this to the suppression of the termination routes by secondary reactions (specifically hydrogenation) of the primary products in the enhanced incorporation range due to the

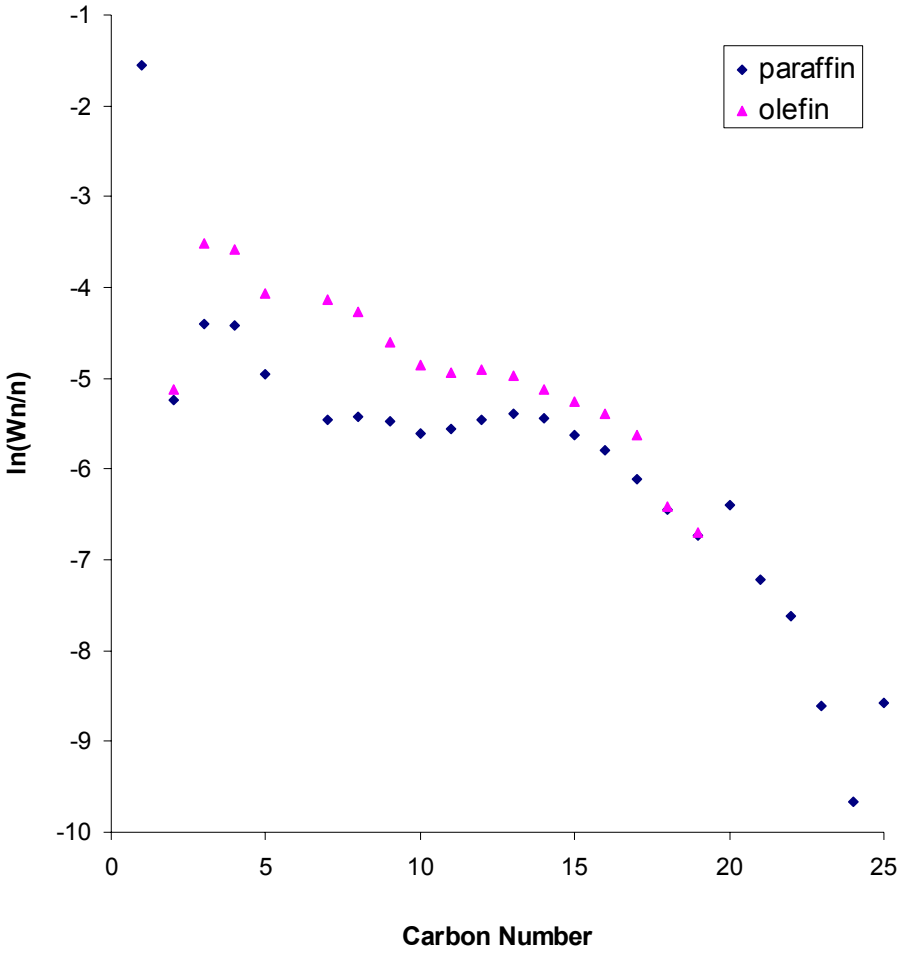

Figure 5.14 Distributions of olefinic and paraffinic compounds in SCH-FTS at 250 °C and 65 bar with syngas flowrate of 50 sccm/g_{cat}, hexane flowrate of 1.0 mL/min, and H_2/CO feed ratio of 2.

enhanced availability of readsorption sites in the supercritical phase. Thus, the paraffin compounds produced follow the same trend as that of the primary product of the synthesis (olefinic compounds), however with lower selectivity. This concurs with the chain growth scheme presented earlier in Figure 5.12*a*. Nevertheless, at mild operation temperatures (260 °C) whereby the medium is of gas-like density both olefinic products and paraffinic products followed ASF with higher probability of olefinic products only in the light hydrocarbons range (Figure 5.15).

5.4 Summary and Conclusions

The analytical investigations presented in this study demonstrates significant deviations of the hydrocarbon distributions from the ASF model when the FTS reaction is conducted in a near-critical and supercritical hexane medium over an alumina supported cobalt catalyst. The degree of these deviations from the standard ASF model was found to be related to the physical properties of the reaction mixture as the medium is shifted from near-critical conditions to supercritical conditions by simply tuning the reaction temperature and pressure. The in situ properties of the reaction mixture under the supercritical phase operation were evaluated by measuring the critical properties of a sample collected directly from the outlet of the reactor using a custom high pressure variable volume view cell apparatus. The region of single phase operation for the FTS mixture was determined by measuring the critical properties of this sample.

Rather than a single chain growth probability (α-value) for the product distribution as in the standard ASF model, three distinct chain growth probabilities (α_{lh}, α_{md}, and α_{hp}) are required to accurately represent the product distributions obtained in the

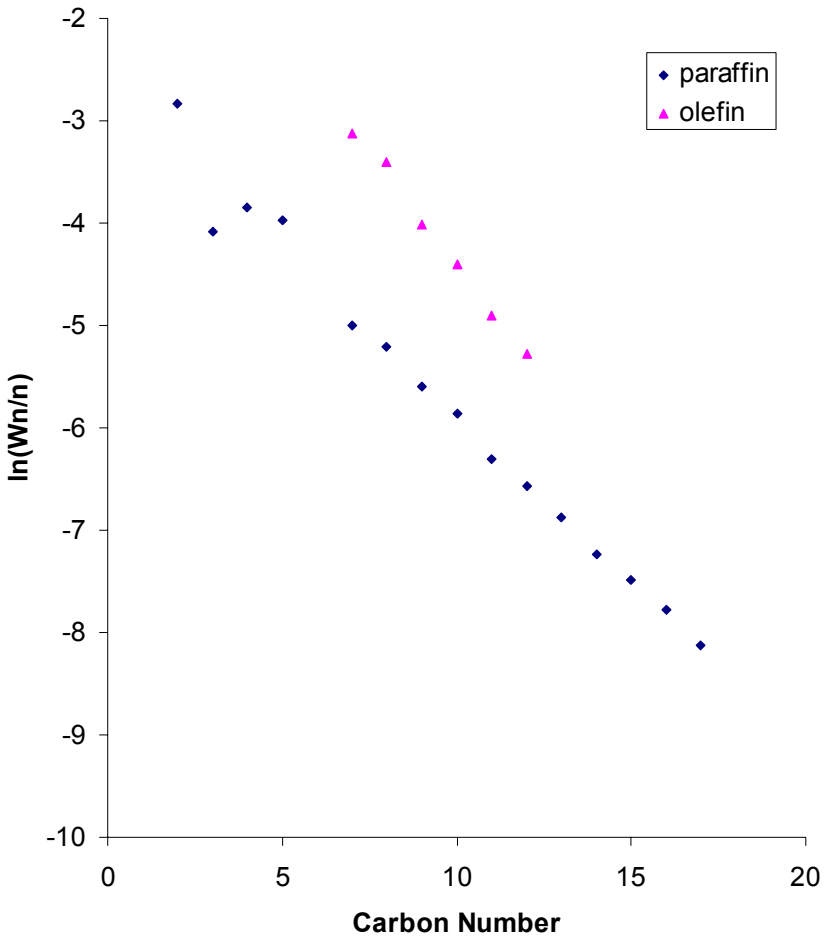

Figure 5.15 Distributions of olefinic and paraffinic compounds in SCH-FTS at 260 °C, and 65 bar with syngas flowrate of 50 sccm/g_{cat}, hexane flowrate of 1.0 mL/min, and H_2/CO feed ratio of 2.

SCH environment. Multiple chain-growth probabilities of the FTS product distributions are not the innovation of this study, since numerous studies have reported the existence of more than one α-value in certain FTS product distributions. Nonetheless, this study reports an interesting phenomenon within the middle hydrocarbon product range of the distributions indicating a unique deviation from ASF behavior with a relatively very high α-value (α_{md} = 0.95) owing to enhanced incorporation of olefins in the SCH medium. The extent to which the middle distillate compounds incorporate in the chain growth and hence deviate from standard ASF is strongly related to the physical properties of the reaction mixture (gas-like properties vs. liquid-like properties) under the specified reaction temperature and pressure. This phenomenon is attributed to the enhanced solubility of heavy products in the dense medium yielding vacant sites made available by supercritical solvent phase. Such an environment has a significant impact on the dynamic adsorption/desorption equilibrium of active species inside the catalyst pores. It also enhances the adsorption rates of olefins within light and middle hydrocarbon ranges and hence increases the possibility for their incorporation in the chain-growth process. However, upon extremely high temperature operation (≥260 °C), whereby the thermophysical properties of the mixture are gas-like, the product distribution follows the standard ASF model. This also indicates that the influence of temperature on the kinetics and different reaction rates is more important than its influence through thermophysical properties of the reaction mixture.

An enhanced-olefin incorporation model for FTS in SCH including a synthesis pathway and chain growth mechanism is suggested to provide explanation for deviations of the middle hydrocarbon products from the standard ASF product distribution trend.

The development of this model takes advantage of the wealth of information accumulated in the literature and is in a good agreement with our experimental observations over a broad range of operating conditions.

CHAPTER 6

REACTION PATHWAY AND KINETIC MODELING OF FISCHER-TROPSCH SYNTHESIS OVER AN ALUMINA SUPPORTED COBALT CATALYST IN SUPERCRITICAL-HEXANE

6.1 Introduction

Conducting Fischer-Tropsch synthesis (FTS) under supercritical fluid (SCF) solvent conditions affords unique opportunities to manipulate the Fischer-Tropsch reaction environment by enhancing the production of liquid fuels and value-added chemicals (such as α-olefins) from syngas. The enhanced performance compared to conventional FTS operation is attributed to several factors including; the in situ extraction of heavy hydrocarbons from the catalyst resulting from high solubility in the supercritical phase (Yokota et al. 1990; Bochniak and Subramaniam 1998; Jacobs et al. 2003), and elimination of interphase transport limitations thus promoting reaction pathways toward the desired products (Bochniak and Subramaniam 1998; Elbashir and Roberts 2004a). These significant improvements can be optimized by manipulating the density of the medium by simply tuning the pressure and temperature of the reaction system. This illustrates the importance of simultaneous evaluation of the influence of both temperature

and pressure on reaction kinetics, chain growth, and solvent/reactant/product phase behavior in supercritical phase FTS.

A few studies have presented kinetic modeling of the FTS reaction in SCF media (Fan et al. 1992; Bochniak and Subramaniam 1998). The proposed FTS reaction rates in the SCF media were based on the power law kinetics for the carbon monoxide consumption rates. Fujimoto and coworkers (Fan et al. 1992) suggest a power law rate that is first order in H_2 partial pressure for the FTS reaction in supercritical hexane. Based on this model they were able to calculate the apparent rate constant for each catalyst (of different pore diameter and size) and to define the catalyst effectiveness factor as the ratio between the rates of reaction in the supercritical fluid to that in gas-phase. An explanation for the increase in syngas conversion with reaction pressure in a supercritical fluid medium was provided by Subramaniam and coworker (Bochniak and Subramaniam 1998). They employed a general stoichiometric equation for FTS reaction to derive an effectiveness factor that is a function of the total pressure. The syngas conversion was then defined as pseudo first order in H_2 partial pressure.

In the present study we are reporting the development of a kinetic model for FTS reaction over a commercial 15% Co/ Al_2O_3 catalyst that will be used to predict CO consumption rates and CH_4 formation rates in both gas phase and supercritical fluid hexane (SCH) phase. Comparison between the model results and our experimental data in both gas phase and SCH reveals that conventional reaction pathways are not sufficient to predict the performance of the cobalt catalyst under supercritical hexane operation while accurately modeling gas phase FTS. Modifications to conventional FTS models are suggested to incorporate the role of the SCF medium on the FTS process.

6.2 Experimental

6.2.1 Reaction system

The FTS reaction over a commercial 15% Co/Al_2O_3 catalyst (purchased from United Catalysts Co.) in supercritical hexane was carried out in our high-pressure FTS unit shown in Figure 3.1. A more detailed description of the unit is given in Chapter 3, however a brief description will be provided here. Three certified cylinders of different ratios of H_2 and CO (1:2, 1:1, 2:1) with trace amount of N_2 as an internal standard for chromatographic analysis were purchased from Air Gas Co. The flow rate of the syngas reactants was controlled by digital mass flow controllers. The hexane solvent flow rate was controlled by an HPLC pump. The hexane/syngas molar ratio was fixed at 3/1 in all experiments. Before entering the reactor, the two streams (syngas and solvent) were mixed in a static mixer that was heated to the desired reaction temperature. The combined stream then entered the top of the down-flow H.I.P reactor (1.27 cm×25.4cm of effective volume: 32 cm^3) that was positioned in a temperature controller tube furnace controlled by an *ATS* temperature controller system. The temperature inside the reactor was measured at six equally distanced positions along the length of the reactor using a profile thermocouple. This allows tracing of the temperature distribution along the length of the reactor. The pressure in the reaction zone was controlled by a back pressure regulator BPR (Tescom Inc.) located between the reactor and a hot trap.

Analysis of reactants and products was carried out by two online GCs as described earlier in Section 3.2.3. The results from the two GCs were used for conversion and selectivity calculations (see Appendix A). A Varian 3300 GC with capillary column (DB-5) and a FID detector was used for the analysis of C_2-C_{40} hydrocarbons and

oxygenates. Analysis of permanent gases (H_2, CO, N_2, CH_4, CO_2, C_2H_4, and C_2H_6) was conducted by a Varian CP-3800 GC with a packed column (Hayesep-DB100/120) and TCD detector. The online injection of our samples to the two GCs was carried out by two automated six-way-valves.

The following FTS reaction conditions in SCH have been examined: syngas space velocity of 93.75-281.25 h^{-1}, temperature from 230 °C -260 °C, pressure from 40 bar -65 bar, and H_2/CO feed ratios from 0.5/1 to 2/1, with a hexane/syngas molar ratio of 3/1. The results are compared to conventional gas-phase FTS operation under similar conditions in the absence of hexane solvent.

6.3 Kinetic Model

Figure 6.1 shows our simplified reaction pathway for FTS largely based on the available kinetic models of cobalt catalysts in literature (Bell 1981; Kellner and Bell 1981; Sarup and Wojciechowski 1989a; Uner 1998). In the first stage, the molecular adsorption of CO with subsequent disassociation in addition to the dissociative adsorption of H_2 take place on a cobalt catalyst active site (*S*). The removal of surface oxygen as represented by water and CO_2 formation is seen in the second stage. The postulation of oxygen removal is based on the modified (Kellner and Bell 1981) surface reaction model that is used to account for the adsorbate mobility (Uner 1998). The hydrogenation of adsorbed carbon and the formation of oligmers are included in the third stage as well as the formation of monomer ($CH_2.S$) and the alkyl species ($CH_3.S$). Termination to methane is included in the fourth stage.

(1) Reactant dissociation and

chemisorption on the active site (*S*)

$$H_2 + 2S \overset{K_H}{\Leftrightarrow} 2H.S$$

$$CO + S \overset{K_{CO_1}}{\Leftrightarrow} CO.S$$

$$CO.S + S \overset{K_{CO_2}}{\Leftrightarrow} C.S + O.S$$

(2) Oxygen removal

$$O.S + H.S \overset{K_{O_1}}{\Leftrightarrow} OH.S + S$$

$$OH.S + H.S \overset{K_{O_2}}{\Rightarrow} H_2O + 2S$$

$$CO.S + O.S \overset{K_{O_3}}{\Rightarrow} CO_2 + 2S$$

(3) Monomer formation

$$C.S + H.S \overset{K_{C_1}}{\Leftrightarrow} CH.S + S$$

$$CH.S + H.S \overset{K_{C_2}}{\Leftrightarrow} CH_2.S + S$$

$$CH_2.S + H.S \overset{K_{C_3}}{\Leftrightarrow} S + CH_3.S$$

(4) Termination to methane

$$CH_3.S + H.S \overset{K_{C_4}}{\Rightarrow} CH_4 + 2S$$

Figure 6.1 FTS reaction network describe the surface reaction kinetic model for the synthesis of CO and H_2 to produce a monomer (CH_2.) and an alkyl group (CH_3.) needed for the growth process. The model also includes an oxygen removal step for the production of H_2O and CO_2, as well as, termination step to methane. This process can take place on an active site S or an evacuated active site S*.

The chain growth reactions are assumed to start by the insertion of a monomer into an alkyl species chemically bound to the surface. Termination reactions are assumed to take place by either hydrogen addition to an alkyl species to give paraffin (irreversible reaction), or hydrogen abstraction to produce α-olefin (reversible reaction).

The derivation of the rate equations for each of the reactions proposed in Figure 6.1 is carried out by using Langmuir–Hinshelwood–Hougen–Watson approach (see Appendix B for the details of the derivations). The hydrogenation of surface carbon (the 1st reaction in stage 3), was considered as the rate limiting step, while the other steps were assumed to be at quasi-equilibrium. After the establishment of steady state operation the rate of oxygen removal by water formation (the 2nd reaction in stage 2) was assumed to be equal to the rate of carbon hydrogenation according to the stoichiometric coefficient of the 3rd reaction in the first stage. Removal of oxygen by CO_2 formation was neglected in the overall rate due to its very low selectivity over our cobalt catalyst (<2% in gas-phase reaction and <0.5% in SCH operation). The total concentration of the active sites (C_t) on the Co surface can be determined as the sum of vacant sites (C_v) and the occupied sites by the adsorbed species C_{adi} (Eqn. 6.1).

$$C_t = C_v + \sum_{i=1}^{m} C_{ad_i.S} \tag{6.1}$$

$$\sum_{i=1}^{m} C_{ad_i.S} = C_{H.S} + C_{C.S} + C_{O.S} + C_{OC.S} \tag{6.2}$$

The occupied sites shown in Eqn. 6.2 do not include the active radicals (.CH. and .CH_2.) and water (OH) since they are not occupying a significant part of the active sites and their desorption rate is much higher than the other species (Bell 1981; Sarup and

Wojciechowski 1989a). Based on the previous assumptions, Eqn. 6.3 represents the fraction of the free active site (θ_s) and Eqn. 6.4 the CO consumption rate ($-r_{CO}$) (see Appendix B for the details of the derivation).

$$\theta_s = \frac{C_V}{C_t} = \frac{1}{1 + K_1 P_{H_2}^{1/2} + (K_2 + K_3) P_{CO}^{1/2} + K_4 P_{CO}} \tag{6.3}$$

$$-r_{CO} = \frac{k P_{CO}^{1/2} P_{H_2}^{1/2}}{[1 + K_1 P_{H_2}^{1/2} + (K_2 + K_3) P_{CO}^{1/2} + K_4 P_{CO}]^2} \tag{6.4}$$

where $k = k_{C_1} K_3 K_1 C_t^2, K_1 = \sqrt{K_{H_2}}, K_2 = \sqrt{\frac{K_c k_{c_1}}{k_{O_1}}}, K_3 = \sqrt{\frac{K_c k_{O_1}}{k_{C_1}}}, K_4 = K_{CO}$

CO consumption rate can also be calculated from the rate of monomer ($CH_2.S$) consumption as described in Appendix B. There are two possibilities for monomer consumption as illustrated in Figure 6.2; either by *forming methyl species* or by *incorporating into a growing chain*. As result the CO consumption rate can also be represented by Eqn. 6.5.

$$-r_{CO} = k_{C_3} C_{H.S} C_{CH_2.S} + k_\alpha C_{CH_2.S} \sum_{n=1}^{\infty} C_{R_n.S} \tag{6.5}$$

For the elimination of the infinite sum in Eqn. 6.5, we assumed that at steady state the initiation rate of the polymerization process should balance its termination rate as illustrated in Figure 6.2 (Sarup and Wojciechowski 1989a; Uner 1998). Therefore, a mass balance around the methyl ($CH_3.S$ or R_1) initiation rate (3rd reaction in stage 3) and termination rate (to methane stage 4 or paraffins) is sufficient for the determination of the infinite sum as illustrated in Eqn. 6.6.

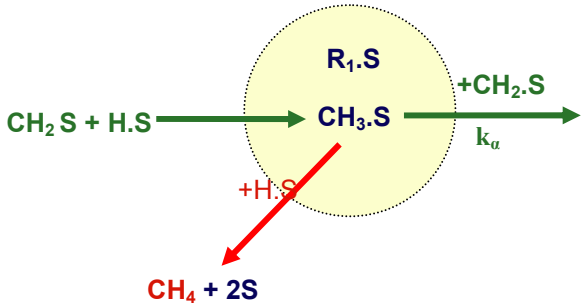

Figure 6.2 Reaction network simulates the chain growth process through the insertion of a monomer (CH_2.) into an alkyl group (CH_3. or R_1). Growth rate continues at a rate of ka, whereas, termination takes place by hydrogen addition to R_1 to produce methane. The dotted line represents the boundaries alkyl formation and consumptions.

$$k_{C_3} C_{CH_2.S} C_{H.S} = k_t C_{H.S} \sum_{n=1}^{\infty} C_{R_n.S} \tag{6.6}$$

As a result, the concentration of both the monomer ($C_{CH2.S}$) and the methyl R_1 ($C_{CH3.S}$) on the cobalt active site can be calculated from Eqns. 6.4-6.6. From stage 4, the rate of methane formation can then be calculated according to Eqn. 6.7 using the assumptions stated by Sarup and Wojcichowski, 1989 in the low CO molecular coverage model.

$$r_{CH_4} = \frac{\phi_1 P_{H_2} \theta_s^2}{\left[\phi_2 \left(\left(1 + \phi_3 P_{CO}^{1/2} P_{H_2}^{-1/2}\right)^{1/2} - 1\right)^{-1} + 1\right]} \tag{6.7}$$

where $\phi_1 = \frac{C_t^{\,2} K_H k_{c_3} k_{c_4}}{k_\alpha}$, $\phi_2 = \frac{K_4}{K_5 k_\alpha}$, $\phi_3 = \frac{K_6 k_{c_1} K_{cf}^{1/2}}{K_H^{1/2}}$

K_{cf} represents the adsorption equilibrium constant for carbon and being defined with the rest of the constants as follows; $K_{cf} = \frac{k_{O1}}{k_{C1}}$, $K_5 = \frac{k_t}{2k_\alpha}$, $K_6 = \frac{4k_\alpha}{k_{C3} k_t}$

The estimation of parameters appearing in Eqns. 6.4 and 6.7 was calculated from the experimental data by minimizing a function of square of the absolute difference between the actual and predicted rates using the *quasi*-Newton method and a finite-difference gradient (see Appendix C for the details of the program).

6.4 Results and Discussion

The performance of the 15% Co/Al_2O_3 catalyst measured by the rate of CO consumption in gas-phase FTS and SCH-FTS under different operating conditions is

shown in Figure 6.3 at 250 °C with a total pressure of 60 bar and a syngas partial pressure, P_{syngas}, of 15 bar at three different H_2/CO ratios. In the gas-phase experiments, a partial pressure of inert helium, P_{helium}, of 45 bar was used as a pressurizing gas to achieve a total pressure of 60 bar. In the SCH experiments, the P_{syngas} was again 15 bar and the partial pressure of hexane solvent, P_{hexane}, was 45 bar thereby yielding the same total pressure of 60 bar. The experiments in both gas-phase and SCH-FTS were conducted at a constant syngas flowrate of 100 sccm/g_{cat}. As shown in Figure 6.3, the increase in H_2/CO molar feed ratio resulted in higher CO consumption rates at fixed reaction temperature in SCH operation. At low H_2/CO, an increase in reaction temperature from 240 °C to 250 °C results in only a slight increase in the CO consumption, however, at a ratio of 2/1 a significant increase in the rate (>30%) is observed with this temperature increase (see Figure 5.5). The activity of the catalyst under SCH operation is higher than in the gas-phase at the same total pressure of 60 bar. The same result was observed in the absence of the helium pressurizing (diluent) gas whereby P_{syngas} was kept constant at 20 bar for both gas-phase and SCH operations (see Table 4.1). However, the CO consumption rate in SCH is shown to be function of pressure that exhibits a maximum of 65 bar (see Figure 5.5). This trend is in agreement with our previous findings (see Chapter 5) and is attributed to the fine balance between the effects of pressure on the bulk diffusion and the intra-particle pore diffusivity.

Figure 6.4 presents the rate of methane formation as a function of the H_2/CO feed ratio at the conditions described above for both gas-phase and SCH FTS at 250 °C. An increase in H_2/CO ratio results in higher methane production rate in both gas-phase and SCH FTS. However, this rate in SCH is much lower than that in gas-phase and the

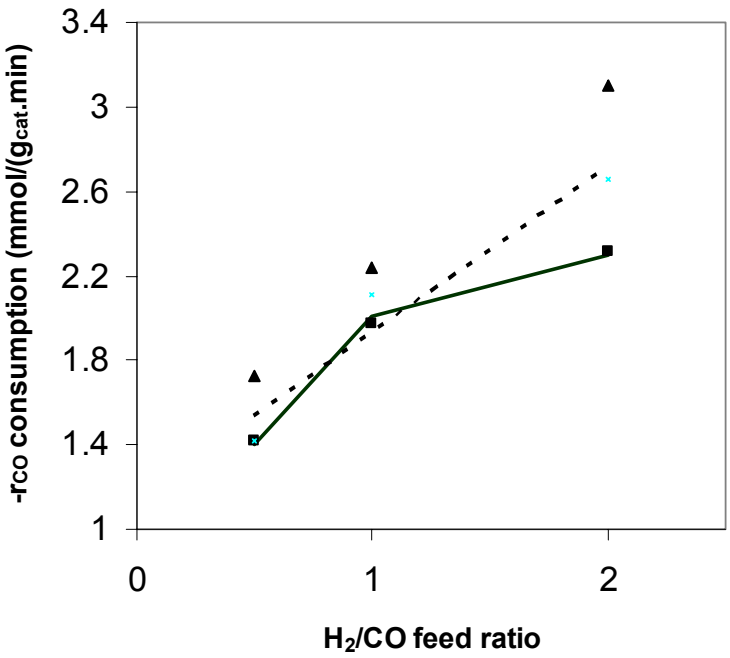

Figure 6.3 CO consumption rate in gas-phase (squares) and SCH phase (triangles) as a function H_2/CO ratio at 250 °C. Total pressure is 60 bar (P_{syngas} = 15 bar) and syngas flow rate 100 sccm/min. The solid line represents the predicted rate in gas-phase while the dotted line represents the predicted rate in SCH FTS operation by using the estimated parameters in Eqn. 6.4 (k = 0631, K_1= 0.007, K_2= 0.51, K_3 = 0.098, $K_4 = 6.64\times10^{-5}$).

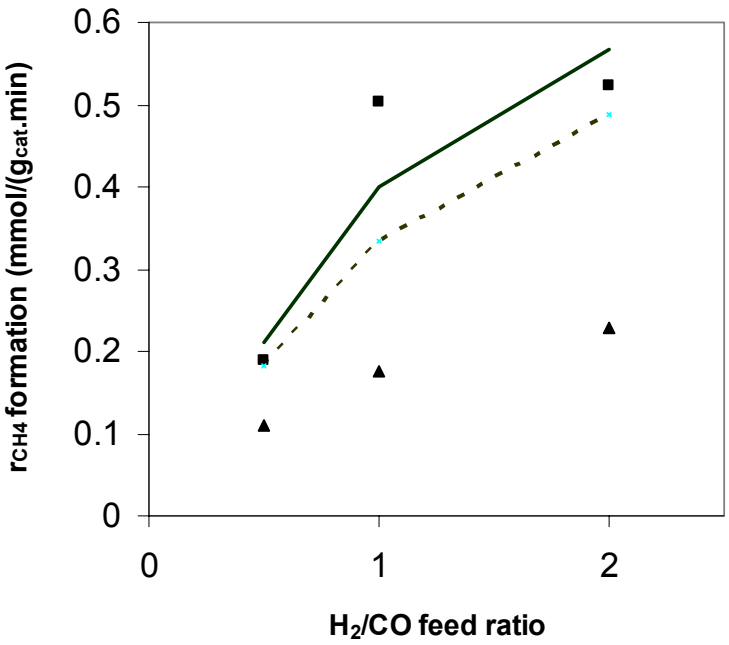

Figure 6.4 CH_4 formation rate in gas-phase (squares) and SCH phase (triangles) as a function H_2/CO ratio at 250 °C. Total pressure is 60 bar (P_{syngas} = 15 bar) and syngas flow rate 100 sccm/min. The solid line represents the predicted rate in gas-phase while the dotted line represents the predicted rate in SCH operation by using the estimated parameters of Eqn. 6.7 ($\phi_1\theta_s^2 = 0.0306$, $\phi_2 = 303$, $\phi_3 = 0.045$).

difference between the two increases with increasing H_2 concentration. In addition to this phenomenon of the reduced methane formation under SCH conditions, it was also observed that SCH FTS resulted in higher olefin/paraffin ratio and shifts of product distributions towards the heavy hydrocarbons (see Chapter 3) compared to gas-phase FTS at the previously specified conditions.

The kinetic model in Eqn. 6.4 and Eqn. 6.7 closely predict the CO consumption rates and CH_4 production in gas-phase operation as seen in Figures 6.3 and 6.4. However, both of the models do a poor job in the prediction of those rates under SCH operation. Higher methane formation rate than the actual was predicted by Eqn. 6.7, while lower CO consumption rate was also predicted by Eqn. 6.4 for the SCH FTS. The inconsistency of the kinetic model in predicting the SCH performance indicates that assumptions stated in developing this model for gas-phase operation is not sufficient to measure the performance under SCH operation. Two factors could contribute to the inability of this model to predict FTS performance under SCH conditions. First of all, the model relies on partial pressure (concentrations) of the reactants rather than their activities in the rate equations due to ideal gas assumptions made in previous model developments. Thermodynamic nonideality must be incorporated into the model through use of activities rather than simply partial pressures to accurately predict the kinetic rates under SCH conditions. Secondly, this model does not include solvent effects on individual rate constants in the critical region and particularly for the initiation steps. The FTS reaction pathway (Figure 6.1) is modified as illustrated earlier in Figure 5.12 to include enhanced olefin incorporation in chain growth process (stage 6) as a result of significant in situ extraction in the SCH medium, especially for heavier hydrocarbons (Huang and Roberts

2003). This modification accounts for the increased availability of active sites in the supercritical medium. This site (S^*) is assumed to promote both adsorption of the reacting molecules (CO and H_2) and incorporation of primary products (α-olefins) into the chain growth process. It is also assumed that S* would have a higher coverage of active carbon than the regular site, *S*, and therefore it suppresses methane formation (Bertole et al. 2002). In addition the effective reaction order of higher hydrocarbon formation on S^* is higher than the methane formation since the monomer involved on this site is likely a desorbed olefin close to the active site. The increased probability of covering S^* by a monomer derived from the readsorbed α-olefin rather than an initiating monomer (-CH_2-) decreases the probability of methane formation.

6.5 Conclusions

While the role of enhanced in situ extraction of heavy products in SCH operation has not being quantified at this stage, it is clear that the removal of heavy hydrocarbons in the SCH would result in more active sites availability (S^*). Moreover, including thermodynamic nonidealities into the rate expression will improve the model predictions under supercritical FTS operation. The difference between the reaction medium in gas-phase FTS and SCH FTS can result in modified active site chemical characteristics, enhancement in active site availability and different thermodynamic activities of the reacting species. Further model development should address each of the factors described above.

CHAPTER 7

CHARACTERIZATION OF FISCHER-TROPSCH COBALT-BASED CATALYTIC SYSTEMS (Co/SiO_2 AND Co/Al_2O_3) BY X-RAY DIFFRACTION AND MAGNETIC MEASUREMENTS

7.1 Introduction

Cobalt-based catalysts are known to provide the best compromise between performance and cost for the synthesis of hydrocarbons from syngas (CO/H_2 mixtures). Cobalt catalysts were also found to give the highest yields and longest lifetime producing mainly linear alkanes (paraffins) (Chaumette et al. 1995). Since cobalt catalysts are not inhibited by the water-gas-shift (WGS), it gives a high productivity at high syngas conversion (Van Berge and Everson 1997). Optimum catalysts with high cobalt concentration and site density can be prepared by controlled reduction of nitrate precursors introduced via melt or aqueous impregnation methods (Iglesia 1997a). Most of the industrial cobalt-based catalytic systems used in the FTS reaction are supported on either Al_2O_3 or SiO_2. Therefore, cobalt dispersion on the supported catalyst surface (Tauster and Fung 1978) and the interaction of the Co with the metal oxide support that affect the electronic density as well as the structure of the metal crystallites (Iglesia et al. 1992) are assumed to play significant role on the catalyst performance measured by the hydrocarbon selectivity (C_{5+}) and the catalyst activity. In this chapter, X-ray diffraction

(XRD), magnetic and electron magnetic resonance (EMR) measurements, and BET surface area measurements are used to characterize three supported cobalt-based catalytic systems (low surface area (LSA) 15% Co/SiO_2, high surface area (HSA) 15% Co/SiO_2, and 15% Co/ Al_2O_3). These catalytic systems were used in a conventional gas-phase FTS study conducted in a fixed-bed-reactor. The structure sensitivity of these catalysts is correlated to their activity and selectivity in the synthesis of CO and H_2. Another important objective of this study is to provide a detailed characterization of the structure and valence state of cobalt and the surface composition of those catalysts in a fresh form (i.e. after preparation), after calcination (calcined samples), and after use in the reaction (used sample).

7.2 Experimental

7.2.1 Catalysts preparation

Three cobalt-based catalytic systems were investigated in this study. The alumina supported catalyst (15% Co/Al_2O_3) is a commercial catalyst purchased from United Catalysts. The two silica supported catalysts (15% Co/SiO_2) were prepared using the impregnation technique. Highly pure fumed silica (99.8%) purchased from Aldrich was used to support the cobalt catalyst. The LSA-15% Co/SiO_2 catalyst was supported on a 200 m^2/g surface area fumed SiO_2, while the HSA-15% Co/SiO_2 was supported on a 380 m^2/g surface area fumed SiO_2. The cobalt precursor is highly pure (98%) cobalt nitrate $Co(NO_3)_2.6H_2O$ and was purchased from Aldrich Chemical Co. In a typical preparation procedure, a total amount of 74.31g of the cobalt nitrate precursor was dissolved in 250 ml of distilled water while stirring at room temperature. After a clear solution was

formed, the addition of 40g of the support SiO_2 was commenced bit by bit while stirring. This step is very important to avoid formation of large particles during the mixing process. The mixture was then continuously stirred for more than 48 hr at room temperature until a heavy paste was formed. The paste was then dried in an oven at 110 °C for about 4 hr. The sample was then crushed into a powder (100-150 μm) and stored as a fresh catalyst sample. The catalyst powder was then calcined (calcined sample) in air environment at 400 °C in a special rotary oven (temperature programming of the oven is 3K/min) for about 4 hrs.

7.2.2 BET surface area characterization

The BET surface area of the calcined silica supported catalysts (LSA and HSA), and the alumina supported catalyst was measured by N_2 physisorption using a TriStar 3000 gas adsorption analyzer of high-quality surface area and porosimetry measurements. The surface area measurements of those catalysts were certified by Micromeritics Co. The BET surface area, pore volume, and average pore diameter of our catalysts was measured by N_2 physisorption using a TriStar 3000 gas adsorption analyzer of high-quality surface area and porosimetry measurements. The analytical technique for BET surface area is as follows: a sample of our catalyst was first contained in an evacuated sample tube and cooled (typically) to cryogenic temperature, and then it was exposed to analysis gas at a series of precisely controlled pressures. With each incremental pressure increase, the number of gas molecules adsorbed on the surface increases. The equilibrated pressure (P) is compared to the saturation pressure (Po) and their relative pressure ratio (P/Po) is recorded along with the quantity of gas adsorbed by the sample at each

equilibrated pressure. The BET surface area was then measured from the plot of $1/Q(P_0/P)$ versus. the relative pressure (P/P_0), where Q is the quantity adsorbed in (cm^3/g STP). From the adsorptive properties of the catalyst pores a single point desorption was used to determine the total pore volume of pores less than 4397.296 Å diameter at P/Po = 0.9956. The desorption average pore width (DAPW) was then calculated from the pore volume (V) and BET surface area using the following formula;

$$\text{DAPW (Å)} = 4V/A_{BET} \quad (7.1)$$

The BET analysis of the catalyst samples were conducted by Micromeretics Instrument Co.

The measured BET surface areas of the calcined samples are listed in Table 7.1.

7.2.3 Sampling and Characterization Procedures

In Table 7.1, the six catalysts investigated in this work are listed. These include fresh Co/SiO_2 catalysts A1 (HSA-15% Co/SiO_2) and B1 (LSA-15% Co/SiO_2) and their calcined forms A1/C and B1/C. The remaining two catalysts are: C1 which is 15% Co/Al_2O_3 (used as received from United Catalyst) and C1/U which is C1 used for 12 days in FTS experiments. Room temperature X-ray diffraction (XRD) patterns of these catalysts were obtained with a Rigaku diffractometer using CuK_α radiation with λ = 0.15418 nm. Measurements of magnetization M vs T and H were done with a commercial SQUID (superconducting quantum interference devices) magnetometer. Electron magnetic resonance (EMR) studies were carried out at the X-band frequency of 9.278 GHz with a variable temperature cryostat from Oxford Instruments. In this system, the microwave cavity remains at room temperature whereas the sample temperature can be

Table 7.1 Results of characterization of the cobalt-based catalytic systems.

Sample	Description	BET Surface Area (m^2/g)	XRD	Magnetic	EMR
A1	15%HSA Co/SiO_2-Fresh	-	SiO_2	Curie-Weiss, Co^{2+}	Co^{2+} line $g \approx 4.3$
B1	15%LSA Co/SiO_2-Fresh	-	SiO_2	Curie-Weiss, Co^{2+}	Co^{2+} line $g \approx 4.3$
A1/C	Calcined A1	256	SiO_2, Co_3O_4	Co_3O_4	No line
B1/C	Calcined B1	158	SiO_2, Co_3O_4	Co_3O_4	Co^{2+}-weak line $g \approx 4.3$
C1/C	15%Co/Al_2O_3-calcined	95	Co_3O_4, δ-Al_2O_3	Co_3O_4	Co^{2+}-line,$g \approx 4.3$ with sharp line
C1/U	C1 used in FTS reaction for 12 days	-	Co_3O_4, $Al_2O_3(\alpha,\delta,\chi)$	Co^0, Co^{2+}	Co^{2+}-line. Co^0-line

varied from 4 K to 300 K. In the EMR resonance condition $h\nu = g\mu_B H_0$, the microwave frequency ν is accurately measured by a frequency counter and the resonance field H_0 by a NMR probe. The magnetic field is modulated at 100 kHz so that the experimental traces represent dP/dH versus H, with P being the power absorbed.

7.2.4 Fischer-Tropsch Study

The FTS experiments were conducted in a high pressure stainless steel fixed-bed-reactor that composed of three sections described in Chapter 3. Before using the catalyst in the reaction two methods of pretreatment were conducted. The alumina supported catalyst was pretreated in CO environment (50 sccm) at 280 °C for 18 hr, while the silica supported catalysts were reduced in H_2 environment (100 sccm) at 340 °C for 4 hr. The flow rate of syngas (H_2/CO ratio of 2) was fixed at 50 sccm, unless otherwise mentioned.

7.3 Results and Discussion

7.3.1 Background theory for magnetic studies

In order to provide a basis for the interpretation of the magnetic data, we briefly outline the theoretical expressions used in the analysis. We have measured the magnetization M against temperature T from 2 K to 350 K at a fixed field H = 100 Oe and the magnetization M versus H at 2 K for H upto 55 kOe. For a paramagnetic system, the magnetic susceptibility χ = M/H is expected to follow the Curie-Weiss law given by (Kittel 1996)

$$\chi = \chi_0 + \frac{C}{T - \theta} \qquad (7.2)$$

where the constants χ_0, C and θ are determined from the fit. The Curie constant $C = Ng^2\mu_B^2S(S+1)/3k_B$ with N being the number of paramagnetic ion, g is the electronic g-value with spin S and μ_B and k_B are respectively the Bohr magneton and the Boltzmann constant. The Curie-temperature θ measures the exchange interaction between the neighboring paramagnetic ions, $\theta > 0$ for ferromagnetic and $\theta < 0$ for antiferromagnetic interactions. χ_0 includes the diamagnetic and other contribution of the lattice and the bonds. Knowing g and S, and experimental C, the concentration N of the paramagnetic ions can be determined.

The magnetization M of an assembly N of paramagnetic ions with the applied field H is also expected to vary according to the Brillouin function $B_S(x)$ (Kittel 1996; Dutta et al. 2004b):

$$\frac{M}{M_0} = B_S(x) = \frac{2S+1}{2S}\coth\left(\frac{2S+1}{2S}x\right) - \frac{1}{2S}\coth\left(\frac{x}{2S}\right) \qquad (7.3)$$

where $x = g\mu_BSH/k_BT$ and $M_0 = Ng\mu_BS$ is the magnetization of a perfectly aligned system of N ions, each with moment = $g\mu_BS$. Since this occurs only at absolute zero for a paramagnetic system, the M vs H measurements must be carried out at the lowest possible temperature, T = 2 K for our experiments. This analysis provides the magnitudes of g, S and M_0 and hence the magnitude of N. The two measurements combined yields the electronic state of the paramagnetic ion from the magnitude of g and S and the concentration from N. A peak in the χ vs T is usually observed in systems due to a magnetic transition. For CoO and Co_3O_4, this transition to antiferromagnetic ordering occurs near T_N = 290 K (Seehra and Silinsky 1979) and $T_N \approx 40$ K (Roth 1964),

respectively. Elemental Co^0 is a ferromagnet with the Curie ordering temperature T_C well above room temperature (T_C = 1388 K) (Kittel 1996), so at room temperature hysteresis loop should be observed if Co^0 is present.

7.3.2 X-ray Diffraction and Magnetic Studies

Fresh samples. The room temperature XRD patterns of the fresh samples A1 and B1 are shown in Figure 7.1. The broad line centered around $2\theta \approx 24^0$ is due to the SiO_2 (Moradi et al. 2003). No peaks due to crystalline phases are observed indicating that in 15% Co/SiO_2, Co is not present in any of its usual forms such as Co^0, CoO or Co_3O_4. Further confirmation of this comes from the χ vs T data discussed next.

The data of χ vs T for A1 and B1 samples measured with H = 100 Oe are shown in Figure 7.2 with the log-scale for the temperatures in order to give details of the low temperature data. The solid lines are fits to Eqn 7.1 with the parameters of the fit (χ_0, C and θ) given in Figure 7.2. The fits are excellent with negligible θ, showing that Co must be in the paramagnetic state, either as Co^{2+} or Co^{3+}, with the expected moment $\mu = gS$ equal to 3.3 for Co^{2+} and 4.4 for Co^{3+} (Kittel 1996) in the high spin states. To determine g and S for the present cases, the plot of M vs. H at T = 2 K is fit to the Brillouin function (Eq. 2) with S = 3/2 and g = 2.2 expected for Co^{2+} (Roth 1964; Kittel 1996). Excellent fits are obtained for both for the A1 and B1 samples (Figure 7.3) with the M_0 values given in Figure 7.3. Thus we conclude Co^{2+} in the high spin state to be the electronic state of cobalt in these samples. This state is possible for Co^{2+} surrounded by either tetrahedral or octahedral crystalline fields (Roth 1964). Thus Co^{2+} is either substituting for Si as in

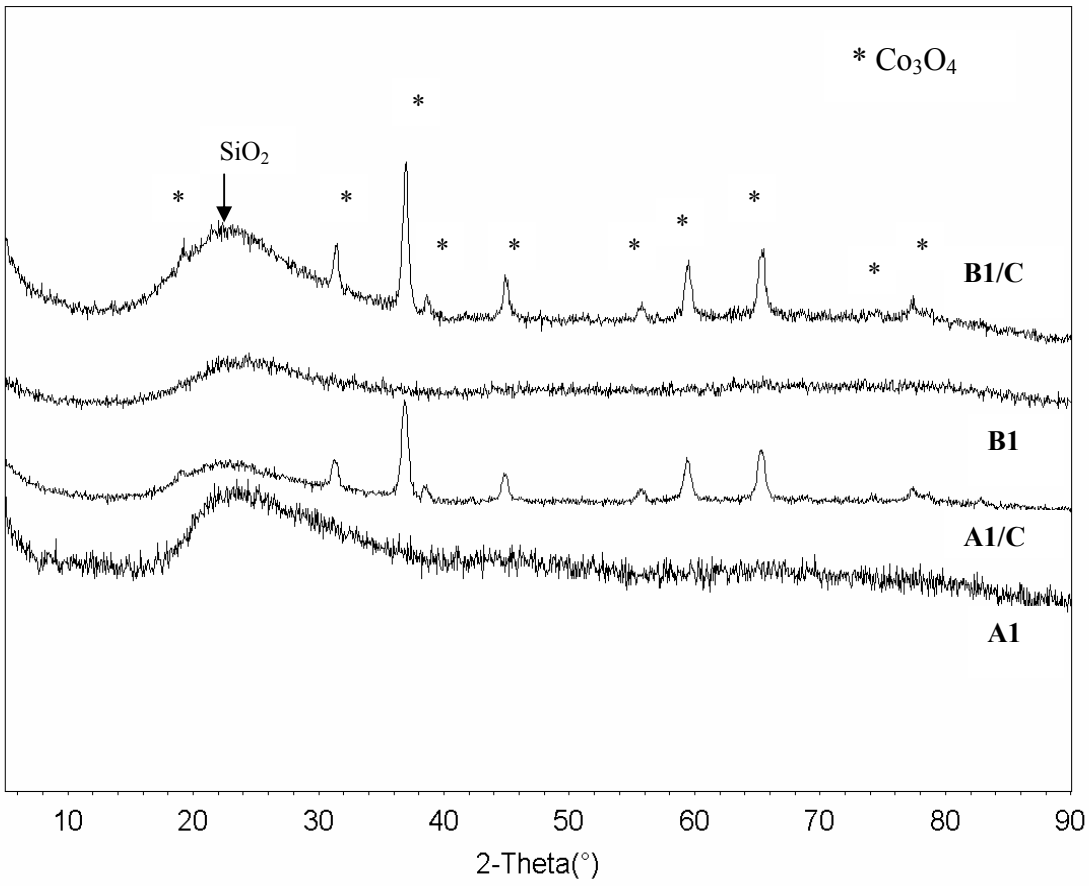

Figure 7.1 Room temperature XRD patterns of the catalysts shown using λ = 0.15418 nm. The Co_3O_4 and SiO_2 lines are identified.

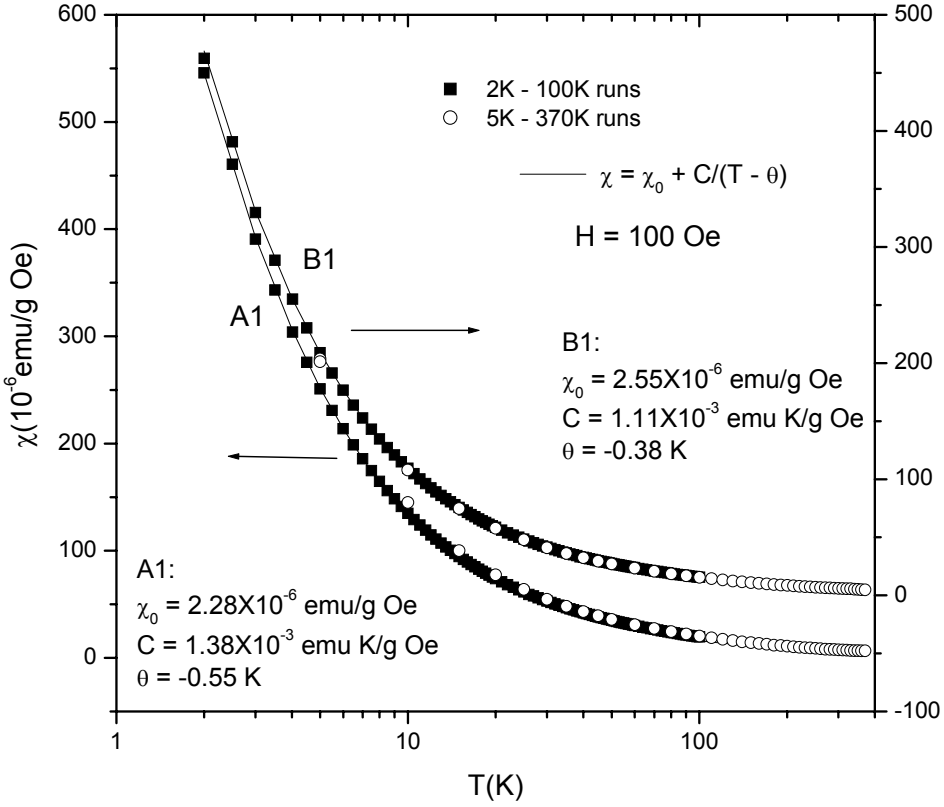

Figure 7.2 Temperature variations of the magnetic susceptibility χ for the A1 and B1 catalysts. The solid lines are fits to Eqn. (7.1) with the magnitude of the parameters listed.

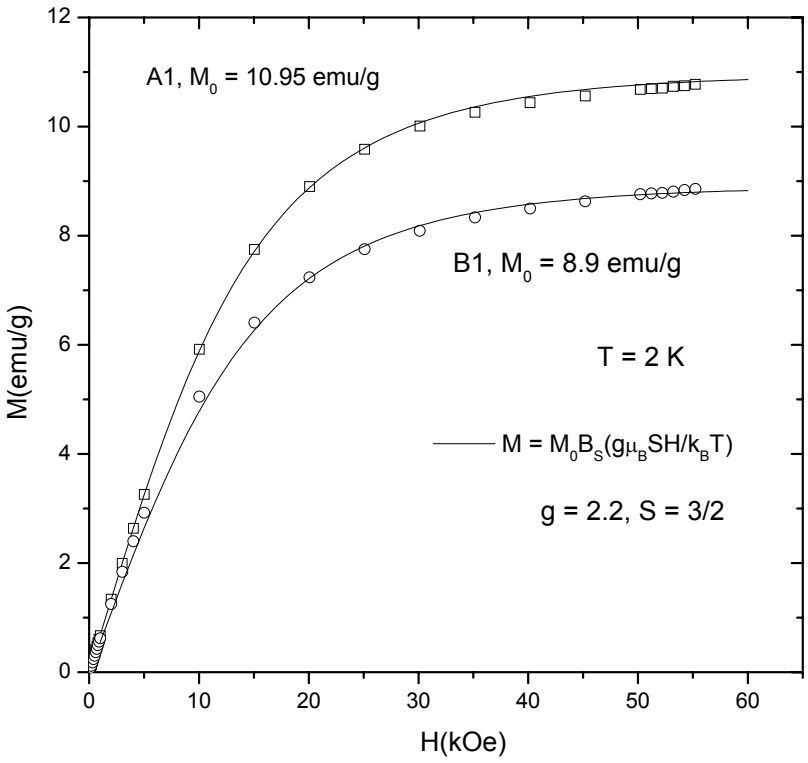

Figure 7.3 Magnetic field variations of the magnetization M at 2 K for the A1 and B1 samples. The solid lines are fits to Eq. (2) with the magnitudes of the parameters shown.

$Co_xSi_{1-x}O_2$ or perhaps chemisorbed on the surface of SiO_2 with bonding provided by surface absorbed H_2O and O_2.

The concentration of Co^{2+} ions in the A1 and B1 samples can be calculated both from C and M_0 as discussed earlier. The two sets of calculated values are in excellent agreement and these are 3.7% for A1 and 3.0% for B1, much less the 15% nominal doping (The differences between the atomic and weight percentages of Co^{2+} in $Co_xSi_{1-x}O_2$ is negligible). A possible explanation for this large discrepancy between the nominal and measured concentration is the presence of a part of Co in the Co^{3+} state in the low-spin configuration of S = 0, which occurs in strong octahedral crystalline field (Roth 1964). In this case Co^{3+} has no magnetic moments and hence not measured in the magnetic studies. This indeed is the case of for Co_3O_4 which contains both Co^{2+} and Co^{3+} configuration, the latter carrying no magnetic moment (Roth 1964).

In summary then, while XRD provided a null result for Co^0, CoO and Co_3O_4 in the fresh samples, magnetic measurements yielded the presence of Co^{2+} ions in the range of around 3%, with the rest of Co perhaps in the low-spin Co^{3+} state. The detection of Co_3O_4 in the calcined samples discussed next confirms this characterization.

Calcined samples. The XRD patterns of the calcined samples A1/C and B1/C are also shown Figure 7.1. All the observed Bragg peaks can be identified with crystalline Co_3O_4 with the crystallite size ≈ 14 nm. The other oxide of cobalt viz. CoO is not observed. A similar result of the presence of Co_3O_4 is reported in Zr-promoted Co/SiO_2 (Moradi et al. 2003). Additional confirmation of the presence of Co_3O_4 and absence of CoO comes from the measurements of χ vs T shown in Figure 7.4. The observation of a peak in χ

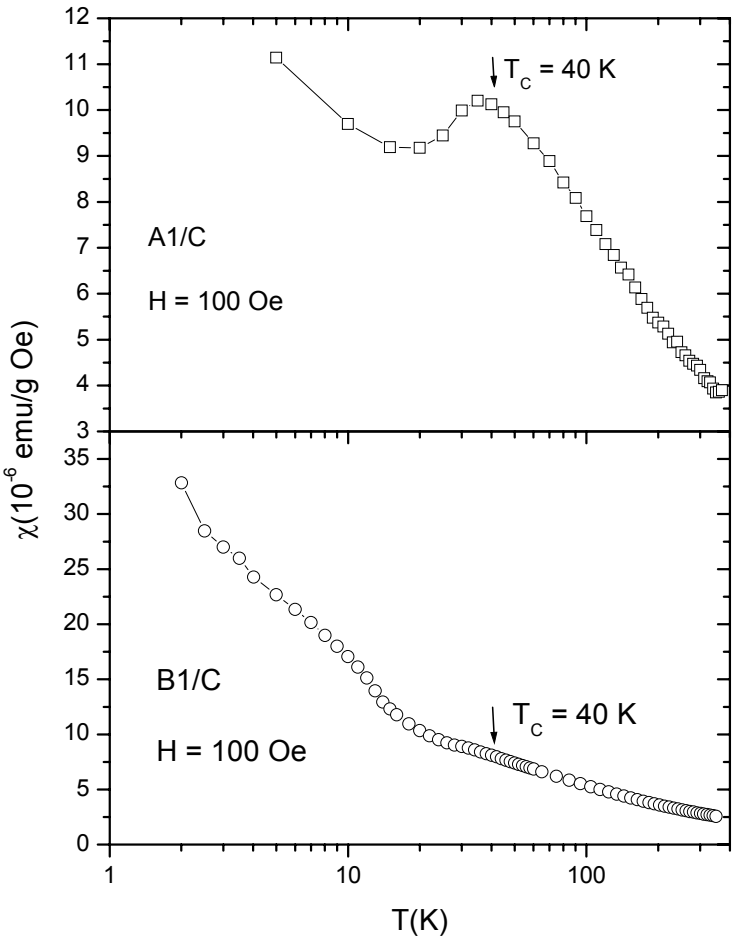

Figure 7.4 Temperature variation of the magnetic susceptibility χ for the A1/C and B1/C samples. T_C = 40 K represents the magnetic transition due to Co_3O_4.

near the known $T_N \approx 40$ K of Co_3O_4 (Roth 1964) in both A1/C and B1/C samples is a definite confirmation of the presence of Co_3O_4 in these samples. Comparing the magnitude of χ with that of pure Co_3O_4 (Roth 1964), more of the Co in the A1/C sample is converted to Co_3O_4, as compared to that in B1/C, the latter having more of the background paramagnetic contribution thereby masking the peak at 40 K. There is no peak near the expected $T_N \approx 290$ K of CoO, thereby indicating the absence of CoO. The magnitude of χ in the A1/C sample is consistent with about 15% concentration of Co_3O_4. These observations agree with the conclusion drawn from the XRD results.

Co/Al_2O_3 samples. The XRD patterns of the Co/Al_2O_3 based samples (C1/C and C1/U of Table 7.1) are shown in Figure 7.5. These results indicate that in the calcined but un-used sample C1/C, Co_3O_4 and Al_2O_3 (α,δ,χ) are present. After using the sample for 12 days in the reaction, Co_3O_4 is partly reduced to Co^0, whereas several different forms of Al_2O_3 are observed. The magnetic measurements shown in Figure 7.6 for C1/C do indicate the presence of Co_3O_4 since the signature anomaly of Co_3O_4 near 40 K is indicated. For C1/U, the χ vs T data shown in Figure 7.6 show considerably enhanced χ and behavior characteristic of magnetic nanoparticles as indicated by the bifurcation of the FC (field-cooled) and the zero-field-cooled (ZFC) data. The M vs H data at 300 K yields a hysteresis loop with coerceivity $H_C = 325$ Oe. The hysteresis loops measured at 5 K for C1/U cooled in H = 0 and H = 20 kOe from 300 K shows loop shift (Figure 7.7) to negative fields with exchange-bias $H_e = -42$ Oe. This is characteristic of ferromagnetic/antiferromagnetic interface, in this case Co^0/Co_3O_4 (Berkowitz and Takano 1999). The presence of Co^0 in the C1/U sample is barely evident from XRD since

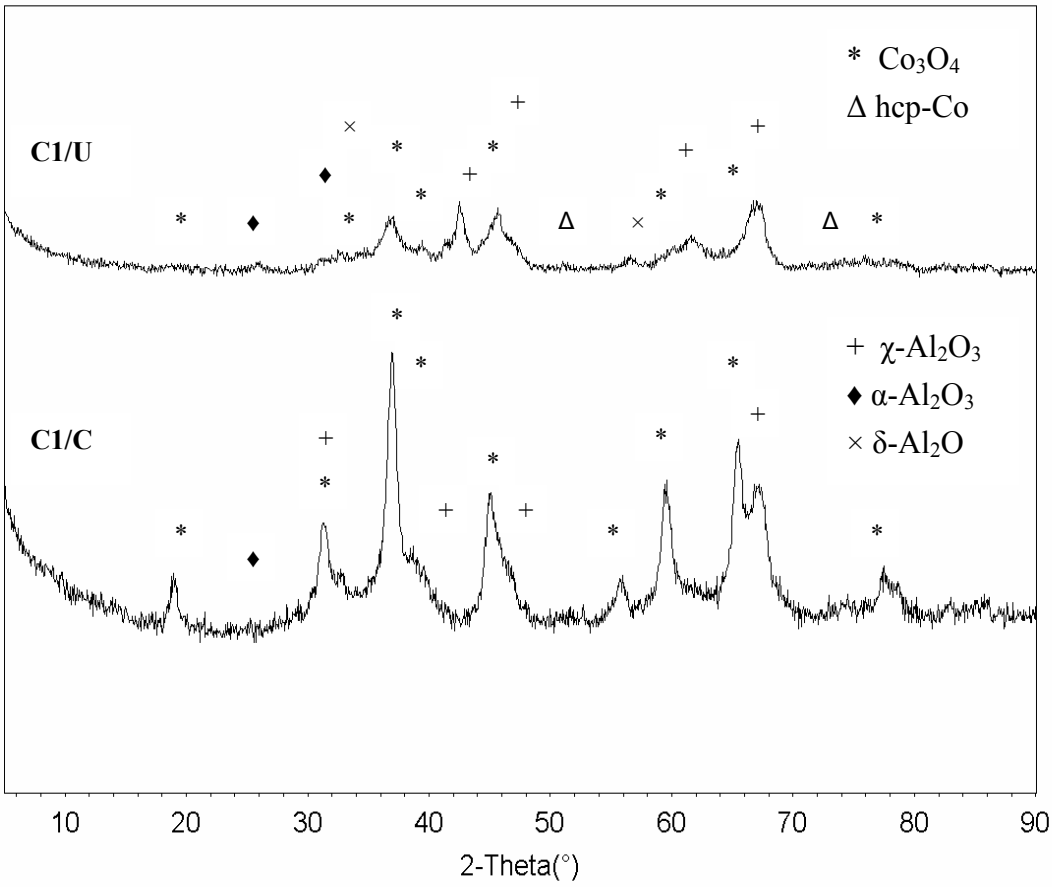

Figure 7.5 Room temperature XRD patterns of the C1/C and C1/U catalysts with the identified phases as shown.

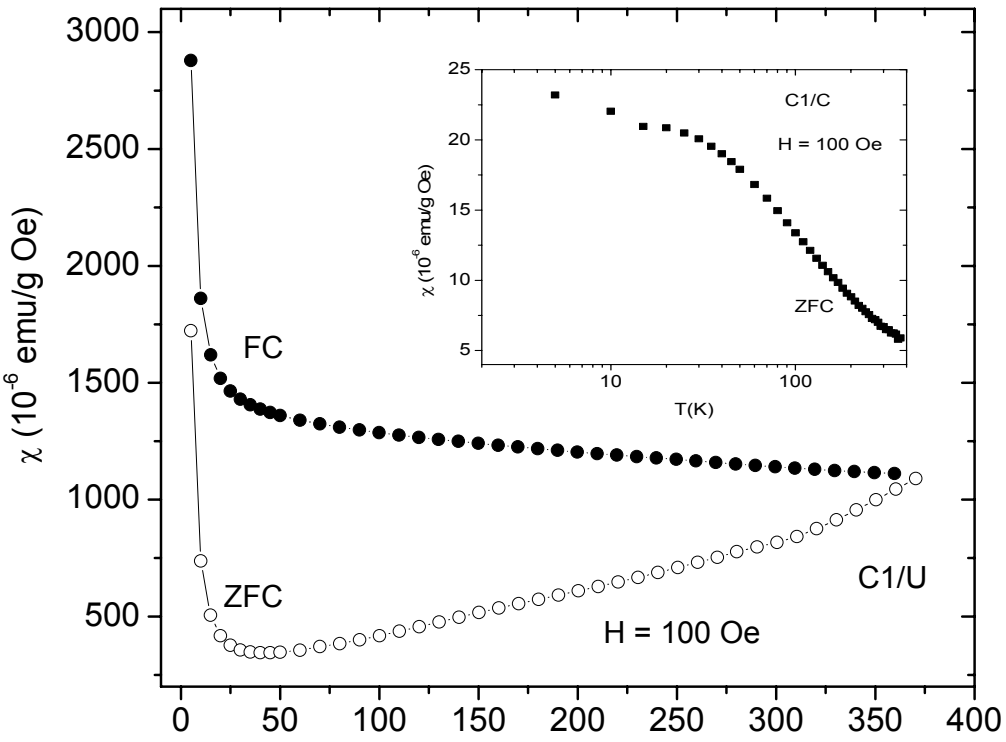

Figure 7.6 Temperature variations of the magnetic susceptibility χ for the C1/C (left scale) and C1/U (right scale) samples under ZFC (zero-field-cooled) and FC (field-cooled) conditions. The sharp rise in χ at low temperatures for C1/U is due to Co^{2+}.

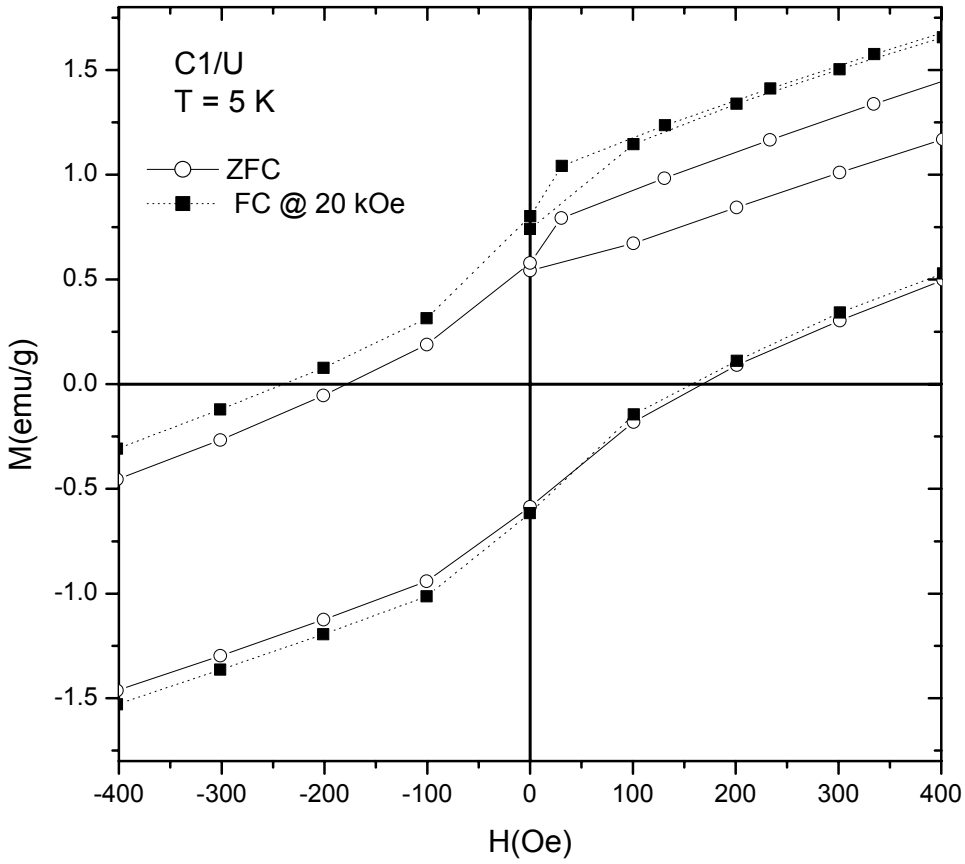

Figure 7.7 Low field part of the hysteresis loop data of magnetization vs. applied field H for the ZFC and FC cases in C1/U. The shifted loop for the FC cases suggests Co^0/Co_3O_4 interface.

concentrations less than 1% is difficult to detect by XRD. However, because of the large χ for Co^0 compared to that for CoO and Co_3O_4, even minute quantities of Co^0 are easily detected by magnetic measurements.

7.3.3 EMR Characterization

The low temperature (5 K) EMR data (Figure 7.8) for the fresh samples A1 and B1 give a broad line at g = 4.3 due to Co^{2+} state (Low 1958). The intensity of the EMR line decreases with increasing temperature. For the A1/C sample, an EMR line is not observed even at 5 K suggesting the absence of Co^{2+}. On the other hand, B1/C gives a weak line for g = 4.3 only at low temperature and with increasing temperature the line becomes weaker and after 32 K it is not observed. These results suggest that in A1/C, cobalt is present only as Co_3O_4 whereas in B1/C, both Co_3O_4 and Co^{2+} are present. These results are consistent with the magnetic measurements shown in Figure 7.4.

In case of C1/C, we observe a line at g = 4.3 (Figure 7.8) due Co^{2+} superposed with another sharp line. The position of the line does not change with increasing temperature except the reduction of intensity. In the used sample (C1/U), the EMR data show the lines both for Co^{2+} (g = 4.3) and the broad line due to Co^0. These observations are consistent with the magnetic data shown in Figures 7.6 and 7.7.

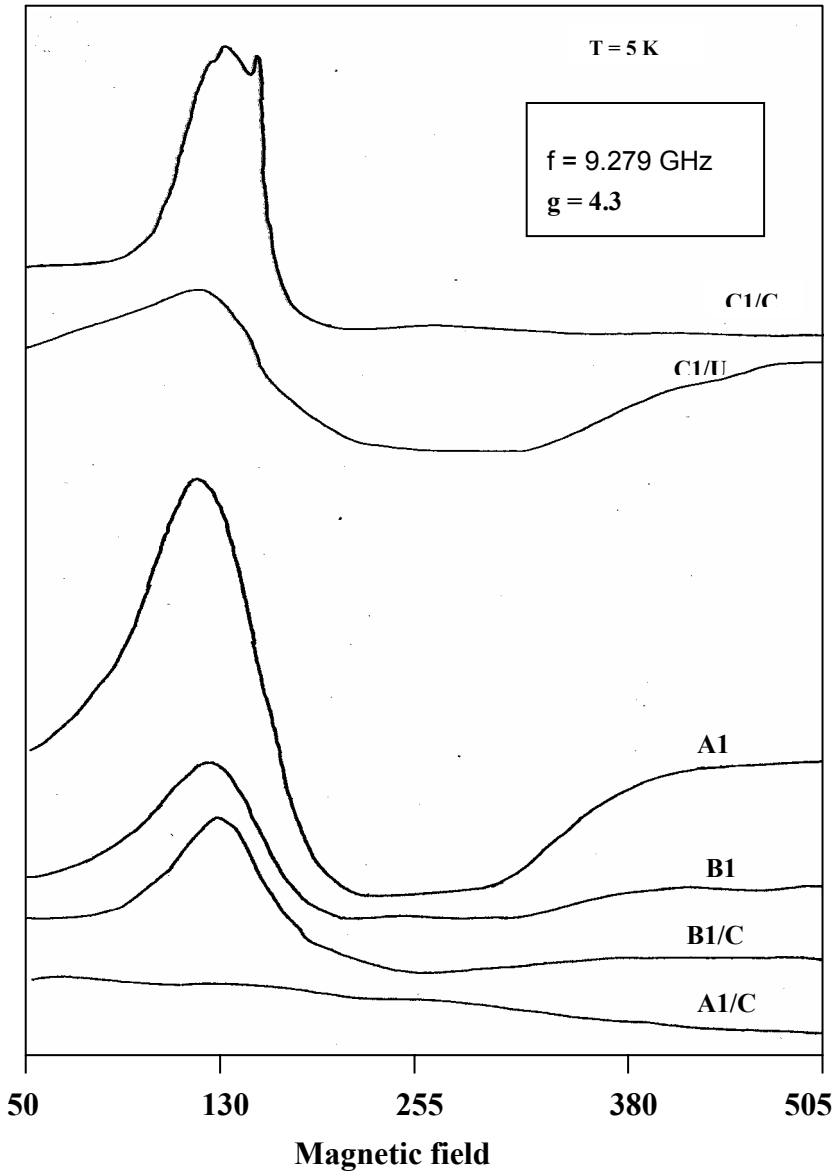

Figure 7.8 The EMR scans for various samples at 5 K.

7.3.4 Performance of the Cobalt-based Catalysts in Fischer-Tropsch Synthesis

The performance of the cobalt-based catalysts in FTS was tested in a high pressure reactor system under controlled temperature and pressure as shown in Figure 3.1. The reaction conditions and the set of operation modes were selected to mimic that of industrial conditions (favors high conversion rate of CO and H_2 per single pass at an acceptable chain growth probability of α-value above 0.60). Table 7.2 show the catalysts activity and selectivity at a reaction temperature of 240 °C and pressure of 20±2 bar. The reported results in Tables 7.2 have been collected after steady-state operation and prior to any deactivation of the catalyst taking place. A previous study has reported that the quasi steady state in reaction rates and selectivity of cobalt-based catalyst can be reached within as low as 4 hr of time-on-stream (TOS) (Sun et al. 2000). In the current study, the reported activity and selectivity is for samples analyzed after long times (ca. 40 hr TOS) to ensure stability of the catalysts under the studied conditions. Figure 7.9 shows an example of the A1/C catalyst stability with time on stream at relatively high reaction temperature of 250 °C. No significant changes (up to 55 hr.) in both activity (CO conversion, H_2 conversion and syngas conversion) and selectivity (CH_4 and CO_2) with TOS are observed as shown in Figure 7.9.

Under the studied conditions, the silica supported catalysts (A1/C and B1/C) were found to achieve higher CO and syngas conversions than the alumina supported one (C1/C) (see Table 7.2). This is also accompanied by higher methane selectivity of the silica supported catalysts (A1/C 21.3% and B1/C 18.9%) than that of the alumina supported one (C1/C 16%). In addition, the alumina supported catalyst (C1/C) gave much higher selectivity towards olefins (almost more than double of the silica supported ones,

Table 7.2 Activity and selectivity of three cobalt-based catalysts at 240 °C and pressure 20±2 bar. H_2/CO ratio is 2, and the syngas flowrate is 50sccm/gcat.

	Catalyst		
	A1/C	B1/C	C1/C
Activity			
CO Conversion%	83.2	87.9	76.8
Syngas (H_2+CO) conversion %	71.9	80.8	65.4
Selectivity			
CH_4 select.%	21.3	18.9	16
CO_2 Select. %	5.1	5.1	3.3
Alkanes select.% *	63	66	58
Alkenes select.%*	10.6	10	22.7
Chain growth probability α-value **	0.65	0.71	0.78

* Alkanes and alkenese selectivity include the isomers for hydrocarbon range of C2+.
** The chain growth probability was determined from the slope of the best fitting line of the Andesron-Shultz-Flory distribution by using the following equation: $\ln(W_n/n) = n\ln\alpha + \ln[(1-\alpha)^2/\alpha]$ where W_n is the weight of hydrocarbons (paraffins, olefins and isomers) for a carbon number n. The heaviest hydrocarbon separated in our GC analysis is C_{30} and included in the α-value calculation is C_{35}.

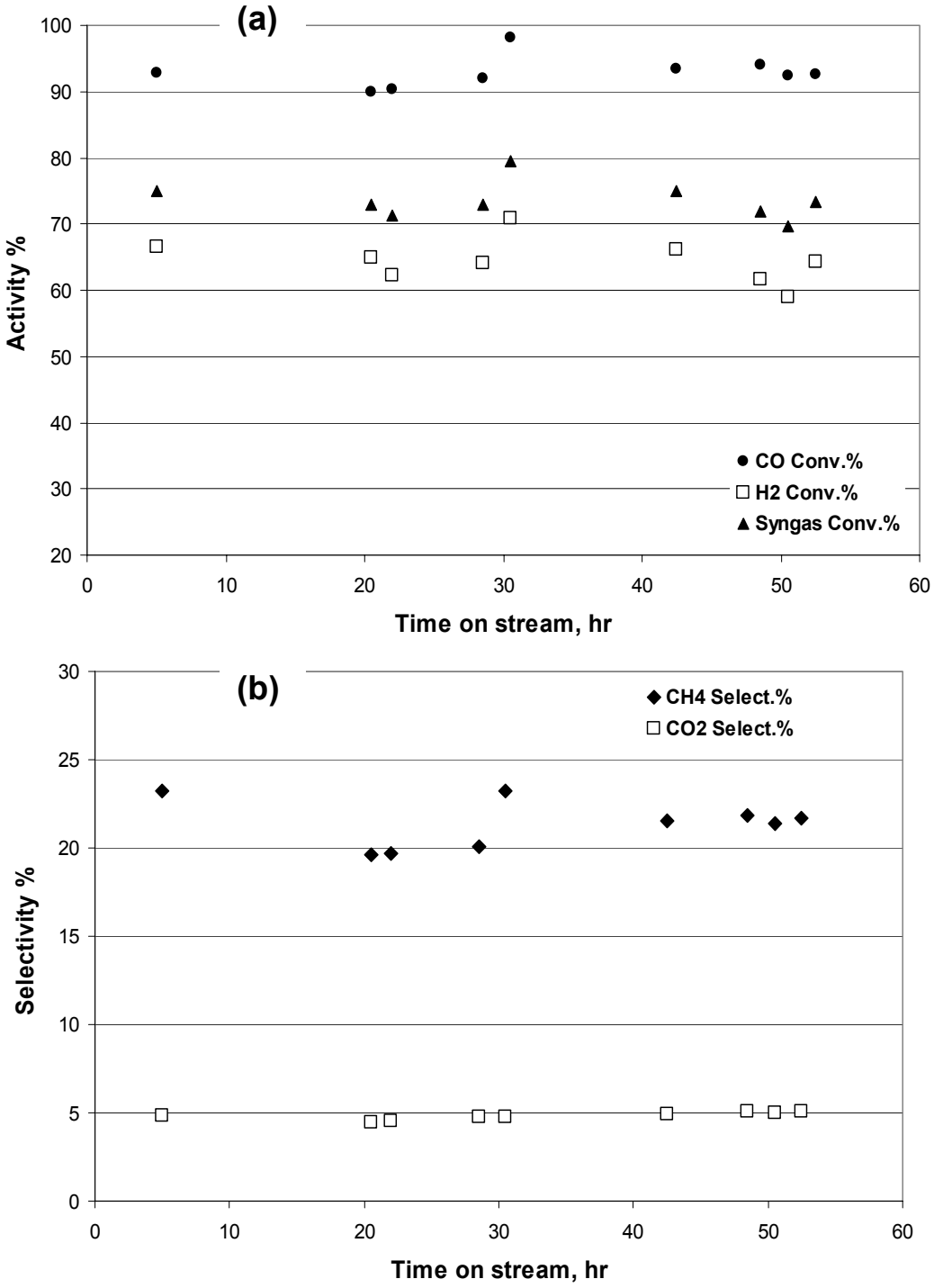

Figure 7.9 Stability of the activity and selectivity of the silica supported catalyst (A1/C) with time-on-stream.

A1/C and B1/C). The C1/C catalyst also yields higher chain growth probability than the silica supported catalyst as shown in Table 7.2.

Initial inspection of the results suggests a correlation between the catalyst BET area and methane selectivity. A1/C catalyst has the highest surface area and shows the highest methane selectivity, followed by B1/C and C1/C. While a relation between catalyst surface area and methane selectivity has not been previously drawn, recent reports shows that the active phase reducibility of the cobalt catalyst is a function of the support's BET surface area (Enache et al. 2004). Another characteristic that is known to give an indication of the methane selectivity is the size of Co particles (Khodakov et al. 2002). The smaller the Co particles the higher would be the methane selectivity. Since the XRD pattern for the silica supported catalyst (A1/C and B1/C) showed almost the same crystallite size of Co_3O_4 (≈ 14 nm), one can not correlate the methane selectivity to the Co particle size from these results. Nevertheless, our EMR analysis shows interesting valence states of the cobalt particles on the catalyst surface. On the high surface area silica catalyst, A1/C, cobalt particles are present mainly as Co_3O_4 whereas in B1/C both Co_3O_4 and Co^{2+} are present on the catalyst surface. On the other hand, Co^{2+} is found to dominate the surface of the alumina supported catalyst (C1/C) and even after long use for12 days TOS under mild reaction conditions (up to 260 °C and 30 bar) stable forms of Co^{2+} still exist accompanied by Co^0. These observations are also consistent with magnetic data shown in Figure 7.6. As a result, lower methane selectivity accompanied by higher chain growth probability (α-value) and olefin selectivity and in the case of C1/C can be attributed to the presence of stable form of Co^{2+}. This is in agreement with previous findings of many cobalt-based catalytic systems, whereas a direct correlation

between the extent of reduction and the catalyst selectivity was drawn (Reuel and Bartholomew 1984; Fu and Bartholomew 1985; Ernst et al. 1999; Khodakov et al. 2002). Khodakov et al (Khodakov et al. 2002)reported that crystallite Co_3O_4 was observed in all partially reduced catalysts (cobalt supported on mesoporous silica) of higher methane selectivity than the completely reduced. Reuel and Batholomew (Reuel and Bartholomew 1984) suggested that the presence of stable unreduced oxide phases capable of catalyzing water-gas shift reaction will result in higher methane selectivity.

The other interesting result is the relatively higher CO and syngas conversions in the silica supported catalysts (A1/C and B1/C) compared to that of the alumina supported catalyst (C1/C). In a previous study Reuel and Batholomew (Reuel and Bartholomew 1984) reported the activity of different cobalt-based catalytic systems and they ranked their catalysts in the following order: Co/TiO_2>Co/Al_2O_3>Co/SiO_2>100% Co>Co/MgO. Such ranking indicates that alumina supported catalyst should yield higher activity than the silica supported one. Nevertheless, Igelsia, et al. (Iglesia et al. 1992) have shown that the activity of cobalt catalysts is function of the metal dispersion and mostly independent of the type of support. Our results also showed that the lower surface area catalyst (B1/C) yield higher activity than the higher surface area catalyst (A1/C) which suggests no correlation between the catalyst surface area and its activity.

7.4 Conclusions

Results of the characterization of six Co-based Fischer-Tropsch (FT) catalysts, with 15% Co loading and supported on SiO_2 and Al_2O_3, are presented. Room temperature x-ray diffraction (XRD), temperature and magnetic field (H) variation of the

magnetization (M), and low-temperature (5 K) electron magnetic resonance are used for determining the electronic states (Co^0, CoO, Co_3O_4, Co^{2+}) of cobalt. Performance of these catalysts for FT synthesis is tested at a reaction temperature of 240 ^oC and pressure of 20 bars. Under these conditions, 15% Co/SiO_2 catalysts yield higher CO and syngas conversions with higher methane selectivity than 15%Co/Al_2O_3 catalysts. Conversely the Al_2O_3 supported catalysts gave much higher selectivity towards olefins than Co/SiO_2. These results yield the correlation that the presence of Co_3O_4 yields higher methane selectivity whereas the presence of Co^{2+} species yields lower methane selectivity but higher olefin selectivity. The activities and selectivities are found to be stable for up to 55 hrs on-stream.

CHAPTER 8

IMPACT OF COBALT-BASED CATALYST CHARACTERISTICS ON THE PERFORMANCE OF CONVENTIONAL GAS-PHASE AND SUPERCRITICAL-PHASE FISCHER-TROPSCH SYNTHESIS

8.1 Introduction

Industrial gas-phase Fischer-Tropsch synthesis (FTS) is accompanied by local overheating of the catalyst surface and high degrees of methane selectivity, thereby, decreasing the yield of the desired products. Furthermore, slurry phase Fischer-Tropsch reaction processes suffer from slow diffusion of syngas into the catalyst pores resulting in lower rates of reaction and other disadvantages. These considerations have driven research in FTS towards the application of supercritical fluid solvents in order to improve product control within the liquid fuels range. Supercritical fluid solvents combine the desirable properties of gas-like diffusion along with liquid-like heat transfer and solubility to overcome several of the current industrial limitations. Fine adjustments in operating conditions near the critical point can result in superior control of the Fischer-Tropsch process including tunable product distributions (Yan et al. 1998; Elbashir and Roberts 2004c)). As a result, conducting Fischer-Tropsch synthesis (FTS) under supercritical fluid solvent conditions was found to afford unique opportunities to manipulate the Fischer-Tropsch reaction environment to enhance production of liquid

fuels and value-added chemicals (such as α-olefins) from synthesis gas or syngas (a mixture of H_2 and CO) (Bukur et al. 1997; Fan and Fujimoto 1999; Subramaniam 2001; Jacobs et al. 2003; Elbashir and Roberts 2004a; Huang et al. 2004).

Previous studies (Yokota et al. 1990; Bukur et al. 1997; Jacobs et al. 2003; Elbashir and Roberts 2004a; Elbashir and Roberts 2004c; Huang et al. 2004) on the utilization of the supercritical fluids in FTS have shown several distinct advantages of the process compared to other conventional media including: (1) in situ extraction of heavy hydrocarbons from the catalyst; (2) enhancement of pore-transport and elimination of interphase transport limitations, thus, promoting reaction pathways to desired fuel range products; (3) enhanced desorption and selectivity of value added products (α-olefins); (4) improved heat transfer resulting in more of the long chain products. As a result, the utilization of a supercritical solvent phase in Fischer-Tropsch synthesis represents a promising new technique that will provide a clean, economical and efficient means of producing sulfur free fuels and chemicals.

Utilization of cobalt-based catalysts in FTS is known to provide the best compromise between performance and cost for the synthesis of hydrocarbons from syngas (CO/H_2 mixtures). Cobalt catalysts were also found to give the highest yields and longest lifetime producing mainly linear alkanes (paraffins) (Chaumette et al. 1995). Since cobalt catalysts are not inhibited by the water-gas-shift (WGS), they give high productivity at high syngas conversion (Van Berge and Everson 1997). The efficiency of the synthesis process is critically dependent on the effectiveness and the stability of the cobalt catalyst. Well known methods of preparing cobalt catalytic systems include impregnation of the metal precursor in the support or incipient wetness impregnation using an aqueous cobalt

precursor at low pH (Iglesia 1997a). Optimum catalysts with high cobalt concentration and site density can be prepared by controlled reduction of nitrate precursors introduced via melt or aqueous impregnation methods (Iglesia 1997a). Most of the industrial cobalt-based systems used in the FTS reaction are either alumina supported or silica supported catalysts. Therefore, cobalt dispersion on the supported catalyst surface (Tauster and Fung 1978) and the interaction of the Co with the metal oxide support (which affects the electronic density as well as the structure of the metal crystallites (Iglesia et al. 1992)) are assumed to play significant roles in the catalyst performance measured by the hydrocarbon selectivity (C_{5+}) and the catalyst activity.

Stability of the cobalt catalyst with time-on-stream (TOS) represents a major challenge to commercial-scale plants. The catalyst cost in addition to its regeneration cost represents a considerable proportion of the overall process cost. In many cases the cost of regenerating the catalyst is more expensive than the fresh catalyst cost (Zhan et al. 2004). Deactivation of the catalyst was assumed to be due to carbonaceous formations (specifically crystalline carbides) in the catalyst surface (Gruver et al. 2004), and also as a result of re-oxidation by the by-product water (Li et al. 2002a). In the current study, we have investigated the activity, selectivity, and stability of three cobalt based catalytic systems in both conventional gas-phase FTS and supercritical phase FTS (low surface area (LSA) 15% Co/SiO_2, high surface area (HSA) 15% Co/SiO_2, and 15% Co/ Al_2O_3). These catalytic systems were characterized by x-ray diffraction, magnetic and electron magnetic resonance (EMR) measurements before (fresh, calcined) and after the reaction (used catalysts). In addition, surface characterization (BET, pore volume, and pore diameter) was conducted for all catalysts.

In this work we will discuss the sensitivity of the cobalt and support structure and surface characteristics of the silica and alumina supported catalysts on both activity and selectivity of the FTS reaction. A comparative study of the stability of the physico-chemical characteristics, surface characteristics, and the oxidation states of the cobalt-based catalysts before and after the reaction in both conventional gas-phase FTS and supercritical phase FTS is presented.

8.2 Experimental

8.2.1 Catalyst Preparation and Reduction

The silica supported catalysts (high-surface-area (HSA) 15% Co/SiO_2, and low-surface-area (LSA) 15% Co/SiO_2) were prepared in our lab through the impregnation of fumed SiO_2 (99.0% purity purchased from Sigma-Aldrich) in an aqueous solution of cobalt nitrate (precursor $Co(NO_3)_2.6H_2O$-99.8% purity purchased from Aldrich Chemical Co). The 15% Co/ SiO_2 LSA was supported on fumed silica oxide of surface area 200 m^2/g, while the 15% Co/ SiO_2 HSA was supported on 380 m^2/g fumed silica oxide. The preparation technique of the silica-supported catalysts is reported in Chapter 7. Before running the reaction our calcined catalysts were reduced in a H_2 environment (50 sccm) at 320 °C and 1 atm for 4 hrs. This process took place in our high pressure reactor. Prior to initiating the reaction experiments, the reduced catalyst was cooled in a helium blanket to room temperature.

The alumina catalyst (15% Co/Al_2O_3) is a commercial catalyst purchased from United Catalyst Co. This catalyst was reduced in carbon monoxide at 280 °C for 18 hr before being used in the reaction.

8.2.2 Catalyst Characterizations

BET surface characterizations. The BET surface area, pore volume, and average pore diameter of our catalysts were measured by N_2 physisorption using a TriStar 3000 gas adsorption analyzer of high-quality surface area and porosimetry measurements. The details of the BET measurements is discussed earlier in Chapter 7.

X-ray diffraction (XRD). Room temperature X-ray diffraction (XRD) patterns of these catalysts were obtained with a Rigaku diffractometer using CuK_α radiation with λ = 0.15418 nm. Measurements of magnetization M versus. T and H were done with a commercial SQUID (superconducting quantum interference devices) magnetometer.

Electron magnetic resonance (EMR). Electron magnetic resonance (EMR) studies were carried out at the X-band frequency of 9.278 GHz with a variable temperature cryostat from Oxford Instruments. In this system, the microwave cavity remains at room temperature whereas the sample temperature can be varied from 4 K to 300 K. In the EMR resonance condition $h\nu = g\mu_B H_0$, the microwave frequency ν is accurately measured by a frequency counter and the resonance field H_0 by a NMR probe. The magnetic field is modulated at 100 kHz so that the experimental traces represent dP/dH versus H, with P being the power absorbed. The back ground for the magnetic theory and the interpretation of the magnetic data was discussed in details in our previous study (Dutta et al. 2004a).

8.2.3 Fischer-Tropsch Study

Reaction system. The FTS reaction was carried out in our high-pressure FTS unit shown in Figure 3.1. A more detailed description of the unit is given in Chapter 3, however a brief description will be provided here. A certified cylinder (purchased from Air Gas Co.) of H_2/CO ratio of 2 with a trace amount of N_2 (less than 2%) as an internal standard for chromatographic analysis was used in this study. The flow rate of the syngas reactants was controlled by digital mass flow controllers. For the supercritical FTS studies, the flow rate of the solvent hexane (HPLC grade of 99.9% purity purchased from Fisher Co.) was controlled by an HPLC pump. Before entering the reactor, the two streams (syngas and solvent) were mixed in a static mixer that was heated to the desired reaction temperature. The combined stream then entered the top of the downflow H.I.P reactor (1.27 cm×25.4cm of effective volume: 32 cm^3) that was positioned in a temperature controller tube furnace controlled by an *ATS* temperature controller system. The temperature inside the reactor was measured at six equally distanced positions along the length of the reactor using a profile thermocouple. This allows tracking of the temperature distribution along the length of the reactor. The pressure in the reaction zone was controlled by a back pressure regulator BPR (Tescom Inc.) located between the reactor and a hot trap.

Activity and selectivity measurements. Analysis of reactants and products was carried out by two online GCs as described previously in Chapter 3. The results from the two GCs were used for conversion and selectivity calculations. A Varian 3300 GC with capillary column (DB-5) and a FID detector was used for the analysis of C_2-C_{40} hydrocarbons and

oxygenates. Analysis of permanent gases (H_2, CO, N_2, CH_4, CO_2, C_2H_4, and C_2H_6) was conducted by a Varian CP-3800 GC with a packed column (Hayesep-DB100/120) and TCD detector. Quantitative analysis of the results from the Varian CP-3800 provided the necessary data for the calculations. Reactants conversion (CO conversion and H_2+CO (syngas) conversion), CH_4 selectivity, CO_2 selectivity, and C_2 (ethane and ethylene) selectivities were calculated using the response factor of N_2 from the TCD analysis as a reference. On the other hand, hydrocarbon product distributions (i.e. C_2 to C_{30} selectivity data) were determined from the FID and TCD analysis as described in Appendix A.

8.3 Results and Discussion

8.3.1 BET and Surface Measurements

A summary of the BET measurements of the catalysts is shown in Table 8.1. As shown in the table the BET surface area was found to vary over a wide range (from 94.94 m^2/g to 255.7 m^2/g), while the silica supported catalysts showed almost similar pore volume (1.24 and 1.23 cm^3/g) despite the difference in surface area. The alumina supported catalyst showed much lower pore volume (0.28 cm^3/g) than the silica supported catalysts (1.2 cm^3/g). The 15% Co/SiO_2 (LSA) was found to have the highest pore radius (309.7 Å). The variety in the characteristics of the three different cobalt-based catalytic systems offers our study an opportunity to compare the influence of the catalyst surface characteristics on both activity and selectivity of FTS under conventional gas-phase and supercritical phase conditions.

Table 8.1 BET surface measurements of the cobalt-based catalytic systems.

	Catalyst		
	15% Co/SiO_2 HSA	15% Co/SiO_2 LSA	15% Co/ Al_2O_3
BET area (m^2/g)	255.67	158.4	94.94
Pore volume (cm^3/g)	1.2441	1.227	0.276256
Pore radius (Å)	194.65	309.73	114.83

8.3.2 XRD and EMR characterizations

Four used catalyst samples supported on either silica or alumina, and one unused reduced catalyst were characterized by XRD and EMR. Detailed descriptions of the XRD and EMR characterization of these catalytic systems, as both fresh samples (before the reaction) and calcined samples (after the calcination process), are given in Chapter 7. In this study, the characterization of the used catalysts (after reaction) following conventional gas-phase FTS and supercritical FTS is presented. The objective of this characterization is to examine changes in the catalyst valence states and structure after long TOS under high-pressure high-temperature FTS reactions. Such comparisons are expected to provide insights into the advantages that supercritical phase FTS provides over conventional gas-phase FTS in terms of catalyst stability. The results of the XRD and EMR characterizations are summarized as follows:

i. S1 (15%Co/SiO_2 – LSA). The S1 sample is a 15% Co/ SiO_2 (LSA) catalyst used for 10 days on-stream under gas-phase FTS conditions. The XRD pattern of this catalyst shows no distinct peak that can be identified with Co^0, CoO, Co_3O_4. All the observed peaks are

due to different forms of SiO_2 mostly in non-crystalline form (Figure 8.1). In the magnetic susceptibility χ versus temperature data (Figure 8.2), a sharp peak at $T_b \approx 5$ K is observed. The large magnitude of χ and the absence of any observable peak due to Co_3O_4 (near 40 K) or CoO (200-300 K) confirms that in this sample, the oxides of Co are absent. If we associate $T_b \approx 5$ K with Co nanoparticles, then from the known T_b versus D (diameter of the nanoparticles) relationship, we estimate that the size of these nanoparticles is ≈ 1 nm or less. In the hysteresis loop, there is no shift of the loop in the field-cooled (FC) case, confirming that Co/CoO or Co/Co_3O_4 interface are absent in this sample (Figure 8.2). In the EMR studies, we observe a very symmetrical line at all temperatures from 5 K to 300 K, whose EMR parameters are characteristic of Co nanoparticles.

In summary, analysis of our results strongly suggest the presence of cobalt nanoparticles of about 1 nm size, without the presence of any of the oxides of Co (see Table 8.2).

ii. S2-15%Co/SiO₂ – HSA. The S2 sample is a 15% Co/ SiO_2 (HSA) catalyst used for 13 days on-stream under gas-phase FTS conditions. In XRD studies (Figure 8.1), distinct peaks due to FCC (face-centered cubic) phase of Co are identified along with smaller peaks due to CoO. All the remaining peaks are due to different forms of SiO_2.

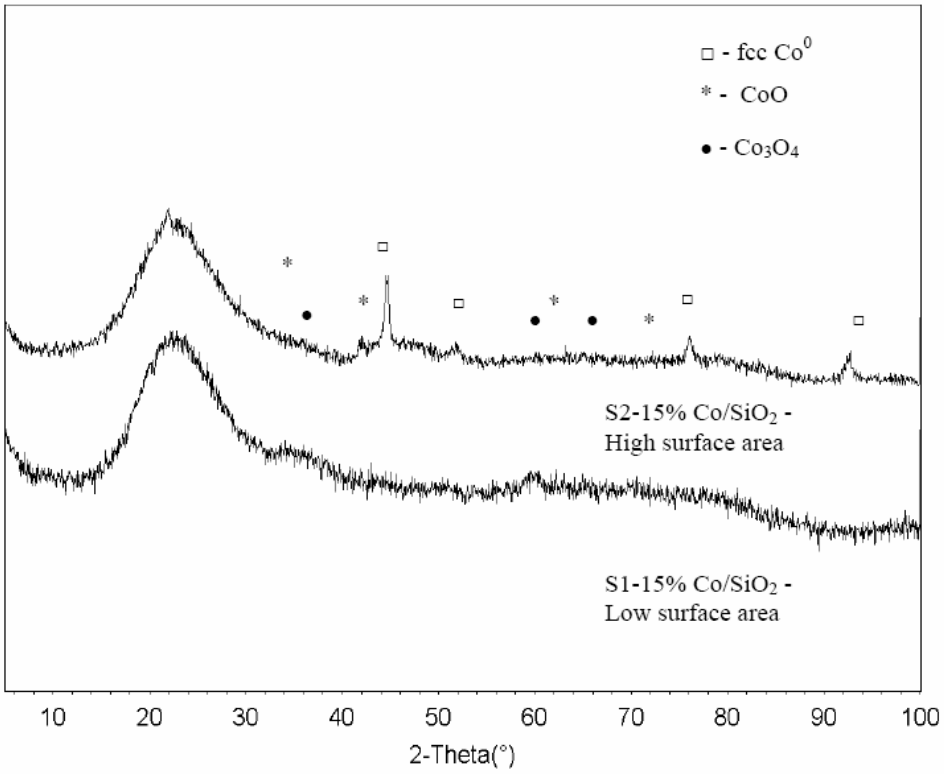

Figure 8.1 Room temperature XRD patterns of the catalysts shown using $\lambda = 0.15418$ nm.

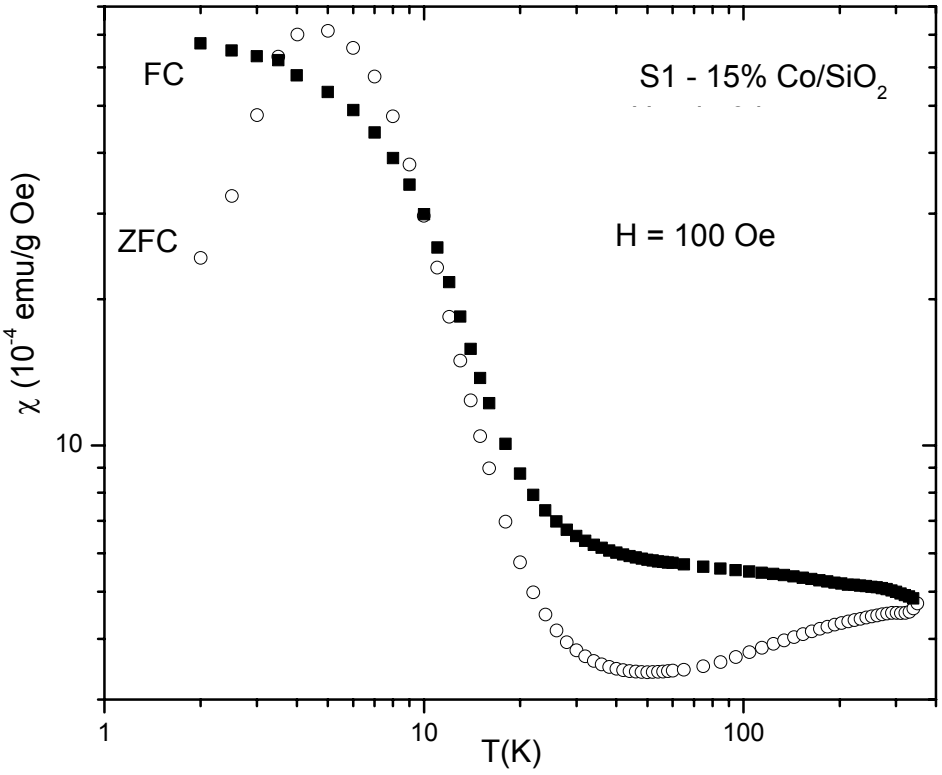

Figure 8.2 Temperature variations of the magnetic susceptibility χ for the S1 catalyst sample (used 15% Co/SiO_2 LSA).

Table 8.2 Summary of the XRD and EMR characterization of the used cobalt-based catalytic systems under both gas-phase FTS and supercritical hexane FTS**.**

Samples	Particle size of Co^0 (nm)	Coercivity (Oe)	EMR	XRD	Calcined samples[a]
S1 (HSA 15%Co/SiO_2) Used 10 days	≤ 1	35 at 5 K 230 at 300 K	g ≈ 2.7 at 6 K, g ≈ 2.1 at 300K	SiO_2(quartz, cristobalite, tridymite)	SiO_2, Co_3O_4
S2 (LSA 15%Co/SiO_2) Used 13 days	≈ 3	1107 at 5 K 475 at 300 K	g ≈ 2.073 at 6K	fcc-Co^0, CoO, Co_3O_4 (small) SiO_2 (cristobalite)	SiO_2, Co_3O_4, Co^{2+}-weak line g ≈ 4.3.
A1 (15%Co/Al_2O_3) Used 11 days	> 12	65 at 5 K 150 at 300 K	g ≈ 4.0 at 6 K	hcp-Co^0, CoO Co_3O_4; γ-Al_2O_3 ε -Al_2O_3	Co_3O_4, δ-Al_2O_3, Co^{2+}-line,g ≈4 .3 with sharp line[b]
A2 (15%Co/Al_2O_3) Used 7 days	≈ 10	No at 5 K 32 at 300 K	g ≈ 2.7 at 6 K	hcp-Co^0, fcc-Co^0; γ -Al_2O_3	
A3 (15%Co/Al_2O_3) Unused, reduced catalyst	> 12	No at 5 K 12 at 300 K	g ≈ 4.2 at 6 K	Co_3O_4;γ- Al_2O_3 ε-Al_2O_3 CoO, hcp Co^0	

[a]Calcined samples before reduction and reaction characterized by XRD, magnetic, and EMR; details of the characterizations are illustrated elsewhere (Dutta et al. 2004a).
[b]XRD, magnetic, and EMR characteristics of the alumina catalyst before the reduction.

In magnetic studies, a broad peak near 200 K and a sharper peak near 20 K are observed (Figure 8.3). The peak near 200 K is identified with CoO whereas the peak near 20 K with Co nanoparticles. Using $T_b \approx 20$ K, the particle size of Co is estimated to about 3 nm. The hysteresis loop is considerably broader compared to that in S1 and it shifts when the sample is cooled in a magnetic field (Figure 8.4). This loop-shift confirms the presence of Co/CoO interface. In EMR studies, a very asymmetric broad line is observed which does not provide any additional useful information.

In summary, this sample confirms Co/CoO nanoparticles of about 3 nm size. It is possible that the presence of small amounts of CoO may be due to surface oxidation of the nanoparticles (see Table 8.2).

iii. A1-15%Co/Al_2O_3. The A1 sample is a 15% Co/ Al_2O_3 catalyst used for 11 days on-stream under supercritical hexane phase FTS conditions. In XRD studies, we can identify hcp (hexagonal-closed packed) Co^0, CoO and two forms of Al_2O_3 which is the support material. Co_3O_4, if present, is negligible in quantity (Figure 8.5).

In magnetic studies of χ versus T (Figure 8.6) under ZFC (zero field cooled) and FC conditions, the blocking temperature T_b of Co^0 is above 350 K, suggesting that the particle size of $Co^0 > 12$ nm. A broad hump near 270 K observed in Figure 8.6 is due to CoO and a weak peak near 50 K may be due to minute quantities of Co_3O_4. In hysteresis loop, we do not observe a loop shift under FC conditions, suggesting that oxides of Co and Co^0 are separate entities. The small value of the coercivity supports this conclusion. The sharp rise in the χ for $T < 20$ K suggests the presence of a paramagnetic species such

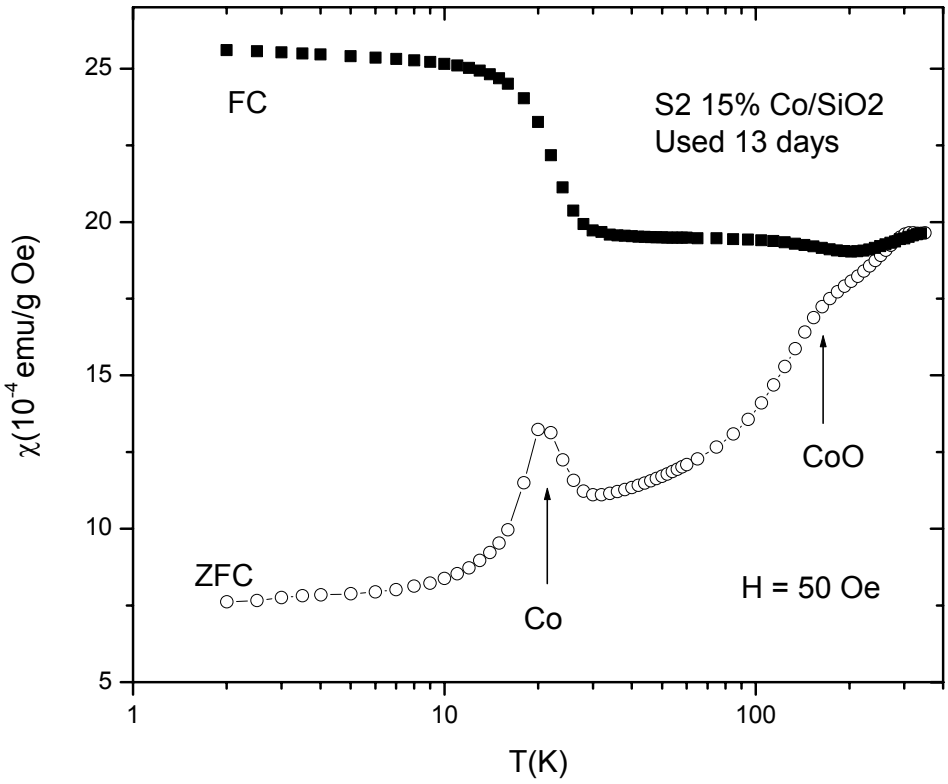

Figure 8.3 Temperature variations of the magnetic susceptibility χ for the S2 catalyst sample (used 15% Co/SiO_2 HSA).

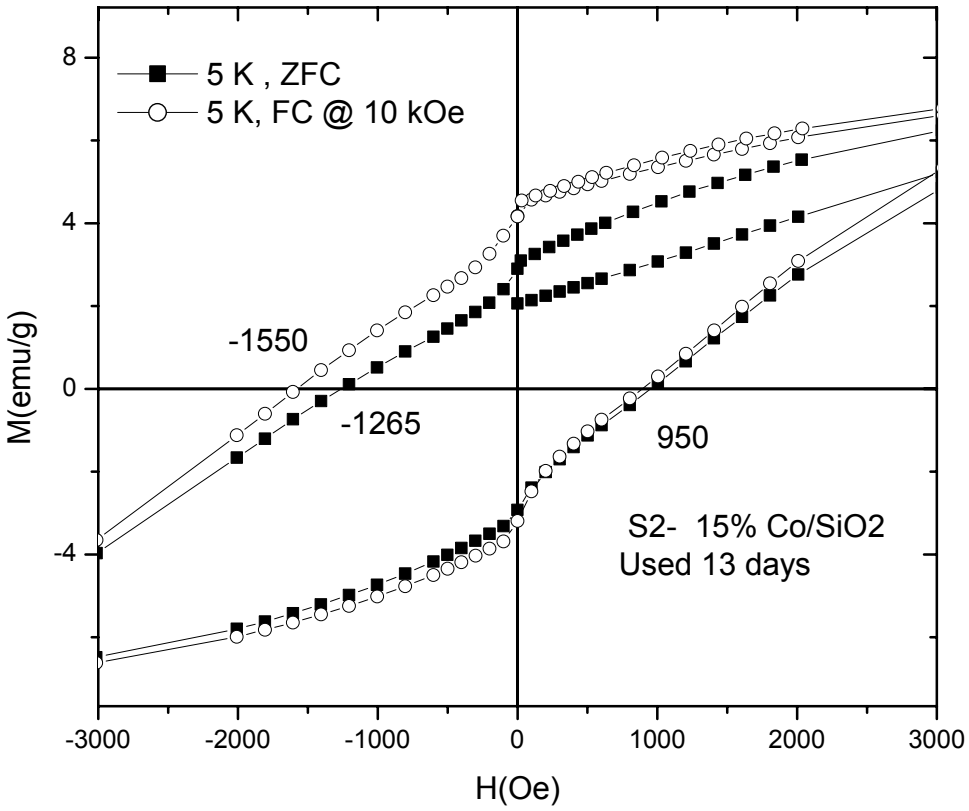

Figure 8.4 Magnetic field variations of the magnetization M at 2 K for the S2 sample.

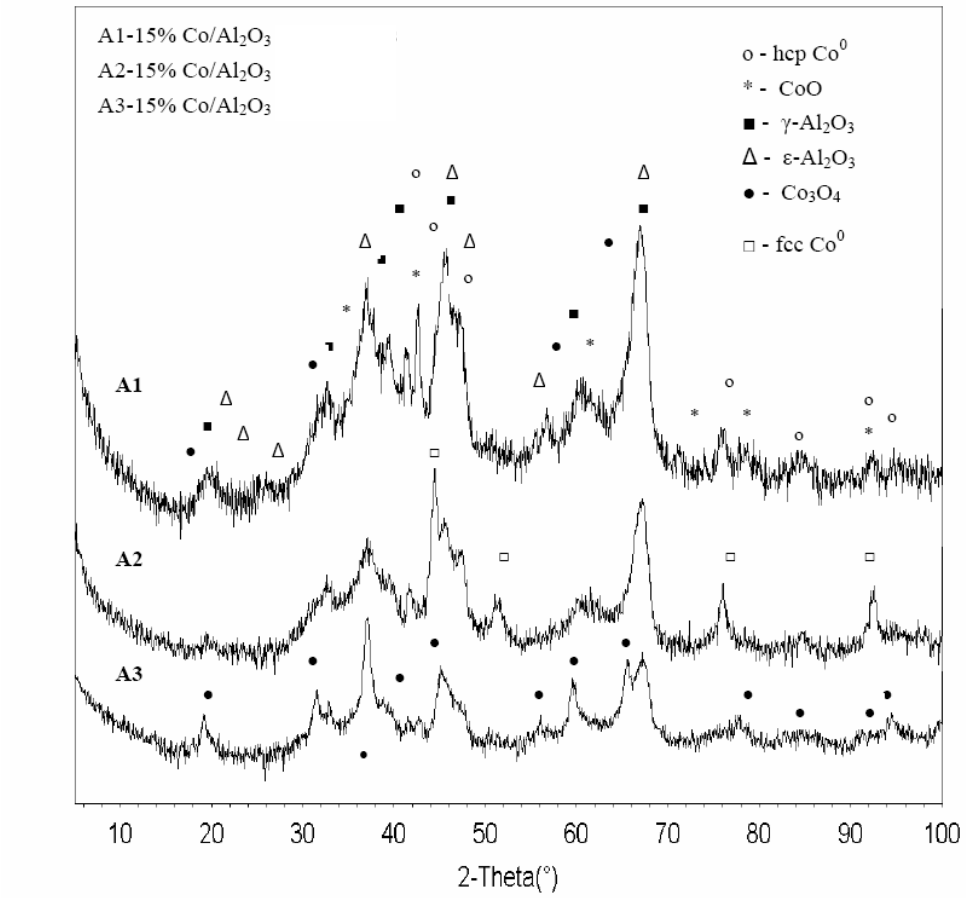

Figure 8.5 Room temperature XRD patterns of the alumina supported catalysts (A1, A2, and A3) shown using $\lambda = 0.15418$ nm.

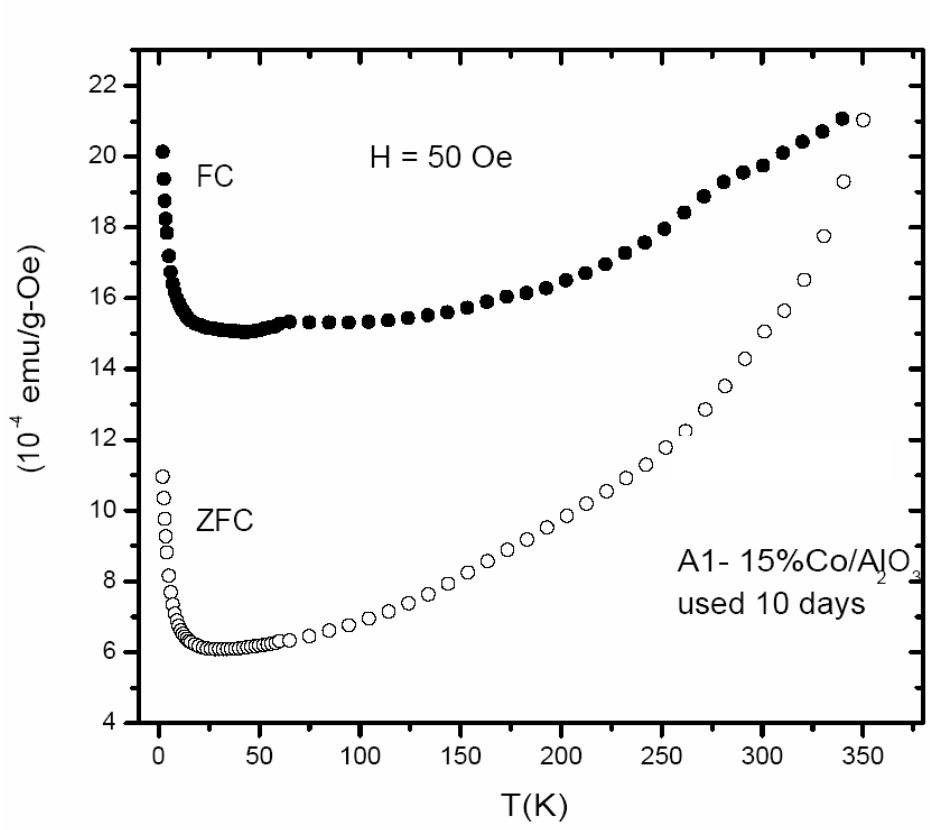

Figure 8.6 Magnetic field variations of the magnetization M at 2 K for the A1 sample.

as Co^{2+} doped into Al_2O_3 lattice. In the EMR studies, we see a broad line near g ≈ 4.0, most likely to Co^{2+} ions doped into Al_2O_3 and a broad line from the Co^0 particles.

In summary, the analysis of the XRD and magnetic data indicate the presence of hcp Co^0 nanoparticles of size > 12 nm, CoO and minute quantities of Co_3O_4 and Co^{2+} doped in Al_2O_3. Two forms of the support Al_2O_3 (γ-Al_2O_3 & ε-Al_2O_3) are also identified (see Table 8. 2).

iv. A2-15%Co/Al$_2$O$_3$. The A2 sample is a 15% Co/ Al_2O_3 catalyst used for 7 days on-stream under gas-phase FTS conditions. The XRD diffractogram shown in Figure 8.5 yields lines for FCC Co^0 and Al_2O_3, with a smaller amount for hcp Co^0. All the observed lines are identified by these three phases.

In the magnetic studies, the χ versus T plot for the ZFC and FC data bifurcates near 200 K which is identified as the blocking temperature T_b of Co^0 Figure 8.7. From this value of T_b, a particle size of about 10 nm for Co^0 is estimated. The hysteresis loop at 5 K for the FC and ZFC samples gives no loop shift under field-cooling and negligible coercivity. This is consistent with the presence of Co^0 nanoparticles without the presence of any of the oxides of Co. In EMR studies, a broad line with linewidth ΔH = 2500 Oe, observed both at room temperature and 5 K, is in line with the above conclusion.

In summary, the electronic state is Co^0, with larger amount of the FCC phase and a smaller amount of the hcp phase. The particle size of about 10 nm is estimated (see Table 8.2).

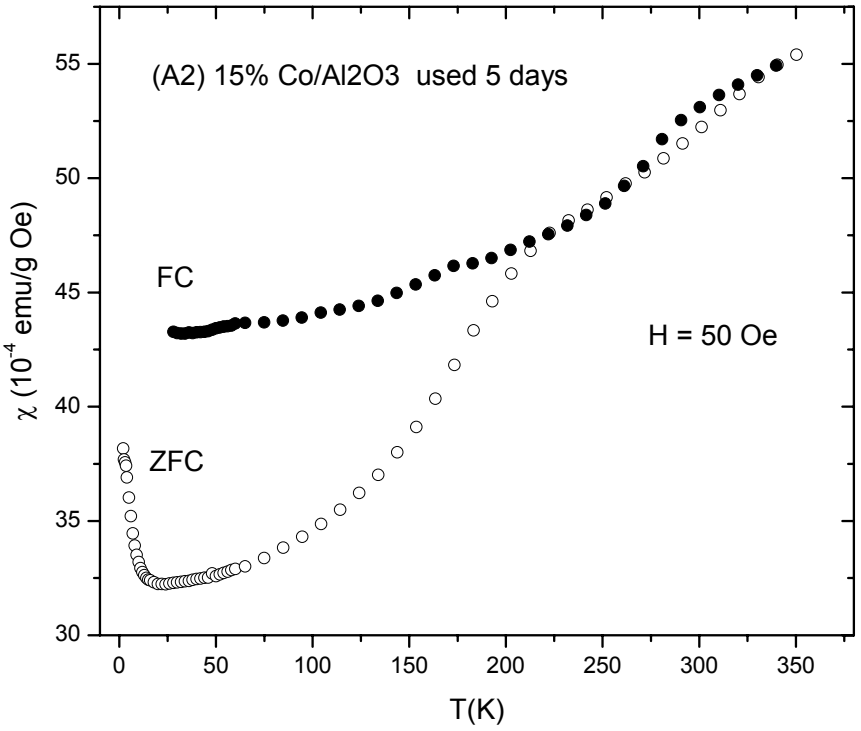

Figure 8.7 Magnetic field variations of the magnetization M at 2 K for the A2 sample.

v. A3-15%Co/Al_2O_3. The A3 sample is a 15% Co/ Al_2O_3 catalyst reduced in CO environment for 18 hr at 280 °C (has not been used in FTS reaction). From the XRD studies (Figure 8.5), we can identify a significant amount of Co_3O_4 and two phases of Al_2O_3. In addition, only a small amount of hcp Co^0 is identified.

In the χ versus T data (Figure 8.8), the bifurcation of the FC and ZFC data begins to occur at the maximum temperature of 350 K used in these experiments. Therefore, the blocking temperature $T_b > 350$ K indicates that a particles size > 12 nm for Co^0 is present in the surface. There are weak broad peaks near 200 K and 50 K which are respectively associated with CoO and Co_3O_4. The reason the Co_3O_4 peak is not more evident is because of the large χ values of Co^0. The rise of χ at lower temperatures is due to a paramagnetic species. The EMR studies shows a line at $g \approx 4.0$ which can be definitely associated with Co^{2+} ions doped in the Al_2O_3 matrix.

In summary, the electronic state of cobalt in this sample is primarily Co_3O_4. Further confirmation of the negligible reduction is a lack of any hysteresis loop shift under FC conditions (Figure 8.8) and negligible coercivity.

8.3.3 Fischer-Tropsch studies under supercritical hexane media and conventional gas-phase media

Selection of appropriate conditions for supercritical hexane FTS

Both conventional gas-phase FTS and supercritical hexane FTS reactions were carried out at relatively high syngas partial pressure (P_{syngas} of 20 bar) and high reaction temperatures (230 °C- 250 °C). These conditions are similar to that of industrial fixed-bed reactors and favor high syngas conversion at reasonable chain growth probability

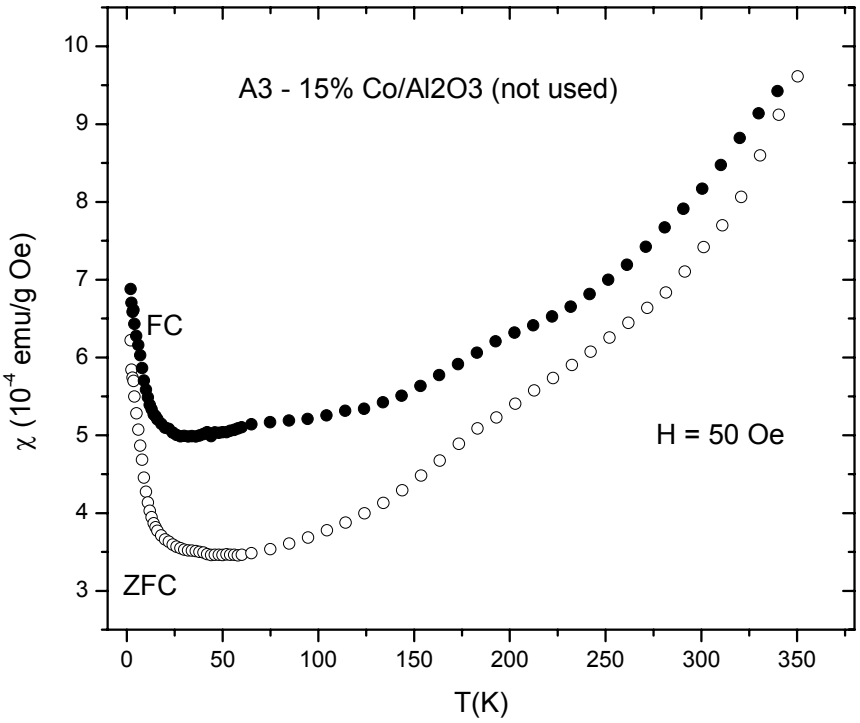

Figure 8.8 Magnetic field variations of the magnetization M at 2 K for the A2 sample.

(α-value above 0.60). Initially, we evaluated the influence of hexane/syngas ratio on the reaction performance in order to select appropriate conditions for the supercritical hexane FTS. The influence of hexane/syngas molar ratio was studied over a 15% Co/SiO_2 (LSA) at 240 °C and total pressure of 57 bar in three molar ratios (3/1, 6/1, and 9/1). In all cases the syngas flow rate was kept constant at 50 sccm/g_{cat}. The flow rate of hexane was then adjusted to provide the required hexane/syngas molar ratio. A hexane flow rate of 7.72×10^{-3} mol/min was used for a hexane/syngas molar ratio of 3/1, 13.25×10^{-3} mol/min for a 6/1 ratio, and 20.74×10^{-3} mol/min for a 9/1 ratio. As a matter of fact, varying the hexane/syngas molar ratio will affect the concentration of reactants (CO, H_2), the phase behavior and the critical properties of the solvent/reactant mixture, the phase behavior of the solvent/reactant/product mixture, and the residence time, as well as, the contact time.

Figure 8.9*a* shows the influence of hexane/syngas ratio on the activity of the catalyst measured by % CO conversion at 240 °C and total pressure of 57 bar (P_{hexane} = 42 and P_{syngas}= 15 bar; in the case of hexane/syngas ratio = 0 (gas-phase) $P_{total} = P_{syngas}$ = 15 bar). As shown in Figure 8.9*a,* a negligible change in CO conversion was achieved by shifting the process from gas-phase operation to supercritical hexane (3/1) operation. The figure also demonstrates that as the hexane/syngas molar ratio increases (from 3/1 to 9/1) the activity decreases due to dilution by the solvent (decreased mole fraction of the reactants). The relation between CO conversion and hexane/syngas ratio is almost linear within the studied range. Figure 8.9*b* shows the influence of hexane/syngas ratio on the selectivity of the catalyst under the same conditions. A significant drop (almost 40%) in methane selectivity is obtained when shifting the process from gas-phase FTS to supercritical hexane (3/1 ratio), followed by a linear decrease as the ratio increases. Chain

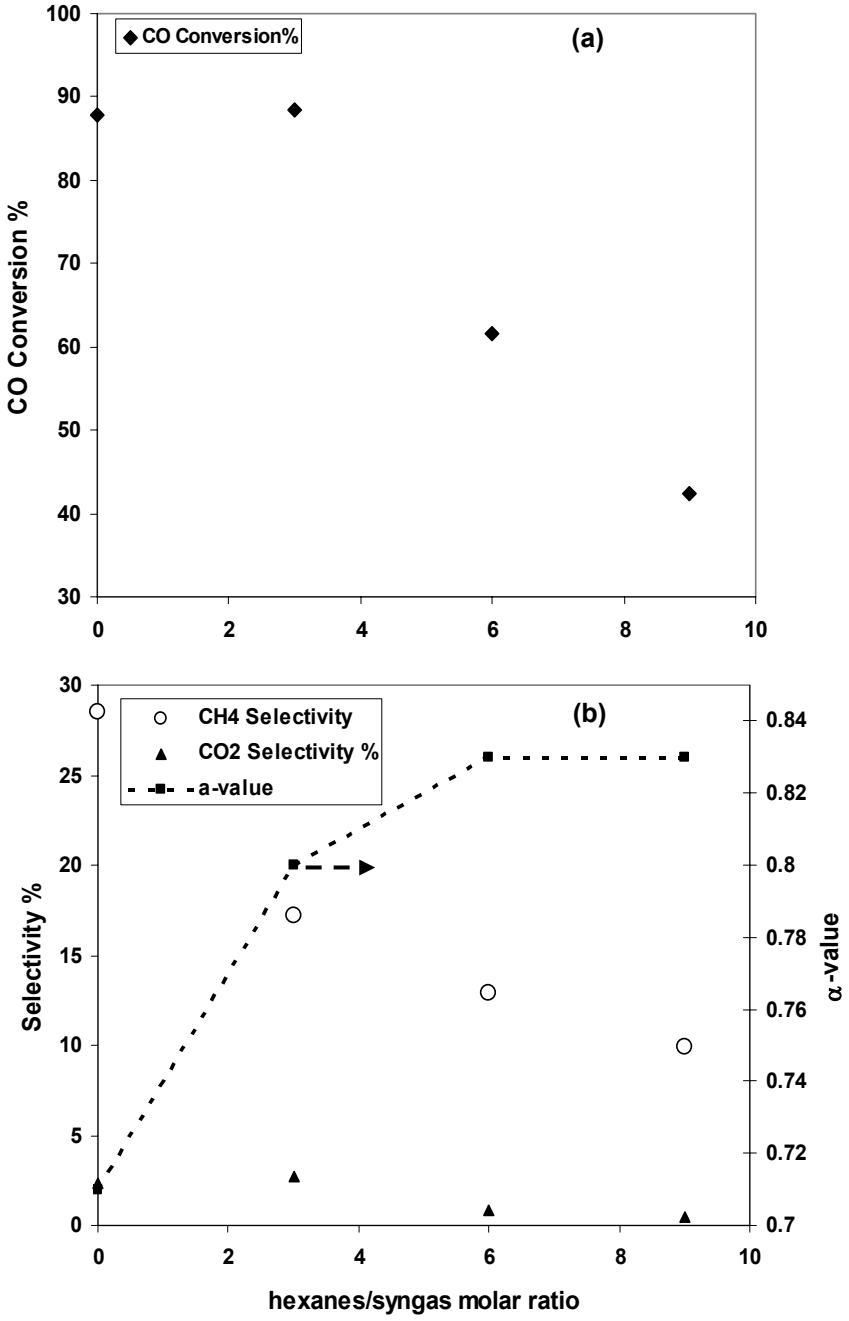

Figure 8.9 Effect of hexane/syngas molar ratio on the activity and selectivity of a 15% Co/SiO_2 (LSA) at 240 °C and syngas flowrate of 50 sccm/g_{cat}.

growth probability (α-value) significantly improved when shifting the process from gas-phase (α= 0.71) to supercritical hexane phase of ratio 3/1 (α= 0.80), however a slight change in α-value was observed from ratio 3/1 up to ratio 6/1 then to ratio 9/1 (α= 0.83 for both ratios). CO_2 selectivity was not affected by shifting the process from gas-phase to supercritical phase or by changing hexane/syngas molar ratio as shown in Figure 8.9*b*.

As a result of the above investigations, the hexane/syngas molar ratio of 3/1 was selected for the supercritical phase FTS studies, because of the high CO conversions and relatively good selectivity (methane and chain growth probability) obtained at this ratio compared to the others.

Influence of the cobalt catalyst surface characteristics on the FTS performance

Table 8.3 shows a summary of the activity and the selectivity of the three cobalt-based catalysts in both SCH-FTS and conventional gas-phase FTS at the same reaction temperature (240 °C) and syngas partial pressure (20 bar). Higher CO conversion and syngas conversion were obtained in SCH-FTS, except for the case of 15% Co/SiO_2 (HSA), where slightly higher conversions were achieved under gas-phase conditions. Conducting the FTS reaction in the SCH medium results in a significant drop (more than 40%) in methane selectivity compared to that in conventional gas phase FTS as shown in Table 8.3. Similarly, the chain growth probabilities (α-values) are higher in SCH-FTS than gas-phase FTS, accompanied with higher α-olefins selectivities (results not shown). In order to see the influence of syngas conversion on selectivity towards CO_2 and CH_4, a plot of conversion versus the selectivity (collected from a broad range of reaction conditions) is shown in Figures 8.10, and 8.11. Even though, it is difficult to conclude a

Table 8.3 Activity and selectivity of the cobalt-base catalysts under both supercritical-hexane FTS and gas-phase FTS.

	15% Co/SiO_2 HSA		**15% Co/SiO_2 LSA**		**15% Co/ Al_2O_3**	
	SCH[a]	Gas-Phase[b]	SCH[a]	Gas-Phase[b]	SCH[a]	Gas-Phase[b]
CO Conversion %	78.3	83.2	88.4	87.9	79.6	76.8
Syngas (H_2+CO) Conversion %	69.1	71.9	81.7	80.8	74.2	65.4
CH_4 Selectivity %	14.2	21.3	17.2	18.9	9.8	16
α-value	0.87	0.65	0.83	0.71	0.81	0.78

[a]SCH: Supercritical-Hexane FTS. Reaction conditions: temperature = 240 °C, total pressure = 60 bar (P_{syngas}= 20 bar, P_{hexane} = 40 bar), syngas flowrate 50 sccm/g_{cat}, hexane flowrate = 1mL/min.
[b]Gas-Phase FTS at 240 °C and 20±2 bar (see Chapter 7).

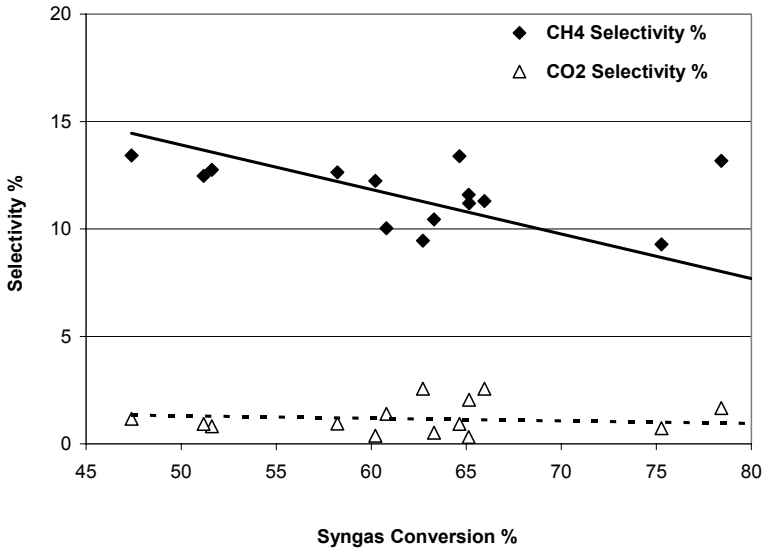

Figure 8. 10 CH_4 and CO_2 selectivities as function of syngas conversion in SCH-FTS. Catalyst is15% Co/SiO_2 HSA; reaction temperature is 240 °C; total pressure is 65 bar; syngas flowrate is 50 sccm/g_{cat}; and molar ratio of hexane to syngas is 3. Symbols are the experimental data, whereas lines are the linear correlation of the data.

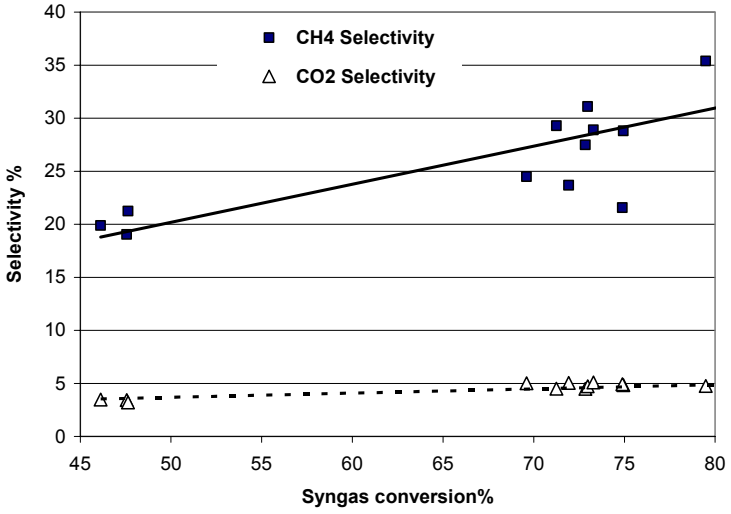

Figure 8.11 CH_4 and CO_2 selectivities as function of syngas conversion in gas-phase FTS. Catalyst is15% Co/SiO_2 HSA; reaction temperature is 240 °C; total pressure is 20 bar; and syngas flowrate is 50 sccm/g_{cat}. Symbols are the experimental data, whereas lines are the linear correlation of the data.

specific trend from Figure 8.10; the linear correlation suggests a decrease in methane selectivity as syngas conversion increases. Nevertheless, in the gas-phase FTS (Figure 8.12) the linear correlation exhibits an increase in methane selectivity with the syngas conversion. CO_2 selectivity is found to be less dependent on conversion in both SCH-FTS and gas-phase FTS. The interesting result shown in Figure 8.10 indicates that operating FTS reaction in SCH media offers a better opportunity to minimize the selectivity of the most undesired product in the hydrocarbon products spectrum (i.e. methane) even at high syngas conversions.

Correlations of the catalyst activity and selectivity (as presented in Table 8.3) with the catalysts surface characteristics (as presented in Table 8.1) reveal that the pore radius of the catalyst has a direct influence on both syngas and CO conversions in gas-phase FTS. As shown in Figure 8.12a as the FTS activity increases with the pore diameter of the catalyst. This result is in agreement with the previous findings of Khodakov et al. (2002) who showed that both the size of the supported Co_3O_4 and their reducibility is strongly dependent on pore diameter of silica supports. They also suggested that small cobalt particles in narrow pores are more difficult to reduce than larger particles in wider pores. On the hand, no direct correlation between the pore diameter and activity of the catalysts in SCH-FTS is observed as shown in Figure 8.12b. Because of the similarity in pore volume of the two silica-supported catalysts, investigations of pore volume effects on the activity and selectivity in both gas-phase FTS and SCH-FTS is limited. An interesting result is that α-value in gas-phase FTS is found to decrease as pore volume increases, whereas, in SCH-FTS it increases with pore volume.

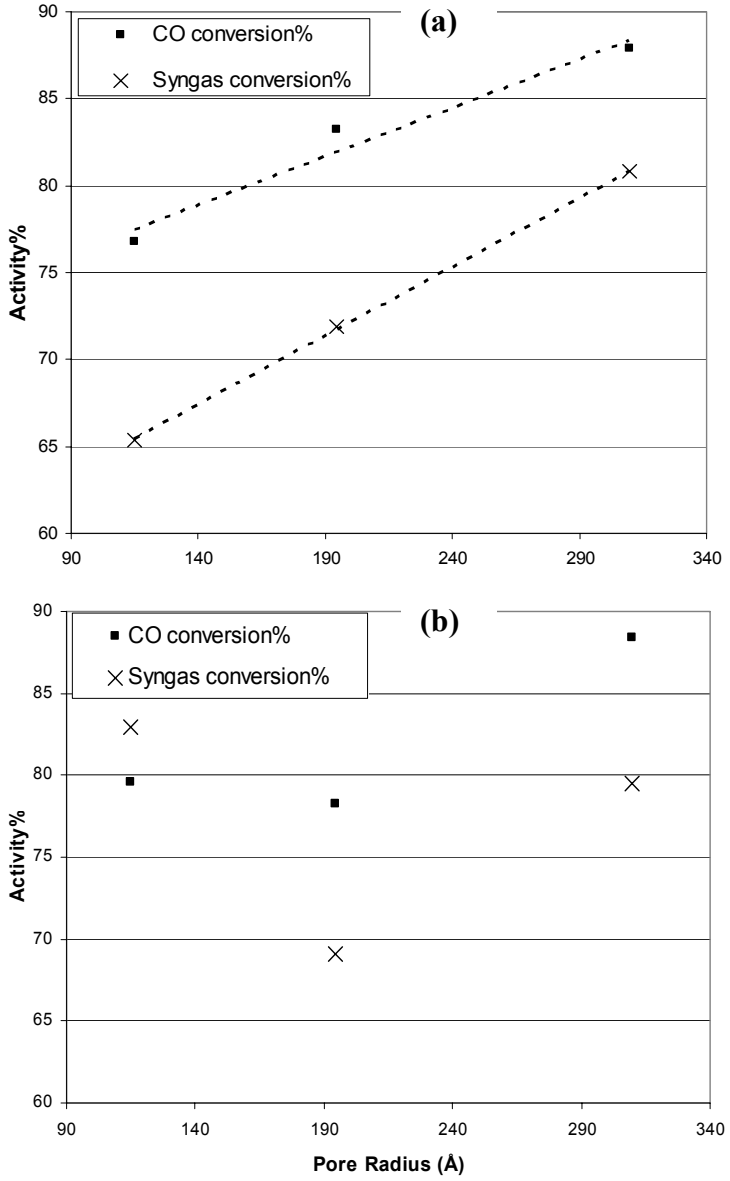

Figure 8.12 Influence of pore diameter on the activity of cobalt-base catalysts under (a) gas-phase FTS, and (b) SCH-FTS at 240 °C and P_{syngas} of 20 bar.

Pressure is known to affect both FTS termination rates and secondary reactions (Iglesia et al. 1993a). High gas phase pressure FTS operation could result in condensation of heavy hydrocarbons that normally exists as gases under atmospheric pressure operations. This condensation will cause diffusion limitations of CO reactant molecules resulting in an increase of the effective H_2/CO ratio, which usually leads to high methane selectivity and lower chain growth probability (Reuel and Bartholomew 1984). These restrictions are obviously influenced by the catalyst pores structure. However, this scenario is changed for the SCH-FTS where the dense supercritical medium provides high solubilities for heavy products and miscibility for reactant gases. This facilitates a single-phase operation for both reactants and products under the SCH operating conditions listed in Table 8.3, rather than two-phase operation (Elbashir and Roberts 2004a). In other words, the SCH-FTS processes are not impacted by mass transfer limitations as is the case in conventional gas-phase FTS. Therefore, neither pore radius nor pore volume has a significant influence on the SCH-FTS activity and selectivity. The slight increase in methane selectivity with the pore volume in SCH-FTS has not been accompanied by lower α-value as the case in the gas-phase FTS. In a previous study (Elbashir and Roberts 2004b), we have shown that classical surface reaction kinetics fails to predict the reaction rates (specifically, CH_4 formation rates) in SCH-FTS, because of the nonideality of the reaction mixture. Methanation rates are different from that of the FTS primary and secondary reaction rates and it more likely to be influenced by the reaction conditions and the cobalt electronic states rather than the mass transfer limitations inside the catalyst pores. A previous report (Khodakov et al. 2002) has shown that higher methane selectivity is observed in narrow pores due to either unreduced cobalt

species or small cobalt particles, which produce higher relative amounts of methane than large cobalt particles. This is in agreement with the cobalt particle size reported in Table 8.2 showing that the sizes of silica supported catalysts are from 1-3 nm whereas that of alumina is 12 nm.

Stability of the cobalt catalyst activity and structure after FTS reaction

Figures 8.13 and 8.14 show an example of stability tests on the alumina-supported catalyst (15% Co/Al_2O_3) under different reaction conditions in the SCH-FTS and gas-phase FTS reactions at relatively long TOS, respectively. Syngas conversion is used to represent the activity of the catalyst, while methane selectivity is used to represent the selectivity. Under SCH (Figure 8.13), the initial catalyst stability test was conducted at 240 °C and 60 bar for 48 hrs TOS. During this time, the catalyst showed good stability in syngas conversion (~ 80%) and in CH_4 selectivity (~17%). The temperature was then decreased to 230 °C, while the pressure was kept constant at 60 bar. As a result, both syngas conversion and CH_4 selectivity decreased to ~58% and ~9%, respectively. A stable trend was observed under these conditions for more than 48 hrs TOS. The stability test was then followed by increasing the temperature to 250 °C and the pressure to 65 bar. At these conditions, syngas conversion reaches its highest level, 93%, at the initial 2 hrs TOS and then declined to ~87% for more than 100 hrs TOS. The trend of CH_4 selectivity with TOS shows good stability at ~20%. The aforementioned conditions were selected

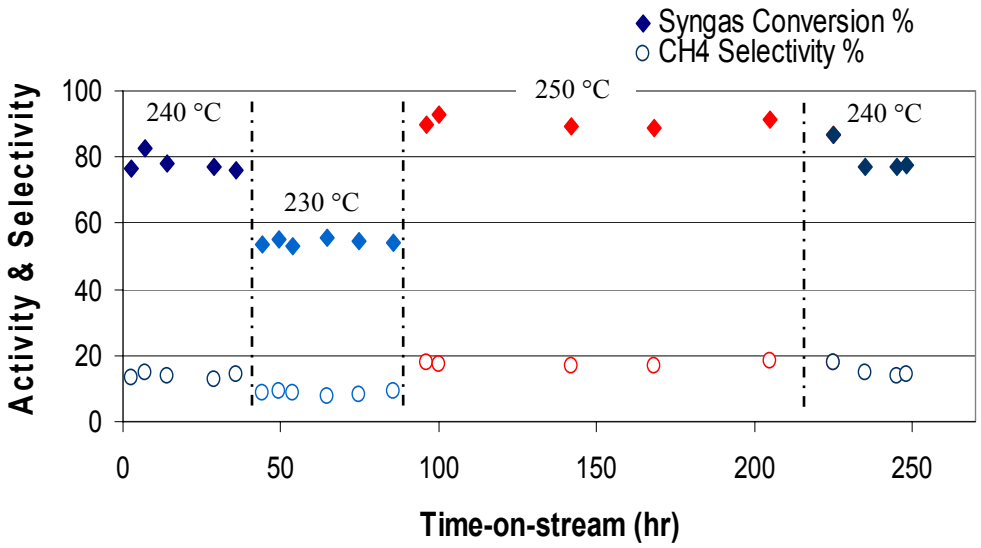

Figure 8.13 Stability of the 15% Co/Al_2O_3 catalyst activity (syngas conversion (%)) and selectivity (CH_4 selectivity (%)) with TOS in SCH-FTS at different reaction conditions (240 °C and 60 bar; 230 °C and 60 bar; 250 °C and 65 bar; and 240 °C and 60 bar). P_{syngas} = 20 bar, syngas flowrate 50 sccm/g_{cat}, and hexane/syngas molar ratio is 3.

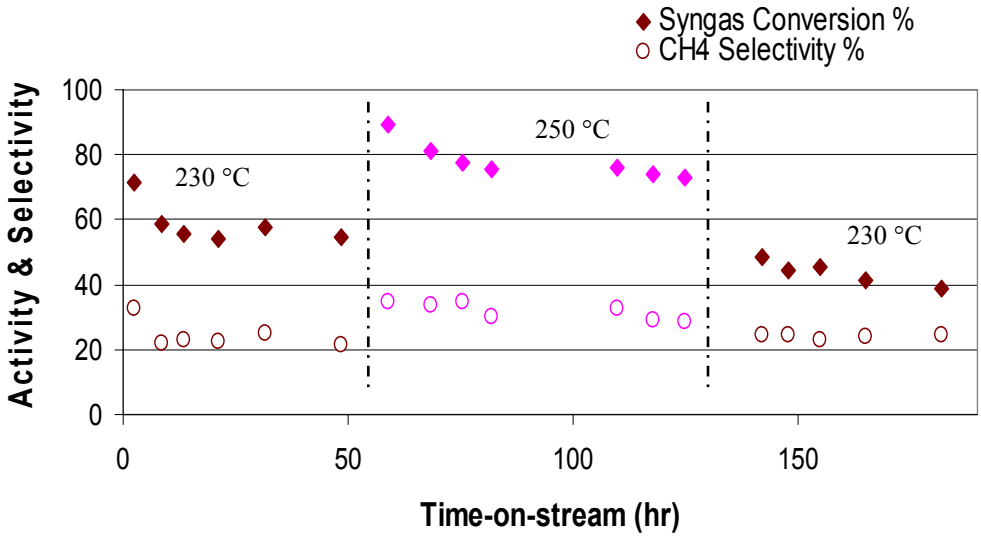

Figure 8.14 Stability of the 15% Co/Al_2O_3 catalyst activity (syngas conversion (%)) and selectivity (CH_4 selectivity (%)) with TOS in gas phase-FTS at different reaction conditions (230 °C and 20 bar; 250 °C and 20 bar; and 230 °C and 20 bar). P_{syngas} = 20 bar, syngas flowrate 50 sccm/g_{cat}.

based on our previous investigations of the alumina-supported catalyst, whereby an optimum performance in both activity and selectivity was observed (Elbashir and Roberts 2004a). Upon returning to the initial conditions (240 °C and 60 bar), no significant changes in either syngas conversions or CH_4 selectivities were observed as shown in Figure 8.13.

In the gas-phase FTS (Figure 8.14), the stability test was initialized at 230 °C and 20 bar for 50 hrs TOS. The catalyst reached a steady value of activity and selectivity within 10 h of ~59% syngas conversion and ~23% CH_4 selectivity. Upon increasing the temperature to 250 °C, significant increase in syngas conversion (~88%) and CH_4 selectivity (~37%) were obtained during the first 7 hrs. However, as the TOS was increased (up to 45 hrs) the syngas conversion decreased to reach 74% with negligible changes in CH_4 selectivity. Both the activity and the selectivity showed a stable trend up to 70 hrs TOS under the above conditions. Returning to the low temperature conditions (230 °C) resulted in a significant drop (c.a. 25%) in syngas conversion; however, CH_4 selectivity is similar to the initial conditions.

Table 8.2 summarizes the characterizations of the catalysts used in the stability test (sample A1 is the used catalyst after the SCH-FTS conditions (Figure 8.13), whereas sample A2 is the used catalyst after the gas-phase FTS conditions (Figure 8.14). The characterizations of the calcined samples (before the reaction) are also included in the last column of Table 8.2. The XRD and magnetic characteristics of sample A3, which represents the un-used but reduced 15% Co/Al_2O_3, are considered as the baseline for the comparison of the catalyst characteristics before and after the FTS reaction. The

characterizations of the calcined but un-used alumina-supported catalyst sample indicates the presence of Co_3O_4 and Al_2O_3 (α,δ,χ). As discussed earlier, upon reduction (sample A3), Co_3O_4 is partly reduced to hcpCo^0 and CoO; this is attributed to either incomplete reduction in the CO environment or the low reduction temperature (280 °C). This is a reasonable conclusion since reduction usually follows the path $Co_3O_4 \rightarrow CoO \rightarrow Co^0$. The characteristics of sample A1 catalyst show the existence of hcpCo^0, CoO and two forms of Al_2O_3 with a negligible amount Co_3O_4. On the other hand, the XRD and magnetic characterizations of the A2 sample reveal that electronic state Co^0, with a larger amount of the FCC phase, and a smaller amount of the hcp phase is present in the used catalyst. This indicates that during both SCH-FTS and gas-phase FTS reaction an in situ reduction of the Co_3O_4 to hcpCO^0 or FCC CO^0 is taking place. Another observation is that two phases of alumina are detected in A1 (γ-Al_2O_3, ε-Al_2O_3), while only one phase is detected in A2 (γ - Al_2O_3).

In a previous study, Rathousky, et al. stated that the metallic cobalt formed on the outer surface of the CoO crystal-lines enhances the adsorption centers of weakly bonded carbon monoxide molecules (Rathouský et al. 1991). Later, Enache et al. confirmed these findings by stating that the catalytic activity of the cobalt catalyst is improved when an amorphous or poorly organized hexagonal form is promoted on the catalyst surface (Enache et al. 2002). Our findings show that the dominant cobalt phase of the A1 sample is hcpCO^0 (hexagonal form), whereas, the dominant phase in the A2 sample is FCC CO^0. It is noteworthy to mention here that the FCC CO^0 was not detected in the reduced catalyst before the reaction (A3 sample). This suggests that the in situ reduction during the SCH-FTS stabilizes the hcpCO^0 form, which has more surface defects (corners and

edges) in the metallic phase than the cubic phase one (FCC CO^0). Another reason that may contribute to the stability in the catalyst activity in the SCH media is the good temperature distribution inside the fixed-bed-reactor compared to the poor one in the gas-phase media (Yokota et al. 1990). The control of temperature distribution in the reduction process is known to avoid the increase of cobalt-support interactions and agglomerations of cobalt nano-particles (as shown in Table 8.2, sample A1 have similar size as that of A2 (>12 nm)) (Khodakov et al. 2002). Small particles could easily be reoxidized by water and other reaction conditions during the FTS reaction.

The used silica-supported catalysts (S1 and S2) showed different characteristics from that of the alumina (A1 and A2). Both the S1 and S2 XRD characterizations show the presence of quartz, cristobalite, and tridymite silicate forms; however, minimal amounts were detected in S2 (SCH-FTS used catalyst). It is also important to mention that no Co^0, CoO, Co_3O_4 XRD pattern was observed in the used catalyst from the gas-phase where only silicate forms were detected. This suggests that the in situ reduction of the catalyst during the gas-phase FTS is minimal. The presence of the silicate forms in the two used catalysts suggests that the in situ reduction during the FTS reaction is different from that in the alumina-supported catalyst and probably follow this trend:

$$Co_3O_4 + H_2 \longrightarrow 3CoO + H_2O$$

$$2\,CoO + SiO_2 \longrightarrow Co_2SiO_4$$

instead of the known second stage in the reduction process (Enache et al. 2002)

$$3CoO + 3\,H_2O \longrightarrow 3Co + 3H_2O$$

Given that no XRD and magnetic characterizations of a silica-supported reduced catalyst (before the reaction) have been included in this study, it would be difficult to reach a

solid conclusion with regards to in situ reduction pathways for the silica-supported catalysts. In addition, the confirmation of the above reduction pathway requires temperature programming reduction (TPR) characterization to trace the reduction of the oxide phases.

8.4 Conclusions

Our FTS investigations of three cobalt-based catalytic systems, of different surface characteristics, and different support materials reveal that neither pore radius nor pore volume has a significant impact on the activity and selectivity when the reaction is conducted under supercritical phase conditions. This observation is attributed to the high solubility of heavy hydrocarbon products in the dense solvent medium and the elimination of mass transfer barriers. Our XRD and magnetic characterizations of the used catalysts show that in situ reducibility of the cobalt oxide takes place during the FTS reaction in both GP-FTS and SCH-FTS conditions. In the latter, the in situ reduction of Co_3O_4 gave active crystal-lines of hcp and fcc Co^0 that were found to be very stable for a long TOS (15 days). As a result, the activity and selectivity of the catalyst in the SCH medium is more stable and recoverable than that under GP-FTS conditions. Our findings also show that the in situ reduction pathway of the silica supported catalyst is different than that of the alumina supported one; however, a stable form of fcc Co^0 has also been detected on the used catalyst from the SCH-FTS operation.

CHAPTER 9

CONCLUSIONS AND RECOMMENDATIONS

9.1 Conclusions

The underlying objective of this dissertation work was to establish optimum operating conditions for FTS within the supercritical region that would maximize the production of value-added chemicals (such as α-olefins) and middle distillate hydrocarbons such as gasoline fuel, jet fuel, and diesel fuel fractions, while at the same time minimizing the production of undesired products such as methane and CO_2. The material covered in this dissertation includes a preliminary investigation (Chapter 3) of the role of the supercritical solvents (n-pentane, and hexanes) and their thermosphysical properties on the FTS reaction performance compared to conventional gas-phase FTS. This comparison was carried out over a broad range of operating conditions (e.g. temperature, pressure, syngas feed ratio, and gas-hourly-space-velocity). The opportunity to selectively control and maximize the production of the desired fuel fractions from the FTS hydrocarbons spectrum, by tuning either reaction temperature and reaction pressure, was addressed in Chapter 4. Chapter 5 covers an attempt to understand and model the enhanced chain growth probability in the supercritical phase FTS that resulted in significant deviations from the standard Anderson-Shultz-Flory (ASF) model (specifically within the middle distillate hydrocarbons). Chapter 6 contains a preliminary

examination of the kinetics of the FTS reactions under high-pressure high temperature conditions in both conventional gas-phase FTS and supercritical hexanes FTS using the standard surface reaction model. The influence of the cobalt catalyst surface characteristics, cobalt valence states, cobalt particles structure and size, as well as the cobalt dispersion on the gas-phase FTS reaction under high-pressure operation is illustrated in Chapter 7. Finally, Chapter 8 covers the influence of cobalt-based characteristics on the supercritical phase FTS activity and selectivity.

The conclusions of this dissertation can be summarized as follows;

- Our investigations over a broad range of operating conditions (temperature of 210 °C- 260 °C; pressure of 30 bar-80 bar; syngas space velocity of 50 sccm/g_{cat} – 150 sccm/gcat; and syngas feed composition (H_2/CO ratio) of 0.5/1-2/1) show that the adjustable thermophysical properties of the supercritical solvent (*n*-pentane, and hexanes) significantly impact the FTS reaction performance (CO conversion%, CH_4 selectivity, CO_2 selectivity, chain growth probability (α-value), and α-olefins to *n*-paraffins ratios). In most cases SCF-FTS showed higher activity and better selectivity towards the most desired products compared to conventional gas-phase FTS.
- Lower reaction temperatures promote chain growth, and therefore, favor the production of middle distillate hydrocarbons and wax components in supercritical phase FTS. Temperature well above the critical temperature of the solvent was found to have a significant negative effect on the α-olefin selectivity in both pentane and hexanes SCF-FTS operations. Within the studied pressure range, our

findings show that the influence of pressure on the rates of reactants consumption is more significant than its effects on the chain-growth probability and in general the selectivity. As a result, there is an existence of an optimum operation region within the supercritical phase whereby high activity can be achieved at a reasonable selectivity towards methane and high chain growth probability towards the middle distillate hydrocarbon products.

- The density of the solvent under supercritical FTS operation had a pronounced effect on both the chain growth probability and the α-olefin selectivity, yielding enhanced chain growth at high densities. Readsorption of α-olefins, followed by subsequent incorporation in the chain growth process, are suggested to be the main reason behind the enhancement of chain growth probability under supercritical phase operation.
- The enhanced chain growth probability phenomenon in SCF-FTS cannot be attributed to internal diffusion limitation effects, as has been done in conventional gas-phase FTS. Instead, this work indicates that factors such as increased solubility in the SCF medium, increased accessibility of vacant adsorption sites, and the elimination of the adsorption layer barrier, play a key role in enhancing the chain growth process in supercritical-phase FTS.
- The critical properties of a reaction mixture collected from the effluent of the reactor and composed of the solvent+syngas+hydrocarbon-products+H_2O+CO_2 (measured in a variable-volume-view cell apparatus) are found to be different from that of a pure supercritical solvent (significantly higher critical pressure and slightly higher critical temperature). Therefore, to ensure a single phase operation

in SCF-FTS the operating conditions should be beyond the critical boundaries of the reaction mixture.

- The analytical analysis presented in this dissertation demonstrates significant deviations of the hydrocarbon distributions from the ASF model when the FTS reaction is conducted in a near-critical and supercritical FTS medium over an alumina supported cobalt catalyst. The degree of these deviations from the standard ASF model was found to be dependent to the physical properties of the reaction mixture as the medium is shifted from near-critical conditions to supercritical conditions by simply tuning the reaction temperature and pressure. Rather than a single chain growth probability (α-value) for the product distribution as in the standard ASF model, three distinct chain growth probabilities (α_{lh}, α_{md}, and α_{hp}) are required to accurately represent the product distributions obtained in the SCH environment. In this study an interesting phenomenon is reported indicating a unique deviation from the standard ASF behavior within the middle hydrocarbon product range of relatively very high α-value (α_{md} = 0.95) owing to enhanced incorporation of olefins in the SCH medium.
- The aforementioned phenomenon is attributed in part to the enhanced solubility of heavy products in the dense supercritical solvent medium yielding enhanced availability of vacant sites. Such an environment has a significant impact on the dynamic adsorption/desorption equilibrium of active species inside the catalyst pores. It also enhances the adsorption rates of olefins within light and middle hydrocarbon ranges and hence increases the possibility for their incorporation in

the chain-growth process. An enhanced-olefin incorporation model for FTS in SCH including a synthesis pathway and chain growth mechanism is suggested to provide explanation for deviations within the middle hydrocarbon products. The development of this model takes advantage of the wealth of information accumulated in the literature and is in a good agreement with our experimental observations over a broad range of operating conditions.

- The surface reaction kinetics model closely predict the CO consumption rates and CH_4 production in gas-phase operation, however, it fails to predict those rates under SCH-FTS operation. The inconsistency of the kinetic model in predicting the SCH performance indicates that assumptions stated in developing this model for gas-phase FTS operation are not sufficient to predict the performance under SCH-FTS operation. One factor could contribute significantly to the inability of this model to predict FTS performance under SCH conditions; the model relies on partial pressures (concentrations) of the reactants rather than their activities in the rate equations (due to ideal gas assumptions made in the surface reaction model).
- The cobalt-based catalyst characteristics play a significant role in the synthesis process. The characterization (BET surface characterizations, XRD, magnetization, and EMR) of six cobalt-based FTS catalysts (alumina and silica supported catalysts with 15% cobalt loading) shows different electronic states of the cobalt (fcp-Co^0, hcp-Co^0, CoO, Co_3O_4, Co^{2+}) and the supports (SiO_2 (quartz, cristobalite, tridymite); δ-Al_2O_3, and γ - Al_2O_3, and ε-Al_2O_3). The cobalt and the support material's electronic states are found to change with calcinations, reduction, and reaction conditions. Correlations of the catalysts characteristics

with activity and selectivity reveals that the presence of Co_3O_4 yield higher methane selectivity whereas the presence of Co^{2+} species yields lower methane selectivity but higher olefin selectivity.

- The cobalt-based catalytic systems show excellent stability in terms of activity and selectivity under high-pressure, high-temperature supercritical phase FTS for relatively long time-on-stream (up to 15 days). No significant changes of either cobalt particle size, electronic state, or surface structure (BET areas, pore radius, and pore volume) was observed after SCF-FTS operation. This indicates that no serious modification of the catalyst structure is taking place as well as no coke deposition.

9.2 Recommendations

There are many investigations that could arise from the work done to this point on the utilization of supercritical fluids in Fischer-Tropsch synthesis. This chapter will cover some recommendations for future work in this field that would benefit the transfer of this technology from lab-scale research to an industrial scale process.

- The *Enhanced α-olefin Incorporation* model should be followed by cofeeding and carbon isotope transient studies of primary and secondary olefins to track their contribution in the chain growth process. This would allow a quantitative evaluation of the role of primary olefins in enhancing α-values rather than the qualitative modeling proposed in this study.
- This can also be followed by suggesting correction factors for the standard ASF model to account for the deviation and to quantify the

influence of both temperature and pressure in the model. We are suggesting a quantitative evaluation of two correction factors (F1 and F2; as in Eqns. 10.1 and 10.2) to be included in the classical ASF model to account for the effect of reaction parameters on the deviation from that model (Eqn. 3.1).

$$W_n = n\alpha^{n-1}(1-\alpha)^2 \tag{3.1}$$

$$W_n = F_1 n\alpha^{n-1}(1-\alpha)^2 \tag{10.1}$$

$$W_{ab} = F_2\left[(a\alpha^{a-1} - b\alpha^b)(1-\alpha) + \alpha^a - \alpha^b\right] \tag{10.2}$$

- Further development of kinetic modeling of supercritical phase FTS should take into account the thermodynamic nonideality of the reaction mixture (using activities rather than concentrations or partial pressures), as well as, considering the evacuated active sites (as a result of the enhanced in situ extraction of heavy compounds from the catalyst pore) in the overall kinetic model (polymerization probability, monomer amounts, and synthesis pathways).
- The phase behavior of the reactants (syngas, CO and H_2)-solvent mixture should also be studied and well understood prior to selection of SCF-FTS operating conditions. This would assist the control of the overall process, especially during the start-up conditions and during the periodic regeneration of the catalyst.
- Utilization of a supercritical phase medium in Fischer-Tropsch synthesis (FTS) presents a paradigm shift to the now 80-year old FTS technology.

However, attempting commercial-scale operation of the high pressure and temperature reactors needed for supercritical fluid Fischer-Tropsch synthesis (SCF-FTS) requires improved understanding of the underlying kinetic, thermodynamic and reaction engineering issues (an attempt to address most of these issues are covered in this dissertation). However, the technoeconomic evaluation of the high-pressure reactor system requires a fine balance between the cost of elevated pressures and the benefits gained from operating the FTS reaction in the supercritical phase media. As addressed in this study these benefits include high conversions, low selectivity towards methane, high chain growth probability, excellent opportunity to maximize the production of desired fuel fractions (namely jet fuels and diesel fractions), in addition to a good stability of the catalyst activity and structure over relatively long time-on-stream.

REFERENCES

Anderson, R. B., W. K. Hall, A. Krieg and B. Seligman (1949). "Studies of the Fischer-Tropsch Synthesis. V. Activities and Surface Areas of Reduced and Carburized Cobalt Catalysts." Journal of American Chemical Society **71**: 183-188.

Anderson, R. B. (1984). The Fischer-Tropsch Synthesis. Orlando, Florida, Academic Press, Inc.

Anikeev, V. I., A. Yermakova and A. L. Moroz (2003). The State of Studies of the Fischer-Tropsch Process in Russia. 2003 Spring Meeting, American Institute of Chemical Engineering, Historical Development of the Fischer-Tropsch Synthesis/Process - I [80c], New Orleans, LA.

Bacha, J., F. Barnes, M. Franklin, L. Gibbs, G. Hemighaus, N. Hogue, D. Lesnini, J. Lind, J. Maybury and J. Morris (2000). Aviation Fuels Technical Review (FTR-3). San Ramon, California., Chevron Products Company**:** 15-31.

Baiker, A. (1999). "Supercritical Fluids in Heterogeneous Catalysis." Chemical Review **99**(2): 453 -474.

Bartholomew, C. H. and R. C. Reuel (1985). "Cobalt-support interactions: Their effects on adsorption and carbon monoxide hydrogenation activity and selectivity properties." Industrial & Engineering Chemistry Product Research and Development **24**(1): 56-61.

Bartholomew, C. H. (2003). History of Cobalt Catalyst Design for FTS. Meeting of the American Institute of Chemical Engineering (AIChE) Historical Development of the Fischer-Tropsch Synthesis/Process - II [83b], New Orleans, LA.

Bell, A. T. (1981). "Catalytic synthesis of hydrocarbons over Group VIII metals. Discussion of the reaction mechanism." Catalysis Reviews - Science and Engineering **23**(2): 203-232.

Berkowitz, A. E. and K. Takano (1999). "Exchange anisotropy -a review." Journal of Magnetism and Magnetic Materials **200**: 552-570.

Bertole, C. J., C. A. Mims and G. Kiss (2002). "The Effect of Water on the Cobalt-Catalyzed Fischer-Tropsch Synthesis." Journal of Catalysis **210**(1): 84-96.

Bianchi, C. L. and V. Ragaini (1997). "Experimental Evidence of [alpha]-Olefin Readsorption in Fischer-Tropsch Synthesis on Ruthenium-Supported ETS-10 Titanium Silicate Catalysts." Journal of Catalysis **168**(1): 70-74.

Blyholder, G., D. Shihabi, W. V. Wyatt and R. Bartlett (1976). "Adsorption and interaction of ethylene, molecular hydrogen, carbon monoxide, and organic acids on iron, cobalt, and nickel." Journal of Catalysis **43**(1-3): 122-130.

Bochniak, D. J. and B. Subramaniam (1998). "Fischer-Tropsch Synthesis in Near-Critical n-Hexane: Pressure-Tuning Effects." AIChE Journal **44**(8): 1889-1896.

Brady, R. C. and R. Pettit (1981). "Mechanism of the Fischer-Tropsch reaction. The chain propagation step." Journal of the American Chemical Society **103**(5): 1287-1289.

Bukur, D. B., X. Lang, A. Akgeman and Z. Feng (1997). "Effect of Process Conditions on Olefin Selectivity during Conventional and Supercritical Fischer-Tropsch Synthesis." Industrial & Engineering Chemistry Research **36**: 2580-2587.

Cagniard de LaTour, C. (1822). "Supercritical fluids." Ann. Chim. Phys. **21**: 127-132.

Chaumette, P., C. Verdon and P. Boucot (1995). "Influence of the hydrocarbons distribution on the heat produced during Fischer-Tropsch synthesis." Topics in Catalysis **2**(1-4): 301-311.

Cornils, B., A. Herrmann and M. Rasch (1994). "Otto Roelen as the pioneer of industrial homogeneous catalysis." Angewandte Chemie **106**(21): 2219-2238.

Craxford, S. R. and E. K. Rideal (1939). "The mechanism of the synthesis of hydrocarbons from water gas." Journal of the Chemical Society, Abstracts: 1604-1614.

Craxford, S. R. (1947). "The Fischer-Tropsch synthesis with cobalt catalysts." Journal of the Society of Chemical Industry, **66**: 440-444.

Davis, B. H. (2001). "Fischer-Tropsch synthesis: Current mechanism and futuristic needs." Fuel Processing Technology **71**(1-3): 157-166.

Davis, B. (2002). "Fischer-Tropsch Synthesis Mechanism-was Storch Correct?" ACS Fuel Chemistry Division Preprints **47**(1): 237-239.

Davis, B. (2003a). "Anderson Schultz Flory product distributions-Can it be avoided for Fischer-Tropsch Synthesis." American Institute of Chemical Engineers (AIChE) 2003 Spring meeting, New Orleans, LA.

Davis, B. (2003b). An Overview of Fischer-Tropsch Synthesis at the U.S. Bureau of Mines. 2003 Spring Meeting, American Institute of Chemical Engineering,

Historical Development of the Fischer-Tropsch Synthesis/Process - I [80b], New Orleans, LA.

Davis, B. H. (2003c). "Fischer-Tropsch synthesis: relationship between iron catalyst composition and process variables." Catalysis Today **84**(1-2): 83-98.

Dictor, R. A. and A. T. Bell (1983). "An Explanatlon for Deviations of Flscher-Tropsch Products from a Schultz-Flory Distrlbution." Industrial Engineering Chemistry & Process Design Development **22**: 678-681.

Dietz, W. A. (1967). "Response factors for gas chromatographic analyses." Journal of Gas Chromatograph **5**(2): 68-71.

Dry, M. E. and T. Shingles (1983). Catalytic conversion of synthesis gas to hydrocarbons. Ger. Offen. De, (Sasol One (Pty.) Ltd., S. Afr.): 14.

Dry, M. E. (1996). "Practical and theoretical aspects of the catalytic Fischer-Tropsch process." Applied Catalysis A: General **138**(2): 319-344.

Dry, M. E. (2001). "High quality diesel via the Fischer-Tropsch process - a review." Journal of Chemical Technology and Biotechnology **77**(1): 43-50.

Dutta, P., N. O. Elbashir, A. Manivannan, M. S. Seehra and C. B. Roberts (2004a). "Characterization of Fischer-Tropsch Cobalt-based Catalytic Systems (Co/SiO2 and Co/Al2O3) by X-ray Diffraction and Magnetic Measurements." Catalysis Letters **In press**.

Dutta, P., A. Manivannan, M. S. Seehra, P. M. Adekknattu and J. A. Guin (2004b). "Determination of the electronic state and concentration of nickel in NiSAPO catalysts by magnetic measurements." Catalysis Letters **94**: 181-185.

Duvenhage, D. J. and T. Shingles (2002). "Synthol reactor technology development." Catalysis Today **71**(3-4): 301-305.

Editor (2003). "Today's Feature: 'Supercritical Phase' FT, CO_2-Rich Scheme Highlights Japan SAE Conference Papers." World Fuels TODAY **July 3**: P1 & P5-6.

EIA (2001). Annual Energy Outlook 2002,. Washington, DC, Department of Energy (DOE), Energy Information Administration (EIA), http://www.eia.doe.gov/oiaf/ieo/tbl_b2.html.

Eidus, Y. T. and N. D. Zelinskii (1942). " Carbide formation as an intermediate stage in the catalytic synthesis of hydrocarbons from water gas." Bull. Acad. Sci. U.R.S.S., Classe Sci. Chim.: 190-194.

Eidus, Y. T. (1944). "Catalysts for hydrogenation of CO by joint application of the dynamic and static methods. I. Activity of the complex Fe-Cu-ThO_2-K_2CO_3 kieselguhr catalyst." Bull. Acad. Sci. U.R.S.S., Classe Sci. Chim. **255-262**.

Eidus, Y. T., A. L. Lapidus and V. I. Mashinskii (1976). "Catalytic hydrocondensation of carbon monoxide with olefins and their hydropolymerization in the presence of carbon monoxide and hydrogen. 53. Hydropolymerization of ethylene and propylene on a cobalt-alumina catalyst." Izvestiya Akademii Nauk SSSR, Seriya Khimicheskaya **6**: 1307-1310.

Elbashir, N. O. and C. B. Roberts (2004a). "Enhanced Incorporation of α-olefins in the Fischer-Tropsch Synthesis Chain-growth Process over an Alumina Supported Cobalt Catalyst in Near-critical and Supercritical Hexane Medium." Industrial & Engineering Chemistry Research **In press.**

Elbashir, N. O. and C. B. Roberts (2004b). "Reaction pathway and kinetic modeling of Fischer-Tropsch synthesis over an alumina supported cobalt catalysts in supercritical-hexane." ACS Division of Petroleum Chemistry Preprints **49**(2): 157-160.

Elbashir, N. O. and C. B. Roberts (2004c). "Selective Control of Hydrocarbon Product Distribution in Supercritical Phase Fischer-Tropsch Synthesis." ACS Division of Petroleum Chemistry Preprints **49**(4): 422-425.

Enache, D. I., B. Rebours, M. Roy-Auberger and R. Revel (2002). "In Situ XRD Study of the Influence of Thermal Treatment on the Characteristics and the Catalytic Properties of Cobalt-Based Fischer–Tropsch Catalysts." Journal of Catalysis **205**: 346-353.

Enache, D. I., M. Roy-Auberger and R. Revel (2004). "Differences in the characteristics and catalytic properties of cobalt-based Fischer–Tropsch catalysts supported on zirconia and alumina." Applied Catalysis A: General **268**: 51-60.

Ernst, B., S. Libs, P. Chaumette and A. Kiennemann (1999). "Preparation and characterization of Fischer-Tropsch active Co/SiO_2 catalysts." Applied Catalysis A: General **186**(1-2): 145-168.

Espinoza, R. L., A. P. Steynberg, B. Jager and A. C. Vosloo (1999). "Low temperature Fischer-Tropsch synthesis from a Sasol perspective." Applied Catalysis A: General **186**(1-2): 13-26.

Fan, L., K. Yokota and K. Fujimoto (1992a). "Supercritical phase Fischer-Tropsch synthesis: catalyst pore-size effect." AIChE Journal **39**(10): 1639-1648.

Fan, L. and K. Fujimoto (1999). "Fischer-Tropsch synthesis in supercritical fluids: Characteristics and application." Applied Catalysis A: General **186**(1-2): 343-354.

Fan, L., K. Yoshii, S. Yan, J. Zhou and K. Fujimoto (1997). "Supercritical-phase process for selective synthesis of wax from syngas: Catalyst and process development." Catalysis Today **36**(3): 295-304.

Fischer, F. and H. Tropsch (1925a). Hydrocarbons. De**:** Addn. to 484,337 (C. A. 24, 1119).

Fischer, F. and H. Tropsch (1925b). "The reduction of carbon monoxide to methane in the presence of various metals." Brennstoff-Chemie **6**: 265-271.

Fischer, F. and H. Tropsch (1926a). Hydrocarbons. De.

Fischer, F. and H. Tropsch (1926b). Hydrocarbons from hydrogen and oxides of carbon. De**:** Addn. to 484,337 (C. A. 24, 1119).

Fischer, F. and H. Tropsch (1926c). The synthesis of petroleum at atmospheric pressures from gasification products of coal. Brennstoff-Chemie. **7:** 97-104.

Fischer, F. and H. Tropsch (1928). "The composition of products obtained by the petroleum synthesis." Brennstoff-Chem. **9**: 21-4.

Fischer, F. and H. Tropsch (1932). "Petroleum syntheses." Ges. Abhandl. Kenntnis Kohle **10**: 313-501.

Flory, P. J. (1936). "Molecular Size Distribution in Linear Condensation Polymers." Journal of the American Chemical Society **58**(10): 1877-1885.

Freemantle, M. (1997). "Continuous SCF reactor." Chemical Engineering News **79**: 30.

Friedel, R. A. and R. B. Anderson (1950). "Composition of Synthetic Liquid Fuels. I. Product Distribution and Analysis of C5-C8 Paraffin Isomers from Cobalt Catalyst." Journal of the American Chemical Society **72**: 1212-1215.

Fu, L. and C. H. Bartholomew (1985). "Structure sensitivity and its effects on product distribution in CO hydrogenation on cobalt/alumina." Journal of Catalysis **92**: 376-387.

Gao, L., Z. Hou, H. Zhang, J. He, Z. Liu, X. Zhang and B. Han (2001). "Critical Parameters of Hexane + Carbon Monoxide + Hydrogen and Hexane + Methanol + Carbon Monoxide + Hydrogen Mixtures in the Hexane-Rich Region." Journal of Chemical Engineering Data **46**: 1635-1637.

Gaube, J.; Hochstadt, G.; Sudheimer, G. (1982). "Kinetic and Reaction-Engineering Studies for Fischer-Tropsch Synthesis of 1-Alkenes (C_4-C_{20})." Institut fur Chemische Technologie, TH Darmstadt: Darmstadt, Germany, 1982: 125.

Geertesma, A. (1990). Consideration in the the selection of Fischer-Tropsch Reactor for synfuel production. DOE Indirect Liquification Contractors' Review Meeting Proc. G. J. Stigel and R. D. Srivastava. Pittsburg, US Department of Energy**:** 272-281.

Gruver, V., X. Zhan, J. Engman and H. J. Robota (2004). "Deactivation of a Fischer-Tropsch Catalyst through the Formation of Cobalt Carbide under Laboratory Slurry Reactor Conditions." ACS Division of Petroleum Chemistry Preprints **49**(2): 192-194.

Guisnet, M. and P. Magnoux (1997). "Deactivation by coking of zeolite catalysts. Prevention of deactivation. Optimal conditions for regeneration." Catalysis Today **36**(4): 477-483.

Hall, W. K., R. J. Kokes and P. H. Emmett (1960). "Mechanism Studies of the Fischer-Tropsch Synthesis: The Incorporation of Radioactive Ethylene, Propionaldehyde and Propanol." Journal of the American Chemical Society **82**(5): 1027-1037.

Hanoglu, C., M. Claeys, Z. Nie and H. Schulz (1995). "Initial activity and selectivity in a Fischer-Tropsch synthesis on Iron catalysts." Wissenschaftliche Abschlussberichte - Internationales Seminar fuer Forschung und Lehre in Chemieingenieurwesen, Technischer und Physikalischer Chemie, 30th, Karlsruhe, July, 1995: 146-155.

Henrici-Olive, G. and O. S. Olive (1976). Angew. Chem., Int. Ed. Engl. **15**: 136.

Herington, E. F. G. (1946). "The Fischer-Tropsch synthesis considered as a polymerization reaction." Chemistry & Industry (London, United Kingdom): 346-347.

Herrington, E. F. G. (1946). "The Fischer-Tropsch synthesis considered as a polymerization reaction." Chemistry & Industry (London, United Kingdom): 346-347.

Hill, C. (1999). Sasol's experience in the conversion of gas into liquids. PeRsian Gulf Gas Resources, 7-8 November 1999, Tehran.

Hilmena, A. M., D. Schanke, K. F. Hanssen and A. Holmen (1999). "Study of the effect of water on alumina supported cobalt Fischer–Tropsch catalysts." Applied Catalysis A: General **186**(1-2): 169-188.

Hindermann, J. P., G. J. Hutchings and A. Kiennemann (1993). "Mechanistic aspects of the formation of hydrocarbons and alcohols from carbon monoxide hydrogenation." Catalysis Reviews - Science and Engineering **35**(1): 1-127.

Huang, X., C. W. Curtis and C. B. Roberts (2002a). "Reaction behavior of Fischer-Tropsch synthesis in near critical and supercritical hexane media." Preprints of Symposia - American Chemical Society, Division of Fuel Chemistry **47**(1): 150-153.

Huang, X., N. O. Elbashir and C. B. Roberts (2002b). Application of Supercritical Fluids as Reaction Medium for FTS, 2002 Annual Report for the Consortium for Fossil Fuel Science.

Huang, X., N. O. Elbashir and C. B. Roberts (2004). "Supercritical Solvent Effects on Hydrocarbon Product Distributions in Fischer-Tropsch Synthesis over an Alumina Supported Cobalt Catalyst." Industrial & Engineering Chemistry Research **In press**.

Huang, X. and C. B. Roberts (2003). "Selective Fischer–Tropsch synthesis over an Al2O3 supported cobalt catalyst in supercritical hexane." Fuel Processing Technology **83**: 81-99.

Huff, G. A., Jr. and C. N. Satterfield (1984). "Evidence for two chain growth probabilities on iron catalysts in the Fischer-Tropsch synthesis." Journal of Catalysis **85**(2): 370-9.

Hurlbut, R. S., I. Puskas and D. J. Schumacher (1996). "Fine details on selectivity and kinetics of the Fischer-Tropsch synthesis over cobalt catalysts by combination of quantitative gas chromatography and modeling." Energy & Fuels **10**: 537-545.

Hyde, J. R., P. Licence, D. Carter and M. Poliakoff (2001). "Continuous catalytic reactions in supercritical fluids." Applied Catalysis A: General **222**: 119-131.

Iglesia, E., S. L. Soled and R. A. Fiato (1988). Cobalt-ruthenium catalysts for Fischer-Tropsch synthesis and process for their preparation. U.S. Us, (Exxon Research and Engineering Co., USA).

Iglesia, E., S. C. Reyes and R. J. Madon (1991). "Transport-enhanced a-olefin readsorption pathways in ruthenium-catalyzed hydrocarbon synthesis." Journal of Catalysis **129**(1): 238-56.

Iglesia, E.; Soled, S. L.; Fiato, R. A. (1988). "Exxon Research and Engineering Co., USA) Cobalt-Ruthenium Catalysts for Fischer-Tropsch Synthesis and Process for Their Preparation. U.S. Patent No. 4,738,948" April 19, 1988.

Iglesia, E., S. C. Reyes, R. J. Madon and S. L. Soled (1993a). "Selectivity control and catalyst design in the Fischer-Tropsch synthesis: Sites, pellets, and reactors." Advances in Catalysis **39**: 221-302.

Iglesia, E., S. C. Reyes and S. L. Soled (1993b). "Reaction-transport selectivity models and the design of Fischer-Tropsch catalysts." Chemical Industries (Dekker) **51**(Computer-Aided Design of Catalysts): 199-257.

Iglesia, E. (1997a). "Design, synthesis, and use of cobalt-based Fischer-Tropsch synthesis catalysts." Applied Catalysis, A: General **161**(1-2): 59-78.

Iglesia, E. (1997b). "Fischer-Tropsch synthesis on cobalt catalysts: structural requirements and reaction pathways." Fuel and Energy Abstracts **38**(6): 448.

Inoue, M., T. Miyake and T. Inui (1987). "Simple criteria to differentiate a two-site model from a distributed-site model for Fischer-Tropsch synthesis." Journal of Catalysis **105**: 266-269.

Jacobs, G., K. Chaudhari, D. Sparks, Y. Zhang, B. Shi, R. Spicer, T. K. Das, J. Li and B. H. Davis (2003). "Fischer-Tropsch synthesis: Supercritical conversion using a Co/Al2O3 catalyst in a fixed bed reactor." Fuel **82**(10): 1251-1260.

Jacobs, G., P. M. Patterson, Y. Zhang, T. Das, J. Li and B. H. Davis (2002). "Fischer-Tropsch synthesis: deactivation of noble metal-promoted Co/Al_2O_3 catalysts." Applied Catalysis A: General **233**(1-2): 215-226.

Jager, B. and R. Espinoza (1995). "Advances in low temperature Fischer-Tropsch synthesis." Catalysis Today **23**(1): 17-28.

Johnson, K. P. and J. M. L. Penninger, Eds. (1989). Supercritical Fluid Science and Technology. ACS Symposium Series 406. Washington, DC, American Chemical Society.

Joyce, P. C., J. Gordon and M. C. Thies (2000). "Vapor-liquid equilibria for the hexane+tetracosane and hexane+hexatriacontane systems at elvated temperatures and pressures." Journal of Chemical Engineering Data **45**: 424-427.

Joyce, P. C., B. E. Leggett and M. C. Thies (1999). "Vapor–liquid equilibrium for model Fischer–Tropsch waxes (hexadecane, 1-hexadecene, and 1-hexadecanol) in supercritical hexane." Fluid Phase Equilibria **158-160**: 723-731.

Karn, F. S., J. F. Shultz and R. B. Anderson (1965). "Hydrogenation of carbon monoxide and carbon dioxide on supported ruthenium catalysts at moderate pressures."

Industrial & Engineering Chemistry Product Research and Development **4**: 265-269.

Kellner, C. S. and A. T. Bell (1981). "The kinetics and mechanisms of carbon monoxide hydrogenation over alumina-supported ruthenium." Journal of Catalysis **70**(2): 418-32.

Khodakov, A. Y., A. Griboval-Constant, R. Bechara and V. L. Zholobenko (2002). "Pore size effects in Fischer Tropsch synthesis over cobalt-supported mesoporous silicas." Journal of Catalysis **206**: 230-241.

Kittel, C. (1996). Introduction to Solid State Physics. New York, John Wiley & Sons.

Koelbel, H. and K. D. Tillmetz (1974). " Model studies of the interaction of carbon monoxide and hydrogen on transition metals. II. Role of chemisorption complexes in primary reactions." Journal of Catalysis **34**(2): 307-316.

Kokes, R. J. and P. H. Emmett (1960). "The activity of Raney nickel as a function of hydrogen content." Journal of American Chemical Society **82**: 4497.

Kolbel, H. and M. Ralek (1980). "The Fischer-Tropsch Synthesis in the Liquid-Phase." Catalysis Reviews **21**(2): 225-274.

Kraum, M. and M. Baerns (1999). "Fischer-Tropsch synthesis: The influence of various cobalt compounds applied in the preparation of supported cobalt catalysts on their performance." Applied Catalysis A: General **186**(1-2): 189-200.

Kreglewski, A. and W. B. Kay (1969). "The Critical Constants of Conformal Mixtures." Journal of Physical Chemistry **73**: 3359.

Kuipers, E. W., I. H. Vinkenburg and H. Oosterbeek (1995). "Chain Length Dependence of [alpha]-Olefin Readsorption in Fischer-Tropsch Synthesis." Journal of Catalysis **152**(1): 137-146.

Kuipers, E. W., C. Scheper, J. H. Wilson, I. H. Vinkenburg and H. Oosterbeek (1996). "Non-ASF Product Distributions Due to Secondary Reactions during Fischer-Tropsch Synthesis." Journal of Catalysis **158**(1): 288-300.

Kummer, J. T. and P. H. Emmett (1953). "Fischer-Tropsch synthesis mechanism studies. The addition of radioactive alcohols to the synthesis gas." Journal of the American Chemical Society **75**: 5177.

Lahtinen, J., T. Anraku and G. A. Somorjai (1994). "Lahtinen, J.; Anraku, T.; Somorjai, G. A. C, CO and CO_2 hydrogenation on cobalt foil model catalysts: evidence for the need of CoO reduction." Catalysis Letters **25**: 241-255.

Lang, X., A. Akgeman and D. B. Bukur (1995). "Steady state F-T synthesis in Supercritical propane." Industrial & Engineering Chemistry Research **34**: 72-77.

Lappin, G. R., L. H. Nemec, J. D. Sauer and J. D. Wnager (1996). Higher Olefins. Kerk-Othemer Encyclopedia of Chemical Technology. New York, Wiley. **17:** 839-858.

Li, S., G. Jacobs, T. Das, Y. Zhang and B. Davis (2002a). "Fischer-Tropsch synthesis: Effect of water on the catalytic properties of a Co/SiO2 catalyst." Applied Catalysis A: General **236**(1-2): 67-76.

Li, S., S. Krishnamoorthy, A. Li, G. D. Meitzner and E. Iglesia (2002b). "Promoted Iron-Based Catalysts for the Fischer-Tropsch Synthesis: Design, Synthesis, Site Densities, and Catalytic Properties." Journal of Catalysis **206**(2): 202-217.

Li, S., R. J. O'Brien, G. D. Meitzner, H. Hamdeh, B. H. Davis and E. Iglesia (2001). "Structural analysis of unpromoted Fe-based Fischer-Tropsch catalysts using X-ray absorption spectroscopy." Applied Catalysis, A: General **219**(1-2): 215-222.

Lopatto, J. and D. Malcomb (2003). Ultra-Clean Transportation Fuels Plant Is Step Toward Reduced Vehicle Emissions. Press Room, US DOE. Washington, D.C.**:** http://www.energy.gov/engine/content.do?PUBLIC_ID=14241&BT_CODE=PR_PRESSRELEASES&TT_CODE=PRESSRELEASE.

Low, W. (1958). "Paramagnetic resonance spectrum of trivalent gadolinium in the cubic field of calcium fluoride." Physical Review **109**: 265-271.

Madon, R. J., S. C. Reyes and E. Iglesia (1991). "Primary and secondary reaction pathways in ruthenium-catalyzed hydrocarbon synthesis." Journal of Physical Chemistry **95**(20): 7795-804.

Madon, R. J. and E. Iglesia (1993). "The importance of olefin readsorption and hydrogen/carbon monoxide reactant ratio for hydrocarbon chain growth on ruthenium catalysts." Journal of Catalysis **139**(2): 576-90.

Madon, R. J., E. Iglesia and S. C. Reyes (1993). "Non-Flory product distributions in Fischer-Tropsch synthesis catalyzed by ruthenium, cobalt, and iron." ACS Symposium Series **517**(Selectivity in Catalysis): 383-96.

Madon, R. J. and E. Iglesia (1994). "Hydrogen and CO Intrapellet Diffusion Effects in Ruthenium-Catalyzed Hydrocarbon Synthesis." Journal of Catalysis **149**: 247-489.

Matsumoto, D. K. and C. N. Satterfield (1989). "Effects of temperature and hydrogen/carbon monoxide ratio on carbon number product distribution from iron Fischer-Tropsch catalysts." Energy & Fuels **3**(2): 249-54.

McHugh, M. and M. E. Paulaitis (1980). "Solid solubilities of naphthalene and biphenyl in supercritical carbon dioxide." Journal of Chemical Engineering Data **24**: 326-329.

McHugh, M. A. and V. J. Krukonis (1994). Supercritical Fluid Extraction. Boston, Butterworth-Heinemann.

Moradi, G. R., M. M. Basir, A. Ataeb and A. Kiennemann (2003). "Promotion of Co/SiO_2 Fischer–Tropsch catalysts with zirconium." Catalysis Communications **4**: 27-32.

Ohe, S. (1976). Computer Aided Data Book of Vapor Pressure. Tokyo, Data Book Publishing Co.

Overett, M. J., R. O. Hill and J. R. Moss (2000). "Organometallic chemistry and surface science: Mechanistic models for the Fischer–Tropsch synthesis." Coordination Chemistry Reviews **206-207**: 581-605.

Patzlaff, J., Y. Liu, C. Graffmann and J. Gaube (1999a). "Studies on product distributions of iron and cobalt catalyzed Fischer-Tropsch synthesis." Applied Catalysis A: General **186**(1-2): 109-119.

Patzlaff, J., Y. Liu, C. Graffmann and J. Gaube (1999b). "Studies on product distributions of iron and cobalt catalyzed Fischer-Tropsch synthesis." Applied Catalysis, A: General **186**(1,2): 109-119.

Patzlaff, J., Y. Liu, C. Graffmann and J. Gaube (2002). "Interpretation and kinetic modeling of product distributions of cobalt catalyzed Fischer-Tropsch synthesis." Catalysis Today **71**(3-4): 381-394.

Peluso, E., C. Galarraga and H. de Lasa (2001). "Eggshell catalyst in Fischer–Tropsch synthesis: Intrinsic reaction kinetics." Chemical Engineering Science **56**: 1239-1245.

Peng, D. and D. B. Robinson (1976). "A New Two-Constant Equation of State." Industrial Engineering Chemical Fundamentals **15**: 59-64.

Pichler, H. (1952). Twenty-five years of synthesis of gasoline by catalytic conversion of carbon monoxide and hydrogen. New York, N.Y., Academic Press Inc.

Polishuk, I., R. P. Statevab, J. Wisniakc and H. Segurad (2004). "Simultaneous prediction of the critical and sub-critical phase behavior in mixtures using equations of state IV. Mixtures of chained n-alkanes." Chemical Engineering Science **59**(3): 633-643.

Prajapati, D. and M. Gohain (2004). "Recent advances in the application of supercritical fluids for carbon–carbon bond formation in organic synthesis." Tetrahedron **60**(4): 815-833.

Puskas, I., R. S. Hurlbut and R. E. Pauls (1993). "Telomerization Model for Cobalt-Catalyzed Fischer-Tropsch Products." Journal of Catalysis **139**: 591-601 (and refernces therein).

Puskas, I. and R. S. Hurlbut (2003). "Comments about the causes of deviations from the Anderson-Schulz-Flory distribution of the Fischer-Tropsch reaction products." Catalysis Today **84**(1-2): 99-109.

Rathouský, J., Z. A., A. Lapidus and A. Krylova (1991). "Hydrocarbon synthesis from carbon monoxide + hydrogen on impregnated cobalt catalysts Part III. Cobalt (10%)/silica-alumina catalysts." Applied Catalysis A: General **79**: 167-180.

Reuel, R. C. and C. H. Bartholomew (1984). "Effects of support and dispersion on the CO hydrogenation activity/selectivity properties of cobalt." Journal of Catalysis **85**: 78-88.

Ribeiro, F. H., A. E. S. Von Wittenau, C. H. Bartholomew and G. A. Somorjai (1997). "Reproducibility of turnover rates in heterogeneous metal catalysis: compilation of data and guidelines for data analysis." Catalysis Reviews - Science and Engineering **39**(1&2): 49-76.

Roberts, C. B. and N. O. Elbashir (2003). "An overview to `Advances in C1 chemistry in the year 2002'." Fuel Processing Technology **83**(1-3): 1-9.

Roth, W. L. (1964). "Magnetic structure of Co3O4." Physics and Chemistry of Solids **25**: 1-10.

Sarup, B. and B. W. Wojciechowski (1988). "Studies of the Fischer-Tropsch Synthesis on a cobalt catalyst. I. Evaluation of product distribution parameters from experimental data." Canadian Journal of Chemical Engineering **66**(5): 831-42.

Sarup, B. and B. W. Wojciechowski (1989a). "Studies of the Fischer-Tropsch synthesis on a cobalt catalyst. II. Kinetics of carbon monoxide conversion to methane and to higher hydrocarbons." Canadian Journal of Chemical Engineering **67**(1): 62-74.

Sarup, B. and B. W. Wojciechowski (1989b). "Studies of the Fischer-Tropsch synthesis on a cobalt catalyst. III. Mechanistic formulation of the kinetics of selectivity for

higher hydrocarbon formation." Canadian Journal of Chemical Engineering **67**(4): 620-9.

Satterfield, C. N. and G. A. Huff, Jr. (1982). "Carbon number distribution of Fischer-Tropsch products formed on an iron catalyst in a slurry reactor." Journal of Catalysis **73**(1): 187-97.

Savage, P. E., S. Gopalan, T. I. Mizan, C. J. Martino and E. E. Brock (1995). "Reactions at supercritical conditions: applications and fundamentals." AIChE Journal **41**: 1723-78.

Schulz, H. (1999). "Short history and present trends of Fischer-Tropsch synthesis." Applied Catalysis A: General **186**(1-2): 3-12.

Schulz, H. and M. Claeys (1999). "Kinetic modelling of Fischer-Tropsch product distributions." Applied Catalysis A: General **186**(1-2): 91-107.

Seehra, M. S. and P. Silinsky (1979). "Non-stoichiometry and temperature-dependent magnetic susceptibility of CoO." Solid State Communication **31**: 183-185.

Smith, D. F., C. O. Hawk and P. L. Golden (1930). "The mechanism of the formation of higher hydrocarbons from water gas." Journal of the American Chemical Society **52**(8): 3221-3232.

Snavely, K. and B. Subramaniam (1997). "On-line Gas Chromtographic Analysis of Fischer-Tropsch Synthesis Products Formed in a Supercritical Reaction Medium." Industrial & Engineering Chemistry Research **36**: 4413-4420.

Snel, R. (1989a). "The nature of hydrocarbons synthesis by means of hydrogenation of CO on iron-based catalysts." Journal of Molecular Catalysis **53**: 143-154.

Snel, R. (1989b). "Secondary reactions of primary products of the Fischer-Tropsch synthesis : Part III. The role of butene." Journal of Molecular Catalysis **54**: 119-130.

Snel, R. and R. L. Espinoza (1987). "Secondary reactions of primary products of the Fischer-Tropsch synthesis : Part 1. The role of ethene." Journal of Molecular Catalysis **43**(2): 237-247.

Snel, R. and R. L. Espinoza (1989). "Secondary reactions of primary products of the fischer-tropsch synthesis : Part II. the role of propene." Journal of Molecular Catalysis **54**(1): 103-117.

Stanley, H. E. (1971). Introduction to Phase Transitions and Critical Phenomena. Oxford, Clarendon Press.

Stelmachowski, M. and L. Nowicki (2003). "Fuel from the synthesis gas--the role of process engineering." Applied Energy **74**: 85-93.

Stenger, H. G., H. E. Johnson and C. N. Satterfield (1984). "Molecular weight distribution of the heavy wax fraction from Fischer-Tropsch synthesis." Journal of Catalysis **86**(2): 477-80.

Steynberg, A. P., R. L. Espinoza, B. Jager and A. C. Vosloo (1999). "High temperature Fischer-Tropsch synthesis in commercial practice." Applied Catalysis A: General **186**(1-2): 41-54.

Storch, H. H., N. Golumbic and R. B. Anderson (1951). The Fischer-Tropsch and Related Synthesis. New York, Wiley.

Stranges, A. N. (2003a). Germany's Synthetic Fuel Industry 1927-45. 2003 Spring Meeting, American Insitute of Chemical Engineers (AIChE) Historical

Development of the Fischer-Tropsch Synthesis/Process - I [80a], New Oreleans, LA.

Stranges, A. N. (2003b). Synthetic Fuel Production in Prewar and World War II Japan: A Case Study in Technological Failure. 2003 Spring Meeting of the American Insitute of Chemical Engeering (AIChE) Historical Development of the Fischer-Tropsch Synthesis/Process - I [80d], New Orleans, LA.

Subramaniam, B. (2001). "Enhancing the stability of porous catalysts with supercritical reaction media." Applied Catalysis A: General **212**: 199-213.

Sun, S., K. Fujimoto, Y. Yoneyama and N. Tsubaki (2002). "Fischer-Tropsch synthesis using Co/SiO_2 catalysts prepared from mixed precursors and addition effect of noble metals." Fuel **81**(11-12): 1583-1591.

Sun, S., N. Tsubaki and K. Fujimoto (2000). "The reaction performances and characterization of Fischer-Tropsch synthesis Co/SiO_2 catalysts prepared from mixed cobalt salts." Applied Catalysis A: General **202**(1): 121-131.

Tauster, S. J. and S. C. Fung (1978). "Strong metal-support interactions: Occurrence among the binary oxides of groups IIA–VB." Journal of Catalysis **55**: 29.

Taylor, L. T. (1996). Supercritical Fluid Extraction. New York, John Wiley & Sons.

Tester, J. W., H. R. Holgate, F. J. Armellini, P. A. Webley, W. R. Killilea, G. T. Hong and H. E. Barner (1993a). Supercritical water oxidation technology: process development and fundamental research. Emerging Technologies in Hazardous Waste Management III.

Tester, J. W., P. A. Webley and H. R. Holgate (1993b). "Revised global kinetic measurements of methanol oxidation in supercritical water." Industrial & Engineering Chemistry Research **32**(1): 236-239.

Tsubaki, N. and K. Fujimoto (2000). "Product control in Fischer-Tropsch synthesis." Fuel Processing Technology **62**(2-3): 173-186.

Tsubaki, N., K. Yoshii and K. Fujimoto (2002). "Anti-ASF Distribution of Fischer-Tropsch Hydrocarbons in Supercritical-Phase Reactions." Journal of Catalysis **207**(2): 371-375.

Uner, D. O. (1998). "A Sensible Mechanism of Alkali Promotion in Fischer-Tropsch Synthesis: Adsorbate Mobilities." Industrial & Engineering Chemistry Research **37**(6): 2239-2245.

Van Berge, P. J. and R. C. Everson (1997). "Cobalt as an alternative Fischer-Tropsch catalyst to iron for the production of middle distillates." Studies in Surface Science and Catalysis (Natural Gas Conversion IV) **107**: 207-212.

Vannice, M. A. (1976). "The catalytic synthesis of hydrocarbons from carbon monoxide and hydrogen." Catalysis Reviews - Science and Engineering **14**(2): 153-191.

Wender, I., S. Friedman, W. A. Steiner and R. B. Anderson (1958). " Exchange of carbonyl groups in anhydrides with carbon monoxide. Mechanisms of carbon monoxide transfer to organic molecules via transition metals." Chemistry & Industry (London, United Kingdom): 1694-1695.

Wender, I. (1996). "Reactions of synthesis gas." Fuel Processing Technology **48**(3): 189-297.

Wolfe, H. and O. Mills (1999). Research to Focus on New Chemical Pathways for Converting Coal, Biomass, Wastes and Other Resources into Alternative Fuels. Techline News: US Department of Energy, Office of Fossil Fuels. Washington, DC.

Yakobson, D. L. (2003). Fischer-Tropsch Diesel-Meeting the California Supply Challenge. Alternative Diesel Fuel Symposium, Sacramanto, California.

Yan, S., L. Fan, Z. Zhang, J. Zhou and K. Fujimoto (1998). "Supercritical-phase process for selective synthesis of heavy hydrocarbons from syngas on cobalt catalysts." Applied Catalysis A: General **171**(2): 247-254.

Yokota, K., Y. Hanakata and K. Fujimoto (1990). "Supercritical phase Fischer-Tropsch synthesis." Chemical Engineering Science **45**(8): 2743-2749.

Zappoli, B. (2003). "Near-critical fluid hydrodynamics." Comptes Rendus Mecanique **331**: 713-726.

Zennaro, R., M. Tagliabue and C. H. Bartholomew (2000). "Kinetics of Fischer-Tropsch synthesis on titania-supported cobalt." Catalysis Today **58**(4): 309-319.

Zhan, X., K. Arcuri, R. Huang, Agee K, J. Engman and H. J. Robota (2004). "Regeneration of cobalt-based slurry catalysts for Fischer-Tropsch synthesis." Preprint Paper-American Chemical Society, Petroleum Division **49**(2): 179.

Zhan, X. and B. Davis (2002). "Assessment of internal diffusion limitation on Fischer–Tropsch product distribution." Applied Catalysis A: General **236**(1-2): 149-161.

Zhang, J., J. Chen, J. Ren, Y. Li and Y. Sun (2003). "Support effect of Co/Al2O3 catalysts for Fischer-Tropsch synthesis." Fuel **82**(5): 581-586.

Zhang, Y., D. E. Sparks, R. Spicer and B. H. Davis (2000). Steady-State Supercritical Fischer-Tropsch Synthesis on Co/SiO_2 Catalyst. Symposium on Advances in Fischer-Tropsch Chemistry, 219th National Meeting, American Chemical Society, San Francisco, American Chemical Society.

Zhou, Z., Y. Zhang, J. W. Tierney and I. Wender (2003). "Hybrid zirconia catalysts for conversion of Fischer–Tropsch waxy products to transportation fuels." Fuel Processing Technology **83**: 67-80.

APPENDIX A

A. Calculation Methods for the Activity and Selectivity

The calculations of the activity and selectivity of our catalysts (15% Co/SiO_2, HSA and LSA) were carried out from the TCD and FID results sheets.

A typical TCD results sheet as obtained from the HP integrator, that includes components detected and their retention time, is shown in Table A1. Using the example in Table A1 as case study the procedure for the calculations of conversion and methane and carbon dioxides selectivities will be carried as follows.

Table A.1 Typical TCD column detection of permanent gases as from HP integrator.

Retention Time	Gas	Area
3.224	H_2	25103
4.773	N_2	171536
5.335	CO	930233
9.616	CH_4	132134
18.231	CO_2	43637
22.345	C_2H_4	-
24.563	C_2H_6	-

A.1 CO, and H_2 Conversion, and Syngas ($CO+H_2$) Conversion Calculations

The first step in is to calculate the response factor of CO (F_{CO}) in the TCD results using the N_2 response factor (F_{N2}) as reference. The first assumption made for the this calculations is that F_{N2} is equal to unity and all other gases response factors will then be calculated relevant to that of N_2 as follows;

$$F_i = \frac{n_i \times A_{N_2} \times F_{N_2}}{n_{N_2} \times A_i} \qquad \text{(A1.1)}$$

Where n_i is the moles of either, CO, H_2, CH_4, CO_2, and C_2H_4 and n_{N2} is number of moles N_2. A_i is the area of either, CO, H_2, CH_4, CO_2, and C_2H_4 and A_{N2} is the area of N_2. F_{N2} by definition is equal to one. A standard gas cylinder with known moles percentages of N_2, CO, H_2, CH_4, CO_2, and C_2H_4 was used to calculate F_i for each of those components and the results are illustrated in Table A1.2.

Table A1.2 Response factor of permanent gases as calculated by Eqn. A1.1.

Gas	F_i
H_2	81.0[1]
N_2	1.0
CO	1.159
CH_4	1.5078
CO_2	0.8364
C_2H_4	1.342

For the determination of n_i as from the reactor effluent the percentage of N_2 in the sample is calculated as follows;

$$\%N_2 = \left(\frac{A_{Ni}}{A_{CO} \times F_{CO} + A_{Ni}}\right)100\% \tag{A1.2}$$

The initial no of moles of CO, and H_2 (n_{0j}) is then calculated as follows:

$$n_{0\,j} = \frac{n_{0\,(j+N_2)} \times (100 - \%N_2)}{100} \tag{A1.3}$$

Where $n_{0(j+N2)}$ is the initial number of mole of CO, or H_2 plus N_2 before the reaction takes place. For example, for the case of the syngas cylinder with (31.2% CO, 2% N_2 and the balance is H_2), the initial moles of CO, N_2, and H_2 at a flow rate of 50 cm^3/min is 15.6 moles, 1 moles, and 33.4 moles respectively. Therefore, $n_{0(CO+N2)}$ as in Eqn. A3 is equal to 16.6 moles. The initial number of moles is function of volumetric flow rate and syngas feed ratio. Since N_2 is not participating in the reaction the moles enter the reactor ($n_{0,\,N2}$) is actually moles leaving the reactor (i.e. $n_{0N2} = n_{1N2}$). Then moles of CO, and H_2 (nj) leaving the reactor can then be calculated as follows;

$$n_j = \frac{A_j \times F_j \times n_{0\,N_i}}{A_{N_2}} \tag{A1.4}$$

[1] The response factor of H_2 is higher than the other gases by an order of magnitude because He is used as a carrier gas in the TCD column. Detection of H_2 in He environment is poor compared to Ar for example. However, the same problem exists with Ar since it poorly detects CO_2. This is due to similarity in molecular weight which makes it difficult for the TCD detector to measure those gases relative to the carrier gas.

Then CO, and H_2 conversions can be calculated as moles consumed during the reaction per initial number of moles.

$$Convesion\ \% = \frac{n_{0j} - n_{1j}}{n_{0j}} \times 100\% \tag{A1.5}$$

Syngas ($CO+H_2$) conversion is then calculated as follows;

$$(CO + H_2\ Conversion\%) = \frac{(moles\ of\ CO\ consumed) + (moles\ of\ H_2\ consumed)}{moles\ of\ H_2 + CO\ fed}$$

or

$$(CO + H_2)\ Conversion\% = \frac{(n_{0H_2} - n_{1H_2}) + (n_{0CO} - n_{1CO})}{n_{0H_2} + n_{0CO}} \tag{A1.5}$$

The consumption rate of CO as measured by moles of CO reacted over 1 gram catalyst per second is calculated as follows;

$$CO\ Consumption\left(\frac{mol\ CO\ reacted}{g_{catalyst\ Co}\ s}\right) = \frac{n_{0CO} - n_{1CO}}{g_{Co} \times 60(s) \times 22414\left(\frac{ml}{mol}\right)} \times 100\% \tag{A1.6}$$

Table A3 shows the calculated conversions using the method illustrated in Eqn. (A1.1) to Eqn. (A1.6).

Table A1.3: Calculated activity (conversions and consumptions rate) for the data in Table A1.

Calculated term	**Value**
n_{1CO}	5.443
CO Conversion%	65.143
CO consumption rate (mol CO reacted/ g_{cat}.s)	7.565E-06
n_{1H2}	11.854
H_2 Conversion %	64.563
Syngas (H_2+CO) Conversion %	64.747

A.2 Methane, Carbon Dioxide and Ethylene Selectivity Calculations

The selectivity of CH_4, CO_2, and C_2H_4 (S_k) is calculated according to the following equation.

$$S_k = \frac{n_{1k} \times N_{k_4}}{n_{0CO} - n_{1CO}} \times 100\% \quad \text{(A2.1)}$$

Where n_{1k} is the measured moles of CH_4, CO_2, and C_2H_4 in the outlet stream of our reactor. Nk is the number of carbon molecules in the gas (i.e N_{CH4}, and N_{CO2} is equal to 1, while N_{C2H4} is 2). The calculations of n_{1k} are similar to that of n_j as in Eqn. A1.3, whereby the response factor F_k is listed in Table A1.2.

Either methane or ethylene calculated selectivity from the TCD results can be used to calculate the overall selectivity of hydrocarbon products. This will also assist in the calculation of the overall carbon balance for the reaction. This is an actual merge of TCD results and FID results for the overall analysis of the catalyst performance in FTS under the specified conditions. Eqn. A2.2 illustrates the method of calculating the selectivity of hydrocarbon (S_x) using the calculated selectivity of either methane or ethylene from the TCD results ($S_{k,TCD}$) and multiply it by the ratio of the FID areas of the hydrocarbon ($A_{x,\,FID}$) to that of either methane or ethylene ($A_{k,\,FID}$).

$$S_x = \frac{A_{x,FID}}{A_{k,FID}} \times S_{k,TCD} \quad \text{(A2.1)}$$

The results of the selectivity calculations are shown in Table A2.1.

Table A2.1 Selectivity calculations used the method illustrated in Eqn. A2.1.

Calculated term	**Value**
n_{1CH4}	1.138
CH_4 Selectivity%	11.192
n_{1CO2}	0.2088
CO_2 Selectivity %	2.053

Appendix B

B. Surface Reaction Kinetic Model

B1 Reaction network and the synthesis process illustrated in Figure 6.1

The scheme of the reaction pathway is illustrated in Figure 6.1. Rate equations are determined using Langmuir–Hinshelwood–Hougen–Watson approach as follows.

B1.1 Hydrogen adsorption on cobalt active site (S)

$$H_2 \quad + \quad 2S \overset{K_H}{\Leftrightarrow} \quad 2H.S \tag{1}$$

$$r_{H_2} = k_H P_{H_2} C_V^2 - k_{-H} C_{HS}^2 \tag{A}$$

where the hydrogen adsorption equilibrium constant $K_H = k_H/k_{-H}$ and its value is much greater than 1 (i.e. $k_H >> k_{-H}$).

B1.2 Adsorption and Disassociation of CO

i. Adsorption of CO on cobalt active site

$$CO \quad + \quad S \overset{K_{CO_1}}{\Leftrightarrow} \quad CO.S \tag{2}$$

$$r_{CO_1} = k_{CO_1} P_{CO} C_V - k_{-CO_2} C_{CO.S} \tag{B}$$

ii. Disassociation of CO

$$CO.S \quad + \quad S \overset{K_{CO2}}{\Leftrightarrow} \quad C.S \quad + \quad O.S \tag{3}$$

$$r_{CO2} = k_{CO2} C_{CO.s} C_V - k_{-CO2} C_{CO.S} \tag{C}$$

iii. The overall resulting from the two equilibriums (Eqns. 2 and 3) is

$$CO \quad + \quad 2S \overset{K_C}{\Leftrightarrow} \quad C.S + O.S \tag{4}$$

$$r_C = k_C P_{CO} C_V^2 - k_{-C} C_{C.S} C_{O.S} \tag{D}$$

B1.3 Monomer formation on the active site

The active specie **.**CH_2**.** is the monomer for the polymerization stage. The formation of this polymer is a result of the surface carbon hydrogenation in two consecutive reactions as follows;

i. Hydrogenation of surface carbon

$$C.S \quad + \quad H.S \overset{K_{C_1}}{\Leftrightarrow} \quad CH.S + S \tag{5}$$

$$r_{C-H} = k_{C_1} C_{C.S} C_{H.S} - k_{-C_1} C_{CH.S} C_V \tag{E}$$

ii. Formation of monomer **.**CH_2**.**

$$CH.S \quad + \quad H.S \overset{K_{C_2}}{\Leftrightarrow} \quad CH_2.S + S \tag{6}$$

$$r_{CH_2} = k_{C_2} C_{CH.S} C_{H.S} - k_{-C_2} C_{CH_2.S} C_V \tag{F}$$

This stage is considered as the rate controlling step for the Fischer-Tropsch synthesis and polymerization reaction to form long chain hydrocarbons.

B1.4 Oxygen removal by water formation

The oxygen removal from the active site is assumed to take place only by water formation. This is because CO_2 formation in the cobalt catalysts is minimal. Our experimental results in supercritical fluids FTS show CO_2 selectivity less than 1%. The formation of water is considered to take place in two consecutive dehydrogenation reactions as follows;

$$O.S \quad + \quad H.S \overset{K_{O_1}}{\Leftrightarrow} \quad OH.S + S \tag{7}$$

$$r_{O_1} = k_{O_1} C_{O.S} C_{H.S} - k_{-O_1} C_{OH.S} C_V \tag{G}$$

and

$$OH.S \quad + \quad H.S \overset{K_{O_2}}{\Leftrightarrow} \quad H_2O + 2S \tag{8}$$

$$r_{O_2} = k_{O_2} C_{OH.S} C_{H.S} - k_{-O_2} P_{H_2O} C_V^2 \tag{H}$$

B2 Determination of overall reaction rates

The reactant syngas (CO and H_2) disassociated on the active site of Co catalyst, followed by the hydrogenation of surface carbon (the initiation step for the monomer formation (**.**CH_2**.)**). This step is considered as the rate controlling step for the FTS reaction on a cobalt catalyst surface. Therefore, the rate of CO conversion can be determined from Eqns. (5 and E) assuming that the rate of hydrogenation on the cobalt surface is much higher than the possible dehydrogenation rate at the FTS reaction conditions.

The rate of CO consumption can then be written as follows;

$$-r_{CO} = k_{C_1} C_{C.S} C_{H.S} \tag{9}$$

B2.1 Determination of $C_{H.S}$:

From the first reaction in stage 1 (see Figure 5.12)

$$C_{H.S} = K_H^{1/2} P_{H_2}^{1/2} C_V \tag{10}$$

B2.2 Determination of $C_{C.S}$:

From the second reaction in stage 2 (see Figure 5.12)

$$C_{C.S}C_{O.S} = K_C P_{CO} C_V^2 \quad (11)$$

At steady state, each time an adsorbed carbon atom at the surface of the catalyst hydrogenated to form .CH. (its rate detereming step), an adsorbed oxygen atom must also pass through the same adsorption step to form .OH. As a result, the rate of oxygen removal (Eqn. 7) is equal to the rateof carbon hydrogenation (Eqn. 5) as follows;

$$k_{c_1} C_{C.S} C_{H.S} = k_{O_1} C_{O.S} C_{H.S}$$

$$C_{C.S} = \frac{k_{O_1}}{k_{C_1}} C_{O.S} \quad (12)$$

Substituting $C_{C.S}$ in Eqn. 11, $C_{O.S}$ can then be determined as function of CO partial pressure and the free active site as follows;

$$C_{C.S} = \sqrt{K_C \frac{k_{O_1}}{k_{C_1}}} P_{CO}^{1/2} C_V \quad (13)$$

$$C_{O.S} = \sqrt{K_C \frac{k_{C_1}}{k_{O_1}}} P_{CO}^{1/2} C_V \quad (14)$$

B2.3 Determination of the free active site concentration (C_V)

The total active sites concentration (C_t), represents the vacancies and occupied sites on a Co catalyst, can be calculated as follows;

$$C_t = C_V + \sum_{i=1}^{m} C_{ri.S} \quad (15)$$

where $C_{ri.S}$ represents the concentration of the active site occupied by one of the adsorbed components (r). We can assume here that the active radicals (.CH. and .CH_2.) and water (OH) do not occupy a significant part of the active sites and their desorption rate is higher than the others. Therefore, Eqn. 15 can be rewritten as follows;

$$C_t = C_V + C_{H.S} + C_{O.S} + C_{C.S} + C_{OC.S} \quad (16)$$

The substitution of $C_{H.S}$, $C_{C.S}$, and $C_{O.S}$ from Eqns. 10, 13, and 14 respectively, is used to determine $C_{OC.S}$ as follows

$$C_{OC.S} = K_{CO_1} P_{CO} C_V \quad (17)$$

Then C_V is calculated as follows;

$$C_V = \frac{C_t}{1 + K_1 P_{H_2}^{1/2} + K_2 P_{CO}^{1/2} + K_3 P_{CO}^{1/2} + K_4 P_{CO}} \quad (18)$$

Where,

$$K_1 = \sqrt{K_{H_2}}, \quad K_2 = \sqrt{\frac{K_c k_{c_1}}{k_{O_1}}}, \quad K_3 = \sqrt{\frac{K_c k_{O_1}}{k_{C_1}}}, \quad K_4 = K_{CO_1}$$

Then the CO rate of consumption, as in Eqn. 9, can be written as function of CO and H_2 partial pressures after substituting the corresponding values of $C_{C.S}$ and $C_{H.S}$ as follows;

$$-r_{CO} = \frac{kP_{CO}^{1/2}P_{H_2}^{1/2}}{[1+K_1P_{H_2}^{1/2}+K_2P_{CO}^{1/2}+K_3P_{CO}^{1/2}+K_4P_{CO}]^2} \quad (19)$$

where

$k = k_{C_1}K_3K_1C_t^2$

B3 Rate of methane formation

The following equations illustrate the methane formation

$$C.S + H.S \xrightarrow{k_{C_1}} CH.S + S \quad (5')$$

$$CH.S + H.S \xrightarrow{k_{C_2}} CH_2.S + S \quad (6')$$

$$CH_2.S + H.S \xrightarrow{k_{C_3}} CH_3.S + S \quad (20)$$

$$CH_3.S + H.S \xrightarrow{k_{C_4}} CH_4 + 2S \quad (21)$$

Eqn. 20 represents the formation of growth-indicating species (monomer), while Eqn. 21 is the hydrogenation of monomer to be terminated to methane. The methane rate of formation can then be determined from Eqn. 21 as follows;

$$r_{CH_4} = k_{C_4}C_{CH_3.S}C_{CH.S} \quad (22)$$

B3.1 Determination of $C_{CH3.S}$

The chain growth rate as shown in Figure 5.12 can be determined as follows;

$$R_{n-1}.S + H_2C.S \xrightarrow{k\alpha} R_n.S + S \quad (23)$$

where R_n is the growing chain containing n carbon atoms.

Two termination steps are considered in this model. The first one is the hydrogenation of R_{n-1} to produce paraffin. The second one is the hydrogenation of the alky group to produce methane. The following equations represent the two termination reactions:

$$CH_3.S + H.S \xrightarrow{k_{C_4}} CH_4 + 2S \quad (21)$$

$$R_n.S + H.S \xrightarrow{k_{t3}} R_n.H + 2S \quad (24)$$

The rate of CO consumption ($-r_{CO}$) to produce hydrocarbons can then be defined as the rate of monomer consumption in the chain growth net work. This relation described by the following equation:

$$-r_{CO} = -\frac{d(C_{CH_2.S})}{dt} \quad (26)$$

Two possibilities of monomer consumption are taking place as illustrated in Figure 5.12; either by *forming methyl species* or by *incorporating into growing chains*. Therefore, the total rate of CO consumption can also be re-written in the following format:

$$-r_{CO} = k_{C_3} C_{H.S} C_{CH_2.S} + k_\alpha C_{CH_2.S} \sum_{n=1}^{\infty} C_{R_n.S} \tag{27}$$

The assumption made here is that the rate constant for chain propagation is independent of chain length. In order to eliminate the infinite sum in Eqn. 27 the following assumption is used; at steady state the initiation rates must equal the termination rates. In this case initiation and termination of the polymerization can be represented by mass balance around the monomer .CH_3. as shown in Figure 6.2

Rate of initiation (methyl formation) = Rate of termination (methyl termination) (28)

or

$$k_{C_3} C_{CH_2.S} C_{H.S} = k_{t_3} C_{H.S} \sum_{n=1}^{\infty} C_{R_n.S} + k_{t_4} C_{CH_3.S} \sum_{n=1}^{\infty} C_{R_{n-1}.S} \tag{29}$$

The infinite term of Eqn. 29 can be replaces as follows:

$$\sum_{n=1}^{\infty} C_{R_n.S} = \frac{k_{C_3}}{k_{t_3}} C_{CH_2.S} \tag{30}$$

Then the rate consumption of CO as in Eqn. 27 can be modified as follows:

$$-r_{CO} = k_{C_3} C_{H.S} C_{CH_2.S} + k_\alpha \frac{k_{C_3}}{k_{t_3}} C^2_{CH_2.S} \tag{31}$$

From the above quadric equation $C_{CH2.S}$ can be determined as follows:

$$C_{CH_2.S} = K_5 \, C_{H.S} \left[\left(1 + \frac{K_6 (-r_{CO})}{(C_{H.S})^2} \right)^{1/2} - 1 \right] \tag{32}$$

where the parameters K5 and K6 are defined as follows:

$$K_5 = \frac{k_{t_3}}{2k_\alpha} \quad , \quad K_6 = \frac{4k_\alpha}{k_{c_3} k_{t_3}}$$

The steady state mass balance around the alkyl (Figure 6.2) can then be determined as follows:

$$k_{C_3} C_{CH_2.S} C_{H.S} = k_{C_3} C_{CH_3.S} C_{H.S} + k_\alpha C_{CH_2.S} C_{CH_3.S} \tag{33}$$

Where the concentration of methyl on the active site can be calculated as follows:

$$C_{CH_3.S} = \frac{k_{C_3} C_{CH_2.S} C_{H.S}}{k_{c_4} C_{H.S} + k_\alpha C_{CH_2.S}} \tag{34}$$

B3.2 Determination of methane rate of formation

Now the rate of methane production in Eqn. 22 can easily be determined by subsisting $C_{CH3.S}$ from Eqn. 34.

$$r_{CH_4} = \frac{K_5 k_{C_3} k_{C_4} (C_{H.S})^2 \left[\left(1 + \frac{K_6 (-r_{CO})}{(C_{H.S})^2} \right)^{1/2} - 1 \right]}{k_{c_4} + K_5 k_\alpha \left[\left(\left(1 + \frac{K_6 (-r_{CO})}{(C_{H.S})^2} \right)^{1/2} - 1 \right)^{-1} \right]} \tag{35}$$

Rate of CO consumption can then be substituted from Eqn. 9 to define methane rate of formation as function of only hydrogen and carbon surface concentrations. After substitution and rearrange of Eqn. 35, r_{CH4} can be defined as follows;

$$r_{CH_4} = \frac{\left(k_{C_3} k_{C_4} \Big/ K_5 \right) C_{H.S}^2}{k_{C_4} \Big/ K_5 k_\alpha \left[\left(\left(1 + \frac{K_6 k_{C_1} C_{C.S}}{C_{H.S}} \right)^{1/2} - 1 \right)^{-1} + 1 \right]} \tag{35}$$

The hydrogen and carbon surface concentration can then be determined from (Eqn. 10 and Eqn 13).

$$C_{H.S} = K_H^{1/2} P_{H_2}^{1/2} \frac{C_V}{C_t} \times C_t \tag{36}$$

$$C_{C.S} = K_{c_f}^{1/2} P_{CO}^{1/2} \frac{C_V}{C_t} \times C_t \tag{37}$$

where $K_{cf} = K_C \frac{k_{O_1}}{k_{C_1}}$

K_H and K_{cf} represent the adsorption equilibrium constants for hydrogen and carbon, respectively. Ct is the total concentration of the absorbed components in the cobalt surface. The fraction of the free site (θ_s) can be calculated from Eqn. 18 as follows:

$$\theta_s = \frac{C_V}{C_t} = \frac{1}{1 + K_1 P_{H_2}^{1/2} + K_2 P_{CO}^{1/2} + K_3 P_{CO}^{1/2} + K_4 P_{CO}} \tag{38}$$

Then the overall rate of methane production in presence of higher hydrocarbon formation can be calculated by substituting $C_{C.S}$ and $C_{H.S}$ (Eqns. 36 and 37) into Eqn. 35 as follows;

$$r_{CH_4} = \frac{\phi_1 P_{H_2} \theta_s^2}{\left[\phi_2 \left(\left(1 + \frac{\phi_3 P_{CO}^{1/2}}{P_{H_2}^{1/2}} \right)^{1/2} - 1 \right)^{-1} + 1 \right]} \quad (39)$$

where

$$\phi_1 = \frac{C_t^2 K_H k_{c_3} k_{c_4}}{k_\alpha}$$

$$\phi_2 = \frac{K_4}{K_5 k_\alpha}$$

and

$$\phi_3 = \frac{K_6 k_{c_1} K_{cf}^{1/2}}{K_H^{1/2}}$$

An initial investigation to the above model shows that as either P_{H2} or P_{CO} goes to zero the rate of both methane production and CO consumption whereby the power-law model that has a negative exponent of P_{CO} shows poor results especially at low hydrogen partial pressure in syngas.

More details on the surface reaction kinetic model are given in the following references:

(1) Kellner, C. S.; Bell, A. T. *Journal of Catalysis* **1981**, *70*, 418.
(2) Sarup, B.; Wojciechowski, B. W. *Canadian Journal of Chemical Engineering* **1989**, *67*, 62.
(3) Uner, D. O. *Industrial & Engineering Chemistry Research* **1998**, *37*, 2239.
(4) Bell, A. T. *Catalysis Reviews - Science and Engineering* **1981**, *23*, 203.

APPENDIX C

C. Program for the determination of rate equation constants

C1. BCONF/DBCONF (Single/Double precision)

Minimize a function of N variables subject to bounds on the variables using a quasi-Newton method and a finite-difference gradient.

Usage

```
CALL BCONF (FCN, N, XGUESS, IBTYPE, XLB, XUB, XSCALE,
FSCALE, IPARAM, RPARAM, X, FVALUE)
```


Arguments

FCN — User-supplied SUBROUTINE to evaluate the function to be minimized. The usage is CALL FCN (N, X, F), where
N – Length of X. (Input)
X – Vector of length N at which point the function is evaluated. (Input)
X should not be changed by FCN.
F – The computed function value at the point X. (Output)
FCN must be declared EXTERNAL in the calling program.

N — Dimension of the problem. (Input)

XGUESS — Vector of length N containing an initial guess of the computed solution. (Input)

IBTYPE — Scalar indicating the types of bounds on variables. (Input)

IBTYPE	Action
0	User will supply all the bounds.
1	All variables are nonnegative.
2	All variables are nonpositive.
3	User supplies only the bounds on 1st variable, all other variables will have the same bounds.

XLB — Vector of length N containing the lower bounds on variables. (Input, if IBTYPE = 0; output, if IBTYPE = 1 or 2; input/output, if IBTYPE = 3)

XUB — Vector of length N containing the upper bounds on variables. (Input, if IBTYPE = 0; output, if IBTYPE = 1 or 2; input/output, if IBTYPE = 3)

XSCALE — Vector of length N containing the diagonal scaling matrix for the variables. (Input)
XSCALE is used mainly in scaling the gradient and the distance between two points. In the absence of other information, set all entries to 1.0.

FSCALE — Scalar containing the function scaling. (Input)
FSCALE is used mainly in scaling the gradient. In the absence of other information, set FSCALE to 1.0.

IPARAM — Parameter vector of length 7. (Input/Output)
Set IPARAM(1) to zero for default values of IPARAM and RPARAM. See Comment 4.

RPARAM — Parameter vector of length 7. (Input/Output)
See Comment 4.

X — Vector of length N containing the computed solution. (Output)

FVALUE — Scalar containing the value of the function at the computed solution. (Output)

Comments

1. Automatic workspace usage is
BCONF N * (2 * N + 8) + N units, or
DBCONF 2 * N * (2 * N + 8) + N units.
Workspace may be explicitly provided, if desired, by use of
B2ONF/DB2ONF. The reference is

```
CALL B2ONF (FCN, N, XGUESS, IBTYPE, XLB, XUB,
XSCALE, FSCALE, IPARAM, RPARAM, X,
FVALUE, WK, IWK)
```

The additional arguments are as follows:
WK — Real work vector of length N * (2 * N + 8). WK contains the following information on output: The second N locations contain the last step taken. The third N locations contain the last Newton step. The fourth N locations contain an estimate of the gradient at the solution. The final N2 locations contain a BFGS approximation to the Hessian at the solution.
IWK — Work vector of length N.
IPARAM — Integer vector of length 7.
IPARAM(1) = Initialization flag.
IPARAM(2) = Number of good digits in the function.
Default: Machine dependent.
IPARAM(3) = Maximum number of iterations.
Default: 100.
IPARAM(4) = Maximum number of function evaluations.
Default: 400.
IPARAM(5) = Maximum number of gradient evaluations.
Default: 400.
IPARAM(6) = Hessian initialization parameter.
If IPARAM(6) = 0, the Hessian is initialized to the identity matrix; otherwise, it is initialized to a diagonal matrix containing on the diagonal where t = XGUESS, fV = FSCALE, and s = XSCALE.
Default: 0.
IPARAM(7) = Maximum number of Hessian evaluations.
Default: Not used in BCONF.
RPARAM — Real vector of length 7.
RPARAM(1) = Scaled gradient tolerance.
The i-th component of the scaled gradient at X is calculated as

$$\frac{g\,x\,s}{f\,x\,f}$$

where $g = \nabla f(x)$, s = XSCALE, and fV = FSCALE.
Default:

$$\varepsilon\,\varepsilon\,,3$$

in double where ε is the machine precision.
RPARAM(2) = Scaled step tolerance. (STEPTL)
The i-th component of the scaled step between two points x and y is computed as

$$\frac{x\,y}{x\,s}$$

where s = XSCALE.
Default: ε2/3 where ε is the machine precision.
RPARAM(3) = Relative function tolerance.
Default: max(10-10, ε2/3), max (10-20, ε2/3) in double where ε is the machine precision.
RPARAM(4) = Absolute function tolerance.
Default: Not used in BCONF.

RPARAM(5) = False convergence tolerance.
Default: 100ε where ε is the machine precision.
RPARAM(6) = Maximum allowable step size.
Default: 1000 max(ε1, ε2) where
RPARAM(7) = Size of initial trust region radius.
Default: based on the initial scaled Cauchy step.
If double precision is required, then DU4INF is called and RPARAM is declared double precision.
5. Users wishing to override the default print/stop attributes associated with error messages issued by this routine are referred to "Error Handling" in the Introduction.

Algorithm

The routine BCONF uses a quasi-Newton method and an active set strategy to solve minimization problems subject to simple bounds on the variables. The problem is stated as follows:

$$\min_{x \in \mathbf{R}^n} f(x)$$

subject to $l \le x \le u$

From a given starting point xF, an active set IA, which contains the indices of the variables at their bounds, is built. A variable is called a "free variable" if it is not in the active set. The routine then computes the search direction for the free variables according to the formula

$d = -B\text{-}1\ gF$

where B is a positive definite approximation of the Hessian and gF is the gradient evaluated at xF; both are computed with respect to the free variables. The search direction for the variables in IA is set to zero. A line search is used to find a new point xQ ,

$xQ = xF + \lambda d, \lambda \in (0, 1]$

such that

$f(xQ) \le f(xF) + \alpha g7\ d, \alpha \in (0, 0.5)$

Finally, the optimality conditions

$||g(xL)|| \le \varepsilon, lL < xL < uL$

$g(xL) < 0, xL = uL$

$g(xL) > 0, xL = lL$

are checked, where ε is a gradient tolerance. When optimality is not achieved, B is updated according to the BFGS formula:

$$B\ B$$

$$Bss\ B$$

where $s = xQ - xF$ and $y = gQ - gF$. Another search direction is then computed to begin the next iteration.

C2. Program Sample

USE numerical libraries

```
C       EXTERNAL IVPAG
        INTEGER N
        PARAMETER (N=5)
        INTEGER IPARAM(7), ITP, L, NOUT
        REAL F, FSCALE, RPARAM(7), X(N), XGUESS(N),
     & XLB(N), XSCALE(N), XUB(N)
        EXTERNAL ROSBRK
 C Initial values for the rate constants
        DATA XGUESS/0.00005E0, 0.00004E0, 0.000001E0, 0.00009E0, 0.0001E0/
        DATA XSCALE/1.0E0, 1.0E0, 1.0E0,1.0E0,1.0E0/
        DATA FSCALE/1.0E0/
        DATA XLB/0.0E0, 0.0E0, 0.0E0, 0.0E0, 0.0E0/
        DATA XUB/5000.0E0, 5000.0E0, 100.0E0, 100.0E0, 100.0E0/

        ITP = 0
        IBTYPE = 1
        IPARAM(1) = 0
        IPARAM(3) =1000
        RPARAM(2) = 0.01

        CALL BCONF (ROSBRK, N, XGUESS, ITP, XLB, XUB, XSCALE, FSCALE,
     &IPARAM, RPARAM, X, F)


        WRITE (*,*) X, F, (IPARAM(L),L=3,5)
        STOP
        END

        SUBROUTINE ROSBRK (N, X, F)
        INTEGER N
        REAL X(N), F

        REAL actualrate(2), PCO(2), calc_rate(2), PH2(2)
C Write actual rate (1) Input
        actualrate(1)=1.155
C Write actual rate (2) Input
        actualrate(2)=0.859
C Write CO partial pressures (1) and (2) correspond to the actual rates (1) and (2),
C respectively.
        PCO(1)=88.9
        PCO(2)=152


C Write H2 partial pressures (1) and (2) correspond to the actual rates (1) and (2),
C respectively.
```

```
      PH2(1)=244
      PH2(2)=201
C Calculate the rate of the reaction
      DO 9 K=1,2,1
      calc_rate(k)=(X(1)*(PCO(k)**0.5)*(PH2(k)**0.5))/((1+X(2)
     &*(PH2(k)**0.5)+X(3)*(PCO(k)**0.5)+X(4)*(PCO(k)**0.5)+X(5)
     &*PCO(k))**2)
 9   CONTINUE
C Minimize the difference between the actual rate and the calculated rate
      DO 10 J=1,2,1
      FF = FF+(calc_rate(j)-actualrate(j))**2
 10  CONTINUE
      F=FF

      RETURN
      END
```